SERBIAN ACADEMY OF
NONLINEAR SCIENCE

2nd CONFERENCE ON NONLINEARITY

Editors

B. Dragovich, Ž. Čupić

Belgrade, 2022

SERBIA

P r o c e e d i n g s

of the

2nd CONFERENCE ON NONLINEARITY

(October 18 – 22, 2021, Belgrade, Serbia)

Editors

B. Dragovich, Ž. Čupić

Publisher

Serbian Academy of Nonlinear Sciences

Belgrade, 2022

SERBIA

Naslov: 2nd CONFERENCE ON NONLINEARITY
(Druga konferencija o nelinearnosti) Autor: Grupa autora
Izdavač: Srpska akademija nelinearnih nauka, Beograd, Srbija
Godina izdanja: 2022
Štampa: Skripta internacional, Beograd
Tiraž: 120
ISBN: 978-86-905633-7-1
Urednici: Dragović Branko, Čupić Željko
Nelinearne nauke-Zbornici

CIP - Каталогизација у публикацији Народна библиотека Србије, Београд

530.182(082)
51-7:53(082)

CONFERENCE on Nonlinearity (2 ; 2021 ; Beograd)
Proceedings of the 2nd Conference on Nonlinearity, (October 18 – 22, 2021, Belgrade, Serbia) / editors B. [Branko] Dragovich, Ž. [Željko] Čupić ; [organizer] Serbian Academy of Nonlinear Sciences [(SANS)], Belgrade. - Belgrade : Serbian Academy of Nonlinear Sciences = Beograd : Srpska akademija nelinearnih nauka,
2022 (Beograd : Skripta internacional). - VIII, 300 str. : ilustr. ; 25 cm

Nasl. u kolofonu: Druga konferencija o nelinearnosti. - Str. V-VI: Preface / Branko Dragovich, Zeljko Cupic. - Napomene uz radove. - Bibliografija uz većinu radova. - Registar.

ISBN 978-86-905633-7-1

a) Нелинеарне теорије -- Зборници b) Математичка физика -- Зборници

COBISS.SR-ID 81001225

2nd Conference on Nonlinearity

Belgrade, October 18 - 22, 2021

Organizer

- **Serbian Academy of Nonlinear Sciences (SANS), Belgrade**

Coorganizers

- **Mathematical Institute, Serbian Academy of Sciences and Arts, Belgrade,**
- **Faculty of Mathematics - University of Belgrade,**
- **Institute of Chemistry, Technology and Metallurgy - University of Belgrade,**

and

- **Faculty of Sciences and Mathematics - University of Niš**

Sponsor

- **Ministry of Education, Science and Technological Development, Republic of Serbia**

INTERNATIONAL ADVISORY COMMITTEE

- Andrew Adamatzky (Bristol, UK)
- Irina Ya. Arefeva (Moscow, Russia)
- Milan S. Dimitrijević (Belgrade, Serbia)
- Ćemal Dolićanin (Novi Pazar, Serbia)
- Nenad Filipović (Kragujevac, Serbia)
- Dezso Horvath (Szeged, Hungary)
- Zoran Jakšić (Belgrade, Serbia)
- Dušan Jovanović (Belgrade, Serbia)
- Nenad Mladenovic (UAE)
- Sergei D. Odintsov (Barcelona, Spain)
- Zoran Ognjanović (Belgrade, Serbia)
- Zoran Rakić (Belgrade, Serbia)
- Branislav Sazdović (Belgrade, Serbia)
- Ryo Yoshida (Tokyo, Japan)
- Anatoly Zagorodny (Kiev, Ukraine)

INTERNATIONAL PROGRAM COMMITTEE

- Milivoj Belić (Doha, Qatar)
- Livija Cvetićanin (Novi Sad, Serbia)
- Željko Čupić (Belgrade, Serbia)
- Vladan Djordjević (Belgrade, Serbia)
- Branko Dragovich (Belgrade, Serbia)
- Miloš Kojić (Houston, USA)
- Ljiljana Kolar Anić (Belgrade, Serbia)
- Miguel A. F. Sanjuan (Madrid, Spain)
- Igor V. Volovich (Moscow, Russia)

LOCAL ORGANIZING COMMITTEE

- Branko Dragovich , Chairman (SANS, Inst. Phys., Belgrade)
- Željko Čupić, Vice Chairman (SANS, IHTM, Belgrade)
- Ivana Atanasovska (SANS, MI SASA, Belgrade)
- Ivan Dimitrijević (Faculty of Mathematics, Belgrade)
- Goran Djordjević (SANS, SEENET, Faculty of Sciences, Niš)
- Božidar Jovanović (SANS, MI SASA, Belgrade)
- Predrag Jovanović (SANS, Astron. Observatory, Belgrade)
- Branko Urošević (SANS, School of Computiong, Belgrade)

PREFACE

This book contains some papers related to the talks presented at the *2nd Conference on Nonlinearity*, held online on October 18–22, 2021. The conference is organized by the Serbian Academy of Nonlinear Sciences (SANS) in cooperation with the Mathematical Institute (Serbian Academy of Sciences and Arts), Faculty of Mathematics (University of Belgrade), Institute of Chemistry, Technology and Metallurgy (University of Belgrade), and Faculty of Sciences and Mathematics (University of Niš).

It is well known that nonlinear phenomena and processes are present everywhere in nature – from fundamental interactions between elementary particles, via various terrestrial processes in fluids and optics, to the dynamics of celestial objects and the evolution the universe as a whole. Nonlinear methods, in particular nonlinear differential equations, are used in research of all sciences – from fundamental to applied. Contemporary comfortable human life largely depends on technological achievements based on nonlinear processes.

Serbian Academy of Nonlinear Sciences is a scientific society whose members are scientists that significantly contributed to developments of nonlinear sciences in Serbia. The main goal of SANS is a strong fruitful support to versatile developments of nonlinear sciences, particularly in Serbia. Organization of scientific meetings – colloquiums and conferences on nonlinearity – are among principal activities of SANS. SANS strives to connect as much as possible with scientists and related scientific activities throughout the world. More information on the Serbian Academy on Nonlinear Sciences is available at its website http://www.sann.kg.ac.rs/en/sans/.

About 70 scientists from 19 countries participated in this conference (Australia, Austria, France, Germany, Hungary, India, Israel, Japan, Poland, Qatar, Romania, Russia, Serbia, Slovenia, Spain,

UAE, UK, Ukraine, USA). Lectures were given by 4 keynote speakers (45 min.), 9 invited speakers (35 min.) and 35 other participants (25 min.). Some details can be seen on the conference website http://www.nonlinearity2021.matf.bg.ac.rs/.

On behalf of the Serbian Academy of Nonlinear Sciences, we would like to express our gratitude to the Ministry of Education, Science and Technological Development of the Republic of Serbia for a financial support to publish these Proceedings. We are also thank the Coorganizers and the management of the journal Symmetry for a support of this conference. In particular, we are thankful to all speakers and the authors of contributions to the Proceedings. We hope very much that this collection of papers will be useful not only to participants of this conference but also to all others who are interested in nonlinearity.

The Serbian Academy of Nonlinear Sciences plans to continue with the organization of Conferences on Nonlinearity regularly with a period of two years. It is our great wish that next year there will be no problem with the Corona virus epidemic and that the third conference will be held in person. We will be happy to see all participants of the first two conferences again, as well as many new ones.

Belgrade, Summer 2022

E d i t o r s

Branko Dragovich
(President of SANS)

Zeljko Cupic
(General secretary of SANS)

CONTENTS

M. P. Cartmell
On the terrestrial measurement of frame-dragging 1

I. D. Atanasovska, D. B. Momcilovic
Analysis of contact fatigue coupled with geometry and material nonlinearities by Theory of critical distances 27

M. M. Filipovic, Lj. B. Kevac
The procedure of generating trajectory of motion of carrier conveyor for granular material in dependance of pod systems characteristics 48

F. Geogriades
Design of a mechanical system to admit similar rigid body nonlinear modes and the correlation with perpetual mechanics 63

K.-Y. Huang, Y. Zhao, L. Xue, J.-R. He, K.-W. Wang, S.-L. Xu, M. R. Belić, B. A. Malomed
Supporting quantum squeezing in two component solitons by means of electromagnetically-induced transparency 79

A. Obradović
Mass minimization of an AFG Timoshenko beam with coupled axial and bending vibrations 96

V. Skarka, M. Lekić
Self-organized bridge connecting THEORY to EXPERIMENTS 109

S. Zdravković, D. Ranković
W-potentials in nonlinear biophysics of microtubules 136

S. Paunović,
Modelling the Steel Fibre Reinforced Concrete material nonlinearity with ANSYS 150

Ž. Čupić, A. Ivanović-Šašić
Bray-Liebhavsky reaction: From monotonous to chaotic evolution 170

C. N. Babalic, R. Constantinescu
Auxiliary equations for solving nonlinear evolutionary equations 200

D. Jovanović, O. Alexandrova, M. Maksimović, M. Belić
Fluid theory of coherent magnetic vortices in high-β space plasmas 212

P. Jovanović, V. Borka Jovanović, D. Borka, A. F. Zakharov
Graviton mass and Yukawa-like nonlinear correction to the gravitational potential: constraints from stellar orbits around the Galactic Center 232

A. Maluckov, D. Leykam, S. Flach, A. Mančić, E. Smolina, D. Smirnova
Scanning band topology by the modulation instability 246

Nikola Petrović
Exact traveling and solitary wave solutions to the generalized Gross-Pitaevskii equation with cylindrical potential 259

R. Cimpoiasu, R. Constantinescu, G. Florian, A. Pauna
Reduction methods and travelling wave solutions for nonlinear evolutionary phenomena 268

B. Dragovich
On *p*-adic scalar matter 280

Talks not presented to the Proceedings 297

List of participants 299

On the terrestrial measurement of frame-dragging [*]

Matthew P. Cartmell[†]
Department of Mechanical & Aerospace Engineering, University of Strathclyde, Glasgow, G1 1XJ, Scotland, UK.

ABSTRACT

This paper considers the Foucault pendulum and its possible application as a measurement instrument for the relativistic effect of Lense-Thirring precession from frame-dragging. We discuss the Foucault pendulum under different forms of excitation. The first is through parametric excitation of the length, effective for overcoming natural aerodynamic and frictional dissipations and for amplification and ellipticity control of the response. The second is through coupling between a strong bob magnet and an exciter coil directly underneath, without the bob moving vertically at the frequency of parametric excitation. The achievements of the GP-B and LAGEOS missions in measuring frame-dragging in low Earth orbit are noted for comparison. The natural location for a frame-dragging measurement is polar and we derive an expression for Lense-Thirring precession using a gravitoelectromagnetic analogy for non-polar locations. The paper attempts to clarify the main challenges of this measurement.

1. Introduction

We start with the premise that an *inertial* frame is defined as one that is not accelerating in the usual detectable sense. General Relativity states that inertial frames are 'influenced and dragged by the distribution and flow of mass–energy in the universe', noting the relativistic equivalence of mass and energy [1]. This dragging of inertial frames is simply called frame-dragging and influences, for example, the flow of time around a spinning body.

A theory for frame-dragging was proposed by Lense and Thirring in 1918, in which inertial frames are dragged around a central *rotating* mass due to the

[*] The author would like to thank the following people for their valuable comments and suggestions: J.E.Faller, J.Hough, N.A.Lockerbie, R.Schumacher, and K.S.Thorne. Acknowledgement is also due to the University of Strathclyde for on-going access to laboratory facilities.

[†] e-mail address: matthew.cartmell@strath.ac.uk

effect of its angular momentum on the surrounding spacetime [2]. The rotation of the central mass twists the surrounding spacetime, which will perturb any nearby spinning gyroscope. For such a gyroscope in orbit around the Earth, for example, its axis of rotation will precess: this effect is known as Lense-Thirring precession, and henceforth as LT precession. In fact, Earth's curvature of spacetime is capable of generating frame-dragging that is generally considered to be demonstrable in three gravitomagnetic manifestations:

- by the precession of a gyroscope in orbit around the Earth, just mentioned,
- by the precession of orbital planes, where a mass orbiting the Earth constitutes a gyroscope whose orbital axis will precess, under appropriate conditions, and
- by the precession of the periapsis of the orbit of a test mass about the Earth.

GP-B measured the first two [3], and the LAGEOS satellites measured the second one only [4]. LAGEOS measured the LT drag of the satellite orbital planes to be ~0.031 arcsecs/year [1], which is ~ $8.611*10^{-6}$ °/year. This was subject to error that was difficult to quantify, due to uncertainty in the Earth's mass distribution, and the effects of atmospheric drag, and there is still some debate about the true size of the error in LAGEOS's measurement, but it is thought mainly to have derived from the low eccentricity of the LAGEOS orbits and the difficulties in eliminating Earth multipoles. In contrast, GP-B measured LT to be ~ 0.037 arcsecs/year [1], which equates to $10.833*10^{-6}$ °/year. GP-B used *IM Pegasi HR 8703* as the guide star and operated on a highly circular polar orbit of 642 km altitude [1]. The spin axes of GP-B's gyroscopes drifted and the geodetic precession [5] (due simply to the presence of the mass of Earth rather than its presence *and* its rotation) was itself measured to an impressive precision of 1.5 %. The total relativistic precession of such a spinning body is the vector sum of the LT and geodetic precessions, whose components in the case of GP-B were usefully at right angles to each other. Our main interest is the LT component. It is important to note that the relativistic frame-dragging effect evidenced by LT precession is about ten million times smaller than, for example, the classical Newtonian effects operating on the plane of the LAGEOS orbits, requiring an 'enormously accurate treatment of background effects' [6]. The analysis behind LT precession, in terms of (weak) gravitomagnetic effects on an accelerating mass, can be considered analogously with a circulating charge producing a magnetic field. Specifically, the analogy is between the equations that govern the torques on a spinning electric charge with magnetic moment μ moving through a magnetic field, and the torques on a spinning test-mass moving under the influence of a large and nearby rotating mass [1], and this analogy is

made through Maxwell's equations which we return to later. Karl Schwarschild [7] proposed an exact solution, now known as the Schwarschild metric, for the tensor governing the space surrounding a large non-rotating spherical body, and this fully describes curved (non-Euclidean) space. On the other hand, the Kerr metric accounts for the rotation of the massive body [7], and the mean GP-B measurement of LT precession was within ~5 % of the value predicted by using the Kerr metric — but with a measurement error estimated at approximately ±19 % . The general Kerr solution for LT precession is somewhat complicated, but in the vicinity of the Earth we are dealing with weak fields and non-relativistic velocities, so that the full form of general relativity is not necessary and a linearised version of the theory is sufficient [8]. If we consider spacetime to be stationary around the Earth, i.e. mass and fluid velocity distributions are unchanging, in spite of the Earth's rotation, then this simplifying stationarity can be used as a basis for a '3+1 slicing' of spacetime, in terms of the spatial (3) and time (1) dimensions. This means that the spacetime metric tensor $g_{\mu\nu}$ then decomposes naturally into constituent parts, and because of the prevailing conditions of weak gravity and non-relativistic (low) velocities this decomposition can be used to form the basis of a useful analogy with electromagnetism as expressed by Maxwell's equations, from which an expression for LT precession can eventually be obtained [8,9].

1.1 Lense-Thirring precession about the Earth

We start with gravitational analogies for the electromagnetic scalar and vector potentials taken from the Kerr spacetime metric, stated in terms of the time-time and time-space components, where *c* is the speed of light,

$$\Phi = \frac{1}{2}(g_{00} - 1)c^2 \tag{1}$$

$$A_i = g_{0i}c^2. \tag{2}$$

To get the analogies we take Maxwell's equations in their usual form,

$$\nabla . \bar{E} = \frac{\rho}{\varepsilon_0} \tag{3}$$

$$\nabla . \bar{B} = 0 \tag{4}$$

$$\nabla \times \bar{E} = -\frac{\partial \bar{B}}{\partial t} \tag{5}$$

$$\nabla \times \bar{B} = \mu_0 \bar{J} + \mu_0 \varepsilon_0 \frac{\partial \bar{E}}{\partial t}. \tag{6}$$

We then look at the physical context for Maxwell's equations. Equation (3) states that the quantity of electric field coming from a region of space is proportional to the total electric charge in that region of space. Equation (4) states that the magnetic field doesn't come or go but travels in a continuous loop. Equation (5) says that the curl of the electric field is equal to the negative of the rate of change of the magnetic field. Changing the magnetic field alters the curl of the electric field, with the negative sign defining that they go in opposite directions. So, the curl of the electric field pushes electric charge round in a circle in the form of an electric current. Finally, equation (6) says that the curl of the magnetic field is proportional to the current density and a changing electric field. Defining terms precisely: $\bar{E}$ is the electric field, ρ is the electric charge density, ε_0 is the permittivity of free space, $\bar{B}$ is the magnetic field, μ_0 is the permeability of free space, and $\bar{J}$ is the current density.

We then bring in the gravitoelectric field $\bar{E}_G$ and the gravitomagnetic field $\bar{H}$ and it is well known that they are related to the potentials of equations (1) and (2) according to the simplifying Lorentz gauge [10], as follows,

$$\bar{E}_G = -\nabla\Phi - \frac{1}{4c}\frac{\partial \bar{A}}{\partial t} \tag{7}$$

$$\bar{H} = \nabla \times \bar{A}. \tag{8}$$

In the analogy given by [8], the electric field of Maxwell's equations $\bar{E}$ becomes the gravitoelectric field $\bar{E}_G$ and the magnetic field of Maxwell's equations $\bar{B}$ becomes the gravitomagnetic field $\bar{H}$. The electric charge density ρ becomes the mass density ρ_m. The charge current density $\bar{J}$ becomes the mass current density defined by $G\rho_m\bar{v}$, where G is Newton's gravitational constant and $\bar{v}$ is the velocity of the source mass. These substitutions are applied by means of the analogy in order to generate the gravitational analogue of Maxwell's electromagnetic equations,

$$\nabla.\bar{E}_G = -4\pi G\rho_m \tag{9}$$

$$\nabla.\bar{H} = 0 \tag{10}$$

$$\nabla \times \bar{E}_G = 0 \tag{11}$$

$$\nabla \times \bar{H} = 4\left[-4\pi G\frac{\rho_m\bar{v}}{c} + \frac{1}{c}\frac{\partial \bar{E}_G}{\partial t}\right]. \tag{12}$$

Despite some structural similarities between the equations which emerge from the gravitational analogy, (9)-(12), and Maxwell's equations themselves,

equations (3)-(6), there are still some qualifiers and provisos to be made, [8] as follows:

- gravity is attractive, but electromagnetism is both attractive and repulsive (this difference leads to the minus signs in the RHS 'source terms' in equations (9) and (12),
- the gravitational tensor introduces the additional 4 in equation (12),
- the space-space components from the gravitational metric tensor correspond to curved space rather than Euclidean space. As we are only interested here in the effects of the Earth's rotation on an orbiting test mass then we can neglect the curvature of space and also those terms that are not gravitometric and of the order of $\left(\frac{v}{c}\right)^2$.

Assuming that equations (9)-(12) can be used to find the gravitoelectric and gravitomagnetic fields, the force on an orbiting test mass can be found from,

$$\bar{F} = m\bar{E}_G + \frac{m}{c}\bar{v} \times \bar{H} \tag{13}$$

from which we get,

$$m\frac{d\bar{v}}{dt} = -\frac{\alpha}{r^2}\bar{n} + \frac{m}{c}\bar{v} \times \bar{H} \tag{14}$$

and where $\bar{r} = r\bar{n}$ is the orbital radius vector of the test mass m and $\alpha = GMm$, where M is the mass of the Earth. We recall that $\bar{H}$ is the gravitomagnetic field due to the Earth's rotation and note that this can be found from equations (9)-(12). Because, in general, the magnetic moment is given by,

$$\bar{\mu} = \frac{1}{2c}\int [\bar{r} \times \bar{j}]dV$$

where $\bar{j}$ is the electric current density, so the gravitational analogy leads to,

$$\bar{\mu}_G = -4G\frac{1}{2c}\int \rho_m\,[\bar{r} \times \bar{j}]dV = -2G\frac{\bar{S}}{c} \tag{15}$$

where $\bar{S} = \int \rho_m[\bar{r} \times \bar{j}]dV$, this being the rotating gravitating body's proper angular momentum. The conventional magnetic moment $\bar{\mu}$ creates a dipole magnetic field, given by,

$$\bar{B} = \frac{3\bar{n}(\bar{n}\cdot\bar{\mu})-\bar{\mu}}{r^3}$$

so, inserting $\bar{\mu}_G$ instead of μ leads to a form which now represents the Earth's dipolar gravitomagnetic field,

$$\bar{H} = \frac{2G}{c}\left[\frac{\bar{S}-3\bar{n}(\bar{n}\cdot\bar{S})}{r^3}\right]. \tag{16}$$

The abstract angular momentum for the large rotating body $\bar{S}$ can be replaced by the angular momentum specific to the Earth, defined as $\bar{L}'$ in [8], so we can extract the Earth's angular velocity as,

$$\bar{\Omega} = \frac{2G}{c^2 r^3}\bar{L}'. \tag{17}$$

Therefore, the gravitomagnetic field stated in equation (16) can now be restated in terms of the Earth's angular velocity, where $\bar{S} \equiv \bar{L}'$, noting that it is divided by the velocity of light in order to accommodate equation (17) correctly,

$$\frac{\bar{H}}{c} = \bar{\Omega} - 3\bar{n}(\bar{\Omega} \cdot \bar{n}). \tag{18}$$

In order to proceed to the LT precession we need to revert to explicit angular momentum of the Earth, through equation (17) and then rearrange to get the gravitomagnetic field in terms of fundamental quantities and in the conventional form, as follows,

$$\bar{H} = \frac{4G}{c}\left[\frac{\bar{L}'r^2 - 3\bar{r}(\bar{L}'\cdot\bar{r})}{2r^5}\right]. \tag{19}$$

One can find the same result for $\bar{H}$ in [10] although the notation and the aggregation of constants is done differently there. Before we complete the analysis for the LT precessional term we state the general expression for the spin precession rate for LT from the Schiff formula statement of the LT metric [11], which is,

$$\bar{\Omega}_{Tot} = \bar{\Omega}_{Th} + \bar{\Omega}_{Geo} + \bar{\Omega}_{LT} \tag{20}$$

where $\bar{\Omega}_{Tot}$ is the total angular velocity measured, assuming an orbital test mass such as a satellite containing gyrospcopic measurement instruments. The right-hand side terms of equation (20) are the Thomas precession $\bar{\Omega}_{Th}$, the geodetic precession $\bar{\Omega}_{Geo}$, and the LT precession $\bar{\Omega}_{LT}$. Concentrating on the LT precession, averaging over fast orbital motions [8] and persevering with the notation of [8], we find [12] that LT is directly equal to,

$$\bar{\Omega}_{LT} = \frac{\bar{H}}{2c} \tag{21}$$

and so for a closely orbiting body equation (19) gives this for the averaged gravitomagnetic field at the poles,

$$\bar{H}_{poles} = \frac{4G}{c}\frac{\bar{L}\prime}{r^3} \tag{22}$$

and if we now move from a general closely orbiting body to a specific terrestrial location where there is a body elevated at h from the surface of the Earth (therefore at altitude R, where $R = r_E + h$, and r_E is the radius of the Earth at the location), then the LT precession from equation (19) is given for both northern and southern latitudes, by,

$$\Omega_{LT} = \frac{G}{c^2 R^3} L' \left|1 - 3|\bar{z}.\bar{r}|\right|. \tag{23}$$

The scalar angular momentum L' is given by $L' = I_\oplus \Omega_\oplus$, and considering the Earth initially as a non-oblate sphere then $I_\oplus = \frac{2}{5} M {r_E}^2$. But the actual radius of gyration of the Earth is 0.576 r_E [13], so the factor of $\frac{2}{5}$ becomes 0.576^2 which is 0.3316. Therefore $I_\oplus = 0.3316\, M {r_E}^2$, from which we obtain,

$$\Omega_{LT} = \frac{0.3316\, GM\Omega_\oplus}{c^2 R} \left|1 - 3|cos\theta|\right| \tag{24}$$

where $\bar{z} \cdot \bar{r} = cos\theta$ and $R \approx r_E$ for h very small indeed. This result does not include the geodetic precession and is purely the LT component. The angle θ is the colatitude which is the included angle between $\bar{z}$ and $\bar{r}$ (the spin axis of Earth and the local vertical axis at the location, respectively) so $\theta = \frac{\pi}{2} - \phi$, where ϕ is the latitude as measured north or south from the equator. At the poles, from equation (22), we get a reduced form of equation (23) as follows,

$$\Omega_{LT} = \frac{2G}{c^2 R^3} L' (\bar{Z} \cdot \bar{z}). \tag{25}$$

This simplifies to the following after making the appropriate substitutions,

$$\Omega_{LT} = \frac{0.6632\, GM\Omega_\oplus}{c^2 R} cos\theta. \tag{26}$$

1.2 Theoretical predictions for LT precession at the North Pole and at Glasgow

The following numerical data can be used to calculate the precession both at the North Pole and at Glasgow: G = 6.67408*10^{-11} m^3 kg^{-1} s^{-2}, M = 5.972*10^{24} kg, $\Omega_\oplus$ = 7.2921150*10^{-5} rad/s, c = 2.99792488*10^8 m/s, R = 6356*10^3 m at the North Pole, R = 6363.18*10^3 m at Glasgow, ϕ = 1.5707963 rad at the North Pole, ϕ = 0.9750 rad at Glasgow. Pippard [14] gives the LT precession as 220 mas/year at the North Pole. Ruggiero & Tartaglia [12] state the LT precession at the North Pole to be 281 mas/year. Using equations (24) or (26) and the above data we get Ω_{LT} = 219.5 mas/year at the North Pole. By changing both the latitude and the radius of the Earth to the values for the location of Glasgow the LT precession there can be calculated using equation (24) to be Ω_{LT} = 162.6 mas/year.

2. Calculation of LT precession at co-latitude θ

The LT precession measured at co-latitude θ is given by equation (27) and comprises the measured precession of the pendulum bob m with respect to the Earth (first RHS term) minus the apparent precession associated with a guide star relative to the Earth (second RHS term) minus the precession of the pendulum relative to the guide star (third/fourth RHS term), as first explained in [15]. At the poles the third/fourth terms go to zero because θ is zero at both poles. The immediate objective is to calculate a typical numerical value for the third/fourth terms for Glasgow to see how they will influence Ω_{LT_θ}.

$$\Omega_{LT_\theta} = \Omega_{FP_{m/E}} - \Omega_{gs/E} - \Omega_{\oplus}(1 - cos\,\theta) \tag{27}$$

The WGS-84 local terrestrial gravity model [16] can be inverted to get ϕ from g_{local},

$$g_{local} = g_{eq}\left(\frac{1+ksin^2\phi}{\sqrt{1-\varepsilon^2 sin^2\phi}}\right) \tag{28}$$

where,

$$\varepsilon^2 = 1 - \left(\frac{b}{a}\right)^2 \tag{29}$$

$$k = \frac{(bg_p - ag_{eq})}{ag_{eq}} \tag{30}$$

$$\theta = \frac{\pi}{2} - \phi. \tag{31}$$

The acceleration due to gravity measured at the experimental site, g_{local}, could be detected from a MEMS gravimeter as a continuous signal over time, and if we take g_{eq}, g_p, a, b as known values that can be input to a calculation based around the WGS-84 local terrestrial gravity model [16,17,18] (given in equations (28)-(30)) then we can obtain a corresponding value for latitude, ϕ. From that we can easily calculate the associated co-latitude, θ, using equation (31). The gravimeter will give a fluctuating value for g_{local} over time, and this will have an upper and lower value, and a nominal value, with corresponding values for ϕ, which we define as, ϕ_U, ϕ_L, and ϕ_N, respectively. See Figure 1 for details of a typical time response for the prototype MEMS device of [19]. This means we can calculate three values for the co-latitude too, using equation (31), giving θ_U, θ_L, and θ_N. From that we can calculate the value of the right-hand-side third and fourth terms, as follows,

$$\Omega_{T_{3\&4}} = -\Omega_{\oplus}(1 - cos\,\theta) \tag{32}$$

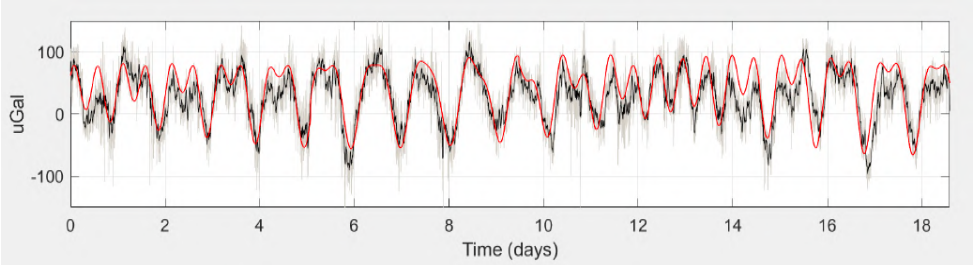

Figure 2.1 Measurement of fluctuations in the local gravitational acceleration in the city of Glasgow, Scotland, reproduced with the permission of the authors of [19].

If we take the upper, lower, and nominal values of the third/fourth terms of the right-hand-side of equation (27) we get this,

$$\Omega_{T_{3\&4_U}} = -\Omega_{\oplus}(1 - cos\,\theta_U), \tag{33}$$

$$\Omega_{T_{3\&4_L}} = -\Omega_{\oplus}(1 - cos\,\theta_L) \quad \text{and} \tag{34}$$

$$\Omega_{T_{3\&4_N}} = -\Omega_{\oplus}(1 - cos\,\theta_N) \tag{35}$$

The three values of g_{local} can be found to be as follows from published data for Glasgow, Scotland [17], noting the predicted fluctuation of around $\pm$ 100 μGal of Figure 2.1 which equates to $\pm$ 0.000001 m/s^2: g_{local_U}= 9.8156 + 0.000001 = 9.815601 m/s^2 , g_{local_L}= 9.8156 – 0.000001 = 9.815599 m/s^2, g_{local_N}= 9.8156 m/s^2.

Using the WGS-84 model [16] with free air correction for elevation of Glasgow at $h = 38$ m, we get the following latitude fluctuations: $\phi_U = 0.973206$ rad/s, $\phi_L = 0.973165$ rad/s, and $\phi_N = 0.973186$ rad/s. Therefore, equation (31) gives,

$\theta_U = 0.597589$ rad/s, $\theta_L = 0.597631$ rad/s, and $\theta_N = 0.597610$ rad/s.

Substituting the values for $\theta_U, \theta_L,$ and θ_N into equations (33)-(35), taking $\Omega_{\oplus} = 7.2921150 * 10^{-5}$ rad/s, gives the following upper, lower, and nominal predicted values for the third and fourth terms of the right-hand-side of equation (27) and the right-hand-side of equation (32), $\Omega_{T_{3\&4_U}} = -0.0000126376$ rad/s, $\Omega_{T_{3\&4_L}} = -0.0000126393$ rad/s, and $\Omega_{T_{3\&4_N}} = -0.0000126385$ rad/s.

Converting these values from rad/s to mas/year requires a multiplicative conversion factor of 6.50477*10^{15} leading to: $\Omega_{T_{3\&4_U}} = -8.2204934323 * 10^{10}$ mas/year, $\Omega_{T_{3\&4_L}} = -8.2216143848 * 10^{10}$ mas/year, and $\Omega_{T_{3\&4_N}} = -8.2210538999 * 10^{10}$ mas/year. The numerical range of the third and fourth

right-hand-side terms shows how significant their contribution is to the measurement of LT precession, and is given by $\Omega_{T_{3\&4_U}} - \Omega_{T_{3\&4_L}}$, for which we get an absolute value of, $\left|\Omega_{T_{3\&4_U}} - \Omega_{T_{3\&4_L}}\right| = 1.12095 * 10^7$ mas/year. As we have seen, this range is due to a fluctuation in g_{local} = $\pm$ 100 μGal and so it is confirmed that these terms will dominate the measurement defined by equation (27). Results have also been obtained for g_{local} = $\pm$ 0 μGal, g_{local} = $\pm$ 50 μGal, g_{local} = $\pm$ 75 μGal, g_{local} = $\pm$ 125 μGal, and g_{local} = $\pm$ 150 μGal, and the values calculated for $Range_{T_{34}} = \left|\Omega_{T_{3\&4_U}} - \Omega_{T_{3\&4_L}}\right|$, and plotted on the graph shown in Figure 2.2.

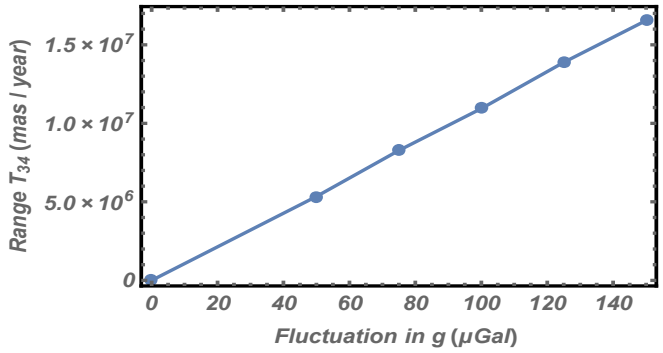

Figure 2.2 $Range_{T_{34}}$ as a function of $\pm$ fluctuations in the local gravitational acceleration in the city of Glasgow, Scotland.

The linear relationship in Figure 2.2 confirms that the lower the measured fluctuation in g_{local} the lower the value of the range of terms T_{34} in equation (27), and therefore the correspondingly reduced dominance of these terms within Ω_{LT_θ}. Note that a measurement of Earth motion is required to define numerically the second term on the right-hand side of equation (27). This will be obtained via online data from [20], however a detailed discussion of this is outside the scope of this present paper and is reserved for a future publication.

3. Pendulum tracking geometry

The motion of the pendulum has to be measured in such a way that the extremely small component due to LT precession is detectable. The primary requirement is for a non-contacting measurement system that can track the pendulum's motion continuously over time, and resolve the LT component. High resolution cameras and autocollimators were considered but it was clear that in the case of the former the necessary resolution would only be available at extremely high cost, and the autocollimator option comes with a considerable additional complication in terms of the necessary tracking instrumentation and control. It was decided to pursue a

different approach in which an optical beam-crossing system using a small array of four laser line generators can be used to detect the presence of the pendulum bob. Sequential information extracted from this system can then be used then to infer the instantaneous position of the bob periodically, and then the time-base associated with the continuous sampling of that data can be used to detect the small shifts in the timing of key points in the sequence, to detect and quantify the LT precession. We now summarise the three beam crossing geometries, in sub-sections 3.1 to 3.3.

3.1 Pendulum swing plane orthogonal to the optical transmission path

This measurement geometry analysis initially assumes that the swing plane of the precessing pendulum is instantaneously orthogonal to the optical path of the array of four laser line generators. This is one of three cases for which a precise analysis is needed to be able to compute the overall time taken to cross the optical transmission path. We consider two half-periods, where the pendulum initially swings from left to right and then from right to left, to cover one complete swing that is perfectly orthogonal to the optical transmission path. The four beams are denoted Top Left (TL), Bottom Left (BL), Top Right (TR), and Bottom Right (TL), and each of the four transmitters is located exactly opposite a specific receiver. When the bob interrupts a beam the associated receiver's output goes to a logical low. An uninterrupted beam generates a logical high at its corresponding receiver output.

3.1.1 Pendulum swinging left to right:

(a) Bob sets TL & BL low as it grazes the beam on approach,
(b) TL, BL, TR, BR – all low as bob is exactly central,
(c) Bob sets TR & BR low as it grazes the beam on departure.

3.1.2 Pendulum swinging right to left:

(a) Bob sets TR & BR low as it grazes the beam on approach,
(b) TR, BR, TL, BL – all low as bob is exactly central,
(c) Bob sets TL & BL low as it grazes the beam on departure.

3.1.3 Analysis of swing in either direction

The period of the pendulum is T and this is given by, $T = \frac{1}{f_n}$ sec. Therefore, one half period; either a left-to-right or right-to-left swing takes, $\frac{T}{2} = \frac{1}{2f_n}$ sec. This is the time it takes to swing through one peak-to-peak amplitude. The peak-to-peak amplitude is defined by $2a$ where a is the peak amplitude of swing. The bob diameter is d_B so the time in seconds that it takes the bob to swing through a distance equal to its own diameter is,

$$t_{d_B} = \frac{d_B}{4af_n}. \tag{36}$$

To calculate this time, we need to know the bob diameter and the pendulum natural frequency of free undumped vibration, and also the peak amplitude. We have to fix d_B and f_n to build the pendulum, and we can estimate a, by assigning a range of values to it so that we can get a corresponding range of values for t_{d_B}. For this case the bob centre covers distance $2d_B$ from the instant the bob grazes the beam as it approaches, to the instant that it still (just) grazes the beam as it departs. So, the overall interrupt time from start to finish for this case is given by $2t_{d_B}$.
Hence we get,

$$t_{2d_B} = \frac{d_B}{2af_n} = \frac{\pi d_B}{a\sqrt{\frac{g}{l_0}}} \tag{37}$$

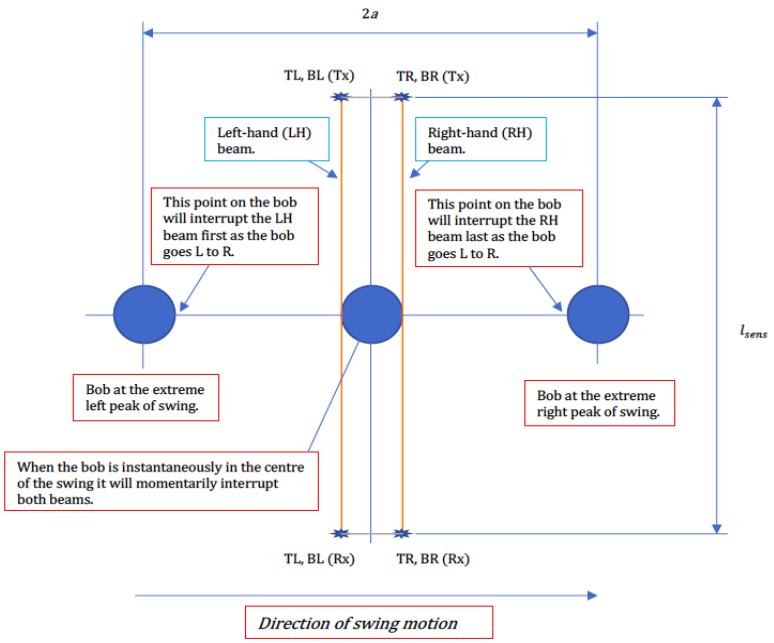

Figure 3.1 Beam crossing geometry: case 1, showing plan view of the bob travelling left to right, exactly the same principles apply in reverse when the bob is travelling right to left. Note also that $l_{sens} > 2a$ so that the pendulum can swing freely when moving under case 3 - see Figure 3.3 below. Key: TL = Top Left sensor, TR = Top Right sensor, BL = Bottom Left sensor, BR = Bottom Right sensor, Tx = laser transmitters, Rx = laser receivers.

where g is the local acceleration due to gravity and l_0 is the effective length of the pendulum. The actual time taken for the beam interrupts for the orthogonal geometry case depends on the precise geometry of the design. So, the beams are designed to be set up so that when the bob is exactly central in its swing it interrupts both beams. Very fine mechanical adjustment will be available to set this up exactly, using high precision parts that are guaranteed to be stable over the planned range of operating temperature. Therefore, the time is exactly governed by twice the diameter of the bob, and is defined by t_{2d_B}. This is because the centre of the bob is at $d_B/2$ to the left of the beam just when the RH side of the bob starts to graze the beam on the approach side, then there is the distance between the beams which is defined by d_B, and then the centre of the bob goes through $d_B/2$ again before the LH side of the bob finally stops interrupting the beam on the departure side. This principle is the same whether it's swinging left-to-right or right-to-left.

3.2 Pendulum swing plane located at an arbitrary angle of precession

In this case the pendulum has precessed through Ω so that the swing plane is no longer orthogonal to the optical transmission path, and instead is at an arbitrary precessional angle of Ω. In that case the geometry is such that the bob has to cover a longer distance d_{pp} to pass across the optical transmission path, and that distance is given by the following where Ω is in degrees,

$$d_{pp} = 2d_B + (2a - 3d_B)\frac{\Omega}{90}. \tag{38}$$

This means that the time to cover the TL, BL pair and then the TR, BR pair is a little longer than for the case of 3.1, and is found as follows,

$$t_{d_{pp}} = \frac{d_{pp}}{4af_n} = \frac{\pi\left(2d_B+(2a-3d_B)\frac{\Omega}{90}\right)}{2a\sqrt{\frac{g}{l_0}}} \quad \text{sec.} \tag{39}$$

(where $t_{d_{pp}} < \frac{T}{2}$, and $\frac{T}{2} = \frac{1}{2f_n} = \frac{\pi}{\sqrt{\frac{g}{l_0}}}$).

This time reaches a maximum as Ω tends to 90° and at that point we move to the final geometrical case (given in 3.3 below). Conversely, when $\Omega = 0$ we get $t_{d_{pp}} = \frac{\pi d_B}{a\sqrt{\frac{g}{l_0}}}$ and this is the same as t_{2d_B}. So, this case then degenerates down to the first geometrical configuration of case 3.1. In general, assuming we approach from bottom left (looking down) we have this sequence,

(a) Bob sets TL & BL low as it grazes beam on approach,

(b) TL, BL, TR, BR – all low as bob is central,
(c) Bob sets TR & BR low as it grazes beam on departure,
(d) Bob sets TR & BR low as it grazes beam on approach,
(e) TR, BR, TL, BL – all low as bob is central,
(f) Bob sets TL & BL low as it grazes beam on departure.

3.3 Swinging exactly along the optical transmission path.

This simple case is shown in Figure 3.3 in which both the beams are continually interrupted for the whole of the time that the swing plane of the pendulum is aligned with the optical transmission path. This is the case when $\Omega = 90°$. The time that the sensors are low over one half period is exactly equal to the half period itself. They will stay low for the remaining half period.
The three cases given above cover all possible motions of the precessing pendulum and provide the necessary theoretical basis for designing the measurement instrumentation discussed in section 6.

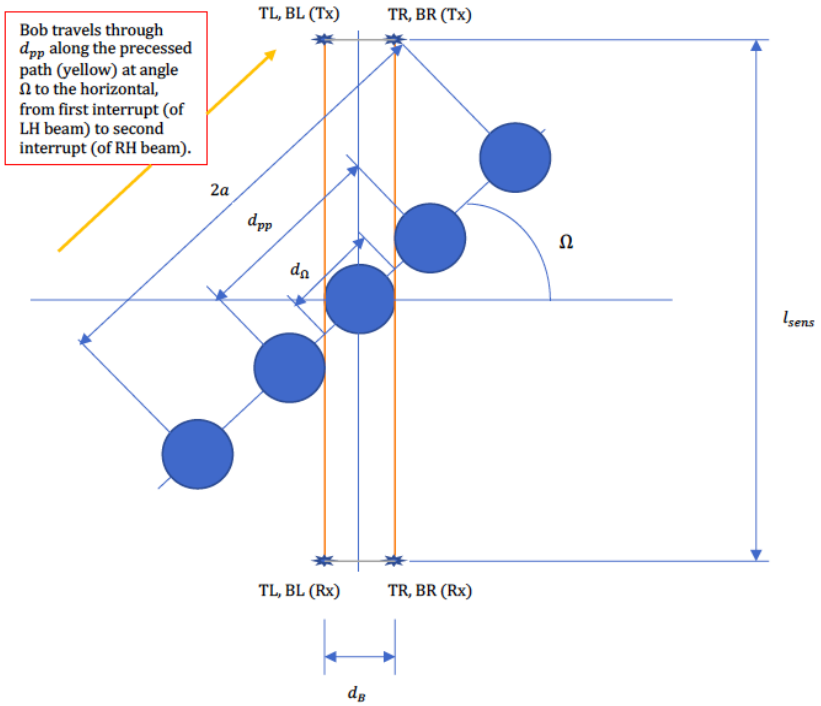

Figure 3.2 Beam crossing geometry: case 2, plan view of the bob going left to right along a path precessed at Ω to the horizontal, same principles apply for right to left (see (a)-(f) below). Key: TL = Top Left sensor, TR = Top Right sensor, BL = Bottom Left sensor, BR = Bottom Right sensor, Tx = laser transmitters, Rx = laser receivers.

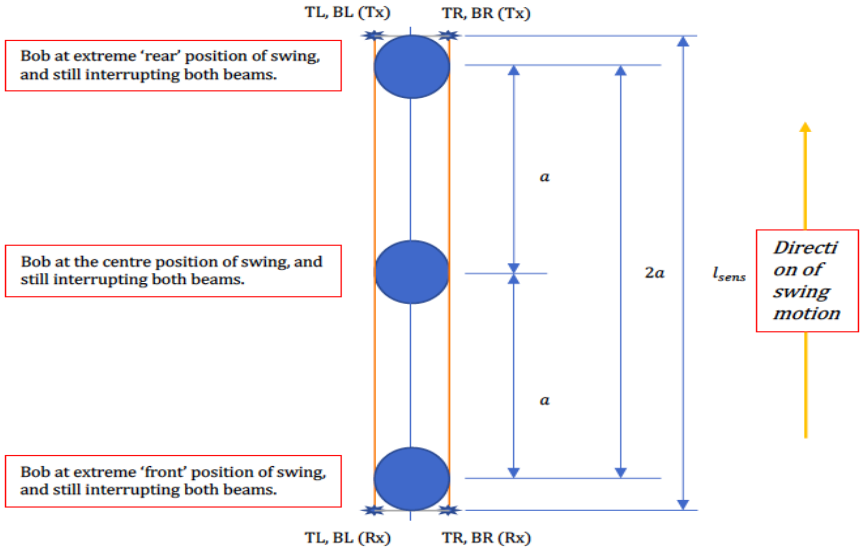

Figure 3.3 Beam crossing geometry: case 3, showing plan view of the bob travelling front to back along a path exactly aligned with the sensor light paths ($\Omega = 90°$), noting that the same principles apply when travelling back to front. Key: TL = Top Left sensor, TR = Top Right sensor, BL = Bottom Left sensor, BR = Bottom Right sensor, Tx = laser transmitters, Rx = laser receivers.

4. Electromagnetic pendulum exciter system

4.1 Ellipticity control

We now summarise the original work of Schumacher and Tarbet [21]. It is repeated in full here, because it is central to the effective operation of the practical system.

The methodology for excitation and also ellipticity control first proposed in [21] uses two concentric electromagnetic sensing and pusher coils to maintain planar motion of the pendulum after launch. This approach has been chosen here over parametric excitation of the length [14, 23, and 24], because it offers a mechanically more robust and simple solution, with the added and very important advantage of offering ellipticity minimisation control that is independent of the magnitude of the minor axis of any residual ellipticity after the pendulum has first been launched. This, together with the fact that it does not in any way intrude on the natural motion of the Foucault pendulum, makes it by far the best approach for pendulum forcing. We start with reference to Figure 4.1, adopted from the original work of [21].

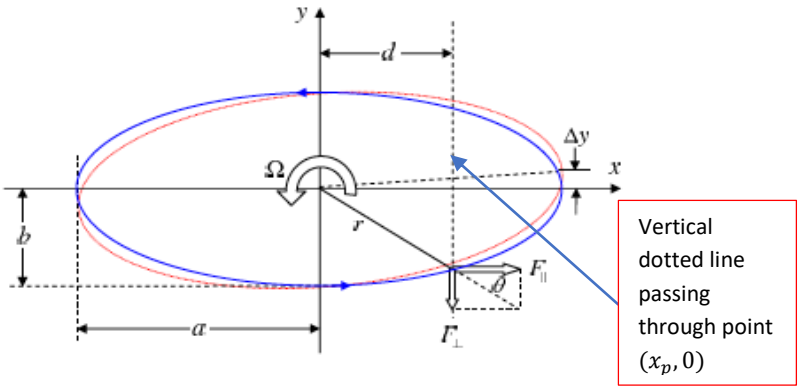

Figure 4.1 Reproduced from [21] with the permission of the authors. The original caption in [21] stated: Planar view of the approximate path of a spherical pendulum with semi-major axis a and semi-minor axis b that is moving in a counter-clockwise ellipse. The suspension is centred on the z-axis above the origin. The pendulum is precessing at rate Ω, and in one full cycle the apex advances by a distance Δy, as suggested by the light dotted and rotated ellipse. The impulsive driving force is applied at x = d, and it is resolved into components parallel and perpendicular at the major axis. The minor axis can be larger or smaller, resulting in a b-dependent magnitude of the transverse force $F_{\perp}$ for a fixed longitudinal force $F_{\parallel}$.

The excitation comes from an impulsive force applied electromagnetically to the bob, resolved into two components, $F_{\perp}$ and $F_{\parallel}$. The parallel component, $F_{\parallel}$ is the bigger of the two and overcomes the dissipation in the system, mainly due to aerodynamic damping and pivot friction. The transverse component, $F_{\perp}$ is used to stop the intrinsic precession of the pendulum, and the objective of the analysis that follows is to relate this to distance d, which defines the point where the impulse excitation force has to occur to stop the unwanted intrinsic precession Ω. It is shown in [21] that d is independent of b. It is shown in detail in [21] that as the pendulum goes from $x = -a$ to $x = +a$ (effectively half a period) it takes $\frac{\Omega T}{2}$ seconds, and the associated precession angle is ϕ. The apex of the ellipse moves through distance Δy. The requirement is therefore for that distance Δy to be reduced to zero by means of an impulse applied at the time when the bob, travelling left to right, crosses the dotted line passing through the point $(x_p, 0)$, after which it passes on through the distance $(a - d)$ to arrive at $(a, 0)$. The momentum associated with the force component $F_{\perp}$ (which performs the neutralisation of the precession associated with Δy) is therefore given by,

$$m\Delta v_y = F_{\perp}\Delta t \tag{40}$$

where Δv_y is the velocity associated with the displacement Δy. The time Δt is the duration of the applied force and as $\Delta t \ll T$ it is appropriate to use the impulsive form of Newton's second law.

Now, the response of the pendulum in the x direction is simply expressed by $x(t) = a \sin \omega_0 t$ where the natural frequency of free undamped oscillation of the pendulum is defined by $\omega_0 = \sqrt{\frac{g}{l}}$ and we note that it takes a definable time t_d for the bob to travel from the origin to the dotted line shown in Figure 4.1 passing through the point $(x_p, 0)$. If $x(t) = d$ then $\frac{d}{a} = \sin \omega_0 t_d$, and this leads to $t_d = \frac{1}{\omega_0} \sin^{-1} \frac{d}{a}$. The geometry of the intrinsic precession shown in Figure 4.1 leads to,

$$\Delta y = \Delta v_y \left(\frac{T}{4} - t_d\right) = a \frac{\Omega T}{2} \tag{41}$$

and combining t_d and the first part of equation (41) gives,

$$\Delta y = \Delta v_y \left(\frac{T}{4} - t_d\right) = \Delta v_y \left(\frac{T}{4} - \frac{1}{\omega_0} \sin^{-1} \frac{d}{a}\right) = \frac{\Delta v_y}{\omega_0} \left(\frac{T\omega_0}{4} - \sin^{-1} \frac{d}{a}\right)$$

where $\frac{T\omega_0}{4} = \frac{\pi}{2}$ because $\omega_0 = 2\pi f_0$ and $f_0 = \frac{1}{T}$. So $\omega_0 = \frac{2\pi}{T}$ and $\frac{T\omega_0}{4} = \frac{\pi}{2}$.

From this, one gets $\Delta y = \frac{\Delta v_y}{\omega_0} \left(\frac{\pi}{2} - \sin^{-1} \frac{d}{a}\right)$.

Using the inverse trigonometrical identity $\cos^{-1} A = \frac{\pi}{2} - \sin^{-1} A$ the last equation simplifies down to,

$$\Delta y = \frac{\Delta v_y}{\omega_0} \cos^{-1} \frac{d}{a} \tag{42}$$

The force components $F_\perp$ and $F_\parallel$ are shown in Figure 4.1 at an arbitrary point on the ellipse, defined by coincidence with the dotted line passing through the point $(x_p, 0)$ and at angle θ to the x-axis. So, we have $\frac{F_\perp}{F_\parallel} = \tan \theta = \frac{y}{d}$. An ellipse is defined by $\left(\frac{x}{a}\right)^2 + \left(\frac{y}{b}\right)^2 = 1$ and from the equation above we have $F_\perp = F_\parallel \frac{y}{d}$, so the ellipse equation gives $y = b\sqrt{1 - \left(\frac{x}{a}\right)^2}$ and therefore we get the following for $F_\perp$,

$$F_\perp = F_\parallel \frac{b}{d} \sqrt{1 - \left(\frac{d}{a}\right)^2} \tag{43}$$

This gives the transverse impulse force component $F_{\perp}$ in terms of the longitudinal component $F_{\parallel}, a, b,$ and d. Next, we take equations (40)-(43) inclusive, and Olsson's expression for Foucault pendulum intrinsic precession [22] which is given by,

$$\Omega = \frac{3}{8}\omega_0 \frac{ab}{l^2}. \tag{44}$$

Then first of all, Δy can be expressed by using equations (41) and (44),

$$\Delta y = \frac{1}{2}a\left(\frac{3}{8}\omega_0 \frac{ab}{l^2}\right)\left(\frac{2\pi}{\omega_0}\right) \tag{45}$$

Next equations (40), (42), and (43) are invoked, to get,

$$\Delta y = \frac{1}{m}\Delta t \frac{1}{\omega_0} F_{\parallel} \frac{b}{d}\sqrt{1-\left(\frac{d}{a}\right)^2}\, cos^{-1}\frac{d}{a} \;=\; \frac{F_{\parallel}\Delta t}{m\omega_0}\frac{b}{d}\sqrt{1-\left(\frac{d}{a}\right)^2}\, cos^{-1}\frac{d}{a} \tag{46}$$

Finally, if the right-hand sides of equations (45) and (46) are equated then it is possible to obtain,

$$\frac{1}{2}a\left(\frac{3}{8}\omega_0 \frac{ab}{l^2}\right)\left(\frac{2\pi}{\omega_0}\right) = \frac{F_{\parallel}\Delta t}{m\omega_0}\frac{b}{d}\sqrt{1-\left(\frac{d}{a}\right)^2}\, cos^{-1}\frac{d}{a}.$$

This reduces down to,

$$\frac{3}{8}\frac{a^2 b\pi}{l^2}\frac{m\omega_0}{F_{\parallel}\Delta t} = \frac{b}{d}\sqrt{1-\left(\frac{d}{a}\right)^2}\, cos^{-1}\frac{d}{a}.$$

Then further to,

$$\frac{3}{4}Q\frac{ab}{l^2} = \frac{b}{d}\sqrt{1-\left(\frac{d}{a}\right)^2}\, cos^{-1}\frac{d}{a} \tag{47}$$

where,

$$Q = \frac{\pi}{2}\frac{ma\omega_0}{F_{\parallel}\Delta t}. \tag{48}$$

It can be seen that b cancels in equation (47), which is an important result in itself. The quantity represented by Q is formally defined as the quality factor 'Q', and in equation (48) this is the ratio of the momentum of the bob at the zero crossing and the momentum kick that it receives when the impulsive force is applied. Equation (47) is simplified further in [21] by introducing the nondimensionalised quantities $\alpha = \frac{a}{l}$ and $\delta = \frac{d}{a}$, to lead to this expression of nullification,

$$\frac{3}{4}Q\alpha^2 = \frac{1}{\delta}\sqrt{1-\delta^2}\,cos^{-1}\,\delta. \tag{49}$$

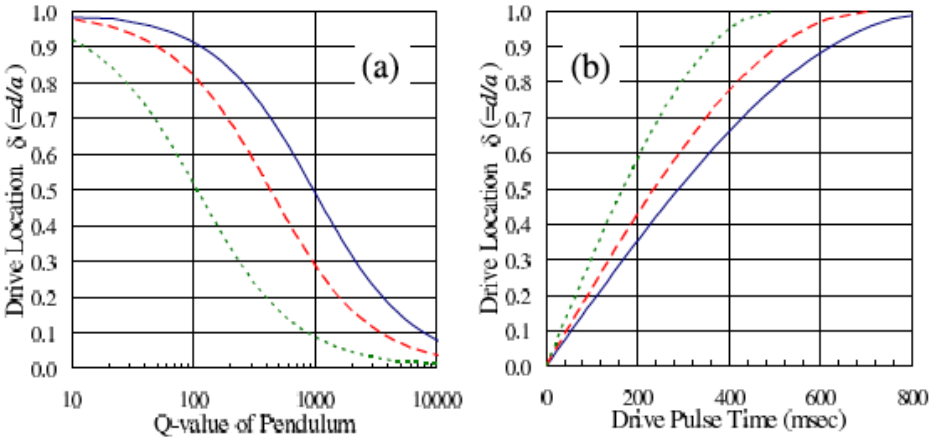

Figure 4.2 Reproduced from [21] with the permission of the authors. The original caption in [21] stated: (a) For three pendulum lengths (L) with amplitude of 0.15 meter, the relationship of the scaled driving distance $\left(\delta = \frac{d}{a}\right)$ versus the quality factor Q for the oscillation. Curves are for an l = 3.0 meter (solid blue), 2.0 meter (dashed red) and 1.0 meter pendulum (dotted green). (b) For the same pendulum lengths as in (a), the distance versus time relationship for the driving pulse.

High Q pendulums need to be pushed closer to the origin, whereas dissipative pendulums need to be pushed further out. This is shown in Figure 3 in [21], reproduced as Figure 4.2 here. We can relate the quality factor to the free decay period directly by using the classical response of a damped harmonic oscillator $x(t) = ae^{-\frac{t}{\tau}}sin\,\omega_0 t$, therefore the momentum loss between $t = 0$ and $t = \frac{T}{2}$ is given by $ma\omega_0\left(1 - e^{-\frac{T}{2\tau}}\right) \cong ma\omega_0\frac{T}{2\tau}$. So, the quality factor can therefore be expressed as,

$$Q = \frac{\pi}{2}\frac{ma\omega_0}{ma\omega_0\frac{T}{2\tau}} = \frac{\pi\tau}{T}. \tag{50}$$

Substituting equation (50) into (49) leads to the following after restoring the dimensional quantities,

$$\frac{3}{4}\left(\frac{\pi\tau}{T}\right)\left(\frac{a}{l}\right)^2 = \frac{a}{d}\sqrt{1-\left(\frac{d}{a}\right)^2}\,cos^{-1}\frac{d}{a}.$$

We know that $\frac{\pi}{T} = \frac{\omega_0}{2}$ and $\omega_0 = \sqrt{\frac{g}{l}}$ so the equation above becomes,

$$\frac{3}{8}\sqrt{\frac{g}{l}}\left(\frac{a}{l}\right)^2 \tau = \frac{\sqrt{a^2-d^2}}{d} cos^{-1}\frac{d}{a}. \tag{51}$$

It is shown in [21] that $F_\perp$ and $F_\parallel$ are related through the dipole-dipole repulsion effect within the magnetic field relations, and within that relationship that there is a minor dependence on b, through the ratio $\left(\frac{b}{d}\right)^2$. However, this ratio is numerically very small, of $\mathcal{O}(0.01)$, in comparison with the principal terms in the expression, so, as shown in [21], it is entirely justifiable to ignore this dependency. The pusher 'on time' t_d can now be calculated from the following algorithmic procedure:
(a) measure experimentally the period T, (b) select an amplitude a based on suitable launch displacement IC, (c) measure experimentally the free decay period τ, (d) select nominal pendulum length l, (e) compute α, (f) then compute Q from equation (50), (g) use equation (49) to get δ, and hence d, (h) finally, calculate t_d from $t_d = \frac{1}{\omega_0} sin^{-1}\frac{d}{a}$.

4.2 Electromagnetic excitation of the pendulum

The equations of motion for the Foucault pendulum have been derived by Cartmell *et al* [23] in terms of local Cartesian coordinates, and are then developed there for the case of principal parametric excitation of the length [23, 24]. Here we exclude parametric excitation and instead replace this with a generalised force term in each equation representing the x and y components of the applied electromagnetic dipole force respectively. Reproducing the equations of motion for the unforced pendulum from [23] and including the generalised forces Q_x and Q_y,

$$\ddot{x} + \eta|\dot{x}|\dot{x} - 2\dot{y}\Omega sin\phi - x\Omega^2 + \frac{gx}{l\sqrt{1-\frac{x^2+y^2}{l^2}}} = Q_x \tag{52}$$

$$\ddot{y} + \eta|\dot{y}|\dot{y} + 2\dot{x}\Omega sin\phi - y\Omega^2 sin^2\phi + r\Omega^2 sin\phi cos\phi + \frac{gy}{l\sqrt{1-\frac{x^2+y^2}{l^2}}} = Q_y. \tag{53}$$

The excitation system, based closely on the proposals in [21], comprises two concentric coils with an outer sense coil and an inner exciter coil. The electromagnetic dipole force results from the interaction from a permanent neodymium magnet in the base of the bob and the inner exciter coil as the bob passes above. The exciter coil is driven by a high current low voltage supply

which is pulsed electronically as the bob is detected by the outer sense coil, and so the form of the electromagnetic force pulse is broadly square, and in phase with the pendulum swing as the bob passes across the coils, noting that this is where the swing velocity is at a maximum. From this we get the generalised forces, as follows,

$$Q_x = F_x \cos\left(\tan^{-1}\frac{y}{x}\right), \tag{54}$$

$$Q_y = F_y \cos\left(\tan^{-1}\frac{y}{x}\right) \tag{55}$$

The excitation components F_x and F_y are pulsatile and can be modelled by use of an inverse tangent function where the argument is the relevant component velocity divided by a scaling parameter k, and suitable pulse shaping, with dipole force magnitude F_{dip}. Clearly F_x and F_y are analogous to $F_\parallel$ and $F_\perp$ in section 4.1 but we use the notation F_x and F_y here in order to distinguish between the uses of these forces for ellipticity control and for general excitation of the pendulum. After division through by the bob mass M the components can be stated as,

$$F_x = \frac{2}{\pi}\frac{F_{dip}}{M}\tan^{-1}\left(\frac{\dot{x}}{k}\right), \tag{56}$$

$$F_y = \frac{2}{\pi}\frac{F_{dip}}{M}\tan^{-1}\left(\frac{\dot{y}}{k}\right) \tag{57}$$

Substituting equations (56) and (57) into (54) and (55) respectively leads to the full forms for the generalised forces,

$$Q_x = \frac{2}{\pi}\frac{F_{dip}}{M}\tan^{-1}\left(\frac{\dot{x}}{k}\right)\cos\left(\tan^{-1}\frac{y}{x}\right), \tag{58}$$

$$Q_y = \frac{2}{\pi}\frac{F_{dip}}{M}\tan^{-1}\left(\frac{\dot{y}}{k}\right)\sin\left(\tan^{-1}\frac{y}{x}\right). \tag{59}$$

Equations (58) and (59) are substituted into (52) and (53) respectively and then the system can be numerically integrated, using practical design data.
Firstly, we show the response of the unforced pendulum just to initial conditions in Figure 4.3, for which $F_{dip} = 0$. The damping is aerodynamic and minimal, so the pendulum shows some precession driven by the rotation of the Earth, $\Omega_\oplus$.

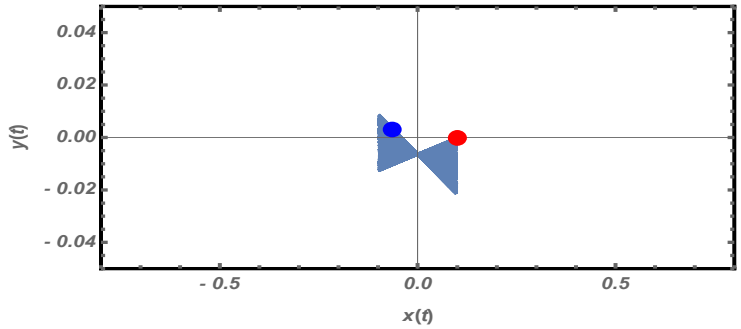

Figure 4.3 Pendulum responses over 1 hour at Glasgow for no excitation ($F_{dip} = 0$). Red dot: displ. ICs $(x_0, y_0) = (0.1, 0)\ m$, blue dot: end points (x_{tend}, y_{tend}), velocity ICs are $\dot{x}_0 = \dot{y}_0 = 0\frac{m}{s}$. Data: $l_0 = 4\,m,\ g = 9.8156\,m/s^2,\ \Omega_\oplus = 7.2921150 * 10^{-5}\ rad/s,\ \phi = 0.9750\,rad,\ r = 6363.18 * 10^3\ m,\ m = 2\,kg,\ \rho = 1.189\ kg/m^3,\ C_D = 10^{-6},\ R_{bob} = 0.0463134\,m,\ t_{end} = 3600\,s$. Axes scaled in metres.

In Figure 4.4 the system is under an electromagnetic excitation where $F_{dip} = 0.05\ N, k = 0.01,$ and $t_{end} = 360\ s,$ all other data are identical to that of Figure 4.3. Amplification is evident, and is based directly on the form of electromagnetic excitation used, such that this excitation can effectively eradicate the tendency to ellipticity for even relatively short pendulums [21].

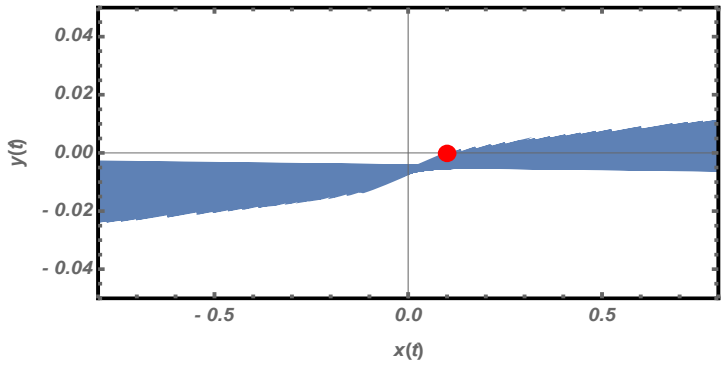

Figure 4.4 Pendulum responses over 6 minutes at Glasgow for excitation $F_{dip} = 0.05\ N$. Red dot: displ. ICs $(x_0, y_0) = (0.1, 0)\ m$, blue dot: end points (x_{tend}, y_{tend}), velocity ICs are $\dot{x}_0 = \dot{y}_0 = 0\frac{m}{s}$. Data: $l_0 = 4\,m,\ g = 9.8156\,m/s^2,\ \Omega_\oplus = 7.2921150 * 10^{-5}\ rad/s,\ \phi = 0.9750\,rad,\ r = 6363.18 * 10^3\ m,\ m = 2\,kg,\ \rho = 1.189\ kg/m^3,\ C_D = 10^{-6},\ R_{bob} = 0.0463134\,m,\ t_{end} = 360\,s,\ \ k = 0.01$. Axes scaled in metres.

The generalised forces in equations (58) and (59) can be plotted against time and then related in terms of phase to the pendulum responses in x and y, as shown in

the plots of Figure 4.5 taking a snap-shot in time of Q_x and also of the response in x. The mid-point of the excitation pulse Q_x coincides with the zero-crossing of the pendulum in x where it reaches its maximum velocity. The very high amplitude gain in x for the particular level of generalised force applied, is quite evident here.

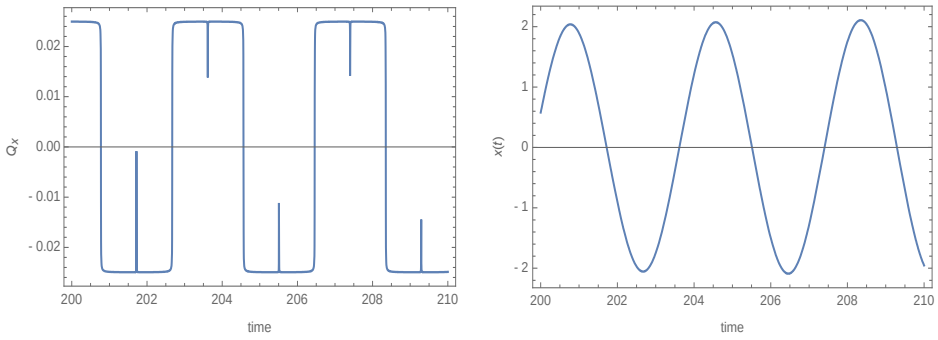

Figure 4.5 Left plot: a snap-shot of the square-wave generalised force Q_x (N) against time (s). Right plot: a snap-shot of the response of the pendulum in x (m) against exactly the same window of time (s), both plots for the data of Figure 4.4.

5. Conclusions

In this paper a derivation is summarised for a simple expression for the Lense-Thirring precession of a test mass in the vicinity of the Earth, using gravitoelectromagnetism, and under the restrictions of locally flat Euclidean space, weak fields, and non-relativistic velocities. The North Pole is used as a basis for predictive comparison and the approximate expression for Lense-Thirring precession derived in this paper shows a very good level of agreement with previously published predictions for that location (~0.2%). The prediction also accounts for numerically symmetrical latitudes either side of the equator and for Earth oblateness. From there the paper discusses how a practical terrestrial measurement of Lense-Thirring precession may be made, referring to the seminal proposals of [15] for a possible polar measurement. An analysis of the correction term needed for non-polar measurement location is given and it is shown that minute variations in the local acceleration due to gravity, g, over time at non-polar locations generate correspondingly large fluctuations in the correction terms. These fluctuations are of a magnitude which would swamp the required Lense-Thirring precession, and so it is concluded that appropriate signal processing analysis needs to be introduced in order to recognise this part of the composite data and extract it accordingly. This is reserved for further work planned for the near future. The paper then goes on to propose a methodology for optical tracking geometry from which relativistic deviations from the Newtonian precession of the pendulum bob can be detected and logged against time. Three sub-geometries are proposed here, with the first and third of these merely the two

extreme cases of the second variant, resulting in a single algorithmic procedure which can be suitably embedded in the data-logging software. From here an ingenious analysis proposed in [21] is examined in some detail, in order to highlight how the work of [21] on an electromagnetic pendulum pusher might be applied to the pendulum system under discussion. The objective is to show that this electromagnetic system could then be analysed in the context of the generalised forces operating on the pendulum, and a discussion of this is given here, showing that the periodic square-wave pulsatile force profile needed to implement the pusher concept of [21] can be arranged in practice. The phase relationship between the generalised force and the response can be seen directly in the results given, confirming that the centres of the square wave excitation pulses, in both the positive and negative excursions, coincide exactly with the zero crossings of the response of the pendulum where it is moving with maximum velocity. This confirms the utility of the design given in [21] in the current context, and provides a framework for practical implementation and test.
In overall terms this paper provides a series of coherent analyses that are required as a basis for building an instrument using a Foucault pendulum for the terrestrial, non-polar, measurement of the frame-dragging effect of Lense-Thirring precession. Whilst the achievement of this goal is still a work in progress the proposals summarised in this paper provides a considerable step forward.

References

1. G. Chartas, Frame Dragging, Department of Physics & Astronomy, College of Charleston, SC 29424, USA, (last accessed 2 November 2021) http://chartasg.people.cofc.edu/chartas/Teaching.html
2. Lense-Thirring precession, Wikipedia, (last accessed 2 November 2021) https://en.wikipedia.org/wiki/Lense%E2%80%93Thirring_precession
3. Gravity Probe B, Wikipedia, (last accessed 2 November 2021) https://en.wikipedia.org/wiki/Gravity_Probe_B
4. B. Tapley, I. Ciufolini, Measuring the Lense-Thirring precession using a second Lageos satellite, Report No. CSR-89-3, Center for Space research, The University of Texas at Austin, TX 78712, USA, September 30 1989.
5. The Geodetic effect, Wikipedia, (last accessed 2 November 2021) https://en.wikipedia.org/wiki/Geodetic_effect
6. J. Kolena, General Relativistic Frame Dragging, North Carolina School of Science and Mathematics, Duke University, NC 27705, USA. http://webhome.phy.duke.edu/~kolena/ncssm.html (last accessed 2 November 2021).
7. D. Butler, General Relativity II – Effects, (last accessed 2 November 2021) http://howfarawayisit.com/

8. O. Chashchina, L. Iorio, Z. Silagadze, Elementary derivation of the Lense-Thirring precession, *Acta Physica Polonica B*, **40** (8), pp 2363-2378, 2009.
9. M.P. Hobson, G. Efstathiou, and A.N. Lasenby, General Relativity: an introduction for physicists, Cambridge University Press, 2006.
10. J.F. Pascuel-Sánchez, TELEPENSOUTH project: Measurement of the Earth gravitomagnetic field in a terrestrial laboratory, arXiv:gr-qc/0207122v1, 30 July 2002.
11. L.I. Schiff, Possible new experimental test of general relativity theory, *Physical Review Letters*, **4**(5), pp 215-217, 1960.
12. M.L. Ruggiero, A. Tartaglia, Gravitometric Effects, arXiv:gr-qc/0207065v2, 8 February 2008.
13. J.B. Hartle, Gravity: An Introduction to Einstein's General Relativity, Addison-Wesley, 2003.
14. A.B. Pippard, The parametrically maintained Foucault pendulum and its perturbations, *Proc. Royal Soc. London A*, **420**, pp 81-91, 1988.
15. V.B. Braginsky, A.G. Polnarev, and K.S. Thorne, Foucault pendulum at the South Pole: Proposal for an experiment to detect the Earth's general relativistic gravitomagnetic field, *Physical Review Letters*, 53, 9, pp 863-866, August 1984.
16. WSG-84 terrestrial gravity model (last accessed 2 November 2021) https://en.wikipedia.org/wiki/Gravity_of_Earth
17. WSG-84 local gravity online calculator, (last accessed 2 November 2021), http://the-mostly.ru/misc/local_gravity_online_calculator.html
18. World elevation map finder, (last accessed 2 November 2021), https://elevation.maplogs.com/poi/glasgow_city_uk.97258.html
19. R.P. Middlemiss, S.G. Bramsiepe, R. Douglas, S. Hild, J. Hough, D.J. Paul, A. Samarelli, S. Rowan, G.D. Hammond, Microelectromechanical system gravimeters as a new tool for gravity imaging. *Philosophical Transactions of the Royal Society A*, 376, 20170291. http://dx.doi.org/10.1098/rsta.2017.0291, 2017.
20. International Earth Rotation and Reference Systems Service, (last accessed 2 November 2021), https://www.iers.org/IERS/EN/Home/home_node.html
21. R. Schumacher, and B. Tarbet, A short Foucault pendulum free of ellipsoidal precession. arXiv:0902.1829 [physics.class-ph] (2009)
15 November 2020.
22. M.G. Olsson, The precessing spherical pendulum, *American Journal of Physics*, 46, 1118, doi: 10.1119/1.11151, 1978.
23. M.P. Cartmell, J.E. Faller, N.A. Lockerbie, and E. Handous, On the modelling and testing of a laboratory-scale Foucault pendulum as a precursor for the design of a high-performance measurement instrument, *Proceedings of the Royal Society A*, 476, 20190680. http://dx.doi.org/10.1098/rspa.2019.0680, 2019.

24. M.P. Cartmell, N.A. Lockerbie, and J.E. Faller, Towards a high-performance Foucault pendulum, *Proceedings of the 2nd International Nonlinear Dynamics Conference*, Sapienza University, Rome, Italy, February 16-19, 2021.

Analysis of contact fatigue coupled with geometry and material nonlinearities by Theory of critical distances*

Ivana D. Atanasovska†
[1]Mathematical Institute of the Serbian Academy of Sciences and Arts, Kneza Mihaila 36, Belgrade, Serbia

Dejan B. Momcilovic‡
The IMS Institute, Bulevar vojvode Misica 43, Belgrade, Serbia

ABSTRACT

The contact fatigue is a localized phenomenon that occurs in highly stressed local zone of the material under the loaded contact region and as such is highly nonlinear problem. This phenomenon exists in almost all real mechanical systems with contact strains coupled with other sources of nonlinear behaviour. The improvements of existing procedures and methods for standard calculation of contact fatigue have a potential to give significant contribution to increase accuracy of calculation of life assessment, reliability and efficiency of complex mechanical systems. This paper gives the basic explanation of the Theory of critical distances and its application on direct estimation of fatigue crack initiation in contact zones. Analysis of contact fatigue when the contact zones are subjected to additional nonlinearities such as geometry manufacturing deviations, geometry microscale-damages or nonlinear material characteristics are presented in detail. Few different real multi-nonlinear problems are used for analysis performing. The benefits of presented approach are discussed by detail analysis of the obtained results, and could be based on the increasing accuracy of contact fatigue prediction considering all existing nonlinearities in loaded contact zones of complex mechanical systems.

Key words: contact, fatigue, coupled nonlinearities, Finite Element Analysis, Theory of Critical Distances

---

* This work has been supported by the Ministry of Education, Science and Technological Development of Republic of Serbia through the Mathematical Institute SANU and the Institute for testing of materials.
† e-mail address: iatanasovska@mi.sanu.ac.rs
‡ e-mail address: dejan.b.momcilovic@gmail.com

1. Introduction

The everyday use of mechanical systems with various mechanical elements would be impossible without contact between parts of elements. It is still particularly difficult to predict the failures which occur at these locations or contact. The getting the right picture in such a cases or basic stress analysis of contact situations is problematic in itself because this analysis is strongly affected by factors which are difficult to estimate, such as the degree of friction and adhesion between moving bodies. At same point of two mechanical elements in contact, the cracking is a common result or precursor of contact-related failures, suggesting the use of fracture mechanics in their solution. Short cracks and non-propagating cracks are frequently involved as a result of crack growth through a rapidly decaying stress field [1, 2, 3].

For many decades, any discussion about contact mechanics was more or less synonymous with Hertzian contact where the contacting bodies are elastic with simple profiles and most of the applications were to traditional machine elements such as rolling bearings, gears and cams. However, in almost all mechanical or engineering systems comprising more than a single object, loads are transmitted between the components by contact, and the nature of this interaction is often critical in determining the overall system behaviour. This transmission of a loads through material, particularly in advanced materials with or without modification by surface engineering become nonlinear problem from mechanistic point of view only. But if we add local material characteristics like presence of non-metallic inclusions and carbides, the main task, predicting a failure at contact become more difficult [4-6].

To solving such a problem, the possible path is multidisciplinary approach. Scientist dealing with solid state mechanics, theoretical mechanics, metallurgy and mechanical engineering have to work together to create procedure for contact fatigue prediction, applicable to various geometries and microstructural features. Only investigations of material characteristics and material behaviour in real load cases simultaneously with calculations of real load distribution and stresses in contact zones of various mechanical elements, could make step forward in solving this problem.

2. Theory of Critical Distance

The Theory of Critical Distances (TCD) is a method or group of methods for the prediction of failure on engineering components and structures with various types of stress raisers, developed in last two decades. Basics of TCD are known, the main concept is that failure usually occurs due to the initiation and fact that materials possess inherent length scales which are related (in complex ways) to their microstructure and modes of deformation and damage. The interaction between the length scale and the stress gradient determines whether crack will occur from a given feature. The second important thing or assumption about TCD is that any type of stress raiser could be considered in the same way [1].
The local stresses around a notch, or any other stress concentration, contact for example, can be represented in a simple form by a diagram of the stress as a function of distance from stress concentration raiser, fig.1. We will assume that the stress analysis is an elastic one, and that the maximum normal stress is drawn. Poor accuracy can be expected if prediction of fatigue life is based on the range of stress at the stress raiser (i.e., at a distance of zero in fig.1). The use of plastic strain range instead of stress range has the disadvantage that an elastic–plastic analysis must be performed (or approximated). In any case it will be still quite inaccurate for the prediction of high-cycle fatigue in features with high K_t - stress concentration factor, [1, 3]. This means that the first step in the application of critical distance methods is to use them explicitly, generating stress–distance diagram such as fig.1 and read the necessary stress values from Finite Element Analysis (FEA).

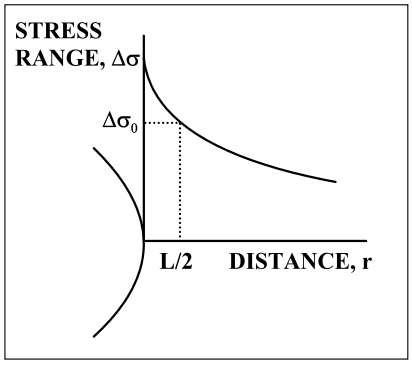

Fig.1. Schematic explanation of TCD point method

The second step is calculating the value of the critical distance. The underlying theory was suggested by and validated against experimental

data by Taylor, [1, 3]. Basically, it is essentially a combination of stress raiser fatigue and linear elastic fracture mechanics (LEFM) concepts. The assumption that the TCD point method and TCD line method are valid for all types of stress raisers, allows to define the stress–distance diagram at the fatigue limit for a cracked body, [2], for which the stress intensity range is equal to the threshold value for the material: $\Delta K = \Delta Kth$. The result is that the critical distance for the point method is *L/2*, [1, 3], where:

$$L = \frac{1}{\pi}\left(\frac{\Delta K_{th}}{\Delta\sigma_0}\right)^2 \quad (1)$$

In this equation $\Delta\sigma_0$ is the fatigue limit of standard, unnotched specimens of the material, and ΔK_{th} is threshold stress intensity. The fact is that is often difficult to define the accurate fatigue limit, the stress range corresponding to a given number of cycles. The range from 1 to 10 million is generally used for determination of fatigue limit. It has been demonstrated by comparison with experimental data [3] that the use of this value of $\Delta\sigma_0$ for L gives good predictions in many different materials [1].

The application of TCD in solving fretting fatigue was successfully so there is no reason why TCD couldn't be applicable to contact fatigue. In practice, however, contact fatigue normally involves a moving point of contact, as in rolling contact between gear teeth and bearing components. Whilst the initiation and early growth of the crack may be similar to that in standing fatigue, the moving force has a considerable effect on the subsequent crack growth and the tendency for the crack to turn back to the surface and cause spalling. Thus, the TCD is useful in modelling the early stages of this process (perhaps for predicting the limit below which only non-propagating microscopic cracks will occur). But, a crack-propagation analysis would be needed to describe the entire process, [9, 10]. Particular problem is application of TCD on small scale due to the fact that the measured mechanical properties of a material are often affected by the size of the test specimen used. It is clear that there are significant differences between the results obtained from macroscopic specimens and from microscopic specimens of this material. This can be explained in terms of the relative importance of surface grains. Grains which lie on the surface of the specimen can deform more easily than

internal grains because they are less constrained by the grains which surround them [11].

3. Contact of two half-cylinders with carbides

The problem of bodies in contact, with the emphasize of engineering application was the subject of many papers [12, 13, 14]. However, the usual assumption was that the bodies in contact are without significant internal features. In this paper a particular theoretical contact problem of two pressure loaded half-cylinders in contact is used for developed methodology investigation. The additional nonlinearity is modelled as a case of material nonlinearity simulated by carbides occurrence under the contact surfaces of these half-cylinders made by steel. The half-cylinders are made by AISI 308 steel, with Cr2C3 carbides existing at subsurface layer with dimensions and positions obtained by experiment [15]. Data about mechanical properties of this particular carbide was taken from literature data [16-18]. The basic mechanical properties of this type of carbide, used in the investigation performed in this research are:

- Hardness, Rockwell: 91 HRV,
- Vickers Microhardness: 2280 HV1, and
- Modulus of Elasticity: 373 - 386 GPa.

In the previous works the Finite Element Analysis (FEA) is performed in order to discuss the influence of the orientation and dimension of carbides on Hertz stresses for two half-cylinders in contact [19], while in the research presented in this paper, the series of nonlinear numerical Finite Element Analysis (FEA) is performed in order to discuss the influence of the position of a rhombohedral carbide in correlation with the point of contact of the half-cylinders in non-loaded state. The both of the modelled half-cylinders have a diameter of 10 mm. In accordance with the real cases [15], the modelled carbide has a rhombohedral scape with dimension 50 x 50 μm, and was positioned to 10, 25 and 50 μm below the contact surface (parameter *b* in fig.2), in the axis of principal force, or is shifted 25 μm (parameter *a* in fig.2) from the main axis and on the depth of 25 and 50 μm. These five cases are defined by parameters *a* and *b* in Tab.1

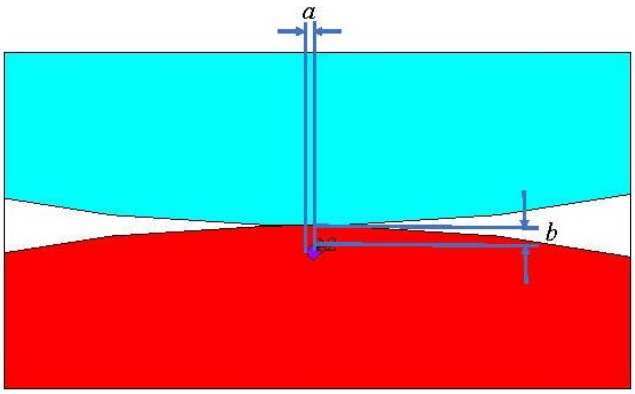

Fig.2. Shape and position of carbide under contact point

Tab.1. Values of the position parameters for the modelled cases

Carbide position	*a*	*b*
Case 1	0	50 μm
Case 2	0	25 μm
Case 3	0	10 μm
Case 4	25 μm	50 μm
Case 5	25 μm	25 μm

In order to make a problem solvable, a few approximations were selected:

- In real case there is a field of residual stress in vicinity of carbide as a result of difference of mechanical and physical properties (density, heat properties, etc) between matrix (AISI 308) and particular carbide. In this model this field of residual stress is neglected;
- Approximation of 3D problem on 2D case (*Plane stress* analysis is performed in FEA);
- Simple shape of carbide – due to the orientation high and low stress raiser is assumed;
- Different orientation of carbide on fixed depth; and
- Size of carbide in FEA model is approximated to a real case.

Fig.3 shows the results for normal stress distribution for ideal isotropic material without imperfections [19] required for future comparison with the investigated problem. Fig.4 shows the FEA model developed for the numerical nonlinear calculations of stress-strain state of the half-cylinders in contact. The 2D four-nodes iso-parametric type of finite

elements is used for model discretization, as well as the ANSYS 2019 R3 software for nonlinear FEA performing. Fig.5 shows the position and orientation of carbide for two of the series of modelled cases.

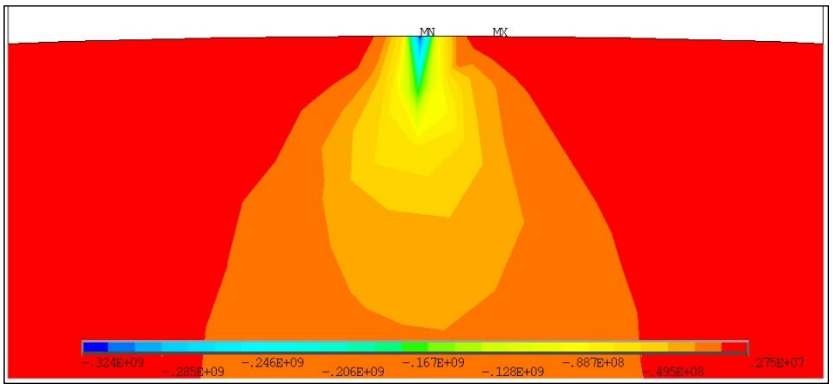

Fig. 3. Normal stress distribution for ideal isotropic material

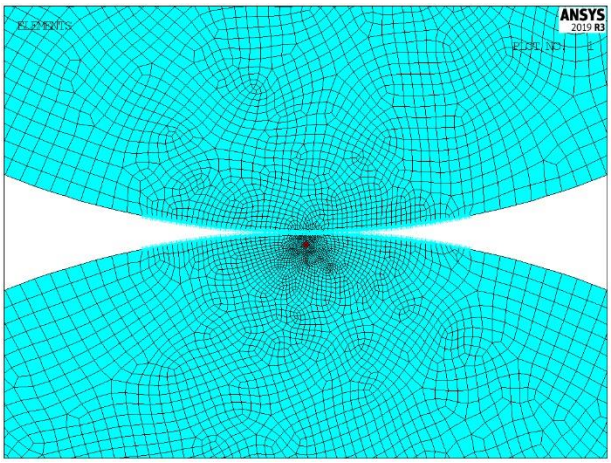

Fig. 4. FEA model for two cylinders in contact

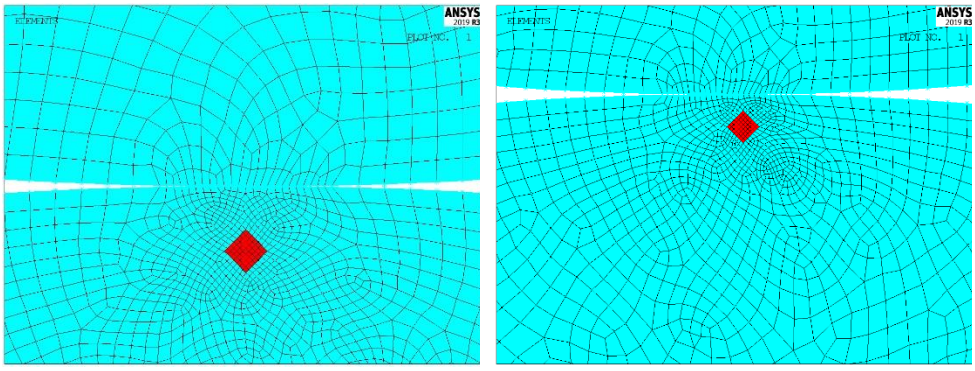

a) b)

Fig. 5. Position of a carbide: a) Case 1; b) Case 5

4. Results and discussion

The results obtained by series of FEA calculations are analyzed and discussed in order to make conclusions about the influence of the carbide position on the stress state of the modelled solids in contact, as well as for creating the diagrams for TCD applying. The strain-stress state of the modelled contact zone with material nonlinearity is analyzed under load conditions defined with external pressure force of 5 KN.

The obtained results for the equivalent VonMises stresses as well as for the normal pressure stresses and plane shear stresses in the investigated contact zone with multi-nonlinearities for the series of calculated cases are presented in fig.5, fig.6 and fig.7 respectively.

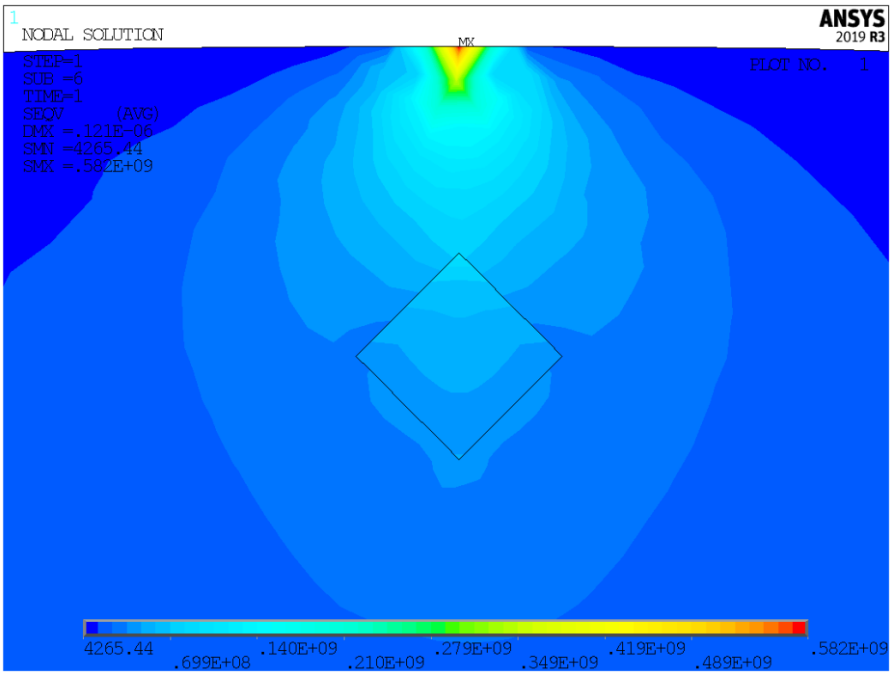

a) Case 1

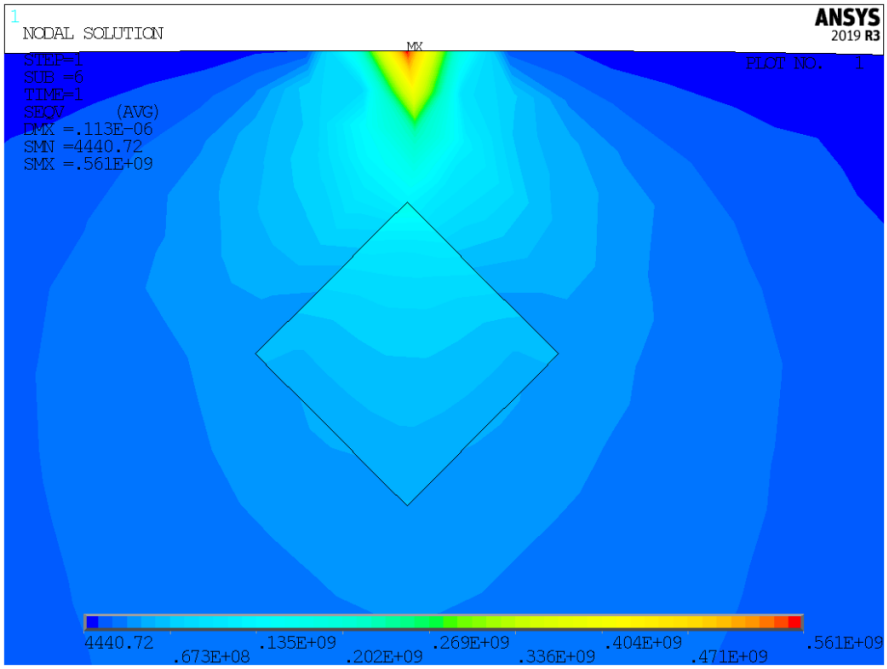

b) Case 2

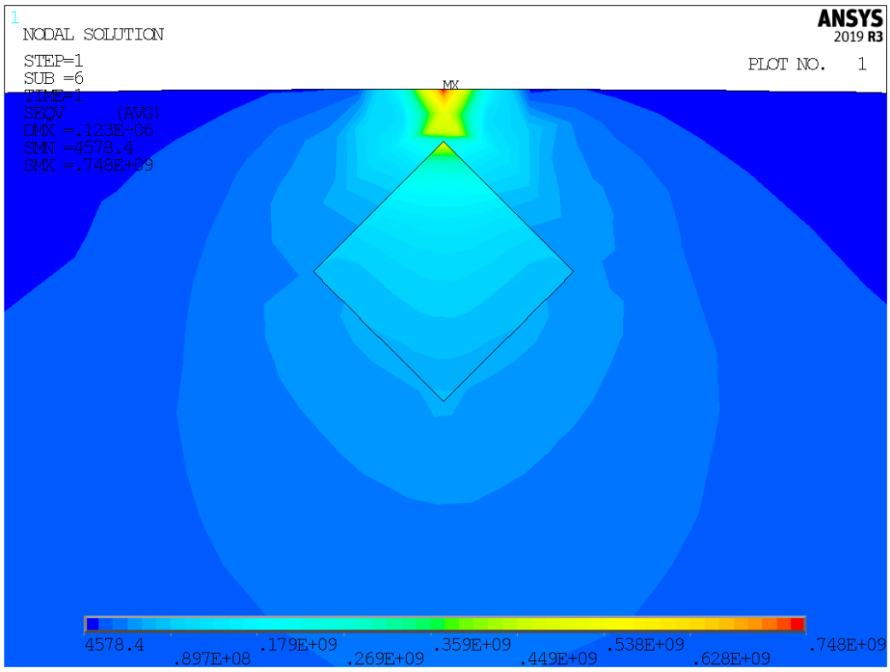

c) Case 3

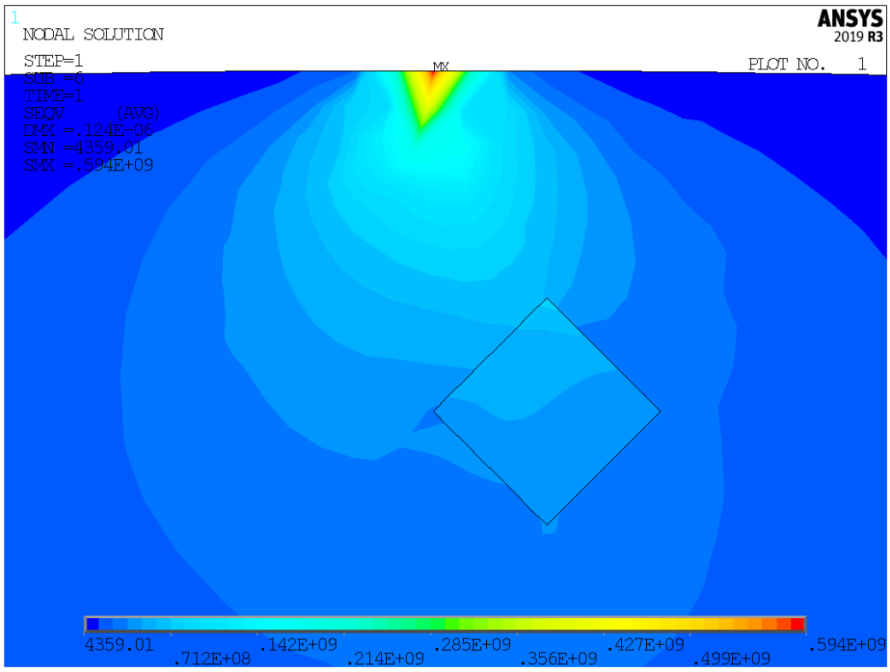

d) Case 4

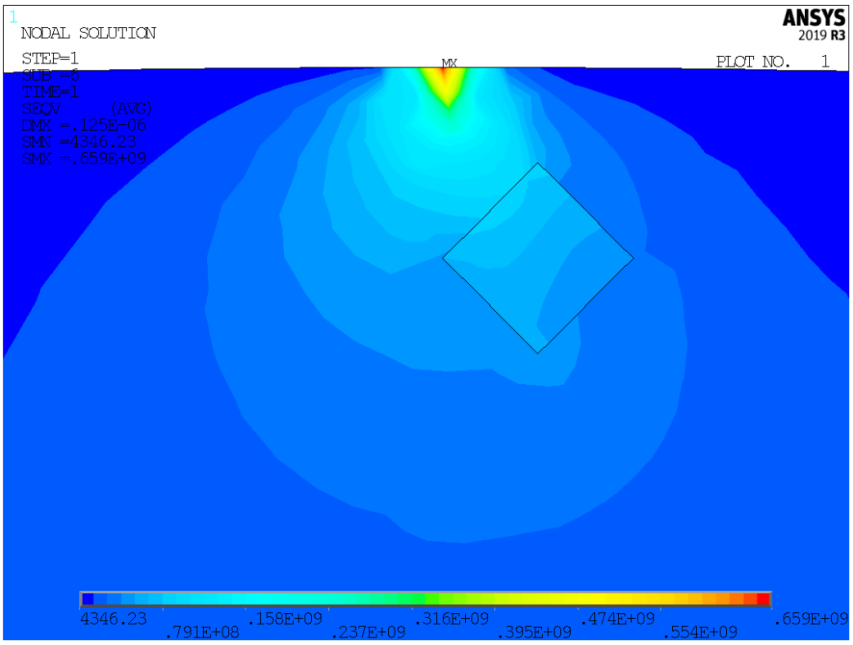

e) Case 5

Fig. 5. VonMises stresses

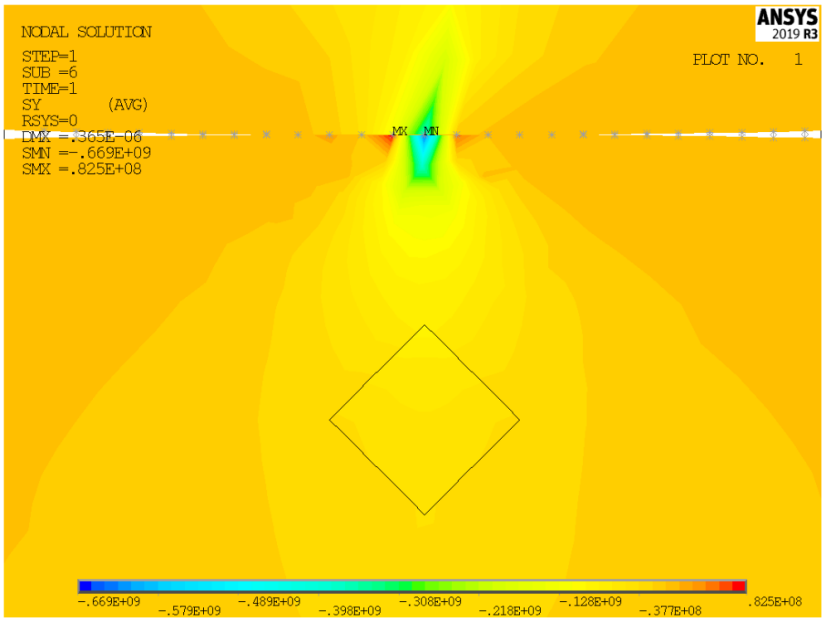

a) Case 1

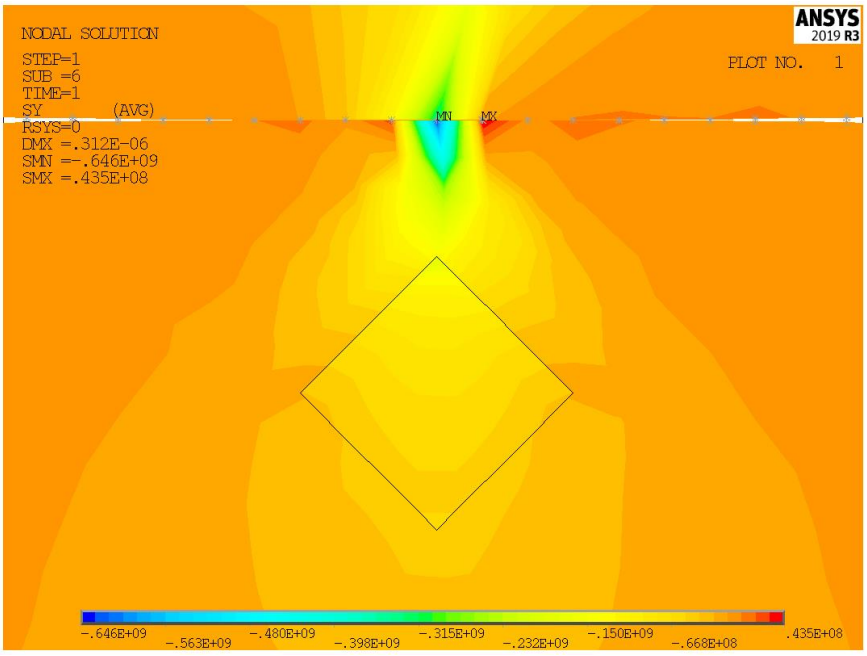

b) Case 2

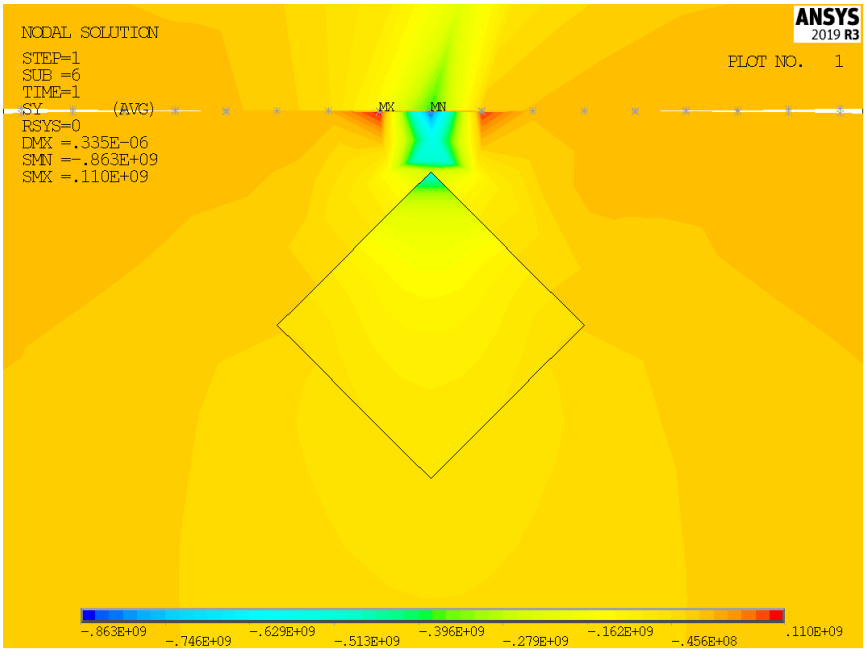

c) Case 3

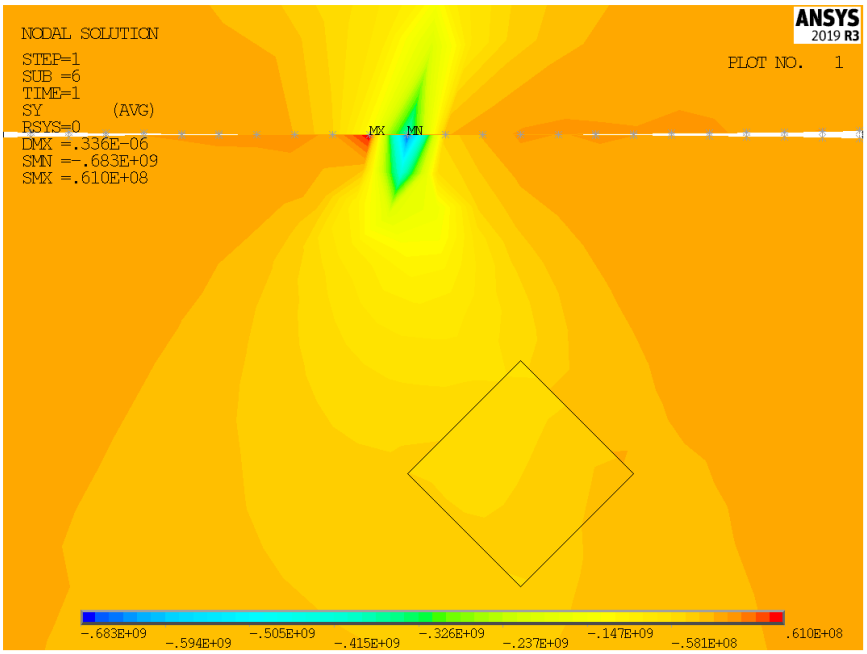

d) Case 4

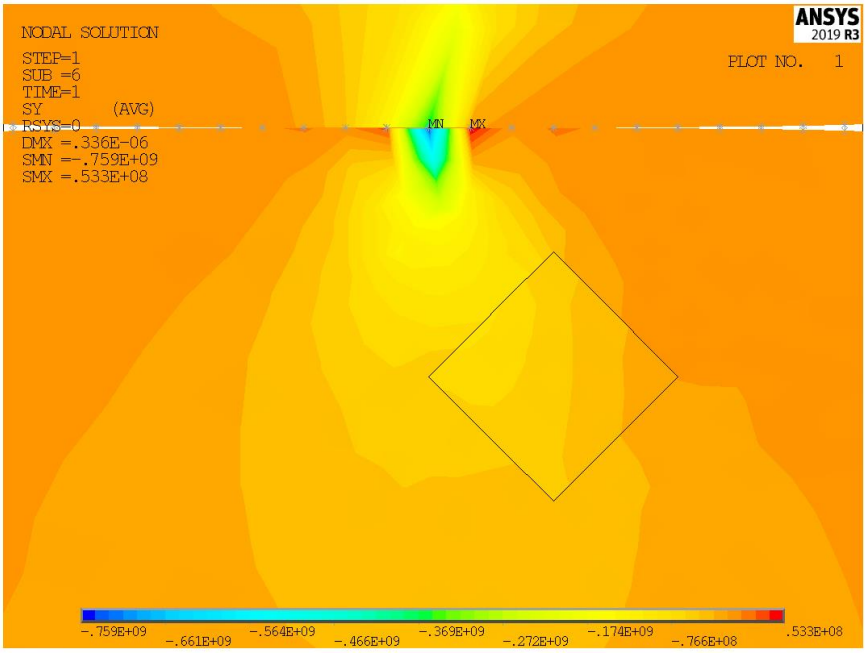

e) Case 5

Fig. 6. Normal pressure stresses

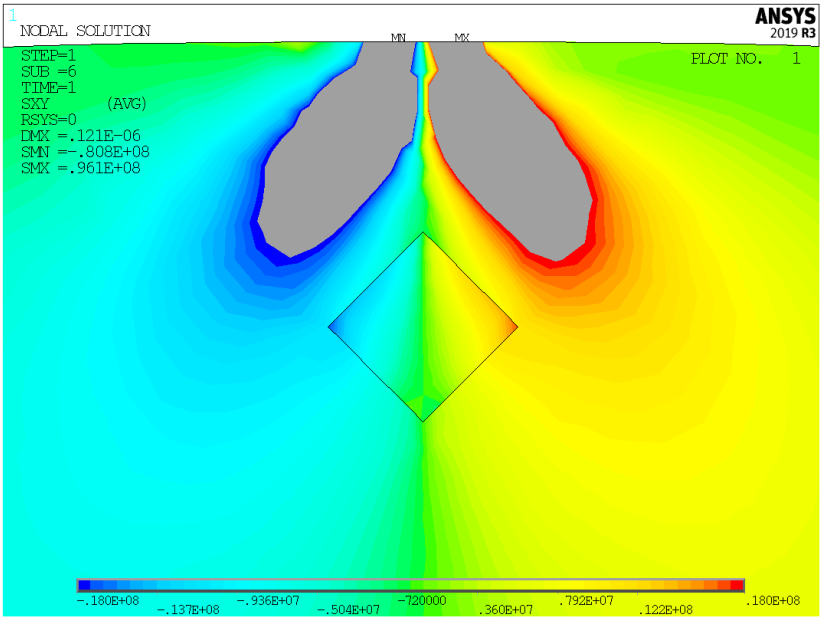

a) Case 1

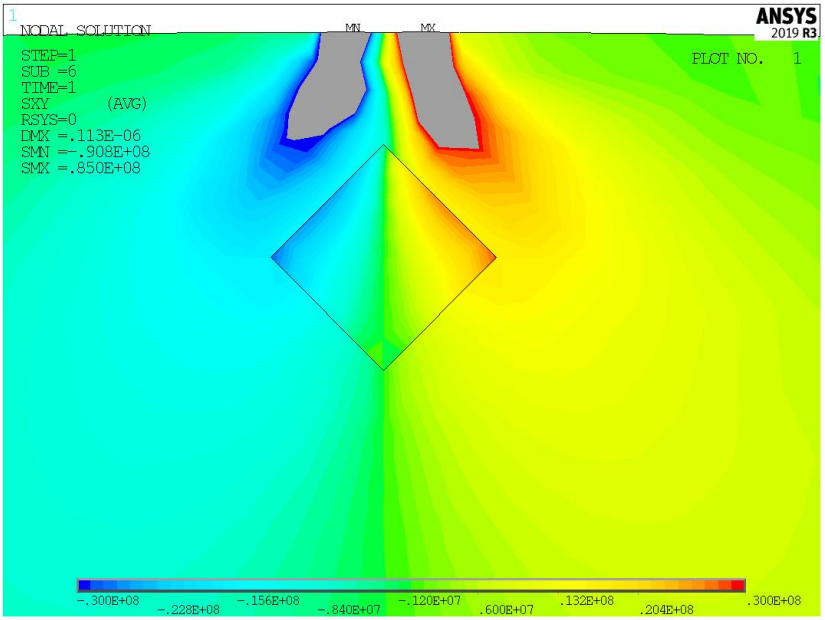

b) Case 2

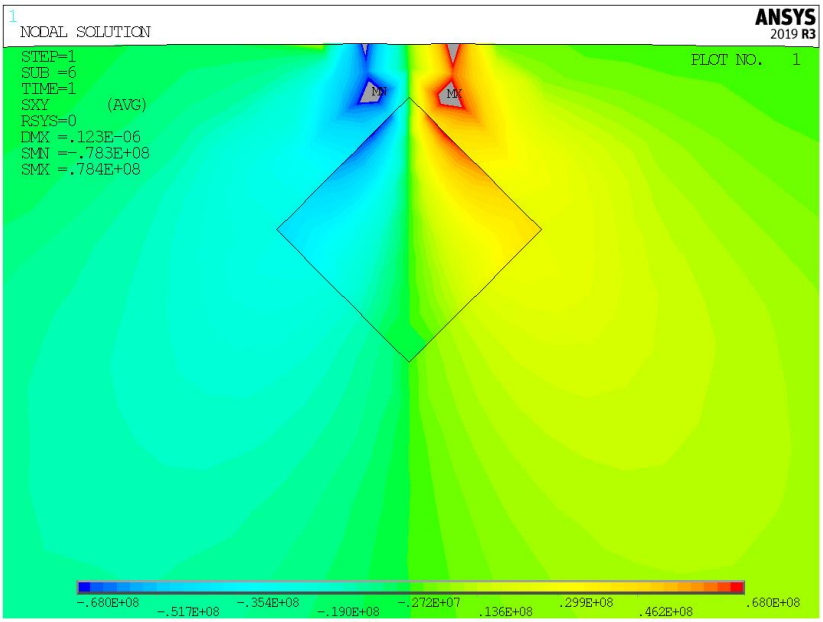

c) Case 3

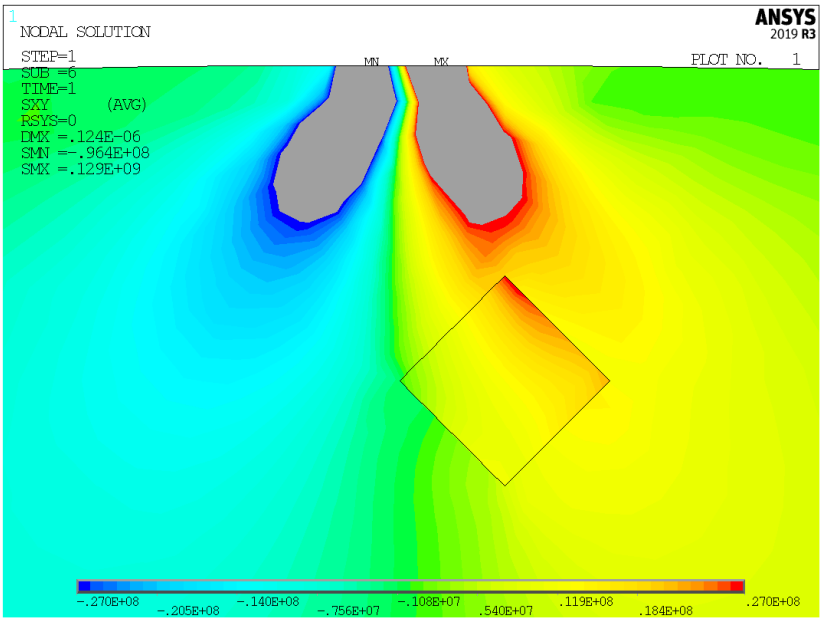

d) Case 4

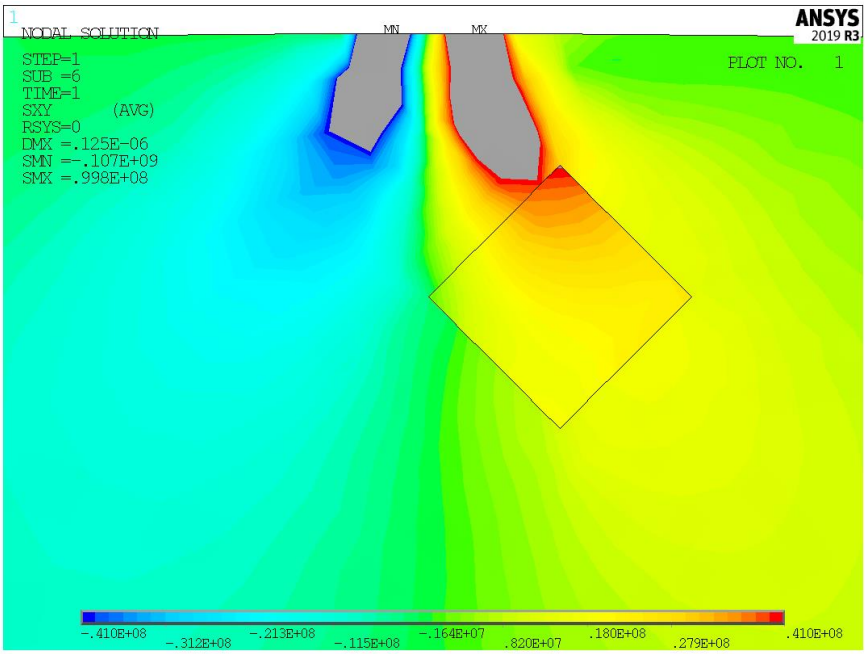

e) Case 5

Fig. 7. Plane shear stresses

The analysis of the FEA results shown in contour plots of stress distributions at contact zone with and without material nonlinearity (fig.3, fig.5-7) lead to the conclusions about the influence of the position and orientation of this type of multi-nonlinearities on the increasing stresses, ie. decreasing load capacity of real elements in contact. The influence coefficient K_c is defined as:

$$K_c = \frac{\sigma_{with\ material\ non-linearity}}{\sigma_{without\ material\ non-linearity}} \qquad (2)$$

and the values of this coefficient for the particular theoretical case considered in this paper are presented in Table 2.

Tab.2. Values of the coefficient K_c calculated for the normal pressure stresses

Carbide position	σ_p (MPa)	K_c (/)
without material non-linearity	324	1.0
Case 1	669	2.065
Case 2	646	1.993
Case 3	863	2.663
Case 4	683	2.108
Case 5	759	2.343

In order to apply TCD on the particular multi-nonlinear problem which was researched in this paper, the diagrams for the stress gradients are drawn based on the FEA results. The diagrams for normal pressure gradients in basic half-cylinder material for cases 1, 2 and 3 are presented in fig. 8 comparatively for different cases (marked in tab.1 as cases 1, 2 and 3), as well as in fig.9 comparatively for the basic material and carbide's material for the same modelled cases.

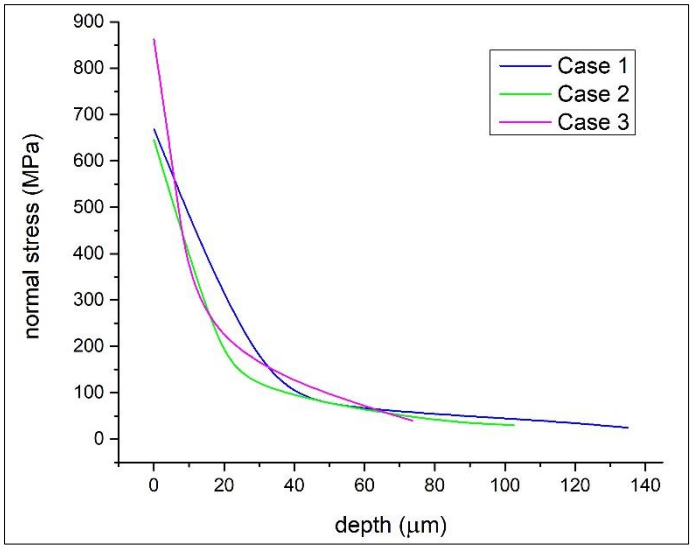

Fig. 8. Normal pressure gradients under contact surface for basic material

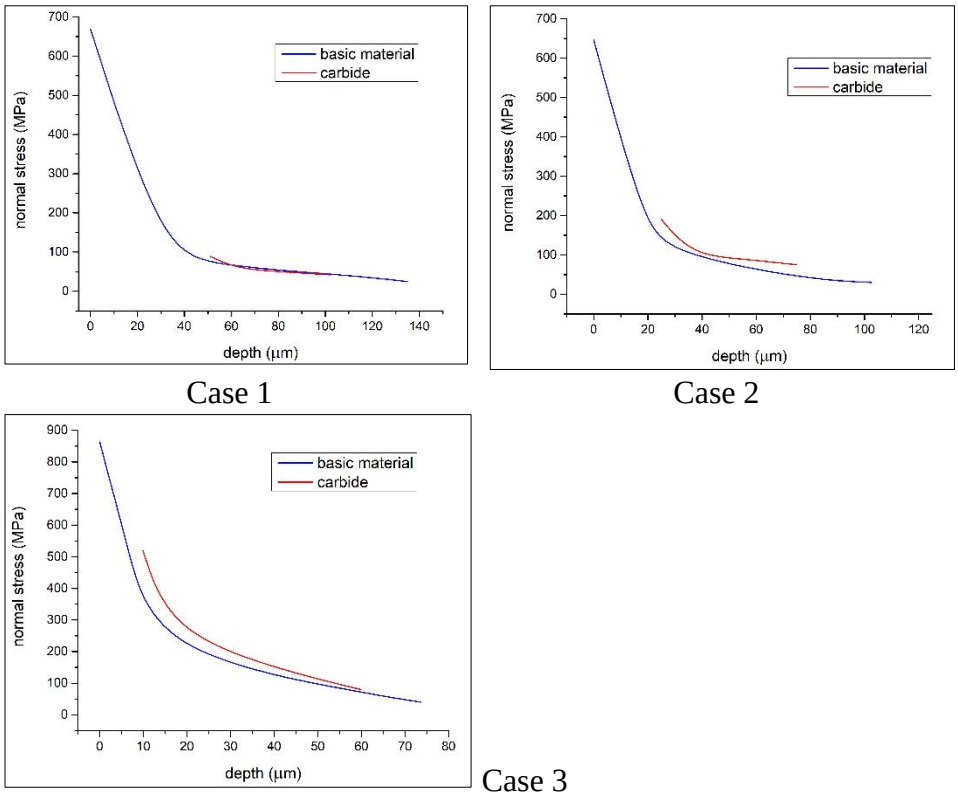

Fig. 9. Normal pressure gradients – basic material vs carbide

From the diagrams above it is clear that the raise internal stress occurs in subsurface zone. For this particular base material AISI 308, the critical length parameter *L/2* is 50μm, and it is clear from the diagrams shown in fig.9 that the crack initiation in the sub-surface zone could be appear in the presented problem with future carbide shifting near the contact surface.

5. Conclusions

The general conclusion based on the obtained results for stress distributions at contact zones is that the closer to the surface, the greater is the influence of the carbide on the change of stress state, regardless of whether equivalent, normal or shear stresses are observed. At a certain small distance from the surface, in this study it is 10 μm, there are multiple stress peaks of approximate same values, both in the base

material at the contact surface and in the carbide on its outer surface with which it borders the base material, which can lead to stress concentrations and fatigue crack occurrence below the contact surface. This is a particularly significant result because the available studies of the contact phenomenon of real elements and their calculations do not introduce coefficients of the influence of the presence of material non-linearities of this type, although, as it could be seen from this research, they can lead to a significant decrease of the load capacity. This also means that modification of TCD toward micro scale can lead to better quantification subsurface stress raisers, in case of contact stress. It is important to take into account superposition with real stress field around carbides which can lead to promoting conditions for premature crack initiation. Future investigation and discussion will present how variation of dimensions, number and position of carbides impact to the Hertz stresses and the proposed method for assessment of crack initiation conditions.

References

[1] D. Taylor, The Theory of Critical Distances, A New Perspective in Fracture Mechanics, Elsevier, 2007.
[2] J. M. Barsom, S.T. Rolfe, Fracture and Fatigue Control in Structures: Applications of Fracture Mechanics, 3rd ed, ASTM, 1999
[3] D. Taylor D, Geometrical effects in fatigue: a unifying theoretical model, *Int J Fatigue*, 1999, Vol. 21, pp. 413–420
[4] H. Hertz, On the contact of elastic solids, Miscellaneous Papers by H. Hertz, Eds. Jones and Schott, London, 1896
[5] A. Fischer-Cripps, Introduction to Contact Mechanics, Second Edition, In: *Mechanical Engineering Series*, Frederick F. Ling (Ed.), Springer, ISBN 0-387-68187-6, United States of America, 2007
[6] I. Gonzalez-Perez, J.L. Iserte, A. Fuentes, Implementation of Hertz theory and validation of a finite element model for stress analysis of gear drives with localized bearing contact, *Mechanism and Machine Theory*, Vol.46, pp. 765–783. 2011
[7] J.R. Barber, Contact mechanics, ISSN 2214-7764, 2018

[8] D. Taylor D. Geometrical effects in fatigue: a unifying theoretical model, *Int J Fatigue*, Vol. 21, 1999, pp. 413–420.
[9] M.F. Frolish, D.I. Fletcher,J.H. Beynon, A quantitative model for predicting the morphology of surface initiated rolling contact fatigue cracks in back-up roll steels, *Fatigue and Fracture of Engineering Materials and Structure*, Vol.25, 2002, pp. 1073–1086.
[10] S. Glodez, Z. Ren, J. Flasker, J. Surface fatigue of gear teeth flanks, *Computers and Structures*, Vol.73, 1999, pp. 475–483.
[11] S. Wiersma, F. Dolan, D. Taylor, Fatigue and fracture in materials used for micro-scale biomedical components, IOS Press, Bio-Medical Materials and Engineering 16 (2006) 137–146
[12] I. Atanasovska, et al., Developing of gear FEM model for nonlinear contact analysis, *Proceedings of 1. International Congress of Serbian Society of Mechanics*, Kopaonik, 10-13.04.2007., ISBN 978-86-909973-0-5. COBISS.SR-ID 138952460, Published by Serbian Society of Mechanics, Belgrade, 2007, pp. 695-703.
[13] I. Atanasovska, I. et al., Finite Element Model for stress analysis and nonlinear contact analysis of helical gears, *Scientific Technical Review*, Vol. LVIX, No.1, YU ISSN 1820-0206, Published by Military Technical Institute, Serbia, 2009, pp. 61-69.
[14] I. Atanasovska, et al. (2010). Analysis of the nominal load effects on gear load capacity using the finite element method, *Proceedings of the Institution of Mechanical Engineers, Part C: Journal of Mechanical Engineering Science*, Vol. 224, No.11/2010, ISSN 0954-4062 (Print), 2041-2983 (online), DOI 10.1243/09544062 JMES2508, Published by Sage Publications, pp. 2539-2548.
[15] Peyman Ahmadian, Mahdi Taghizadeh, *The effect of non-metallic inclusion size and orientation on tensile properties of stainless steel (simulation and experiment)*, Metall. Mater. Eng. Vol 26 (1), pp.43-55, 2020
[16] Sha Liu, Yefei Zhou, Xiaolei Xing, Jibo Wang, Yulin Yang, Qingxiang Yang, Agglomeration model of (Fe,Cr)7C3 carbide in hypereutectic Fe-Cr-C alloy, Materials Letters 183(2016), 272–276

[17] http://www.matweb.com/search/DataSheet.aspx?MatGUID=c5b65890d6e74820a40b517269185cbf&ckck=1
[18] D. Musi, U. Kreissig, R. Mertensa, J.M. Schneider, Electronic structure and mechanical properties of Cr7C3, Physics Letters A 326 (2004) 473–476
[19] Dejan Momčilović, Ivana Atanasovska: Analysis of Hertz contact stresses for metallic material with carbides - Proceedings of the 8th International Congress of Serbian Society of Mechanics, Kragujevac, Serbia, June 28-30, 2021, ISBN 978-86-909973-8-1, COBISS. SR-ID 41508105, Section: Mechanics of Solid Bodies, pp.216-218

The procedure of generating trajectory of motion of carrier conveyor for granular material in dependance of pod systems characteristics[1]

Mirjana M. Filipovic[2]
Mihajlo Pupin Institute, Volgina 15, Belgrade, University of Belgrade, Serbia

Ljubinko B. Kevac[3]
Innovation center of School of Electrical Engineering, Bulevar kralja Aleksandra 73, Belgrade University of Belgrade, Serbia

ABSTRACT

Motion dynamics of carrier conveyor dictates motion dynamics of powder or granular materials which are being transported. The conveyor conveyor should have oscillatory motion with certain velocity. Trajectory of carrier conveyor should be set so that it creates complex oscillatory motion of powder or granular materials. This should cause optimal motion of transported material in regards of velocity and mass flow. This is possible since the analysis of the system indicates that it can be recognized as typical robotic system with rigid and elastic elements. Dynamic and kinematic models of conveyors for powder and granular materials are

[1] This research has been supported by the Ministry of Education, Science and Technological Development, Government of the Republic of Serbia through the following two projects: Grant TR-35003 "Ambientally intelligent service robots of anthropomorphic characteristics", by Mihajlo Pupin Institute, University of Belgrade, Serbia and Grant OI-174001 "The dynamics of hybrid systems of complex structure", by Institute SANU Belgrade and Faculty of Mechanical Engineering University of Nis, Serbia, and partially supported by the project SNSF Care-robotics project no. IZ74Z0-137361/1 by Ecole Polytechnique Federale de Lausanne, Switzerland. We are grateful to Prof. Dr. Katica R. (Stevanovic) Hedrih from Mathematical Institute, Belgrade for supporting this research.

[2] e-mail address: mirjana.filipovic@pupin.rs
[3] e-mail address: ljubinko.kevac@gmail.com

developed in this paper. The effects during and after collision of motor anchor and elastic carrier of conveyor are also modeled in this paper. This is important process since this phenomenon is present in the realization of the transportation process. The mathematical model of the mechanism of the conveyor is highly non-linear.

1. Introduction

Vibratory conveying mechanism represents system which by carrying out and forming of elastic effects realizes the task of motion of bulk and particulate materials. This system is used in many material processing technologies, for example: drying, dust collection, classification, dosing, compaction, crushing, dehydration, etc.

The mathematical models used in the associated control structures are based on appropriate simplifications. Firstly, the impact between vibratory conveyor base and its elastic supports is neglected. In order to obtain a high quality estimate at the output of the state observer, and therefore accomplish an appropriately high performance and (or) control quality, it is necessary to have a detailed mathematical model of the resonant vibratory conveyor with electromagnetic excitation, which takes into account the neglected effects mentioned above. The previously mentioned reasons are the main motivation for deriving a more detailed mathematical model of the resonant vibratory conveyor presented in this paper. Derivation of the mathematical model is based on calculation of the kinetic and potential energies, dissipative function of the mechanical system, and Lagrangian formulation, as well. Also, a set of simulation results is presented and compared to the previously published papers.

Based on the same principle defined in papers [1]-[5], the elasticity of composite spring is introduced in the mathematical model of vibratory conveying mechanism.

The effect of the collision is practically unavoidable in contact tasks transporter work. Chumenko [6] was the first who gave the analysis of collision of the robot with the environment. The papers [7], [8] observe the influence of the friction on bodies in collision. Hurmuzlu and Marghitu [9] consider the collision of absolutely rigid kinematic chains in more contact points. Tornambe [10] considers the problem of collision from the point of elasto-dynamic so that the collision was modeled by the method of distributed masses. In [11], the impact of the collision is modeled. On the same principles it is modeled in this paper.

A number of new effects have been introduced in this paper in comparison to the procedure for defining the mathematical model of the conveyors mechanism in relation to the published papers [12], [13].

The Rayleigh's angle ω is defined in [14] and introduced in this paper as real characteristic of composite spring

Procedure of defining the dynamic model and modeling of collision for observed elastic system with all elements of coupling is presented completely as well as with dynamic effects of present forces defined in Section 2. We presented the kinematic model and the procedure of the „direct kinematics" solutions in Section 3. Section 4 analyzes simulation example for motion dynamic of a transporter with one flexible composite spring and three more springs. Section 5 gives some concluding remarks.

2. Dynamic model of conveyor mechanism

Vibratory-conveying drives with electromagnetic vibratory actuator (EVA) are very popular in the process industry of bulk materials. These drives provide a simple control of bulk material mass-flow.

It is understood that the transporter mechanism powered by the motor force *F*. The motor force *F* is changing in dynamic behavior and in that manner, it changes the dynamic behavior of vibratory-conveyor mechanism, during the realization of task, and in that manner dictates dynamics motion of powder or granular material, which are being transported.

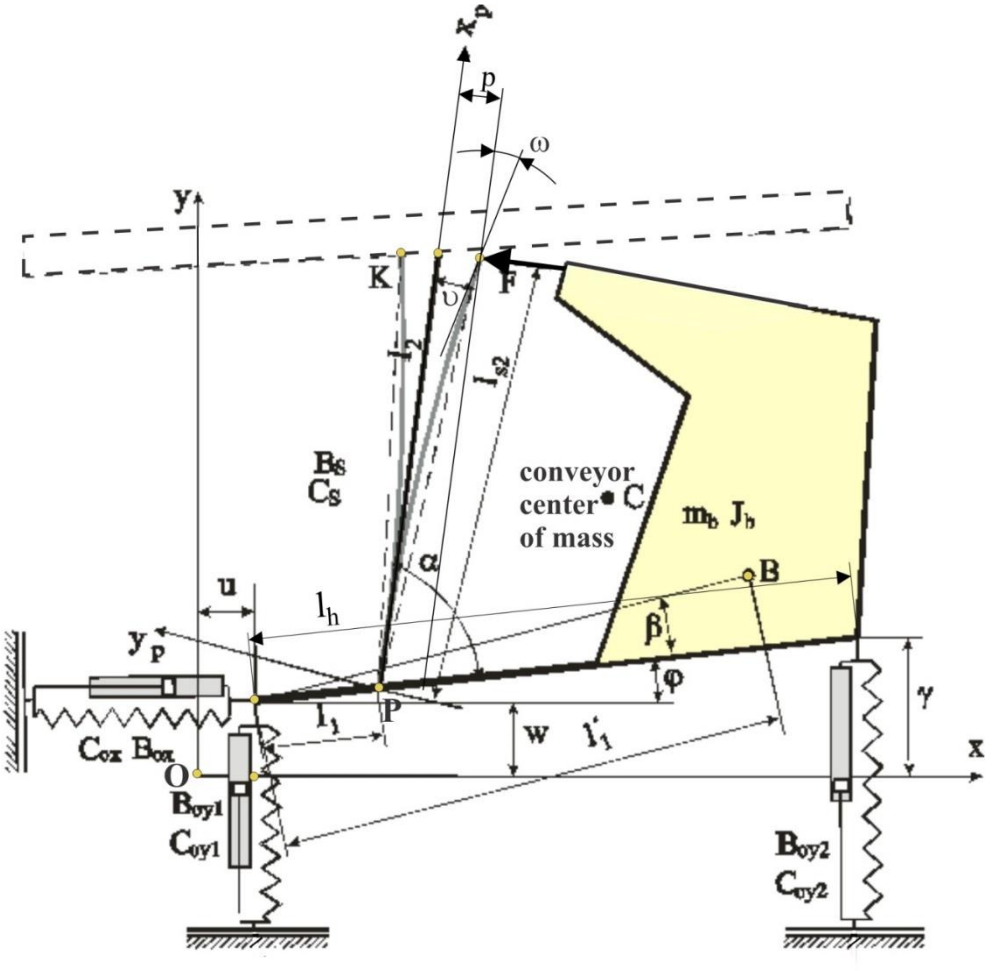

Fig. 1. Conveyor mechanism.

In dependence of shape of motor force *F*, we have two different examples:

1. First example: The motor force *F* changes continuously intensity, programmed, works for all of time of working of transporter mechanism.
2. Second example: This case is composed of two phases which alternate precisely, programmatically, in different time intervals. Motor force is dealing in infinite short period of time and after that follows the response of the system in finite period of time. These two stages are repeated cyclically.

a) The first stage: The impact force deal at a very short time interval. It's just one moment when the conveyor is exposed to the motor force. The action of force F is repeated cyclically with determined intensity. It's must be emphasized that one of integral phenomenon of the dynamics of the conveyor motion is the impact of the collision. It's just one time moment when the conveyor is exposed to the motor force.

b) The second stage: The free motion of the transporter, immediately after the action of motor force. This is time period when the motor force is not working. In this time period $F=0$. This is essentially the response of the conveyor system over a period of time from the moment of the termination of force F until the moment it's re-effect on the system. This is the system response period of the conveyor system on influence of impact force.

We will define a mathematical model of the system for both examples.

By applying Lagrange's equation to expressions for potential and dissipative energy: as result of motion of elasticity composite spring, as result of motion of elasticity horizontal and vertical springs and kinetic energy of the mechanism presented in Fig. 1 with respect to the generalized coordinates: p/l_2, u , w and φ, the equations of motion are obtained in the matrix form.

$$\begin{bmatrix}0\\0\\0\\0\end{bmatrix}=\begin{bmatrix}H_{11}&0&0&H_{14}\\0&H_{22}&0&0\\0&0&H_{33}&0\\H_{41}&0&0&H_{44}\end{bmatrix}\cdot\begin{bmatrix}\ddot{p}/l_2\\\ddot{u}\\\ddot{w}\\\ddot{\varphi}\end{bmatrix}+\begin{bmatrix}h_1\\0\\0\\h_4\end{bmatrix}+\begin{bmatrix}G_1\\0\\G_3\\G_4\end{bmatrix}+\begin{bmatrix}C_{11}\cdot l_2&0&0&0\\0&C_{22}&0&0\\0&0&C_{33}&C_{34}\\0&0&C_{34}&C_{44}\end{bmatrix}\cdot\begin{bmatrix}p/l_2\\u\\w\\\varphi\end{bmatrix}+$$
$$+\begin{bmatrix}B_{11}\cdot l_2&0&0&0\\0&B_{22}&0&0\\0&0&B_{33}&B_{34}\\0&0&B_{34}&B_{44}\end{bmatrix}\cdot\begin{bmatrix}\dot{p}/l_2\\\dot{u}\\\dot{w}\\\dot{\varphi}\end{bmatrix}-\begin{bmatrix}J_{11}&J_{12}&0&J_{14}\\J_{21}&0&J_{23}&J_{24}\end{bmatrix}^{T}\cdot\begin{bmatrix}F_x\\F_y\end{bmatrix}\qquad(1)$$

This mechanism, described in equation (1), is influenced by the force $F=[F_x\ F_y]^T$ of a motor that continuously works on system.

The second example is more interesting. This case is composed of two phases which alternate, programmatically, in different time intervals. In the first phase motor force is dealing in infinite short period time and then the equations of system are obtained:

$$\begin{bmatrix} H_{11} & 0 & 0 & H_{14} \\ 0 & H_{22} & 0 & 0 \\ 0 & 0 & H_{33} & 0 \\ H_{41} & 0 & 0 & H_{44} \end{bmatrix} \cdot \begin{bmatrix} \dot{p}/l_2 \\ \dot{u} \\ \dot{w} \\ \dot{\varphi} \end{bmatrix} = \begin{bmatrix} J_{11} & J_{12} & 0 & J_{14} \\ J_{21} & 0 & J_{23} & J_{24} \end{bmatrix}^T \cdot \begin{bmatrix} F_x \\ F_y \end{bmatrix} \cdot \Delta t \tag{2}$$

After that follows the response of the system for finite period time, described in equation (3):

$$\begin{bmatrix} 0 \\ 0 \\ 0 \\ 0 \end{bmatrix} = \begin{bmatrix} H_{11} & 0 & 0 & H_{14} \\ 0 & H_{22} & 0 & 0 \\ 0 & 0 & H_{33} & 0 \\ H_{41} & 0 & 0 & H_{44} \end{bmatrix} \cdot \begin{bmatrix} \ddot{p}/l_2 \\ \ddot{u} \\ \ddot{w} \\ \ddot{\varphi} \end{bmatrix} + \begin{bmatrix} h_1 \\ 0 \\ 0 \\ h_4 \end{bmatrix} + \begin{bmatrix} G_1 \\ 0 \\ G_3 \\ G_4 \end{bmatrix} +$$
$$+ \begin{bmatrix} C_{11} \cdot l_2 & 0 & 0 & 0 \\ 0 & C_{22} & 0 & 0 \\ 0 & 0 & C_{33} & C_{34} \\ 0 & 0 & C_{34} & C_{44} \end{bmatrix} \cdot \begin{bmatrix} p/l_2 \\ u \\ w \\ \varphi \end{bmatrix} + \begin{bmatrix} B_{11} \cdot l_2 & 0 & 0 & 0 \\ 0 & B_{22} & 0 & 0 \\ 0 & 0 & B_{33} & B_{34} \\ 0 & 0 & B_{34} & B_{44} \end{bmatrix} \cdot \begin{bmatrix} \dot{p}/l_2 \\ \dot{u} \\ \dot{w} \\ \dot{\varphi} \end{bmatrix} \tag{3}$$

These two stages are repeated cyclically.

3. Kinematics model of conveyor mechanism

Relationship between internal coordinates p/l_2, u, w, φ, ω and Cartesian, external, coordinates x_k y_k ψ_k was defined as so-called "direct kinematics" problem. In this case (see Fig. 1):

$$x_k = u + l_1 \cdot \cos\varphi + l_2 \cdot \cos(\alpha^* + \varphi) \tag{4}$$

$$y_k = w + l_1 \cdot \sin\varphi + l_2 \cdot \sin(\alpha^* + \varphi) \tag{5}$$

$$\psi_k = + p/l_2 + \varphi + \omega \tag{6}$$

Where $\alpha^* = \alpha + (p/l_2)$.

The Jacobi matrix J will be formed as a connection between the velocity vector of the external coordinates $\dot{x}_k, \dot{y}_k$, which defines the velocity of a point K of the conveyor carriers in the Cartesian coordinates, and the velocity vector of generalized coordinates $\dot{p}/l_2, \dot{u}, \dot{w}, \dot{\varphi}$.

$$\begin{bmatrix} \dot{x}_k \\ \dot{y}_k \end{bmatrix} = \begin{bmatrix} J_{11} & 1 & 0 & J_{14} \\ J_{21} & 0 & 1 & J_{24} \end{bmatrix} \cdot \begin{bmatrix} \dot{p}/l_2 \\ \dot{u} \\ \dot{w} \\ \dot{\varphi} \end{bmatrix} \tag{7}$$

4. Simulations results

Simulation experiments were performed with the following characteristics of the mechanism: the stiffness C_s=*1.0 e+006 [kg/s^2]* and damping B_s=140[kg/s] characteristics of composite spring; the mass of the troughs carried by the conveyor is m_k=*20[kg]*; while the moment of inertia J_k= *0.02[kgm^2]*; the conveyor body weight is m_b=*1000[kg]*, the stiffness C_{ox}=*1.0 e+006[N/m]* and damping B_{ox}=*10000[N/(m/s)]* characteristics of the horizontal spring; the stiffness C_{oy1}=*1.0e+007[N/m]* and damping B_{oy1}=*10000[N/(m/s)]* characteristics of the left vertical spring; the stiffness C_{oy2}=*1.0 e+007 [N/m]* and damping B_{oy2}=*10000[N/(m/s)]* characteristics of the right vertical spring.

The first example is characterized by the impulse effect of the motor force only at the first time of the time selection *F= 50000[N]*, see Fig. 2. And after that the motor force is *F=0[N]*, i.e, it does not have the effect of the motor force and only the dynamics response of the mechanism of the transporter over the period of *5[s]* is observed.

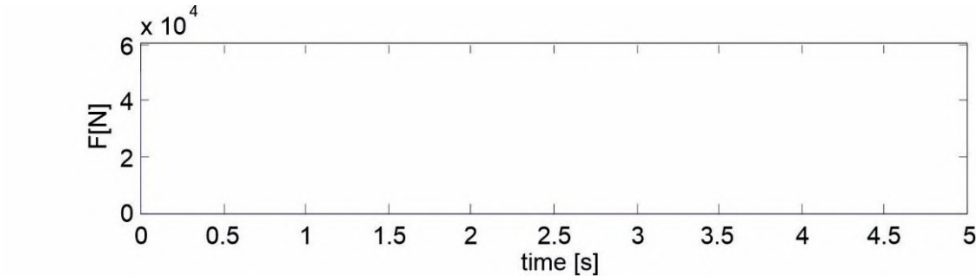

Fig. 2. Motor force *F*, Example I.

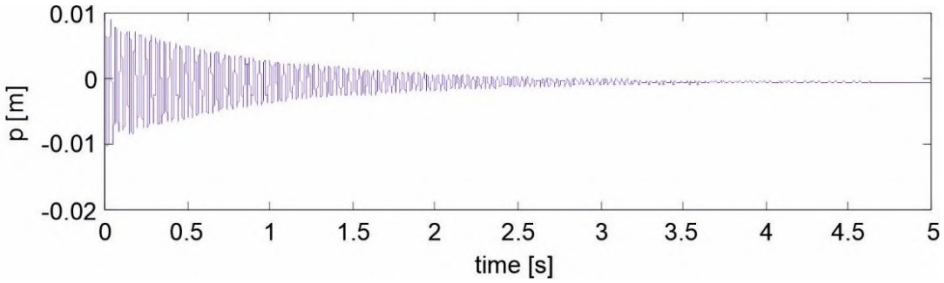

Fig. 3. Elastic deformation of composite spring *p*, Example I.

The response dynamics of all the generalized coordinates show the difference in the dynamics of the response of the system, the different attenuation characteristics, as well as also the evident presence of the influence of gravitational forces.

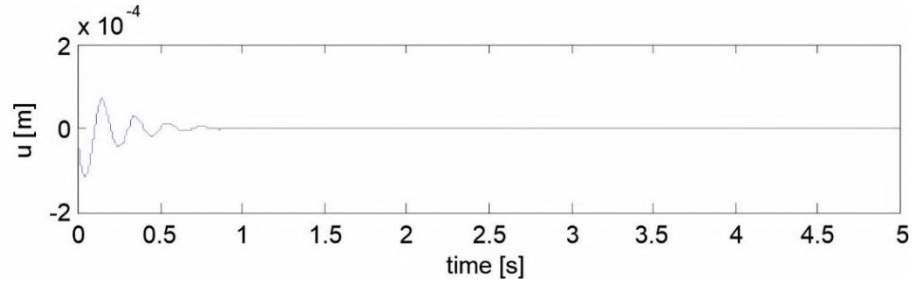

Fig. 4. Elastic deformation of horizontal spring *u*, Example I.

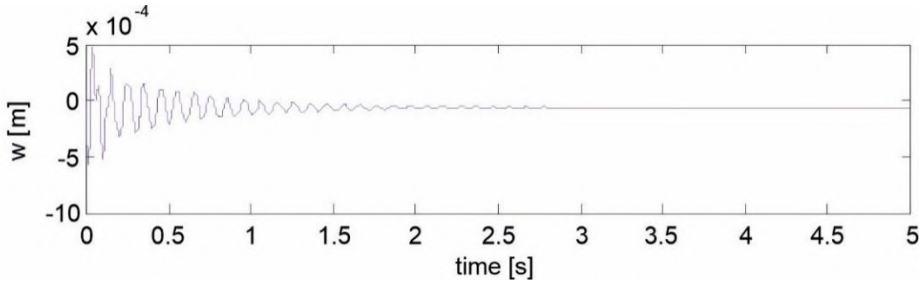

Fig. 5. Elastic deformation of left vertical spring *w*, Example I.

It is clear from Figs. 3-6 that each of the generalized coordinates has the static error size of the elastic deformation due to the presence of gravitational forces.

At the end of the implementation of the task, when the effect of the impulse force becomes zero, the effect of gravitational forces is seen. In the state of static equilibrium generalized coordinates take the following values: elastic deformation of composite spring tends to size $p= -0.0007[m]$, see Fig. 3, elastic deformation of horizontal spring $u= +0.00001[m]$, see Fig. 4, elastic deformation of left vertical spring $w= -0.00006[m]$, see Fig. 5, angle of rotation of the conveyor base $\varphi= -0.0038[rad]$, see Fig. 6.

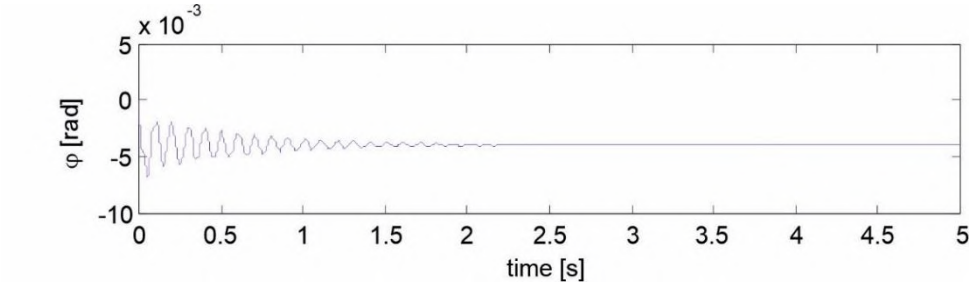

Fig. 6. Angle of rotation of the conveyor base φ, Example I.

The second example is characterized by the impulse effect of the motor force *F= 50000[N]*, which cyclically acts on the conveyor belt, see Fig. 7 and Fig. 8.

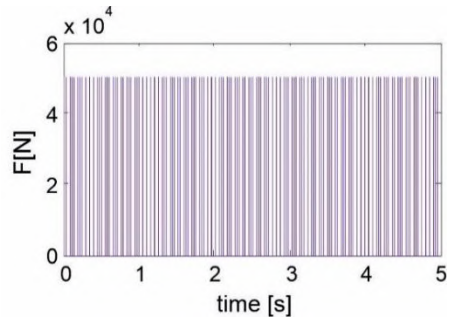

Fig. 7. Motor force *F*, for full time period, Example II

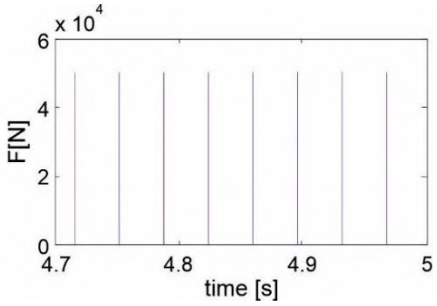

Fig. 8. Motor force *F*, for *t=4.7-5[s]*, Example II.

It's the frequency *f*= 27.78[Hz], while the selection period *T*= 0.036[s].

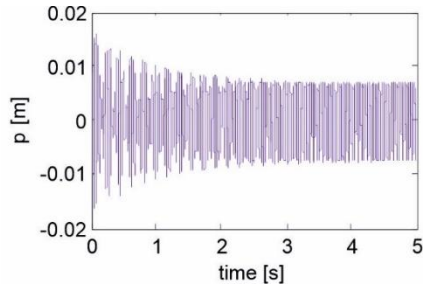

Fig. 9. Elastic deformation *p*, Example II.

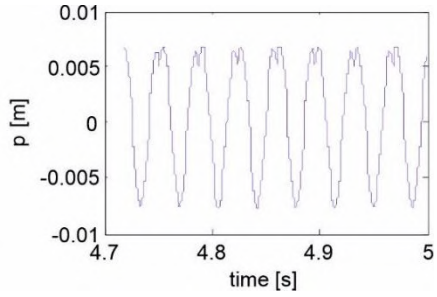

Fig. 10. Elastic deformation *p*, for *t=4.7-5[s]*, Example II.

For selected characteristics of the system, the dynamics of the change of the elastic deformation of composite spring *p* (order magnitudes $10^{-2}[m]$), for Example II, is presented in Fig. 9.

The left Fig. 9 represents the observed size during the realization of the entire task for total time of $T_{tot}=5[s]$, but right Fig. 10 represents the elastic deformation of composite spring *p* during short time period $t=4.7\text{-}5[s]$. It is just a separate detail of the observed size, for the period when the transition mode is completed and we only have influence of a cyclic impact force.

The statical error of the elastic deformation of the composite spring is $p_{ster}\approx -0.0007[m]$.

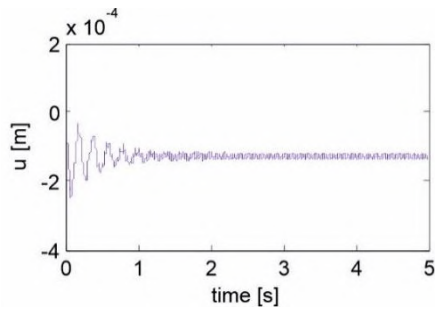

Fig. 11. Elastic deformation *u*, Example II.

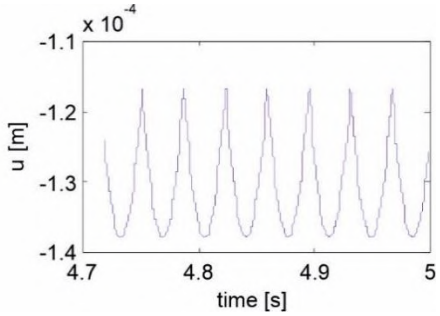

Fig. 12. Elastic deformation *u*, for $t=4.7\text{-}5[s]$, Example II.

The dynamics of the change of the second generalized coordinate, elastic deformation of the horizontal spring *u* (order magnitudes $10^{-4}[m]$), for Example II, is given in picture 11. The picture 12 represents only the selected details from the left image 11 in a short time interval $t=4.7\text{-}5[s]$. It is just a separate detail of the second generalized coordinate *u*, for the period when the transition mode is completed and we only have influence of cyclic impact force. The statical error of elastic deformation of the horizontal spring is $u_{ster}\approx -0.000128[m]$.

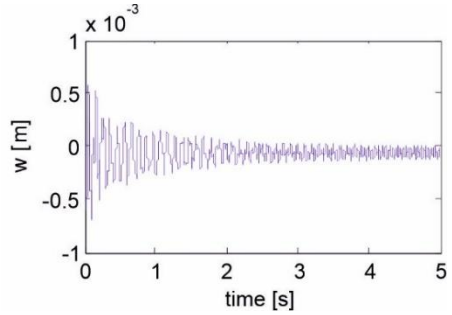

Fig. 13. Elastic deformation *w*, Example II.

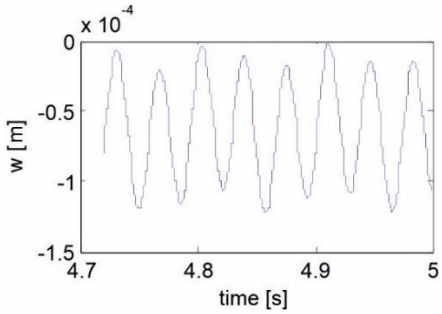

Fig. 14. Elastic deformation *w*, for *t=4.7-5[s]*, Example II.

The dynamics of the change of the third generalized coordinate, elastic deformation of left vertical spring *w* (order magnitudes 10^{-3}[m]), for Example II, is given in Fig. 13.

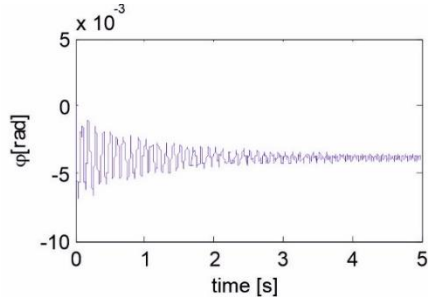

Fig. 15. Angle of rotation φ, Example II.

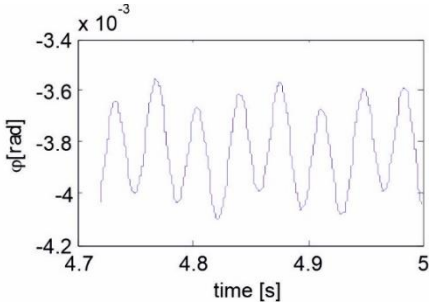

Fig. 16. Angle of rotation φ, for *t=4.7-5[s]*, Example II.

The picture 14 represents only the selected details from the left image 13 in a short time interval *t=4.7-5[s]*. It is just a separate detail of the third generalized coordinate *w*, for the period when the transition mode is completed and we have influence of cyclic impact force, only. The statical error elastic deformation of left vertical spring is $w_{ster} \approx$ *-0.00006[m]*.

The dynamics of the change of the fourth generalized coordinate, angle of rotation of the conveyor base φ (order magnitudes 10^{-3}*[rad]*), for Example II, is given on picture Fig. 15.

The picture 16 represent only the selected details from the left image 15, in a short time interval *t=4.7-5[s]*. It is just a separate detail of

the fourth generalized coordinate φ, for the period when the transition mode is completed and we have influence of cyclic impact force, only.

All four generalized coordinates: p/l_2, u, w, φ, and their velocities: $\dot{p}/l_2, \dot{u}, \dot{w}, \dot{\varphi}$ are used in kinematic relations (4)-(7) to be calculate external coordinates x_k and y_k, and their velocities, also. The x_k and y_k are coordinate of tip of composite spring in point K, in x-y plane. See Fig. 1. The motion and motion velocity of point K of composite spring, for II Example in a short time interval $t=4.7\text{-}5[s]$, are presented in Figs. 17 and Fig 18, respectively. We can see that motion of point K oscillatory, cyclically and that is rhythmically repeating, for the period when the transition mode is completed (when we no longer have the effect of influence deviating of the initial conditions) and we have influence of cyclic impact force, only.

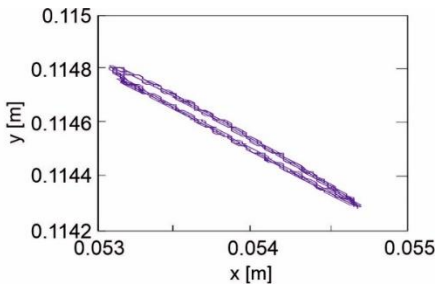

Fig. 17. Motion of point K, for $t=4.7\text{-}5[s]$, Example II.

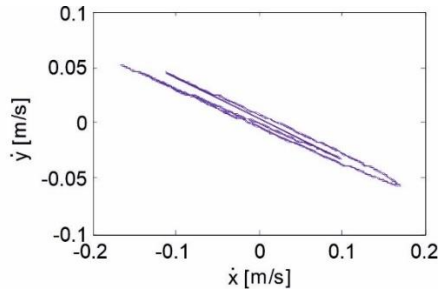

Fig. 18. Motion velocity of point K, for $t=4.7\text{-}5[s]$, Example II.

5. Conclusions

In this paper, a dynamic model of the conveyor mechanism for grain (and scattered) materials is defined using the Lagrangian equation of the second order relative to the chosen generalized coordinates. The equations are obtained by using equations of equilibrium in the classical form that describe the motion of a vibratory conveyor which in addition to rigid elements, build the elastic elements, also.

Three mathematical models of the system are defined when:

1. the motor force works continual in the finite time interval, equation (1),
2. when the motor force works at small time interval, equation (2),
3. conveyor mechanism is working without motor force; this model shows the dynamics of the response of the system after the impact of the motor force, equation (3).

Model 1 is used when we want to generate a certain form of motor force at a finite time interval. Dynamic model of that system is generated but it is not analyzed in detailed, in this paper. If we choose the motor force to be impulse and needs to be repeating rhythmically, the work of the conveyor mechanism defines the model 2 and the model 3 that are cyclically and in the same order repetitive. In model 2, the phenomenon of collision is defined, and this is the moment when the motor hits the trough with force F, at small time period. Influence of the current force F is special phenomenon, which has own legality. At the moment of collision, the motor force does not only work on the elastic deformation of composite spring, coordinate p direction, but it also transmits and acts on other generalized coordinates, also, via Jacobi's matrix. At the moment after impact act of the motor force on the vibratory conveyor, then the dynamics of the behavior of the system is different and it is mathematically formulated by the model 3.

This paper especially analyzed cyclically work of conveyor mechanism when periods of impact force and responses are cyclically alternated.

The kinematic model of that system is generated in first time in literature so far by equations (4)-(7). This paper especially analyzed cyclically work of conveyor mechanism when are periods of: impact force and response of a conveyor mechanism are cyclically alternate. The novelty is the Jacobi matrix, through which the mapping the of motor force on a dynamic motion of system is given. It should be especially emphasized that we now have the ability to calculate and planning the motion of the top of the composite spring, i.e, the motion of the conveyor, which implies the possibility of planning the motion of the transport material.

A comparative analysis of this model was made with the so far known models in this field.

- Different structure of inertia matrix H, different coupling between the generalized coordinates, through the inertial matrix H,
- presence of Coriolis forces h in dynamical model of conveyor, different coupling between the generalized coordinates, through the Coriolis forces h,
- presence of Gravity forces G in dynamical model of conveyor,
- different coupling between the generalized coordinates, through the matrix of rigidity C and matrix of damping B,

- the motor force F that transmitted over the Jacobian matrix J not only to the motion of the generalized coordinate p/l_2 (as interpreted so far in literature), but also to the motion of the other three generalized coordinates u, w and φ,
- the kinematics model of such a mechanism is defined, which is a prerequisite for the correct definition of a dynamic model,
- the Rayleigh's angle ω are introduced as real characteristic of composite spring.

During the realization of this paper, the TRAMECH software package was created using MATLAB which is user-oriented for the synthesis and analysis of the conveyor mechanism. The results of the simulation results are also shown.

The possibility of change of trajectory motion of point K opens new research view in this area, where we have possibility to planning the trajectory and velocity of the transport material and thus its flow, changing of conveyor components characteristics. This result is new and original, in relation to the solutions known so far.

With fundamental approach to analysis of flexibility of the complex mechanism, opened a wide field of working on analyzing and modeling of a mechanism of conveyor and we attempted to give a contribution to the development of this area.

References

[1] M. Filipović, M. Vukobratović, Modeling of Flexible Robotic Systems, *Computer as a Tool, EUROCON 2005, The International Conference,* Belgrade, Serbia and Montenegro, 2, (2005)1196 – 1199.

[2] M. Filipović, M. Vukobratović, Contribution to modeling of elastic robotic systems, *Engineering & Automation Problems, International Journal*, 5(1), (2006)22-35.

[3] M. Filipović, M. Vukobratović, Complement of Source Equation of Elastic Line, *Journal of Intelligent & Robotic Systems, International Journal*, 52(2), (2008)233 – 261.

[4] M. Filipović, M. Vukobratović, Expansion of source equation of elastic line, *Robotica, International Journal,* 26(6), (2008)739-751.

[5] M. Filipović, Relation between Euler-Bernoulli Equation and Contemporary Knowledge in Robotics, *Robotica, International Journal, Cambridge University Press,* 30(1), (2012)1-13.
[6] V. N. Chumenko, A. S. Yuschenko, Impact Effects Upon Manipulation Robot Mechanism, *(in Russian), Technical cybernetics*, 4, 1981.
[7] J. B. Keller, Impact with Friction, *Journal of Applied Mechanics,* 29/1-29/4, 1986.
[8] W. J. Stronge, Rigid Body Collision with Friction, *Proc. R. Soc. Lond. A*, 429, (1990)169-181.
[9] Y. Hurmuzlu, D. B. Marghitu, Rigid Body Collision of Planar Kinematic Chain with Multiple Contact Points, *Intl. J. of Robotic Research*, 13(1), (1994)82-92.
[10] A. Tornambe, Modeling and Controlling Two-Degrees- of-Freedom Impacts, *Proc. 3rd IEEE Mediterranean Conf. On Control and Automation, Lymassol, Cyprus,* 1995.
[11] M. Filipovic, Elastic Robotic System with Analysis of Collision and Jamming, *7th International Symposium on Intelligent Systems and Informatics - SISY 2009, Subotica, Serbia,* 2009.
[12] T. Doi, K. Yoshida, Y. Tamai, K. Kono, K. Naito, T. Ono, Modelling and feedback control for vibratory feeder of electromagnetic type, *J. Robot. Mechatron*. 11(5), (1999)563–572.
[13] Z. Despotovic, Dj. Urukalo, M. Lecic, A. Cosic, Mathematical modeling of resonant linear vibratory conveyor with electromagnetic excitation: simulations and experimental results, *Applied Mathematical Modelling*,41, pp. 1–24, 2017.
[14] J. W. Strutt (Lord Rayligh), Theory of Sound, *second publish, paragraph 186*, 1894-1896.

Design of a mechanical system to admit similar rigid body nonlinear modes and the correlation with perpetual mechanics

Fotios Geogriades[†]
Centre of Perpetual Mechanics & Centre for Nonlinear Systems
Mechanical Engineering Department
Chennai Institute of Technology
Chennai 600069
India

ABSTRACT

Perpetual points defined in mathematics recently and among other research directions they are used, as herein, in mechanics. The perpetual manifolds and the augmented perpetual manifolds are defined that describe the dynamics of mechanical systems while they are moving in rigid body motions. Moreover the dynamics in perpetual manifolds has interest in terms of mechanics, with features such as zero sums of internal forces etc., which lead to the perpetual mechanics concept. In this article the design of a mechanical system with typical solution of differential equations is done. Then the developments in perpetual mechanics are employed to perform the same design and some analysis of the mechanics of this system. The analysis of the mechanics of this system deploys hidden characteristics from the dynamic analysis, and this justifies the term perpetual mechanics. Finally the theoretical results are numerically verified, with excellent agreement.

1. Introduction

The perpetual points have been defined in mathematics recently (Prasad 2015) [1]. They are defined as the sets of points that arise by setting accelerations and jerks of a mechanical system equal to zero, but for nonzero velocities. Their significance in examining dynamics of systems

[†] e-mail address: fotiosgeorgiades@citchennai.net; dr.fotios.georgiadis.gr@gmail.com; fgeorg@yahoo.com

is ongoing research that can be grouped in 4 research directions. The first research direction is about the perpetual points themselves with several definitions and experiments to identify them [1-4]. The second research direction is relevant to the use of the perpetual points to capture characteristics of nonlinear dynamics of systems such as hidden and chaotic attractors [5-14]. The third research direction is relevant to identification of dissipative systems through the perpetual point's concept [15-19]. Finally the fourth research direction is to use the perpetual points in examining dynamics and mechanics of mechanical systems [20-27], that the content of this article belongs to. In linear mechanical systems, and some nonlinear, the perpetual points are associated with rigid body motions [20-21], which lead to the definition of the perpetual mechanical systems in [22]. The perpetual mechanical systems are defined as the systems that admit as perpetual points, the sets of points that are associated with rigid body motion, and they are forming the perpetual manifolds. In [22] the concept of perpetual manifolds to the augmented perpetual manifolds has been extended, and they are defined by the state spaces of mechanical systems that are moving in rigid body motion, and they can be obtained when their accelerations are equal but not necessarily zero. Moreover in [22] a theorem has been proved defining the conditions that the dynamics of mechanical system is described by the augmented perpetual manifolds. Following the theorem developed in [22], a corollary in [23] is stated and proved, that there is zero sum of the perpetual mechanical system's internal forces when their motion is described by the exact augmented perpetual manifolds, and this is significant outcome for the mechanics of these systems. The functional forms of the exact augmented perpetual manifolds, defined by the theorem in [22], for a specific mechanical system they are infinite and this is proved in a corollary [24]. Moreover different mechanical systems can have exactly the same motions defined by the exact augmented perpetual manifolds, as proved in a corollary [25]. In another corollary is proved that the perpetual mechanical systems with nonlinear internal forces and these that are restricted to only linear internal forces for the same external forcing and the same initial conditions they have the same motion. Therefore there is no need for cumbersome nonlinear modelling of the internal forces of the perpetual mechanical system in order to describe the motion in the exact augmented perpetual manifolds. In [26] a theorem is stated and proved, examining the internal forces, and energy dissipation of the perpetual mechanical system when the motion is

described by the exact augmented perpetual manifolds. Under conditions, when the motion of the perpetual dissipative mechanical system is described by the exact augmented perpetual manifolds, all the individual internal forces are eliminated, there is no energy loss due to damping, the external work done is equal to the changes of the kinetic energy and the perpetual mechanical system can behave as perpetual machine of third kind.

Therefore since in [20-27] the augmented perpetual manifolds are not only used for the dynamic analysis of the mechanical systems but also used to examine the mechanics behind the motion in the exact augmented perpetual manifolds these research outcomes are forming the initial step in developing the perpetual mechanic theory.

In this article an example of analytical design of a nonlinear mechanical system to admit similar rigid body motions is done. In section 2.1, without employing any relevant tool associated with a perpetual mechanical system, by seeking solutions which are corresponding to similar rigid body motions the design is done. Then in section 2.2, using the perpetual mechanics concepts [20-26], the design is repeated and also further features in terms of mechanics that cannot be directly identified from the design of section 2.1 are examined. In section 3 the analytical results with numerical simulations are examined.

2. Theoretical analysis

2.1 Dynamic analysis

As an example a four degrees of freedom nonlinear system, with a configuration shown in Figure 1, is going to be designed for admitting similar rigid body modes. The equations of motion are given by,

$$[\boldsymbol{M}] \times \{\ddot{\boldsymbol{x}}_{\boldsymbol{i}}(t)\} + [\boldsymbol{K}] \times \{\boldsymbol{x}_{\boldsymbol{i}}(t)\} + \left\{\boldsymbol{F}_{\boldsymbol{NL,j}}\left(x_p(t)\right)\right\} = \{0\}, \quad (1)$$

with $p \in \{1, \dots, 4\}$, and i,j=1,...,4. The mass matrix is defined by,

$$[\boldsymbol{M}] = \begin{bmatrix} m_1 & 0 & 0 & 0 \\ 0 & m_2 & 0 & 0 \\ 0 & 0 & m_3 & 0 \\ 0 & 0 & 0 & m_4 \end{bmatrix}, \quad (2a)$$

and m_i $(i = 1,..,4)$ are positive constants.

The stiffness matrix is defined by,

$$[\boldsymbol{K}] = \begin{bmatrix} k_1 + k_{ext,1} & -k_1 & 0 & 0 \\ -k_1 & k_1 + k_2 + k_{ext,2} & -k_2 & 0 \\ 0 & -k_2 & k_2 + k_3 + k_{ext,3} & -k_3 \\ 0 & 0 & -k_3 & k_3 + k_{ext,4} \end{bmatrix}. \quad (2b)$$

The nonlinear forces vector associated with an elastic potential is given by,

$$\left\{\boldsymbol{F_{NL,j}}\left(x_p(t)\right)\right\} = \begin{Bmatrix} k_{nl,1} \cdot (x_1 - x_2)^3 \\ -k_{nl,1} \cdot (x_1 - x_2)^3 + k_{nl,2} \cdot (x_2 - x_3)^3 \\ -k_{nl,2} \cdot (x_2 - x_3)^3 + k_{nl,3} \cdot (x_3 - x_4)^3 \\ -k_{nl,3} \cdot (x_3 - x_4)^3 \end{Bmatrix}. \quad (2c)$$

A possible rigid body motion solution is defined by,

$$x_i = x_a, \text{ for } i = 1, \dots, 4, \; x_a \in \mathbb{R}, \quad (3a)$$

and,

$$\dot{x}_i = \dot{x}_a, \text{ for } i = 1, \dots, 4, \; \dot{x}_a \in \mathbb{R}^*, \quad (3b)$$

which leads to,

$$\ddot{x}_i = \ddot{x}_a, \text{ for } i = 1, \dots, 4. \quad (3c)$$

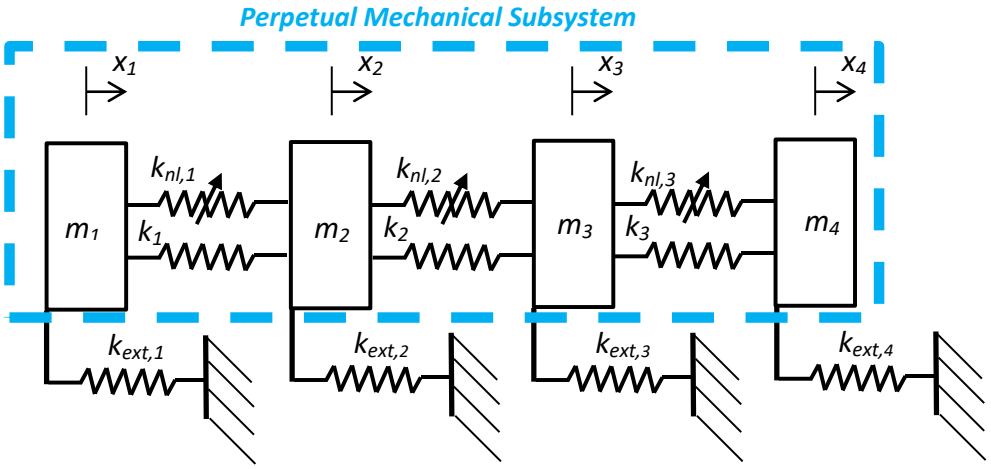

Figure 1. The configuration of the mechanical system, indicating with cyan lines the underlying perpetual mechanical system.

The trial method for a rigid body motion solution of the mechanical system, with configuration shown in Figure 1, is examined by replacing equations (3) in equations (1),

$$[\boldsymbol{M}] \times \{\boldsymbol{1}\} \cdot \ddot{x}_a + [\boldsymbol{K}] \times \{1\} \cdot x_a + \left\{\boldsymbol{F_{NL,j}}\left(x_a(t)\right)\right\} = \{\boldsymbol{0}\}, \quad (4)$$

whereas using equation (2b), leads to,

$$[\boldsymbol{K}] \times \{1\} \cdot x_a =$$

$$= \begin{bmatrix} k_1 + k_{ext,1} & -k_1 & 0 & 0 \\ -k_1 & k_1 + k_2 + k_{ext,2} & -k_2 & 0 \\ 0 & -k_2 & k_2 + k_3 + k_{ext,3} & -k_3 \\ 0 & 0 & -k_3 & k_3 + k_{ext,4} \end{bmatrix} \times \{1\} \cdot x_a$$

$$= \begin{Bmatrix} k_{ext,1} \\ k_{ext,2} \\ k_{ext,3} \\ k_{ext,4} \end{Bmatrix} \cdot x_a. \quad (5a)$$

Also using equation (2c) in equation (4) lead to,

$$\{\boldsymbol{F_{NL,j}}(x_a(t))\} = \{\mathbf{0}\}. \quad (5b)$$

Replacing equations (5a-b) in equation (4) lead to the following decoupled differential equations,

$$\begin{Bmatrix} m_1 \\ m_2 \\ m_3 \\ m_4 \end{Bmatrix} \cdot \ddot{x}_a + \begin{Bmatrix} k_{ext,1} \\ k_{ext,2} \\ k_{ext,3} \\ k_{ext,4} \end{Bmatrix} \cdot x_a = \{\mathbf{0}\}, \quad (6a)$$

which they are not necessarily having the same coefficients, and as it should be expected, in the general case they are inconsistent.

The condition that all the equations would be the same is that the following ratios are true,

$$\frac{k_{ext,1}}{m_1} = \frac{k_{ext,2}}{m_2} = \cdots = \frac{k_{ext,4}}{m_4} = \omega_n^2. \quad (6b)$$

If the parameters defining the internal forces in equation (6a) are following equation (6b) then the solution is rigid body motion, and it is given by any of the equivalent differential equations of equations (6a), which can be written as,

$$\ddot{x}_a + \omega_n^2 \cdot x_a = 0. \quad (6c)$$

The solution of equation (6c) can be found in any vibration textbook and in explicit form is given by [28-29],

$$x_a(t) = A \cdot sin(\omega_n \cdot t + \varphi), \quad (7a)$$

with,

$$A = \sqrt{q_a^2(t_0) + \left(\frac{\dot{q}_a(t_0)}{\omega_n}\right)^2}, \quad (7b)$$

$$\varphi = tan^{-1}\left(\frac{q_a(t_0) \cdot \omega_n}{\dot{q}_a(t_0)}\right). \quad (7c)$$

The velocity is given by,

$$\dot{x}_a(t) = \omega_n \cdot A \cdot cos(\omega_n \cdot t + \varphi), \quad (7d)$$

and the acceleration is,

$$\ddot{x}_a(t) = \omega_n^2 \cdot A \cdot sin(\omega_n \cdot t + \varphi). \tag{7e}$$

In case that equation (6b) is equal to zero, then equation (6c) that defines the motion is taking the form,

$$\ddot{x}_a = 0, \tag{8a}$$

and choosing initial conditions associated with rigid body motion then with direct integration leads to,

$$\dot{x}_a(t) = \dot{x}_a(t_0) = ct, \tag{8b}$$

and,

$$x_a(t) = \dot{x}_a(t_0) \cdot t + x_a(t_0), \tag{8c}$$

whereas for zero initial velocity there is no motion on the system.
Therefore splitting the stiffness matrix $[\boldsymbol{K}]$ defined by equation (2b) as follows,

$$[\boldsymbol{K}] = [\boldsymbol{K_{int}}] + [\boldsymbol{K_{ext}}], \tag{9a}$$

with,

$$[\boldsymbol{K_{int}}] = \begin{bmatrix} k_1 & -k_1 & 0 & 0 \\ -k_1 & k_1 + k_2 & -k_2 & 0 \\ 0 & -k_2 & k_2 + k_3 & -k_3 \\ 0 & 0 & -k_3 & k_3 \end{bmatrix}, \tag{9b}$$

and,

$$[\boldsymbol{K_{ext}}] = \begin{bmatrix} k_{ext,1} & 0 & 0 & 0 \\ 0 & k_{ext,2} & 0 & 0 \\ 0 & 0 & k_{ext,3} & 0 \\ 0 & 0 & 0 & k_{ext,4} \end{bmatrix}, \tag{9c}$$

then, following the derivation of equation (8a) from equation (6c), leads to zero K_{ext}, and the solution of rigid body motion given by equations (8b-c) can be obtained. The equations of motion of this subsystem are given by,

$$[\boldsymbol{M}] \times \{\ddot{\boldsymbol{x}}_{\boldsymbol{i}}(t)\} + \left\{\boldsymbol{F_{L,j}}\right\} + \left\{\boldsymbol{F_{NL,j}}\left(x_p(t)\right)\right\} = \{0\}, \text{ with } p \in \{1, \dots, 4\}, \text{ i,j=1,...,4.} \tag{10a}$$

whereas

$$\left\{\boldsymbol{F_{L,j}}\right\} = [\boldsymbol{K_{int}}] \times \{\boldsymbol{x_i}(t)\}. \tag{10b}$$

The aforementioned dynamic analysis leads to a sufficient design of the mechanical system in such a way to admit similar rigid body modes, but in more complicated systems e.g. N-dof the aforementioned dynamic analysis could become very cumbersome. Moreover there are hidden properties of the mechanical subsystem that is described by equations of motion (10) while the motion is defined by equations (6c), that will be discussed in the next section.

2.2 The design of the mechanical system and the view of perpetual mechanics

Definition of perpetual mechanical system

The perpetual mechanical subsystem arise from equations (1) when the stiffness matrix is comprised of only the first term of equation (9a), and in Figure 1 is shown by considering the internal elements of the cyan boundaries. As shown, this subsystem's motion is described by equation (10a), and admits the rigid body motion solutions defined by the equations (8b-c). These rigid body motion solutions escape to infinity and they are resulting indefinite motion of this subsystem. This observation justifies the terminology of perpetual mechanical system to characterize it [22]. In case of linear systems, the eigenvalue problem leads to zero first natural frequency, which is associated with the rigid body mode, but this is not the case for nonlinear systems since the eigenvalue problem cannot serve as a tool to identify rigid body modes. Therefore this definition leads to a uniform definition of such mechanical systems.

A mechanical system that admits perpetual points associated with rigid body motion solution given by equations (3a-c), means that all accelerations are equal to zero. Therefore, setting accelerations equal to zero this number of equations (N) is insufficient to define N-velocities, and N-displacements.

In case of writing the system as first order and setting the vector field equal to zero the equilibrium points are arising, whereas the accelerations and velocities are equal to zero, which means no motion. Therefore this system of equations is insufficient to characterize the perpetual mechanical systems. In order to obtain an extra set of equations, considering that the accelerations are equal to zero leads that also the jerks are equal to zero, and these equations can be used to define the rest N variables, which are associated with the nonzero velocities. In perpetual mechanical systems, the perpetual points associated with rigid body motions are infinite points, they form manifolds therefore they can form also solutions of the systems of differential equations.

It is still remains to show that the perpetual manifolds of rigid body motions of the perpetual mechanical system of Figure 1 are leading to zero jerks.

The equations of jerks of the perpetual mechanical system, can be obtained after differentiation of the equations (10), with respect to time, and they are given by,

$$[\boldsymbol{M}] \times \{\dddot{\boldsymbol{x}}_{\boldsymbol{i}}(t)\} + [\boldsymbol{K}_{\boldsymbol{int}}] \times \{\ddot{\boldsymbol{x}}_{\boldsymbol{i}}(t)\} + \left\{\dot{\boldsymbol{F}}_{\boldsymbol{NL,j}}\left(x_p(t)\right)\right\} = \{0\}, \tag{11a}$$

with $p \in \{1, \dots, 4\}$, i,j=1,...,4, whereas,

$$\left\{\dot{\boldsymbol{F}}_{\boldsymbol{NL,j}}\left(x_p(t)\right)\right\} =$$

$$= \begin{Bmatrix} 3 \cdot k_{nl,1} \cdot (x_1 - x_2)^2 \cdot (\dot{x}_1 - \dot{x}_2) \\ -3 \cdot k_{,nl,1} \cdot (x_1 - x_2)^2 \cdot (\dot{x}_1 - \dot{x}_2) + 3 \cdot k_{,nl,2} \cdot (x_2 - x_3)^2 \cdot (\dot{x}_2 - \dot{x}_3) \\ -3 \cdot k_{nl,2} \cdot (x_2 - x_3)^2 \cdot (\dot{x}_2 - \dot{x}_3) + 3 \cdot k_{nl,3} \cdot (x_3 - x_4)^2 \cdot (\dot{x}_3 - \dot{x}_4) \\ -3 \cdot k_{nl,3} \cdot (x_3 - x_4)^2 \cdot (\dot{x}_3 - \dot{x}_4) + 3 \cdot k_{nl,4} \cdot (x_4 - x_5)^2 \cdot (\dot{x}_4 - \dot{x}_5) \end{Bmatrix}. \quad (11b)$$

Considering rigid body motion solution defined by equations (3a-c), with substitution of them in equation of jerks (11a), leads to,

$$[\boldsymbol{K_{int}}] \times \{\dot{\boldsymbol{x}}_{\boldsymbol{a}}\} = \begin{bmatrix} k_1 & -k_1 & 0 & 0 \\ -k_1 & k_1 + k_2 & -k_2 & 0 \\ 0 & -k_2 & k_2 + k_3 & -k_3 \\ 0 & 0 & -k_3 & k_3 \end{bmatrix} \times \{1\} \cdot \dot{x}_a = \{\boldsymbol{0}\}, \quad (12)$$

whereas equation (8b) is considered.

The vector term associated with the nonlinear forces in equation (11a), that it is given by the equation (11b) is straightforward to show that in case of rigid body motion (eq. 3a-c) is corresponding to zero vector.

Therefore the perpetual mechanical subsystem for rigid body motion, for nonzero velocities, is associated with accelerations and jerks equal to zero.

Augmented perpetual manifolds definition

In equation (6a) the accelerations are equal but not necessarily zero [22], and this leads to the necessity of defining the augmented perpetual manifolds, whereas they arise as solutions obtained from equation (6a). Upon the initial conditions the augmented perpetual manifolds might correspond to exact rigid body motions solutions whereas all the displacements are equal and the accelerations are equal.

In [22] the following theorem is proved defining the conditions that the solution is in the exact augmented perpetual manifolds:

"Any $N(\geq 2)$-degrees of freedom discrete mechanical system with generalized coordinates $q_i(t)$ that can be written as a perpetual mechanical system with external forcing that is described by the following system of differential equations,

$$\left[\boldsymbol{M_{i,j}}\left(t, q_l(t), \dot{q}_m(t)\right)\right] \times \{\ddot{\boldsymbol{q}}_{\boldsymbol{i}}(t)\} + \left[\boldsymbol{C_{i,j}}\right] \times \{\dot{\boldsymbol{q}}_{\boldsymbol{i}}(t)\} + \left[\boldsymbol{K_{i,j}}\right] \times \{\boldsymbol{q_i}(t)\} + \\ + \left\{\boldsymbol{F_j^{NL}}\left(q_n(t), \dot{q}_o(t)\right)\right\} = \left\{\boldsymbol{F_j}\left(t, q_p(t), \dot{q}_q(t)\right)\right\}, \text{ for} \\ i = 1, \dots, N,\ j = 1, \dots, N,\ l, m, n, o, p, q \in \{1,2, \dots, N\}, \\ \left(q_i(t), \dot{q}_i(t), \ddot{q}_i(t)\right) \in \mathbb{R}^3, \quad (13)$$

and admits unique solutions for the following matrices,

$\left[\boldsymbol{M_{i,j}}\right]$ *is a real $N \times N$ inertia matrix with elements that can be, nonsmooth, nonlinear, time and state dependent, functions but having at least one nonzero sum of k-row for all time instants,*

$[\boldsymbol{K_{i,j}}]$ *and* $[\boldsymbol{C_{i,j}}]$*, are real* $N \times N$ *constant, stiffness and proportional to velocity vector, matrices,*
$\{\boldsymbol{F_j^{NL}}\}$ *is a* $N \times 1$ *vector of nonlinear internal forces with elements state dependent nonlinear functions which can be nonsmooth but single-valued for rigid body motions, and* $F_j^{NL}(q_s, 0) = 0$ *for* $q_s \in \mathbb{R}$*,*
$\{\boldsymbol{F_j}\}$ *is a real* $N \times 1$ *vector of external forces with elements, time and state dependent, maybe nonlinear and nonsmooth functions,*
if the external forces (F_j) *with the reference k-inertia external force* (F_k) *are related as follows,*

$$F_j\big(t, q_a(t), \dot{q}_a(t)\big) = \frac{\sum_{j=1}^{N} M_{j,i}\big(t,q_a(t),\dot{q}_a(t)\big)\cdot F_k\big(t,q_a(t),\dot{q}_a(t)\big)}{\sum_{i=1}^{N} M_{k,i}\big(t,q_a(t),\dot{q}_a(t)\big)}, \text{ for}$$

$$j,k \in \{1,2,\dots,N\}, \text{ and } q_a(t) = q_i(t), \dot{q}_a(t) = \dot{q}_i(t), \quad (14)$$

then, the solution of any of the following differential equations,

$$\ddot{q}_a(t) = \frac{F_k\big(t,q_a(t),\dot{q}_a(t)\big)}{\sum_{i=1}^{N} M_{k,i}\big(t,q_a(t),\dot{q}_a(t)\big)} = G\big(t, q_a(t), \dot{q}_a(t)\big)\,, \quad (15)$$

with vector field G, for the following set of initial conditions at the time instant t_0*,*

$$q_i(t_0) = q_a(t_0), \quad \text{for} \quad i = 1,\dots,N, \quad \text{and,} \quad q_a(t_0) \in \mathbb{R}, \quad (16a)$$

$$\dot{q}_i(t_0) = \dot{q}_a(t_0), \quad \text{for} \quad i = 1,\dots,N, \quad \text{and,} \quad \dot{q}_a(t_0) \in \mathbb{R}, \quad (16b)$$

is defining the generalized coordinates-q_i *and their velocities in the exact augmented perpetual manifold,*

$$X = \big\{\big(t, q_a(t), \dots, q_a(t), \dot{q}_a(t), \dots, \dot{q}_a(t)\big), \big(t, q_a(t), \dot{q}_a(t)\big) \in \mathbb{R}^3\big\}. \quad (17)''$$

Mainly the equations of motion are written in such a way that the internal forces terms in the left side of equation (13), when the right-hand side is a zero vector, correspond to elements of the perpetual mechanical subsystem. In previous section is shown that these equations of motion that corresponds to a perpetual mechanical subsystem are the equations (10).
The system of equations that describes the motion, in our example, written in the form of equation (13), are given by,

$$[M] \times \{\ddot{x}_i(t)\} + [K_{int}] \times \{x_i(t)\} + \left\{F_{NL,j}\left(x_p(t)\right)\right\} = [K_{ext}] \times \{x_i(t)\},$$

with $p \in \{1,\dots,4\}$, and i,j=1,...,4. (18a)

and neglecting the nonlinear forces the underlying perpetual mechanical system arise as follows,

$$[M] \times \{\ddot{x}_{l,i}(t)\} + [K_{int}] \times \{x_{l,i}(t)\} = [K_{ext}] \times \{x_{l,i}(t)\}. \quad (18b)$$

Then, based on the theorem, to obtain a solution in the exact augmented perpetual manifolds/rigid body motion the right hand side elements in equation (17) should follow equation (14), than in this case is taking the form,

$$k_{ext,i} = \frac{m_i \cdot k_{ext,k}}{m_k}, \quad (19)$$

whereas upon the selection of k −reference inertia element lead to maximum four different designs. Equation (19) is actually a re-arrangement of the equation (6b) that similarly defines the conditions for rigid body motion solution of equation (1).

In our design, the similar rigid body normal mode with motion defined by the equation (6c) and solution given by equation (7a) is corresponding to particle-standing wave solution of the system.

As a summary so far, practically instead of repeating the approach of the previous section, using the limits (cyan boundaries) shown in Figure 1, the perpetual mechanical system can be defined and the forces associated with the rest elements can be separated in the right-hand side of equations of motion. Then applying straightforward the conditions defined by the theorem, the design can be easily done.

It should be highlighted that in the right-hand side of equation (13) the forces can be state and time depended, described by not necessarily linear and smooth functions, and as in our nonlinear example the design doesn't necessarily lead to nonlinear modes solutions.

As the theory developed so far, the analysis can be named dynamics of mechanical systems using the perpetual points concept or even, due to the definition of the perpetual mechanical systems, can be called dynamics of perpetual mechanical systems.

In [23] a corollary is stated and proved that the sum of internal forces, for an exact augmented perpetual manifolds solution, is zero, which is rather significant in the mechanics of these systems.

This can be easily verified in our example. For rigid body motions the sum of the internal forces, of the perpetual mechanical system, considering equation (10) with equations (5a-b) is equal to:

$$[\boldsymbol{K_{int}}] \times \{\boldsymbol{x_i}(t)\} + \left\{\boldsymbol{F_{NL,j}}\left(x_p(t)\right)\right\} = [\boldsymbol{K_{int}}] \times \{1\} \cdot x_a + \left\{\boldsymbol{F_{NL,j}}\left(x_a(t)\right)\right\} = \{\mathbf{0}\}, \quad (20)$$

therefore the sum of internal forces is zero.

Moreover in [26] a proved corollary practically states that neglecting the elements associated with the nonlinear internal forces of the perpetual mechanical system, and considering only the linear internal forces the solution and the design will be the same. This can be easily certified in our example, by considering the underlying linear mechanical system arising by neglecting the nonlinear forces vector in equations (1),

$$[\boldsymbol{M}] \times \{\ddot{\boldsymbol{x}}_{\boldsymbol{i}}(t)\} + [\boldsymbol{K}] \times \{\boldsymbol{x_i}(t)\} = \{0\}, \quad (21)$$

and following the same approach with the previous section, it can be easily verified that the rigid body motion is described by equation (6a) with the constraints defined by the equation (6b).

Therefore, there is no need for cumbersome modelling of the nonlinearities of the mechanical system in order to examine exact augmented perpetual manifolds solutions.
The last two mentioned corollaries, are justifying the significance of the exact augmented perpetual manifolds for the mechanics of the perpetual mechanical systems and this leads to the concept of the perpetual mechanics.
The perpetual mechanics is not restricted to deriving the dynamics solutions of the mechanical systems but also the internal forces and the energy exchange with the environment are examined. Moreover the conclusions of this section cannot be obtained from the previous section dynamic analysis, and although they are restricted only to the theorem [22] and the two corollaries [23-26], they are sufficient to justify the significance of perpetual mechanics.

3. Numerical results

In this section, the theoretical design analysis of the previous section, with numerical simulations is confirmed.
Initially the definition of the design parameters using equation (6b) is done. The parameters that define the original system in Table 1 are shown. The design is based by selecting stiffness $\mathrm{k}_{\mathrm{ext},1} = 1800000\ \mathrm{N/m}$, and through equation (6b) leads to the definitions, of the rest stiffness's, and of the natural frequency of this similar rigid body mode which is $\omega_n = 34.641\ rad/s$ (with associated period of $T_n = 0.18138\ s$).

i	m_i *(Kg)*	k_i *(N/m)*	$k_{nl,i}$ *(N/m^4)*
1	1500	1200000	200000
2	2000	1400000	−130000
3	3000	1300000	150000
4	1200	−	−

Table 1. The parameters used for the numerical solutions.

Considering initial conditions obtained from rearrangement of equations (7b-c), using shooting method the periodicity of the nonlinear perpetual mechanical system (eq. 18a), and of the underlying linear perpetual mechanical system (eq. 18b), for the time interval associated with T_n and for various displacement amplitudes (A), through the $\mathrm{L}^2-\mathrm{norm}$, is checked.
In Figure 2, the $\mathrm{L}^2-\mathrm{norm}$ values of the numerical solutions of the nonlinear and linear perpetual mechanical systems, for various amplitudes within the range $[0.01,30]$ m, associated with the natural frequency $34.641\ \mathrm{rad/s}$ are depicted. The minimum values of the $\mathrm{L}^2-\mathrm{norm}$ is with order of magnitude of -9, and this ensures the periodicity. Therefore the constant value of frequency ω_n form the backbone line of this mode for both systems.

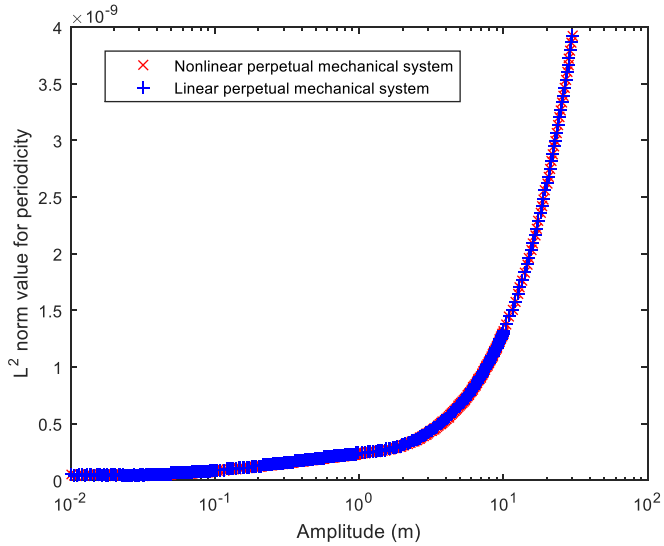

Figure 2. The values of the L^2-norm, obtained from shooting method.

In Figure 3a, the numerically determined transient responses of the original system (eq. 18a), incorporating the analytical solution are depicted, for a normal mode with initial conditions $x_a(0) = 30\,m$ and $\dot{x}_a(0) = 0\,m/s,$ and they seem that they are in good agreement. The perfect agreement between the analytical solution obtained using equation (7a) with the numerical determined responses from equations (18a) can be ensured by considering the maximum difference between the analytical solutions with all the numerically determined displacements. The maximum of all the maxima, for all the considered points associated with the nonlinear perpetual mechanical system of Figure 2, is having the minimum value of $9.66 \cdot 10^{-10}m$, (since the theoretical value is zero, this value is indicative of zero as an error associated with the numerical simulation e.g. different numerical integration tolerances would lead to another error value) which ensures that the numerical simulations are in perfect agreement with the analytical solutions.

In Figure 3b, the numerically determined responses associated with the linear perpetual mechanical system (eq. 18b), for the same initial conditions, incorporating the analytical solution (eq. 7a) are depicted. Similarly with the nonlinear perpetual system they look that they are in good agreement, and this is certified by examining the maximum of the maxima, for all the transient responses of the considered points associated with the linear perpetual mechanical system of Figure 2, which has the minimum value of $9.66 \cdot 10^{-10}m$.

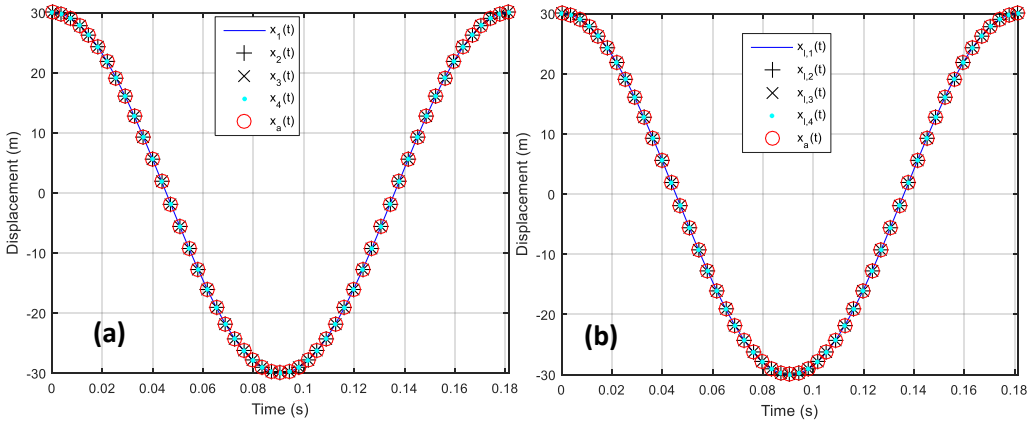

Figure 3. The numerically determined displacements, with initial conditions $x_a(0) = 30\,m$ and $\dot{x}_a(0) = 0\,m/s$, **(a)** associated with a nonlinear normal mode of the original system, incorporating the analytical solution, **(b)** associated with a linear normal mode of the underlying linear perpetual mechanical system, incorporating the same analytical solution.

In Table 2, the maximum of the maximum absolute values of the sum of internal forces applied to each mass, obtained for all the numerical simulations (linear and nonlinear system) of points depicted in Figure 2, are shown. For comparison purposes, the maximum value of the theoretically effective forces that are defined by the product of each mass with its acceleration, associated with each point of Figure 2, can be obtained using equation (7e) and in the third column of Table 2 are shown. Since the minimum values of the effective forces are in the order of magnitude 4, and the maximum values of the sum of the internal forces are of -8 order of magnitude, then it can be concluded that the numerically determined sum of the internal forces is practically equal to zero. Noticeable though the equal values between the nonlinear system (2nd column) and the underlying linear system (3rd column). Starting from the linear internal forces, they are defined (eq. 11a) by a constant multiplying the relative difference between displacements that theoretically is equal to zero, and the nonzero values are attributed to a numerical error e<<1. The internal forces of the nonlinear system are comprised by the sum of the linear internal forces (eq. 11a) that arise by the error e in similar manner and the nonlinear internal forces (eq. 11b)

that are equal to a constant multiplying the error value e<<1 in the power of 3. Therefore, the nonlinear forces are much lower than the linear ones and contribute in much lower order of magnitude (at decimal points).

i	$max\left(max\left\|\begin{matrix}\{\boldsymbol{F}_{L,i}\}+\\ \left\{\boldsymbol{F}_{NL,i}\left(x_p(t)\right)\right\}\end{matrix}\right\|\right)$ *(N)*	$max\left(max\left\|\{\boldsymbol{F}_{L,i}\}\right\|\right)$ *(N)*	Range of $m_i \cdot max\lvert\ddot{x}_a\rvert$ *(N)*
1	$2.98 \cdot 10^{-8}$	$2.98 \cdot 10^{-8}$	$[1.8 \cdot 10^4, 5.4 \cdot 10^7]$
2	$5.47 \cdot 10^{-8}$	$5.47 \cdot 10^{-8}$	$[2.4 \cdot 10^4, 7.2 \cdot 10^7]$
3	$4.80 \cdot 10^{-8}$	$4.80 \cdot 10^{-8}$	$[3.6 \cdot 10^4, 1.08 \cdot 10^8]$
4	$2.31 \cdot 10^{-8}$	$2.31 \cdot 10^{-8}$	$[1.44 \cdot 10^4, 4.32 \cdot 10^7]$

Table 2. The maximum of the maximum of the sum of the internal forces applied to each mass, and of the effective forces, for all the points depicted in Figure 2, for the nonlinear and the linear perpetual mechanical systems. The theoretical values of 2nd and 3rd columns are zero, therefore these almost zero values are indicative of the numerical error.

4. Conclusions

In this article the analytical design of a mechanical system to admit rigid body modes, using theoretical dynamic analysis is done. Then the same design of the mechanical system, using the perpetual mechanics analytical tools has been repeated leading to the same design in an easier way. Moreover, the additional knowledge for the mechanics of this system through perpetual mechanics, that it is hidden in the first design, is discussed. More precisely is shown that the nonlinear perpetual mechanical system with the linear perpetual mechanical system have the same design and leads to the same normal mode. Moreover the sum of the internal forces for all time instants for both systems in the rigid body mode design is equal to zero. Finally the analytical results are confirmed with numerical simulations, whereas the discrepancies are minimal, and can be attributed in numerical errors.

References

[1] A. Prasad, Existence of perpetual points in nonlinear dynamical systems and its applications, *Int. J. of Bifurcat. Chaos* **25** (2) (2015) 1530005. doi: 10.1142/S0218127415300050
[2] P. Brzeski and L. N. Virgin, Experimental investigation of perpetual points in mechanical systems, *Nonlinear Dyn.* **90** (2017) 2917-2928.
[3] D. Dudkowski, A. Prasad, T. Kapitaniak, Perpetual points and periodic perpetual loci in maps, *Chaos* **26** (2016) 103103.
[4] A. Prasad, A note on topological conjugacy for perpetual points, *Int. J. Nonlinear Sci.* **21**(1) (2016) 60-64.
[5] S. N. Chowdhurry and D. Ghosh, Hidden attractors: A new chaotic system without equilibria, *Eur. Phys. J. Spec. Top.*, **229** (2020) 1299-1308.
[6] D. Dudkowski, A. Prasad, T. Kapitaniak, Perpetual points and hidden attractors in dynamical systems, *Phys. Lett. A* **379** (40-41) (2015) 2591-2596.
[7] D. Dudkowski, S. Jafari, T. Kapitaniak, N.V. Kuznetsov, G.A. Leonov, A. Prasad, Hidden attractors in dynamical systems, *Phys. Rep.* 637 (2016) 1-50.
[8] D. Dudkowski, A. Prasad, T. Kapitaniak, Perpetual Points: New Tool for Localization of Coexisting Attractors in Dynamical Systems, *Int. J. of Bifurcat. Chaos* **27**(4) (2017) 1750063.
[9] F. Nazaimehr, S. Jafari, S.M.R.H. Golpayegani, J.C. Sprott, Categorizing Chaotic Flows from the Viewpoint of Fixed Points and Perpetual Points, *Int. J. of Bifurcat. Chaos* **27**(2) (2017)1750023.
[10] F. Nazaimehr, B. Saaeidi, S. Jafari, J.C. Sprott, Are Perpetual Points Sufficient for Locating Hidden Attractors?, *Int. J. of Bifurcat. Chaos* **27**(3) (2017)1750037.
[11] D. Dudkowski, A. Prasad, T. Kapitaniak, Describing chaotic attractors: Regular and perpetual points, *Chaos* 28(3) (2018) 033604.
[12]S. Kumarasamy, D. Dudkowski, A. Prasad, T. Kapitaniak, Ordered slow and fast dynamics of unsynchronized coupled phase oscillators, *Chaos* **31** (2021) 081102. https://doi.org/10.1063/5.0063513
[13] N.V. Kuznetsov, G.A. Leonov, T.N. Mokaev, A. Prasad, M.D. Shrimali, Finite-time Lyapunov dimension and hidden attractor of the Rabinovich system, *Nonlinear Dyn.* **92** (2018) 267-285.
[14] F. Yu, Z. Zhang, L. Liu, H. Shen, Y. Huang, C. Shi, S. Cai, Y. Song, S. Du, Q. Xu, Secure Communication Scheme Based on a New 5D Multistable Four-Wing Memristive Hyperchaotic System with Disturbance Inputs, *Complexity* **2020** (2020) 5859273.
[15] P. Brzeski P and L.N. Virgin, System identification of energy dissipation in a mechanical model undergoing high velocities: An indirect use of perpetual points, *Mech. Syst. Signal Process.* **108** (2018) 115-125.
[16] S. Cang, A. Wu, Z. Wang, Z. Chen, Four-dimensional autonomous dynamical systems with conservative flows: two-case study, *Nonlinear Dyn.* **89** (2017) 2495–2508.
[17] S. Jafari, F. Nazaimehr, J.C. Sprott, S.M.R.H. Golpayegani, Limitation of perpetual points for confirming conservation in dynamical systems, *Int. J. of Bifurcat. Chaos*, **25** (2015) 1550182.

[18] A. Wu, S. Cang, R. Zhang, Z. Wang, Z. Chen, Hyperchaos in a Conservative System with Nonhyperbolic Fixed Points, *Complexity* **2018** (2018) 9430637.
[19] N. Wang, G. Zhang, H. Bao, Infinitely many coexisting conservative flows in a 4D conservative system inspired by LC circuit, *Nonlinear Dyn.* **99** (2020) 3197-3216.
[20] F. Georgiades, Theorem and observation about the nature of perpetual points in conservative mechanical systems, Exploiting NOnLInear Dynamics for Engineering Systems, 'ENOLIDES', eds. I. Kovacic, S. Lenci, in IUTAM Bookseries, (Springer Nature Switzerland AG 2020), pp. 91-104.
[21] F. Georgiades, Perpetual points in natural dissipative with viscous damping mechanical systems: A theorem and a remark, *Proc. Inst. Mech. Eng. C J. Mech. Eng. Sci.*, **235** (20) (2021) 4526-4534. https://doi.org/10.1177%2F0954406220934833
[22] F. Georgiades, Augmented Perpetual Manifolds and Perpetual Mechanical Systems-Part I: Definitions, Theorem and Corollary for Triggering Perpetual Manifolds, Application in Reduced Order Modeling and Particle-Wave Motion of Flexible Mechanical Systems, *J. Comput. Nonlinear Dyn.*, **16** (7) (2021) 071005. https://doi.org/10.1115/1.4050554
[23] F. Georgiades, Augmented perpetual manifolds, a corollary: Dynamics of natural mechanical systems with eliminated internal forces. In: W. Lacarbonara et al. (eds.), Advances in Nonlinear Dynamics, NODYCON Conference Proceedings Series (NODYCON 2021), Vol. 1, pp 189-200, Springer Nature Switzerland AQ 2022. https://doi.org/10.1007/978-3-030-81162-4_17
[24] F. Georgiades, 2021, Exact Augmented Perpetual Manifolds: A Corollary for their Uniqueness, Journal of the Serbian Society for Computational Mechanics, 15(2): 1-9.
[25] F. Georgiades, Exact augmented perpetual manifolds: Corollary about different mechanical systems with exactly the same motions, *Math. Probl. Eng.*, **2021** (2021) 6031142. https://doi.org/10.1155/2021/6031142
[26] F. Georgiades, Corollary for the Exact Augmented Perpetual Manifolds of Linear and Nonlinear Mechanical Systems, *Int. J. NonLinear Mech.* **137** (2021) 103821. https://doi.org/10.1016/j.ijnonlinmec.2021.103821
[27] F. Georgiades, 2022, Augmented perpetual manifolds and perpetual mechanical systems-part II: theorem for dissipative mechanical systems behaving as perpetual machines of third kind, Nonlinear Dynamics, 108 (2) 789-825. https://doi.org/10.1007/s11071-022-07221-z
[28] D.J. Inman, *Engineering Vibrations*, 4th edn. (Pearson Education, Inc. Upper Saddle River, New Jersey 07458, 2014).
[29] L. Meirovitch, *Fundamental of Vibrations*, (Waveland Press. Long Grove, IL, 2010).

Supporting quantum squeezing in two component solitons by means of electromagnetically-induced transparency*

Kai-Yu Huang, Yuan Zhao, Li Xue, Jun-Rong He, Ke-Wei Wang, Si-Liu Xu†
School of Electronic and Information Engineering, Hubei University of Science and Technology, Xianning 437100, China

Milivoj R. Belić‡
Texas A&M University at Qatar, P.O. Box 23874 Doha, Qatar
Institute of Physics Belgrade, Pregrevica 118, 11080 Zemun, Serbia

Boris A. Malomed§
Department of Physical Electronics, School of Electrical Engineering, Faculty of Engineering, Tel Aviv Univesity, P.O.B. 39040, Ramat Aviv, Tel Aviv, Israel
Instituto de Alta Investigación, Universidad de Tarapacá, Casilla 7D, Arica, Chile

ABSTRACT

We investigate squeezing of two-component quantum optical solitons slowly moving in a tripod-type atomic system with double electromagnetically induced transparency (EIT). The evolution of the double probe-field envelopes is governed by a vector quantum nonlinear Schrödinger equation, which are derived from coupled Heisenberg-Langevin and Maxwell equations. Quantum fluctuations of vector soliton pairs and atomic spin are obtained by means of a direct perturbation approach. We find that the quantum squeezing of the vector soliton pairs is generated by the giant Kerr nonlinearity, which is provided by EIT, and the outcome of the squeezing can be optimized by the selection of propagation distance and angle. The atomic spin squeezing is found for short propagation distances.

---

* This work has been supported by the Natural Science Foundation of China (No. 11747044, No. 11747044), the Qatar National Research Fund (No. NPRP 8-028-1-001), the Israel Science Foundation (No. 1286/17).

† e-mail address: xusiliu1968@163.com
‡ e-mail address: milivoj.belic@qatar.tamu.edu
§ e-mail address: malomed@tauex.tau.ac.il

1. Introduction

Vector optical solitons (VOSs) can form when stable balance between the dispersion/diffraction and nonlinearity represented by the self- and cross-modulation in all components is maintained [1]. Due to their fundamental physical significance and potential applications to all-optical technology, optical information processing and transmission, vector solitons have drawn much interest [2,3]. In optical fibers, the solitons travel with speed close to c (the light speed in free space), hence systems with large propagation lengths are required [4], which is an obstacle for the design of optical information-processing devices of small sizes.

In recent years, highly resonant media featuring electromagnetically induced transparency (EIT) have become the preferred option for the creation of robust solitons [5]. EIT systems feature many remarkable properties, including the suppression of optical absorption [6], large reduction of group velocity [7], giant enhancement of the Kerr nonlinearity for very low powers of the light field [8], and offer possibilities for the storage and retrieval of optical signals [9,10]. In particular, the storage and retrieval features strongly depend on the realization of ultraslow optical solitons, that can move with velocities $\upsilon << c$ [11,12].

More recently, a four-level tripod EIT configuration with two weak probe fields and one control field have been proposed for the generation of spatial vector solitons in a cold tripod-type atomic system [13,14]. The spatial vector solitons exist in this four-level tripod EIT, featuring the squeezing and entanglement properties.

Most studies on slow-light solitons in EIT-based media are based on semi-classical methods, while true quantum effects for them were investigated episodically [15,16]. Because slow-light solitons are produced with low powers, and they propagate at very low speeds, the quantum interference effect between atoms and the electromagnetic pulse may be more significant than assumed when the semi-classical method is used. Furthermore, the probe pulses in the quantum EIT system are described by quantized operators which are different from the semi-classical field. Thus the derivation of the corresponding quantum nonlinear Schrödinger equation (QNLSE) and exploration of quantum effects, by means of this equation, are necessary. The objective of this work is to develop the vector (two-component) QNLSE and obtain effects predicted by it.

2. Model

A lifetime-broadened cold atomic gas system with a tripod type four-level configuration, interacting resonantly with two laser fields, is sketched in Fig. 1(a). Two linearly polarized pulsed probe laser fields E_{pl} (with central angular frequency ω_{pl}, half Rabi frequencies Ω_{pl}, wave numbers k_{pl}, and $l=1,2$ referring to the two probe fields) drive transitions $|1\rangle\rightarrow|4\rangle$ and $|2\rangle\rightarrow|4\rangle$, respectively. A strong continuous-wave control laser field E_c (Ω_c) drives the transition $|3\rangle\rightarrow|4\rangle$.

Under electric-dipole, rotating-wave and paraxial approximations, the system′s Hamiltonian reads

$$\hat{H}=\int_{-L/2}^{+L/2}dz\left[-i\frac{\hbar c}{L}\sum_{l=1,2}\left(\hat{E}_{pl}^{\dagger}\frac{\partial}{\partial z}\hat{E}_{pl}\right)-\frac{\hbar N}{L}\left(\sum_{\alpha=2,3,4}\Delta_{\alpha}\hat{S}_{\alpha\alpha}+\sum_{l=1,2}\Omega_{pl}\hat{S}_{l4}^{\dagger}\hat{E}_{pl}+\Omega_c\hat{S}_{34}^{\dagger}+\text{H.c.}\right)\right]. \quad (1)$$

Here N is the total atomic number of the system, $\hat{E}_{pl}$ are the quantized probe fields with commutators $[\hat{E}_{pl}(z,t),\hat{E}_{pl}^{\dagger}(z,t)]=L\delta(z'-z)$, L is the length of the system along the z axis, and c is the speed of light in vacuum. Further, $\hat{S}_{\alpha\beta}(z,t)=\hat{\sigma}_{\beta\alpha}e^{i\left[(k_\beta-k_\alpha)z-(\omega_\beta-\omega_\alpha+\Delta_\beta-\Delta_\alpha)t\right]}$ are atomic transition operators from the states $|\alpha\rangle$ to $|\beta\rangle$, $\Delta_2=-\omega_{21}$, $\Delta_3=\omega_p-\omega_c-\omega_{31}$, $\Delta_4=\omega_p-\omega_{41}$.

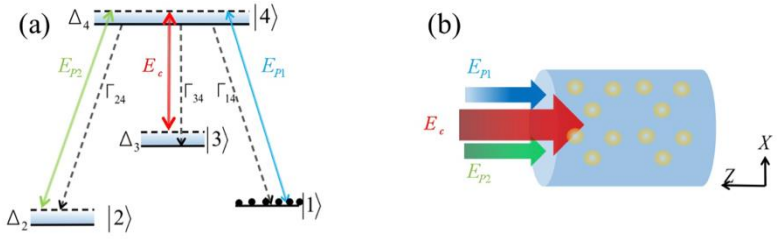

Fig. 1. (a) The double-EIT excitation scheme of the four-level atomic system. Two weak, pulsed probe laser fields $\hat{E}_{pl}$ drive transitions $|1\rangle\rightarrow|4\rangle$ ($|2\rangle\rightarrow|4\rangle$), and a strong, continuous-wave control laser field $\hat{E}_c$ drives $|3\rangle\rightarrow|4\rangle$. Δ_2, Δ_3, and Δ_4 are detunings. $\Gamma_{\alpha\beta}$ is the spontaneous emission decay rates for spontaneous transitions from $|\beta\rangle$ to $|\alpha\rangle$. (b) The geometry of the system.

The dynamics of the system is governed by the Heisenberg-Langevin and the Maxwell equations, *viz.*,

$$\frac{\partial}{\partial t}\hat{S}_{\alpha\beta} = -i\left[\hat{S}_{\alpha\beta}, \frac{\hat{H}}{\hbar}\right] - \hat{L}\left(\hat{S}_{\alpha\beta}\right) + \hat{F}_{\alpha\beta}, \tag{2a}$$

$$i\left(\frac{\partial}{\partial z} + \frac{1}{c}\frac{\partial}{\partial t}\right)\hat{E}_{pl} + \frac{\Omega_{pl}^{*} N}{c}\hat{S}_{4l} = 0, \tag{2b}$$

where $\hat{L}\left(\hat{S}_{\alpha\beta}\right)$ is a 4×4 relaxation matrix including the atomic decay rates of the spontaneous emission and dephasing, $\hat{F}_{\alpha\beta}$ are δ-correlated Langevin noise operators introduced to preserve the Heisenberg commutation relations for the operators of the atom wave functions and probe fields [15].

Equation (2a) can be expanded as the follows:

$$i\left(\frac{\partial}{\partial t} + \Gamma_{31}\right)\hat{S}_{11} - i\left(\Gamma_{13}\hat{S}_{33} + \Gamma_{14}\hat{S}_{44}\right) + \Omega_{p1}^{*}\hat{S}_{41} - \Omega_{p1}\hat{S}_{41}^{*} - i\hat{F}_{11} = 0\ , \tag{3a}$$

$$i\left(\frac{\partial}{\partial t} + d_{21}\right)\hat{S}_{21} + \Omega_{p2}^{*}\hat{S}_{41} - \Omega_{p1}\hat{S}_{42}^{*} - iF_{21} = 0\ , \tag{3b}$$

$$i\left(\frac{\partial}{\partial t} + d_{31}\right)\hat{S}_{31} + \Omega_{c}^{*}\hat{S}_{41} - \Omega_{p1}\hat{S}_{44}^{*} - iF_{31} = 0\ , \tag{3c}$$

$$i\left(\frac{\partial}{\partial t} + d_{41}\right)\hat{S}_{41} + \Omega_{p1}\left(\hat{S}_{11} - \hat{S}_{44}\right) + \Omega_{p2}\hat{S}_{21} + \Omega_{c}\hat{S}_{31} - iF_{41} = 0\ , \tag{3d}$$

$$i\left(\frac{\partial}{\partial t} + \Gamma_{32}\right)\hat{S}_{22} - i\left(\Gamma_{23}\hat{S}_{33} + \Gamma_{24}\hat{S}_{44}\right) + \Omega_{p2}^{*}\hat{S}_{42} - \Omega_{p2}\hat{S}_{42}^{*} - i\hat{F}_{22} = 0\ , \tag{3e}$$

$$i\left(\frac{\partial}{\partial t} + d_{32}\right)\hat{S}_{32} + \Omega_{c}^{*}\hat{S}_{42} - \Omega_{p2}\hat{S}_{43}^{*} - iF_{32} = 0\ , \tag{3f}$$

$$i\left(\frac{\partial}{\partial t} + d_{42}\right)\hat{S}_{42} + \Omega_{p2}\left(\hat{S}_{22} - \hat{S}_{44}\right) + \Omega_{p1}\hat{S}_{21}^{*} + \Omega_{c}\hat{S}_{32} - iF_{42} = 0\ . \tag{3g}$$

$$i\left(\frac{\partial}{\partial t} + \Gamma_{3}\right)\hat{S}_{33} - i\Gamma_{31}\hat{S}_{11} + i\Gamma_{32}\hat{S}_{22} - i\Gamma_{34}\hat{S}_{44} + \Omega_{c}^{*}\hat{S}_{43} - \Omega_{c}\hat{S}_{43}^{*} - i\hat{F}_{33} = 0\ , \tag{3h}$$

$$i\left(\frac{\partial}{\partial t} + d_{43}\right)\hat{S}_{43} + \Omega_{c}\left(\hat{S}_{33} - \hat{S}_{44}\right) + \Omega_{p1}\hat{S}_{31}^{*} + \Omega_{p2}\hat{S}_{32}^{*} - iF_{43} = 0\ , \tag{3i}$$

$$i\left(\frac{\partial}{\partial t} + \Gamma_{4}\right)\hat{S}_{44} + \Omega_{p1}\hat{S}_{41}^{*} - \Omega_{p1}^{*}\hat{S}_{41} + \Omega_{p2}\hat{S}_{42}^{*} - \Omega_{p2}^{*}\hat{S}_{42} + \Omega_{c}\hat{S}_{43}^{*} - \Omega_{c}^{*}\hat{S}_{43} - iF_{44} = 0\ . \tag{3j}$$

These expressions can be solved by means of the Fourier transform. After eliminating the atomic variables, we obtain:

$$\left[i\frac{\partial}{\partial z} + K_{l}(\omega)\right]\tilde{\hat{E}}_{pl}(z,\omega) = i\tilde{\hat{F}}_{pl}(z,\omega)\ . \tag{4}$$

Here ω is the sideband frequency of the probe pulse, $K_l (l=1,2)$ are the linear dispersion relations for the two probe pulses, and $\tilde{\hat{F}}_{pl}$ are δ-correlated Langevin noise operators of the atoms and probe fields, obtained in the following form:

$$K_{1(2)}(\omega) = \frac{\omega}{c} + \frac{\left|\Omega_{p1(2)}\right|^2 N}{c} \frac{\omega + d_{31(32)}}{D_{1(2)}(\omega)} \ , \tag{5a}$$

$$\tilde{\hat{F}}_{p1(2)}(z,t) = \frac{\Omega^*_{p1(2)} N}{c} \frac{\left(\omega + d_{31(32)}\right) F_{41(42)}(z,t) - \Omega_c F_{31(32)}(z,t)}{D_{1(2)}(\omega)} \ . \tag{5b}$$

where $d_{31(32)}$ and $D_{1(2)}$ are parameters in Eq. (3). Substituting Eq. (5) into Eq. (4) and converting it back into the time domain by means of the inverse Fourier transform, we arrive at the quantum linear Schrödinger equation:

$$i\left(\frac{\partial}{\partial z} + \frac{1}{V_{gl}} \frac{\partial}{\partial t}\right) \hat{E}_{pl} + K_{0l} \hat{E}_{pl} - \frac{K_{2l}}{2} \frac{\partial^2}{\partial t^2} \hat{E}_{pl} - i\hat{F}_{pl} = 0 \ , \tag{6}$$

where $\hat{F}_{pl}$ is the δ-correlated Langevin noise operators. One can expand $K_l(\omega)$ in the Taylor series around $\omega = 0$ with $K_l(\omega) = K_{0l} + \frac{\omega}{V_{gl}} + \frac{K_{2l}\omega^2}{2}$, V_{gl} being the group velocity of the probe laser field, $\frac{1}{V_{gl}} \equiv K_{1l} \equiv \left(\frac{\partial K_l}{\partial \omega}\right)\Big|_{\omega=0}$, and $K_{2l} \equiv \left(\frac{\partial^2 K_l}{\partial \omega^2}\right)\Big|_{\omega=0}$ is the coefficient of the group-velocity dispersion.

To obtain equations for the two probe fields E_{p1} and E_{p2}, we employ an iteration method. The solution of Eq. (2b) can be constructed order by order. In the first-order approximation, we get

$$\hat{S}_{\alpha 1(2)} = a^{(1)}_{\alpha 1(2)} \Omega_{p1(2)} \hat{E}_{p1(2)} \ (\alpha = 3,4), \tag{7}$$

where $a^{(1)}_{\alpha 1} = \frac{-\Omega^*_c \delta_{\alpha 3} + d_{31}\delta_{\alpha 4}}{\left|\Omega_c\right|^2 - d_{31}d_{41}}$ and $a^{(1)}_{\alpha 2} = \frac{-\Omega^*_c \delta_{\alpha 3} + d_{32}\delta_{\alpha 4}}{\left|\Omega_c\right|^2 - d_{32}d_{42}}$.

At the second order, the result is

$$S_{\alpha\beta} = a^{(2)}_{\alpha\beta,1(2)} \hat{E}^{\dagger}_{p1(2)} \hat{E}_{p1(2)} \ (\alpha, \beta = 1,2,3,4), \tag{8}$$

where

$$a^{(2)}_{11,1} = \frac{\Gamma_{34} + 2D_c}{\Gamma_{14} D_c} 2\,\mathrm{Im}\left[a^{(1)*}_{41}\right] - \frac{1}{D_c} 2\,\mathrm{Im}\left[\frac{\Omega^*_c}{d_{43}} a^{(1)*}_{31}\right],$$

$$a^{(2)}_{11,2} = \frac{\Gamma_{34} + 2D_c}{\Gamma_{24} D_c} 2\,\mathrm{Im}\left[a^{(1)*}_{41}\right] - \frac{1}{D} 2\,\mathrm{Im}\left[\frac{\Omega^*_c}{d_{43}} a^{(1)*}_{31}\right], \qquad a^{(2)}_{22,1} = \frac{1}{D_c} 2\,\mathrm{Im}\left[\frac{\Omega^*_c}{d43} a^{(1)*}_{31}\right] - \frac{\Gamma_{34} + D_c}{\Gamma_{14} D_c} 2\,\mathrm{Im}\left[\frac{\Omega^*_c}{d_{43}} a^{(1)*}_{41}\right],$$

$$a^{(2)}_{22,2} = \frac{1}{D_{c2}} 2\,\mathrm{Im}\left[\frac{\Omega^*_c}{d_{43}} a^{(1)*}_{31}\right] - \frac{\Gamma_{34} + D_c}{\Gamma_{24} D_{c2}} 2\,\mathrm{Im}\left[\frac{\Omega^*_c}{d_{43}} a^{(1)*}_{41}\right], \qquad a^{(2)}_{33,1} = -\frac{1}{\Gamma_{14}} 2\,\mathrm{Im}\left[a^{(1)*}_{31}\right],$$

$a_{33,2}^{(2)} = -\frac{1}{\Gamma_{24}} 2\,\mathrm{Im}\left[a_{32}^{(1)*}\right]$, $a_{43,1}^{(2)} = -\frac{1}{d_{43}}\left[a_{31}^{(1)*} + \Omega_c\left(a_{33,1}^{(2)} - a_{44,1}^{(2)}\right)\right]$,

$a_{43,2}^{(2)} = -\frac{1}{d_{43}}\left[a_{32}^{(1)*} + \Omega_c\left(a_{33,2}^{(2)} - a_{44,2}^{(2)}\right)\right]$, $a_{44,1}^{(2)} = -\frac{1}{\Gamma_{14}} 2\,\mathrm{Im}\left[a_{41}^{(1)*}\right]$, $a_{44,2}^{(2)} = -\frac{1}{\Gamma_{24}} 2\,\mathrm{Im}\left[a_{41}^{(1)*}\right]$,

$D_c = \frac{2\gamma_{43}\left|\Omega_c\right|^2}{\left|d_{43}\right|^2}$.

At the third order, the result is

$$\hat{S}_{41(42)} = a_{41(42)}^{(1)}\Omega_{p1(2)}\hat{E}_{p1(2)} + a_{41,1(2)}^{(3)}\left|\Omega_{p1(2)}\right|^2\Omega_{p1(2)}\hat{E}_{p1(2)}^{\dagger}\hat{E}_{p1(2)}\hat{E}_{p1(2)}, \quad (9)$$

where $a_{41,1}^{(3)} = \frac{\Omega_c a_{32,1}^{(2)*} - d_{31}\left[a_{33,1}^{(2)} + 2a_{44,1}^{(2)}\right]}{\left|\Omega_c\right|^2 - d_{31}d_{41}}$, $a_{41,2}^{(3)} = \frac{\Omega_c a_{32,2}^{(2)*} - d_{32}\left[a_{33,2}^{(2)} + 2a_{44,2}^{(2)}\right]}{\left|\Omega_c\right|^2 - d_{32}d_{42}}$.

Substituting Eq. (9) into Eq. (2b), we derive a nonlinear equation for E_{p1} and E_{p2}:

$$\left(i\frac{\partial}{\partial z} + K_{0l}\right)\hat{E}_{pl} + W_{4l}\left|\Omega_{pl}\right|^2\hat{E}_{pl}^{\dagger}\hat{E}_{pl}\hat{E}_{pl} = 0, \quad (10)$$

where $l = 1,2$ refer to the two probe fields, $W_{4l} = \hbar^2\omega_{pl}\chi_{pl}^{(3)}/(2c\left|\mathrm{p}_{4l}\right|^2)$, $\chi_{pl}^{(3)} = N_a\left|e_p\,\mathrm{p}_{4l}\right|^4/(\varepsilon_0\hbar^3)a_{41,l}^{(3)}$ is the third-order nonlinear optical susceptibility, and p_{4l} is the electric-dipole matrix element associated with the transition from state $|l\rangle$ to $|4\rangle$.

Taking the transformation $\hat{E}_{pl} \to \hat{E}_{pl}e^{i\,\mathrm{Re}(K_{0l})z}$, the QNLS equation is expressed as follows:

$$\left[i\left(\frac{\partial}{\partial z} + \frac{1}{V_{gl}}\frac{\partial}{\partial t}\right) + K_{0l}\right]\hat{E}_{pl} - \frac{K_{2l}}{2}\frac{\partial^2}{\partial t^2}\hat{E}_{pl} + W_{4l}\left|\Omega_{pl}\right|^2\hat{E}_{pl}^{\dagger}\hat{E}_{pl}\hat{E}_{pl} - i\hat{F}_{pl}e^{-i\,\mathrm{Re}(K_{0l})z} = 0 \quad . \quad (11)$$

Finally, we define Langevin noise operator, $\hat{f}_{pl} \equiv 2L_{\mathrm{disp}}\hat{F}_{pl}e^{-i\,\mathrm{Re}(K_{0l})z}$, and the scaled (dimensionless) wave function $\hat{U}_l = \hat{E}_{pl}/\sqrt{n_{0l}}$, where $n_{0l} \gg 1$ is a typical mean photon number in the probe fields, $s = z/2L_{\mathrm{disp}}$, $\tau = (t - z/V_{gl})/t_0$, $\nu = L_{\mathrm{disp}}/L_{\mathrm{abs}}$, $g_{l1(2)} = L_{\mathrm{disp}}/L_{\mathrm{nlin}}$, $L_{\mathrm{disp}} \equiv t_0^2/\left|\mathrm{Re}(K_{2l})\right|$ is the dispersion length, $L_{\mathrm{nlin}} \equiv \left[n_0\left|\Omega_{pl}\right|^2\mathrm{Re}(W)\right]^{-1}$ is the nonlinearity length, and $L_{\mathrm{abs}} \equiv 1/\mathrm{Im}(K_{0l})$ is the absorption distance. Thus, Eq. (11) can be written as the dimensionless form:

$$i\frac{\partial}{\partial s}\hat{U}_l + \frac{\partial^2}{\partial\tau^2}\hat{U}_l + \left(g_{l1}\left|\hat{U}_1\right|^2 + g_{l2}\left|\hat{U}_2\right|^2\right)\hat{U}_l = -2i\nu\hat{U}_l + i\hat{f}_{pl}. \quad (12)$$

Here $\hat{f}_{pl}$ are scaled Langevin noise operators, $g_{l\rho}$ is the scaled dimensionless Kerr-nonlinearity coefficient with $l=1,2$ and $\rho=1,2$. s, τ and ν are the dimensionless propagation distance, time, and absorption coefficient, respectively.

3. Results and discussion

(1) quantum squeezing in two component solitons

The model described above can be realized by selecting appropriate physical systems. In particular, one can use $^{87}\mathrm{Rb}$ atoms tuned to the D1-line ($5^2\mathrm{S}_{1/2}\rightarrow 5^2\mathrm{P}_{1/2}$) transition with energy levels: $|1\rangle=\left|5^2S_{1/2},F=1,m_F=-1\right\rangle$, $|2\rangle=\left|5S_{1/2},F=2,m_F=1\right\rangle$, $|3\rangle=\left|5S_{1/2},F=2,m_F=0\right\rangle$, $|4\rangle=\left|5^2P_{1/2},F=2,m_F=0\right\rangle$ [17]. The corresponding decay rates are $\Gamma_2\simeq\Gamma_3\simeq 2\pi\times 1.0\,\mathrm{MHz}$ and $\Gamma_4\simeq 2\pi\times 5.75\,\mathrm{MHz}$, electric dipole matrix elements $|P_{14}|\simeq|P_{24}|\simeq 2.54\times10^{-27}\,\mathrm{C\cdot cm}$ (here C stands for the Coulomb unit of electric charge), atomic density $N_a\approx 3.69\times10^{10}\,\mathrm{cm}^{-3}$, other realistic parameters being $\Omega_c=2\pi\times 75\mathrm{MHz}$, $\Delta_2=0$, $\Delta_3=-2\pi\times 15\mathrm{MHz}$, and $\Delta_4=-2\pi\times 8\mathrm{MHz}$ [18].

Based on the physical parameters given above, the dimensionless absorption coefficient is $\nu=1.21\times10^{-2}\ll 1$, which means that the damping term $-2i\nu\hat{U}_l$ in Eq. (12) may be neglected. In addition, in the ultra-cold environment, one has $\hbar\omega_{pj}\gg k_BT$, and $\bar{n}_{th}=0$, thus the two-time correlation functions for the induced Langevin noise operator $\hat{f}_{pl}$ makes no contribution to the normally-ordered correlation functions of the system′s operators [19].

To investigate quantum nonlinear dynamics governed by Eq. (12), we replace operators $\hat{U}_l$ by two c-number functions U_{01} and U_{02} (or U'_{02}), hence the soliton solutions are obtained in the classical form:

$$U_{01}(s,\tau)=\frac{A_{01}\sqrt{g_{11}}+A_{02}\sqrt{g_{12}}}{2}\operatorname{sech}\left[\frac{A_{01}g_{11}+A_{02}g_{12}}{2}(\tau-\tau_{01}-2p_{01}s)\right]\exp\left[ip_{01}(\tau-\tau_{01})-ip_{01}^2s+i\theta_{01}\right],\tag{13a}$$

$$U_{02}(s,\tau)=\frac{A_{01}\sqrt{g_{21}}+A_{02}\sqrt{g_{22}}}{2}\tanh\left[\frac{A_{01}g_{21}+A_{02}g_{22}}{2}(\tau-\tau_{02}-2p_{02}s)\right]\exp\left[ip_{02}(\tau-\tau_{02})-ip_{02}^2s+i\theta_{02}\right],\tag{13b}$$

$$U'_{02}(s,\tau)=\frac{A_{01}\sqrt{g_{21}}+A_{02}\sqrt{g_{22}}}{2}\operatorname{sech}\left[\frac{A_{01}g_{21}+A_{02}g_{22}}{2}(\tau-\tau_{02}-2p_{02}s)\right]\exp\left[ip_{02}(\tau-\tau_{02})-ip_{02}^2s+i\theta_{02}\right].\tag{13c}$$

Here A_{0l} is the amplitude of the input probe field. Equations (13a) and (13b) represent the bright-dark soliton pair, while Eqs. (13a) and Eq. (13c) produce the bright-bright soliton solution.

The amplitudes of these bright-dark and bright-bright soliton pairs ($|U_{01}|$ and $|U_{02}|$, or $|U_{01}|$ and $|U'_{02}|$, respectively) and the respective full widths at half maximum/minimum (FWHM, labeled as F_{01} and F_{02}) are plotted in Figs. 2(a-c), for different values of the Kerr coefficients $g_{l\rho}$. The evolution of the bright-bright and bright-dark soliton pairs is displayed in Figs. 2(d) and Fig. 2(e,f), respectively. The two bright solitons demonstrate similar evolution along the propagation axis. We find that when $g_{l\rho}$=1.2 the amplitude of U_{01} increases with propagation distance s, and its FWHM decrease with s. This phenomenon means that the bright-bright soliton pair is squeezed effectively. However, when the nonlinear coefficient decreases ($g_{l\rho}$=0.8), the bright solitons show an anti-squeezing effect as their amplitudes decrease with s. Figures 2(b,e) show the bright-dark soliton pair with $g_{l\rho}$=1.2. Both the bright and dark solitons are squeezed in the course of the propagation. With smaller nonlinear coefficient ($g_{l\rho}$=0.8), the bright and dark solitons show an anti-squeezing effect [Fig. 2(c,f)]. According to the above discussions, we arrive at the following conclusions: (1) The soliton squeezing has no connection with the types of soliton pair. (2) The soliton squeezing increases with the growth of Kerr nonlinearities $g_{l\rho}$.

(2) Quantum dynamics of slow-light soliton pairs and atomic spin

We here introduce a quantum correction, assuming large photon number n_{0l} and weak quantum fluctuation of the solitons. To this end, we adopt the effective Hamiltonian of the system as

$$\hat{H}_{eff} = H_{01} + \hat{H}_{21} + H_{02} + \hat{H}_{22}, \tag{14a}$$

$$H_{0l} = \int_{-\infty}^{+\infty} d\tau \left(-\frac{\partial^2}{\partial \tau^2} - \mu_l - \left(g_{l1}|U_{01}|^2 + g_{l2}|U_{02}|^2 \right) U_{0l} \right), \tag{14b}$$

$$\hat{H}_{2l} = \int_{-\infty}^{+\infty} d\tau \left\{ U_{1l}^{\dagger} \left[-\frac{\partial^2}{\partial \tau^2} - \mu_j - \left(g_{l1}|U_{01}|^2 + g_{l2}|U_{02}|^2 \right) \hat{U}_{1l} \right] - U_{0l} \left(U_{01} g_{l1} + U_{02} g_{l2} \right) \left(\hat{U}_{1l} \hat{U}_{1l} + \hat{U}_{1l}^{\dagger} \hat{U}_{1l}^{\dagger} \right) \right\}. \tag{14c}$$

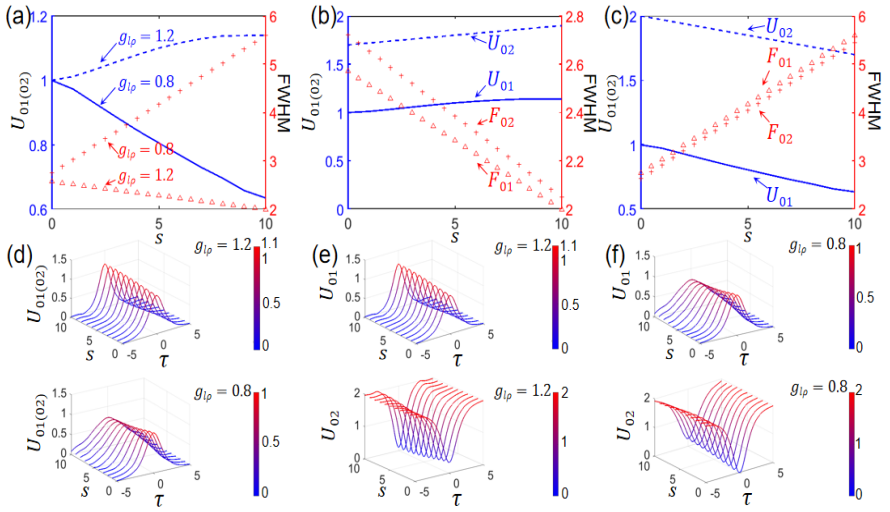

Fig.2 Classical squeezing (compression) of the widths of slow vector bright-bright solitons (a,d) and bright-dark solitons (b,c,e,f) by different Kerr nonlinearities $g_{l\rho}$, where panel (d) corresponds to (a), (e) corresponds to (b), and (f) corresponds to (c). In panels (d,e,f), s is the same scaled propagation distance as in Eq. (12). Other parameters: $A_{01}=2, A_{02}=1$, $g_{1\rho}=1$, $g_{2\rho}=2$, $p_{0l}=0.1$, $\tau_{0l}=0$.

Here the dimensionless probe fields $U_{0l}(\tau)=U_{0l}(s=0,\tau)$, where $\hat{U}_{1l}$ are the annihilation operators of photons in the probe field characterizing the quantum fluctuations, with commutators $[\hat{U}_{1l}(s,\tau),\hat{U}_{1l}^{\dagger}(s,\tau')]=\delta_{1l}\delta(\tau-\tau')$ [20,21]. To perform the rigorous diagonalization of $\hat{H}_{eff}$, we redefine $\sigma_l=(A_{01}g_{l1}+A_{02}g_{l2})(\tau-\tau_0)/2$, $\hat{U}_{1l}=\sqrt{(A_{01}g_{l1}+A_{02}g_{l2})/2}\,\hat{w}_l$. This leads to

$$\hat{H}_{21}=\frac{A_{01}(A_{01}g_{11}+A_{02}g_{12})}{2}\int_{-\infty}^{+\infty}d\sigma_1\left[\hat{w}_1^{\dagger}\hat{L}_1\hat{w}_1-\mathrm{sech}^2\sigma_1\left(\hat{w}_1\hat{w}_1+\hat{w}_1^{\dagger}\hat{w}_1^{\dagger}\right)\right],$$

$$\hat{H}_{22}=\frac{A_{02}(A_{01}g_{21}+A_{02}g_{22})}{2}\int_{-\infty}^{+\infty}d\sigma_2\left[\hat{w}_2^{\dagger}\hat{L}_2\hat{w}_2-\tanh^2\sigma_2\left(\hat{w}_2\hat{w}_2+\hat{w}_2^{\dagger}\hat{w}_2^{\dagger}\right)\right],$$

where $\hat{L}_1=-\frac{\partial^2}{\partial\sigma_1^2}-4\,\mathrm{sech}^2\sigma_1+1$, $\hat{L}_2=-\frac{\partial^2}{\partial\sigma_2^2}-4\tanh^2\sigma_2+1$, and operators $\hat{w}_l$ represents quantum fluctuations in the system, characterized by commutators $[\hat{w}_l(s,\sigma),\hat{w}_l^{\dagger}(s,\sigma')]=\delta(\sigma-\sigma')$.

Thus, the problem of the diagonalization of $\hat{H}_{eff}$ transforms into how to find a set of complete mutually orthogonal eigenfunctions that can be used for the expansion of $\hat{w}_l$. By using the following Bogoliubov canonical transformation, we expand $\hat{w}_l$ as

$$\hat{w}_l(s,\sigma)=\sum_j\left[u_j(\sigma_l)\hat{a}_{jl}(s)+v_j(\sigma_l)\hat{a}_{jl}^{\dagger}(s)\right]+\int_{-\infty}^{+\infty}dk\left[u(\sigma_l,k)\hat{a}_l(s,k)+v(\sigma_l,k)\hat{a}_l^{\dagger}(s,k)\right], \tag{15}$$

Then, spectra of excited solitons are composed of discrete and continuous components. For the discrete part, $u_j(\sigma_l), v_j(\sigma_l)(j=1,2)$ are eigenfunctions and $\hat{a}_{jl}(s)$, $\hat{a}_{jl}^{\dagger}(s)$ are the annihilation operators of photons, while $u(\sigma_l,k), v(\sigma_l,k)$ and $\hat{a}_l(s,k)$, $\hat{a}_l^{\dagger}(s,k)$ are eigenfunctions and annihilation operators for the continuous spectrum. The annihilation operators obey the commutation relations $[\hat{a}_{jl}(s),\hat{a}_{j'l}^{\dagger}(s)]=\delta_{jj'}$, $[\hat{a}_{jl}(s,k),\hat{a}_{jl}^{\dagger}(s,k')]=\delta(k-k')$.

Following Refs. [22,23], both discrete and continuous spectrum satisfy the BdG equations for the eigenstates:

$$\hat{L}_1u_q(\sigma_1)-\left[\operatorname{sech}\sigma_1\operatorname{sech}\sigma_2v_q(\sigma_1)\right]=-\lambda_{q1}u_q(\sigma_1),\ \hat{L}_1u_q(\sigma_2)-\left[\operatorname{sech}\sigma_1\tanh\sigma_2v_q(\sigma_2)\right]=-\lambda_{q2}u_q(\sigma_2) \tag{16a}$$

$$\hat{L}_2v_q(\sigma_1)-\left[\operatorname{sech}\sigma_1\operatorname{sech}\sigma_2v_q(\sigma_1)\right]=\lambda_{q1}v_q(\sigma_1),\ \hat{L}_2v_q(\sigma_2)-\left[\operatorname{sech}\sigma_1\tanh\sigma_2v_q(\sigma_2)\right]=\lambda_{q2}v_q(\sigma_2) \tag{16b}$$

where $q=j$ is for the discrete spectrum, and $q=k$ is for the continuous spectrum. The analytical solutions of Eqs. (16) are found as

$$u(\sigma_1,k)=\frac{-k^2+ik\left[\tanh(\sigma_1)+\tanh(\sigma_2)\right]-\tanh(\sigma_1)\tanh(\sigma_2)}{\sqrt{2\pi}\left(k^2+1\right)}e^{ik\sigma_1}, \tag{17a}$$

$$u(\sigma_2,k)=\frac{-k^2+ik\left[\tanh(\sigma_1)+\operatorname{sech}(\sigma_2)\right]-\tanh(\sigma_1)\operatorname{sech}(\sigma_2)}{\sqrt{2\pi}\left(k^2+1\right)}e^{ik\sigma_2}, \tag{17b}$$

$$v(\sigma_1,k)=-\frac{\operatorname{sech}(\sigma_1)\operatorname{sech}(\sigma_2)}{\sqrt{2\pi}}e^{-ik\sigma_1},\ v(\sigma_2,k)=-\frac{\operatorname{sech}(\sigma_1)\tanh(\sigma_2)}{\sqrt{2\pi}}e^{-ik\sigma_2}, \tag{17c}$$

$$u_1(\sigma_l)=\frac{2-\sigma_l\tanh(\sigma_{3-l})}{2}\operatorname{sech}\sigma_l,\ u_2(\sigma_l)=\frac{\tanh(\sigma_l)+\sigma_{3-l}}{2}\operatorname{sech}(\sigma_l), \tag{17d}$$

$$v_1(\sigma_l)=-\frac{\sigma_{3-l}\tanh(\sigma_l)}{2}\operatorname{sech}(\sigma_l),\ v_2(\sigma_l)=-\frac{\tanh(\sigma_l)-\sigma_{3-l}}{2}\operatorname{sech}(\sigma_l), \tag{17e}$$

We can see that $\hat{w}_l$ can be expanded in terms of u and v, which constitute a complete set of eigenfunctions for both discrete and continuous spectra. Substituting Eq. (15) into Eq. (14), we diagonalize $\hat{H}_{eff}$ as

$$\hat{H}_{eff\,1}=\frac{A_{01}^2\left(A_{01}g_{11}^2+A_{02}g_{12}^2\right)}{12}+\frac{A_{01}\left(A_{01}g_{11}^2+A_{02}g_{12}^2\right)}{8}\left[\hat{P}_{21}^2-\hat{Q}_{11}^2-\int_{-\infty}^{+\infty}dk\lambda_{k1}\hat{a}_1^{\dagger}\left(s,k_1\right)\hat{a}_1\left(s,k_1\right)\right], \tag{18a}$$

$$\hat{H}_{eff\,2}=\frac{A_{02}^2\left(A_{01}g_{21}^2+A_{02}g_{22}^2\right)}{12}+\frac{A_{02}\left(A_{01}g_{21}^2+A_{02}g_{22}^2\right)}{8}\left[\hat{P}_{22}^2-\hat{Q}_{12}^2-\int_{-\infty}^{+\infty}dk\lambda_{k2}\hat{a}_2^{\dagger}\left(s,k_2\right)\hat{a}_2\left(s,k_2\right)\right]. \tag{18b}$$

Here $\hat{Q}_{jl}$ and $\hat{P}_{jl}$ are the coordinate and momentum operators with $\hat{Q}_{jl}=(\hat{a}_{jl}^{\dagger}+\hat{a}_{jl})/\sqrt{2}$ and $\hat{P}_{jl}=i(\hat{a}_{jl}^{\dagger}-\hat{a}_{jl})/\sqrt{2}$, respectively. According to the Heisenberg equation of motion $i\partial\hat{A}/\partial s=[\hat{A},\hat{H}_{eff}]$, we obtain

$$\hat{Q}_{1l}\left(s\right)=\hat{Q}_{1l}\left(0\right),\qquad \hat{P}_{2l}\left(s\right)=\hat{p}_{2l}\left(0\right), \tag{19a}$$

$$\hat{P}_{1l}\left(s\right)=\frac{A_{01}\left(A_{01}g_{11}^2+A_{02}g_{12}^2\right)s}{2}Q_{1l}\left(0\right)+\hat{P}_{1l}\left(0\right),\ \hat{Q}_{2l}\left(s\right)=\frac{A_{02}\left(A_{01}g_{21}^2+A_{02}g_{22}^2\right)s}{2}\hat{P}_{2l}\left(0\right)+\hat{Q}_{2l}\left(0\right), \tag{19b}$$

$$\hat{a}_l\left(s,k\right)=\hat{a}_l\left(0,k\right)\exp\left[i\frac{A_{0l}\left(A_{01}g_{l1}^2+A_{02}g_{l2}^2\right)}{2}\lambda_{kl}s\right]. \tag{19c}$$

According to Eqs. (18) and Eqs. (19), we find that the continuous spectrum gives no contribution to the quantum fluctuations, as there is no phase shift between different modes in the course of the propagation of the waves. For the discrete spectrum, the quantum fluctuations originate from $\hat{Q}_{jl}$ and $\hat{P}_{jl}$. As the waves propagate, $\hat{Q}_{1l}$ and $\hat{P}_{2l}$ remain unchanged, $\hat{P}_{1l}$ and $\hat{Q}_{2l}$ being functions of parameters $g_{l\rho}$. Thus we get $\left\langle\hat{Q}_{jl}(s)\right\rangle=\left\langle\hat{P}_{jl}(s)\right\rangle=0$, $\left\langle\hat{Q}_{jl}^2(0)\right\rangle=\left\langle\hat{P}_{jl}^2(0)\right\rangle=1/2$, $\left\langle\hat{Q}_{1l}^2(s)\right\rangle=\left\langle\hat{P}_{2l}^2(s)\right\rangle=1/2$, $\left\langle Q_{2l}^2\left(s\right)\right\rangle=\frac{1}{2}+\frac{A_{01}\left(A_{01}^3g_{l1}^4+A_{02}^3g_{l2}^4\right)s^2}{16}$, and $\left\langle P_{1l}^2\left(s\right)\right\rangle=\frac{1}{2}+\frac{A_{01}\left(A_{01}^3g_{l1}^4+A_{02}^3g_{l2}^4\right)s^2}{16}$.

To describe quantum features of the vector slow-light solitons, we investigate the quantum squeezing. The quadrature operator $\hat{X}_{jl,\theta}$ is represented as [24,25]

$$\hat{X}_{jl,\theta}=\frac{1}{\sqrt{2}}\left[\hat{a}_{jl}\left(s\right)e^{-i\theta}+\hat{a}_{jl}^{\dagger}\left(s\right)e^{-i\theta}\right]=\hat{Q}_{jl}\left(s\right)\cos\theta+\hat{P}_{jl}\left(s\right)\sin\theta, \tag{20}$$

Here $\hat{X}_{jl,\theta}$ stand for amplitudes $\hat{a}_{jl}$ and angle (phase) θ of the quantum fluctuations for the vector soliton pairs. Thus the probe fields are written as

$$\hat{E}_{pl}=E_{1l}+\hat{E}_{2l}\ , \tag{21a}$$

$$E_{11}=D_{01}\operatorname{sech}\left[\frac{A_{01}g_{11}+A_{02}g_{12}}{2t_0}\left(t-\frac{z}{v_g}\right)\right]\cos\Theta_1\left(z,t\right),\quad E_{12}=D_{01}\tanh\left[\frac{A_{01}g_{21}+A_{02}g_{22}}{2t_0}\left(t-\frac{z}{v_g}\right)\right]\cos\Theta_2\left(z,t\right)\ , \tag{21b}$$

$$\hat{E}_{2l}=\frac{D_{0l}}{\sqrt{A_{0l}}}\left\{\sum_{j=1,2}\left[u_j(t_l)\cos\left(\theta+\Theta_j\right)+v_j(t_l)\cos\left(\theta-\Theta_j\right)\right]\hat{X}_{jl,\theta}-\sum_{j=1,2}\left[u_j(t_l)\sin\left(\theta+\Theta_j\right)+v_j(t_l)\sin\left(\theta-\Theta_j\right)\right]\hat{X}_{jl,\theta+\frac{\pi}{2}}\right\}. \tag{21c}$$

Here E_{1l} are the vector soliton fields, $\hat{E}_{2l}$ describes the quantum fluctuations which are described by the quadrature operators $\left\langle \hat{X}^2_{jl,\theta}(s)\right\rangle$, eigenfunctions $u_j(t_l)$ and $v_j(t_l)$, here $D_{0l}=\frac{\hbar\left(A_{01}g_{l1}+A_{02}g_{l2}\right)}{\left|e_p p_{4l}\right|t_0}\sqrt{\left|\frac{\mathrm{Re}(K_2)}{\mathrm{Re}(W)}\right|}$, $\Theta_l(z,t)=(k_{pl}+K_0)z-\omega_{pl}t+\frac{A_{0l}\left(A_{01}g_{l1}^2+A_{02}g_{l2}^2\right)}{8L_{\mathrm{disp}}}$ [18].

Then the squeezing ratio of the two probe fields (i.e., vector soliton pairs) is defined as $R=R_{jl}=\left\langle \hat{X}^2_{jl,\theta}(s)\right\rangle\Big/\left\langle \hat{X}^2_{jl,\theta}(0)\right\rangle$ [26,27], where the quadrature variances $\left\langle \hat{X}^2_{jl,\theta}(s)\right\rangle$ is obtained in the following form:

$$\left\langle \hat{X}^2_{11,\theta}(s)\right\rangle=\frac{1}{2}+\frac{1}{8}(g_{11}^4A_{01}^4+g_{12}^4A_{02}^4)s^2\sin^2\theta+\frac{1}{2}(g_{11}^2A_{01}^2+g_{12}^2A_{02}^2)s^2\sin\theta\cos\theta, \tag{22a}$$

$$\left\langle \hat{X}^2_{12,\theta}(s)\right\rangle=\frac{1}{2}+\frac{1}{8}(g_{21}^4A_{01}^4+g_{22}^4A_{02}^4)s^2(\sin^2\theta-\cos^2\theta)+\frac{1}{2}(g_{21}^2A_{01}^2+g_{22}^2A_{02}^2)s^2\sin\theta\cos\theta, \tag{22b}$$

$$\left\langle \hat{X}^2_{21,\theta}(s)\right\rangle=\frac{1}{2}+\frac{1}{8}(g_{11}^4A_{01}^4+g_{12}^4A_{02}^4)s^2\cos^2\theta+\frac{1}{2}(g_{11}^2A_{01}^2+g_{12}^2A_{02}^2)s^2\sin\theta\cos\theta, \tag{22c}$$

$$\left\langle \hat{X}^2_{22,\theta}(s)\right\rangle=\frac{1}{2}+\frac{1}{8}(g_{21}^4A_{01}^4+g_{22}^4A_{02}^4)s^2(\cos^2\theta-\sin^2\theta)+\frac{1}{2}(g_{21}^2A_{01}^2+g_{22}^2A_{02}^2)s^2\sin\theta\cos\theta, \tag{22d}$$

From Eq. (22), we find that the values of $\left\langle \hat{X}^2_{jl,\theta}(s)\right\rangle$ are composed of two parts: the vacuum value 1/2 and the quantum-fluctuation part which is the function of the dimensional propagation distance s, angle θ, and Kerr nonlinearity $g_{l\rho}$, as shown in Fig. 3. It is seen that, at the beginning of the propagation of two probe fields, there are no quantum fluctuations, and the variances are $\left\langle \hat{X}^2_{jl,\theta}(s=0)\right\rangle=\frac{1}{2}$ for all the angles. In the course of the propagation, the quantum fluctuations emerge, and these results strongly vary with the change of θ. The optimum angle θ_{opt} is defined as one corresponding to the minimum value $\left\langle \hat{X}^2_{jl,\theta}(s)\right\rangle$. At θ_{opt}, the quadrature variances $\left\langle \hat{X}^2_{jl,\theta}(s)\right\rangle$ in the deep blue domains are much smaller than their vacuum value, while the squeezing ratio R attains its minimum value, $R_{\min}$. We also find that the quantum squeezing become more and more obvious with s.

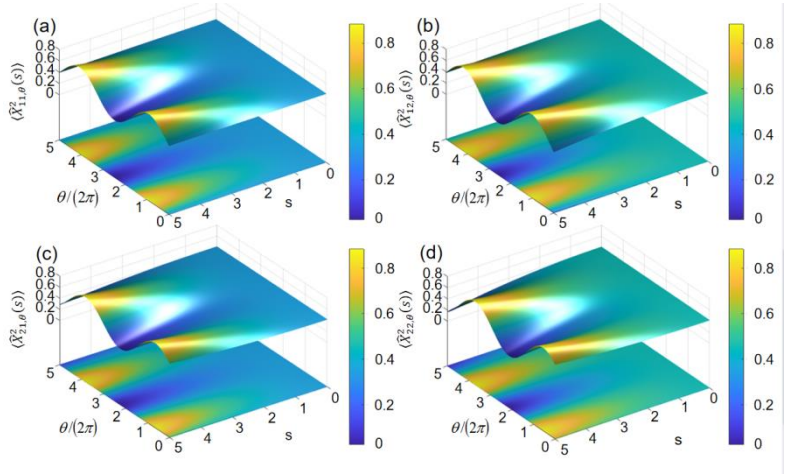

Fig.3 Quadrature variances $\left\langle \hat{X}^2_{jl,\theta}(s) \right\rangle$ as functions of the scaled propagation distance s and $\theta/(2\pi)$ for $A_{01} = A_{02} = g_{l\rho} = 1$. The figures are all plotted as per Eq. (22).

Figure 4 shows the quantum squeezing vs. propagation distance s, angle θ, and Kerr nonlinearity $g_{l\rho}$. In Fig. 4(a), one sees that the squeezing ratio R_{1l} (in dB units) changes periodically with θ. From here, we can obtain the optimal angle θ_{opt}. Furthermore, $\theta_{\text{opt}}(s)$ increases linearly with s for both $\left\langle \hat{X}^2_{11,\theta}(s) \right\rangle$ and $\left\langle \hat{X}^2_{12,\theta}(s) \right\rangle$, as shown in Fig. 4(b). The absolute value of the minimum (maximum) squeezing ratio $R_{\min}$ ($R_{\max}$) increase obviously with s [as shown in Fig. 4(c)], therefore the quantum squeezing effect may be prominent for proper values of distance s. This phenomenon is caused by the Kerr nonlinearity, as shown in Fig. 4(d). We see that $R_{\min}$ is sensitive to the selection of the nonlinearity parameters $g_{l\rho}$, this trend being stronger when the nonlinear coefficient $g_{l\rho}$ is larger.

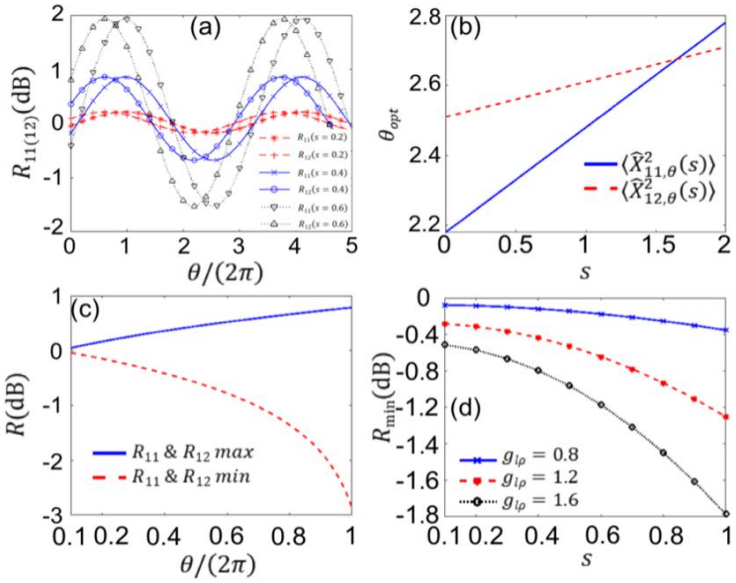

Fig. 4 (a) Squeezing ratio $R_{11(12)}$ versus angle $\theta/(2\pi)$ for the scaled propagation distance $s = 0.2, 0.4, 0.6$. (b) Optimal angle θ_{opt} as a function of s. (c) Minimum squeezing ratio R_{min} and maximum squeezing ratio R_{max} versus s. Panels (a-c) are plotted with the parameters $g_{l\rho} = 1$. (d) R_{min} as a function of s with different nonlinear parameters $g_{l\rho}$

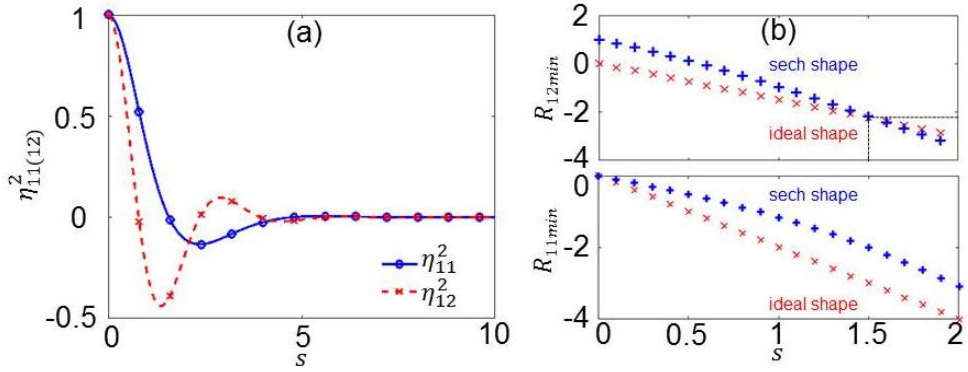

Fig. 5. (a) Atomic spin squeezing degree $\eta^2_{11(12)}$ versus s. (b) Minimum squeezing ratio R_{min} versus s, where the solid and dashed lines are results for the sech-shaped LO (local-oscillator) pulse and the ideal LO pulse, respectively. Parameters $A_{01} = 2$, $A_{02} = 1$, $g_{l1} = 1$, $g_{l2} = 2$, $\theta_{0l} = 0$, $w_{pl} = 1$, $w_c = 1$, $k_{pl} = 10$.

Similar to quantum squeezing of vector optical soliton pairs, atomic spin squeezing is also an important feature of cold atomic system. The atomic spin operators are defined as

$$\hat{s}_x = \frac{1}{2}\left(\hat{\sigma}_{12} + \hat{\sigma}_{21}\right),\ \hat{s}_y = \frac{1}{2i}\left(\hat{\sigma}_{12} - \hat{\sigma}_{21}\right),\ \hat{s}_z = \frac{1}{2}\left(\hat{\sigma}_{11} + \hat{\sigma}_{22}\right); \tag{23}$$

$$\hat{s}_\theta = \frac{1}{2}\left[\hat{\sigma}_{21}e^{-i\theta} + \hat{\sigma}_{21}e^{i\theta}\right] = \cos\theta\hat{s}_x + \sin\theta\hat{s}_y. \tag{24}$$

In this work, the atomic spin squeezing degree is defined as

$$\eta_l^2 = \min_{\theta_l}\left[\left\langle \hat{s}_{\theta_l}^2\right\rangle - \left\langle \hat{s}_{\theta_l}\right\rangle^2\right]\Big/\left\langle \hat{s}_z\right\rangle. \tag{25}$$

Here $\hat{s}_{\theta_l} \approx -\frac{g_{pl}\sqrt{n_0}}{2\Omega_c}\left(s_{\Phi_l} + \hat{s}_{\Phi_l}\right)$,

$S_{\Phi_1} = \left(A_{01}\sqrt{g_{11}} + A_{02}\sqrt{g_{12}}\right)\mathrm{sech}\left[\frac{A_{01}g_{11} + A_{02}g_{12}}{2t_0}\left(t - \frac{z}{V_g}\right)\right]\cos\Phi_1$, and

$S_{\Phi_2} = \left(A_{01}\sqrt{g_{21}} + A_{02}\sqrt{g_{22}}\right)\tanh\left[\frac{A_{01}g_{21} + A_{02}g_{22}}{2t_0}\left(t - \frac{z}{V_g}\right)\right]\cos\Phi_2$, with

$\Phi_l = \Theta_l + \left(k_{pl} - k_c\right)z - \left(\omega_{pl} - \omega_c\right)t - \theta_l$.

The spin squeezing degree η_{1l}^2 with respect to s is shown in Fig. 5(a). There is no spin squeezing effect in the beginning ($\eta_{1l}^2 = 1$), then η_{1l}^2 decrease rapidly with s and remain constant at $s > 5$. The spin squeezing effect is due to the action of the Kerr nonlinearities $g_{l\rho}$ in the system. Furthermore, a balanced homodyne detection technique is performed to measure the quadrature variances $\hat{X}_{jl,\theta}(s)$ which is expressed as

$\hat{X}_{jl,\theta}(s) = \int_{-\infty}^{+\infty} d\sigma\left[\varsigma_{j,\theta}(\sigma)\hat{w}_l^\dagger(s,\sigma) + \varsigma_{jl,\theta}^*(\sigma)\hat{w}_l(s,\sigma)\right]$, where

$\varsigma_{jl,\theta}(\sigma) = \left[\cos\theta\phi_j(\sigma_l) + i\sin\theta\psi_j(\sigma_l)\right]/\sqrt{2}$, $\psi_j(\sigma_l) = u_j(\sigma_l) + v_j(\sigma_l)$, and

$\phi_j(\sigma_l) = u_j(\sigma_l) - v_j(\sigma_l)$. Here $\varsigma_{jl,\theta}(\sigma)$ is a coherent pulse injected into the atomic gas from a local oscillator (LO), which is mixed with the input probe pulses [i.e., quantity $\hat{w}_l$ in Eq. (15)] through a 50:50 beam splitter, and the mixed signals from the two output paths are detected by two photodetectors, respectively. Because reshaping a pulse to be a combination of $\varsigma_{jl,\theta}(\sigma)$ is difficult, we adopt $\varsigma_{j1,\theta}(\sigma) = \mathrm{sech}(\sigma)\exp(i\theta)/\sqrt{2}$ and $\varsigma_{j2,\theta}(\sigma) = \tanh(\sigma)\exp(i\theta)/\sqrt{2}$ as a LO pulse in practice, thus $\hat{X}_{jl,\theta}'(s) = \cos\theta\hat{Q}_{1l} + 2\sin\theta\hat{P}_{1l}$ is obtained. Figure 5(b) displays the predictions for the minimum squeezing ratio $R_{\min}$ of vector optical soliton

pairs as functions of propagation distance s, cf. Ref. [26]. One can see that the minimum squeezing ratio obtained by using the sech-shaped LO pulse is getting close to that produced by the ideal LO pulse with s increases.

4. Conclusions

In this work, we have developed the quantum theory to investigate vector slow-light soliton pairs in the double-EIT-based atomic gas. Using the Heisenberg-Langevin and Maxwell equations, we have derived the vector QNLSE (quantum nonlinear Schrödinger equation) controlling the evolution of the two probe-field envelopes. We have constructed the effective Hamiltonian and performed rigorous diagonalization to deal with quantum fluctuations of vector slow-light soliton pairs and atomic spin associated with the pairs. It is found that vector soliton pairs and atomic spin can be significantly squeezed in the course of the propagation. The squeezing degree depends on the propagation distance, the angle and the strength of the Kerr nonlinearity.

The analysis reported in this work can be extended by considering effects of collisions between vector solitons on the quantum squeezing, and generation of quantum entanglement between solitons by collisions, cf. Ref. [28] and [29].

References

[1] M. J. Ablowitz and P. A. Clarkson, *Solitons, Nonlinear Evolution Equations and Inverse Scattering*, Cambridge, New York, 2003.
[2] Y. V. Kartashov, F. Ye and L. Torner, *Optics Express* **14** (2006) 4808.
[3] Y. S. Kivshar and G. P. Agrawal, *Optical Solitons: From Fibers to Photonic Crystals*, Academic Press, London, 2006.
[4] G. P. Agrawal, *Nonlinear Fiber Optics*, Academic Press, New York, 2019.
[5] M. Fleischhauer, A. Imamoglu and J. P. Marangos, *Rev. Mod. Phys.* **77** (2005) 633.
[6] S. E. Harris, *Phys. Today* **50** (1997) 36.
[7] L. V. Hau, S. E. Harris, Z. Dutton and C. H. Behroozi, *Nature (London)* **397** (1999) 594.
[8] H. Schmidt and A. Imamoglu, *Opt. Lett.* **21** (1996) 1936.

[9] Y. Chen, Z. Bai and G. Huang, *Phys. Rev. A* **89** (2014) 023835.
[10] Z. Bai, W. Li and G. Huang, *Optica* **6** (2019) 309.
[11] H. Michinel, M. J. Paz-Alonso and V. M. Pérez-García, *Phys. Rev. Lett.* **96** (2006) 023903.
[12] C. Shou and G. Huang, *Phys. Rev. A* **99** (2019) 043821.
[13] J. L. Ding and B. P. Hou, *Optics Communications* **284** (2011) 2949.
[14] Y. Qi, F. Zhou, T. Huang, Y. Niu and S. Gong, *Phys. Rev. A* **84** (2011) 023814.
[15] J. Zhu, Q. Zhang and G. Huang, *Phys. Rev. A* **103** (2021) 063512.
[16] M. Tsang, *Phys. Rev. Lett.* **97** (2006) 023902.
[17] D. A. Steck, *Rubidium 87 D Line Data*, http://steck.us/ alkalidata/.
[18] G. M. Li, A. Li, S. J. Su, Y. Zhao, G. P. Zhou, L. Xue and S. L. Xu, *Optics Express* **29** (2021) 14016.
[19] A. V. Gorshkov, A. André, M. D. Lukin and A. S. Sørensen, *Phys. Rev. A* **76** (2007) 033804.
[20] Y. Lai and H. A. Haus, *Phys. Rev. A* **40** (1989) 854.
[21] P.-É. Larré and I. Carusotto, *Phys. Rev. A* **92** (2015) 043802.
[22] G. Huang, L. Deng, J. Yan and B. Hu, *Phys. Lett. A* **357** (2006) 150.
[23] P. G. De Gennes, *Superconductivity of Metals and Alloys*, Benjamin, New York, 1966
[24] L. Mandel and E. Wolf, *Optical Coherence and Quantum Optics*, Cambridge University Press, 1995.
[25] S. J. Carter, P. D. Drummond, M. D. Reid and R. M. Shelby, *Phys. Rev. Lett.* **58** (1987) 1841.
[26] H. A. Haus and Y. Lai, *J. Opt. Soc. Am. B* **7** (1990) 386.
[27] R. K. Lee and Y. C. Lai, *Phys. Rev. A* **80** (2009) 033839.
[28] R. K. Lee, Y. C. Lai and Y. S. Kivshar, *Phys. Rev. A* **71** (2005) 035801.
[29] R. K. Lee, Y. Lai and B. A. Malomed, *Phys. Rev. A* **71** (2005) 013816.

Mass minimization of an AFG Timoshenko beam with coupled axial and bending vibrations*

Obradović Aleksandar†
University of Belgrade, Faculty of Mechanical Engineering, Kraljice Marije 16, Belgrade 35 11120, Serbia

ABSTRACT

The paper considers mass minimization of an axially functionally graded (AFG) Timoshenko beam of a variable cross-sectional area, with a specified fundamental frequency. The analyzed case of coupled axial and bending vibrations involves contour conditions as the cause of coupling. The problem is solved applying Pontryagin's maximum principle, where the beam cross-sectional area is taken for control. The two-point boundary value problem is obtained, and the shooting method is used to solving it. The property of self-adjoint systems is deployed. The percent saving of the beam mass is determined, achieved by using the beam of an optimum variable square cross-section as compared to the beam of a constant cross-section. The procedure developed by the author in his earlier papers is extended herein to the case of a limited cross-sectional area. The second generalization relates to the general case of contour conditions at the beam ends.

1. Introduction

Some elastic bodies can be modeled to obtain sufficient accuracy by using Euler-Bernoulli or Timoshenko beam [1] in the analysis of their vibrations. Determination of optimal shapes applying different optimization criteria is an engineering task of utter importance. In a static sense, these problems are associated with the optimization of columns against buckling. Papers [2,3] employ a buckling optimization approach based on the Hencky bar-chain model of beams, whereas [4-8] consider a series of shape optimization problems of columns against buckling by implementing Pontryagin's maximum principle.

* This work has been supported by Ministry of Education, Science and Technological Development, Republic of Serbia, Project No.451-03-9/2021-14/200105
† e-mail address: aobradovic@mas.bg.ac.rs

In this paper, the dynamic aspect of beam optimization includes references related to the problem of mass minimization of rods when the value of fundamental frequency of these rods oscillation is specified. Among the most outstanding references relevant to this problem are [9-11] where the minimum mass optimization problem is considered within the framework of axial vibrations of cantilever beams with a variable cross-section carrying concentrated mass at their free ends. Moreover, [9,10] deal with the tapered type of beams, whereas [11] is concerned with stepped ones. Paper [12] analyzes the impact of a variable cross- section (the linear relationship between the second area moment and the area) of Euler-Bernoulli beams in bending vibrations on the extremal values of the fundamental frequency, and [13] studies the conditions of equivalence between maximum frequency and minimum mass optimization problems. In [14] an optimality criterion method for weight minimization of structures under the fundamental frequency constraint in the form of inequality is presented. Mass minimization problems with multiple frequency constraints of equality and inequality types are reported in [15,16]. Paper [17], besides frequency constraints, studies simultaneously stress, displacement and cross-sectional area multiple constraints. The mass minimization of structures together with maximization of structural strain energy (multiobjective optimization problems) can be found in [18]. Paper [19] provides an example of the application of bio-inspired algorithms (firefly algorithm, bat algorithm and cuckoo search algorithm) in the problem of mass minimization of a single-girder bridge crane. Today, this type of algorithms has increasing application in complex optimization problems with multiple objective functions, design variables and equality and inequality constraints, for more details refer to [20].

Based on a review of available literature, it is evident that no results are reported in the field of mass minimization of beams with prescribed fundamental frequency, whose oscillatory behavior can be represented in the form of coupling between fundamental types of oscillations (axial vibrations, bending vibrations, torsion vibrations). The fact mentioned above makes this field of research potentially attractive. Otherwise, the coupling of different types of oscillations can be conditioned, for instance, by the cross-section geometry of a beam (cross-section with one symmetry axis, which causes coupling of bending and torsion vibrations [21]), or by complex contour conditions at the beam ends (coupling of bending and axial vibrations [22]).

Our paper [23] considers the second cause of coupled oscillations for the case of simply supported Euler Bernoulli beam with inclined right end. Moreover, the approach from [4-8] based on applying Pontryagin's maximum principle is extended to the mass minimization problem of the mentioned simply supported beam with coupled bending and axial vibrations at prescribed fundamental frequency. Here, it is worth highlighting that in [4-8] it was for the first time in literature that the occurrence of the self-adjoint system is observed in the

problems of determining optimal shapes. This allows for twice fewer differential equations of the TPBVP problem of the Maximum principle as compared to classical problems and it is known that the difficulties in numerical solving are the main reason why the authors of the works dealing with the application of the mathematical theory of optimal processes often avoid using Pontryagin's principle.
Our later works [24-25] research an AFG Timoshenko cantilever beam instead of Euler Bernoulli homogeneous beams.
This paper extends additionally the procedure of shape optimization to the general case of contour conditions and introduces the limits of cross-sectional dimensions. It is necessary to limit the cross-sectional area from the bottom side so as not to disturb the strength of the beam. The upper limit can be defined by the beam initial shape that yields optimal shape by material removal, space limits, or to ensure the validity of the appropriate theory (Euler Bernoulli or, in this case, Timoshenko theory).

2. Problem statement for determining the optimal profile shape

The Timoshenko beam [1] (Fig.1) of length L, variable cross-sectional area $A(z)$ and axial moment of inertia $I_x(z) = sA(z)^2$, where coefficient s depends on the cross-sectional shape (for the square cross-section $= 1/12$, while in the case of circular cross-section $s = 1/4\pi$), is considered. In the case of AFG material, the density $\rho(z)$, Young's modulus of elasticity $E(z)$ and the shear modulus $G(z)$, are variable along the beam axis. At the right end a body of mass M_r and moment of inertia J_{Cr} is fixed eccentrically to the central axis, where the position of the center of mass is defined by quantities e_r and h_r. The corresponding stiffnesses of springs at the right end are c_r, c_{1r} and c_{2r}. All quantities given at the left end have index l instead of index r.

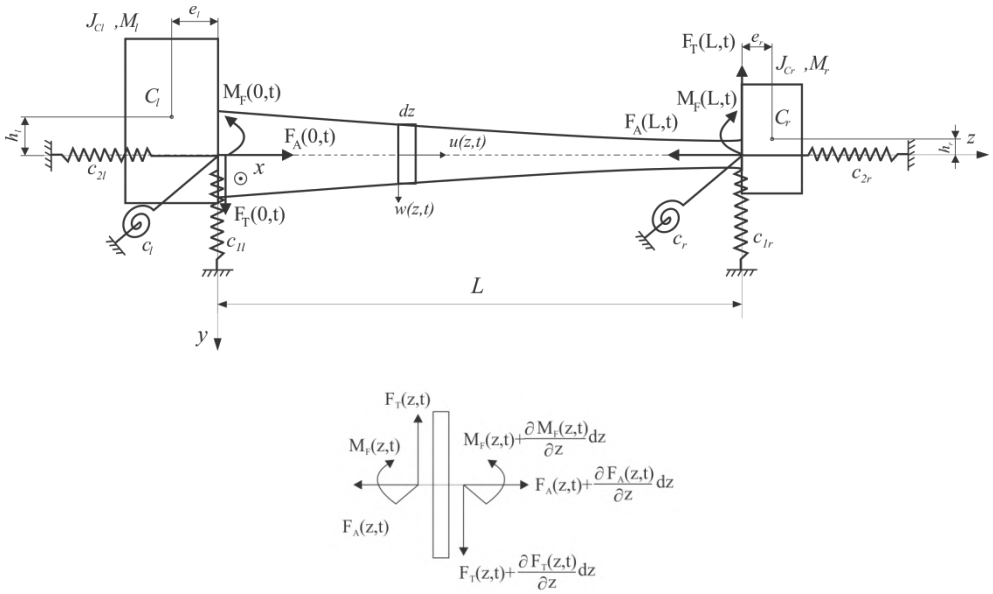

Fig. 1 AFG Timoshenko beam of variable cross-section with bodies eccentrically located at the beam ends

Differential equations of Timoshenko beams, oscillating in the axial and bending direction, in the case of the linear theory, can be derived based on dynamic equations of the elementary particle of the beam of mass $dm = \rho(z)A(z)dz$ and a corresponding moment of inertia of masses $dJ_x = \rho(z)I_x(z)dz$:

$$\begin{aligned}
(\rho(z)A(z)dz)\frac{\partial^2 u(z,t)}{\partial t^2} &= \frac{\partial}{\partial z}\left[F_A(z,t)\right]dz,\\
(\rho(z)A(z)dz)\frac{\partial^2 w(z,t)}{\partial t^2} &= \frac{\partial}{\partial z}\left[F_T(z,t)\right]dz,\\
(\rho(z)I_x(z)dz)\frac{\partial^2 \phi(z,t)}{\partial t^2} &= \left[F_T(z,t)\right]dz - \frac{\partial}{\partial z}\left[M_F(z,t)\right]dz,
\end{aligned} \tag{1}$$

where $u(z,t)$ and $w(z,t)$ are axial and transverse displacements, $\phi(z,t)$ is the cross-sectional angle of rotation, $F_A(z,t)$ represents the axial force:

$$F_A(z,t) = E(z)A(z)\frac{\partial u(z,t)}{\partial z}, \tag{2}$$

the bending moment is given by the expression:

$$M_F(z,t) = -E(z)I_x(z)\frac{\partial \phi(z,t)}{\partial z}, \tag{3}$$

where for Timoshenko beams [1] the slope angle of the elastic line is:

$$\frac{\partial w(z,t)}{\partial z} = \phi(z,t) + \frac{F_T(z,t)}{kA(z)G(z)}, \tag{4}$$

where $F_T(z,t)$ is the transverse force and k is the Timoshenko coefficient.

The system of linear differential equations (1-4) is solved by the method of separation of variables [1]:

$$\begin{aligned} &w(z,t) = W(z)T(t), \\ &\phi(z,t) = \varphi(z)T(t),\ u(z,t) = U(z)T(t),\ F_A(z,t) = F_a(z)T(t), \\ &F_T(z,t) = F_t(z)T(t),\ M_F(z,t) = M_f(z)T(t), \end{aligned} \tag{5}$$

where $\frac{\partial^2 T(t)}{\partial t^2} = -\omega^2 T(t)$ and ω represents a circular frequency. If we want all functions (5) to retain their physical dimensions and units, the function $T(t)$ will be considered to be dimensionless.

Further procedure yields the following differential equations:

$$\begin{aligned} &\frac{\partial U(z)}{\partial z} = \frac{F_a(z)}{E(z)A(z)},\ \frac{\partial W(z)}{\partial z} = \varphi(z) + \frac{F_t(z)}{kA(z)G(z)},\ \frac{\partial \varphi(z)}{\partial z} = -\frac{M_f(z)}{E(z)sA(z)^2}, \\ &\frac{\partial F_a(z)}{\partial z} = -\omega^2 \rho(z)A(z)U(z),\ \frac{\partial F_t(z)}{\partial z} = -\omega^2 \rho(z)A(z)W(z), \\ &\frac{\partial M_f(z)}{\partial z} = F_t(z) + \omega^2 \rho(z)sA(z)^2 \varphi(z). \end{aligned} \tag{6}$$

Optimization problem, considered in this paper, includes defining the function of change of the cross-sectional area $A(z)$ that will lead to the Timoshenko beam mass minimization, where the fundamental frequency of oscillation $\omega_1 = \omega^*$ is specified. In that regard, the functional that is minimized is of the form:

$$J = \int_0^L \rho(z)\, A(z)dz, \tag{7}$$

differential equations (6) represent the equations of state.

Contour conditions at the ends can be written using differential equations of planar motion for each of the added rigid body in a way as described in more detail in [22]. Contour conditions at the left end are of the form:

$$\begin{aligned} &M_l\omega^2(U(0) + h_l\varphi(0)) + F_a(0) - c_{2l}U(0) = 0, \\ &M_l\omega^2(W(0) - e_l\varphi(0)) + F_t(0) - c_{1l}W(0) = 0, \\ &J_{Cl}\omega^2\varphi(0) - M_f(0) - c_l\varphi(0) + e_l(F_t(0) \\ &-c_{1l}W(0)) + h_l(-F_a(0) + c_{2l}U(0)) = 0, \end{aligned} \tag{8}$$

whereas at the right end:

$$\begin{aligned}
&M_r\omega^2(U(L)+h_r\varphi(L))-F_a(L)-c_{2r}U(L)=0,\\
&M_r\omega^2(W(L)+e_r\varphi(L))-F_t(L)-c_{1r}W(L)=0,\\
&J_{Cr}\omega^2\varphi(L)+M_f(L)-c_r\varphi(L)+e_r(F_t(L)\\
&+c_{1r}W(L))+h_r(F_a(L)+c_{2r}U(L))=0.
\end{aligned} \tag{9}$$

3. Determining the optimal profile shape of a beam by applying Pontryagin's maximum principle

The optimal control problem (6-9) will be solved by applying Pontryagin's maximum principle [26]. To this end, let us write Pontryagin's function:

$$\begin{aligned}
H=&\lambda_0\rho(z)A(z)+\lambda_U(z)\frac{F_a(z)}{E(z)A(z)}+\lambda_W(z)(\varphi(z)+\frac{F_t(z)}{k\,A(z)G(z)})\\
&+\lambda_\varphi(z)\frac{-M_f(z)}{E(z)sA(z)^2}-\lambda_{F_a}(z)\omega^2\rho(z)A(z)U(z)\\
&-\lambda_{F_t}(z)\omega^2\rho(z)A(z)W(z)+\lambda_{M_f}(z)(F_t(z)+\omega^2\rho(z)sA(z)^2)
\end{aligned} \tag{10}$$

where $\lambda_0,\lambda_U(z),\lambda_W(z),\lambda_\varphi(z),\lambda_{F_a}(z),\lambda_{F_t}(z),\lambda_{M_f}(z)$ are costate variables, which satisfy the coupled system of equations:

$$\begin{aligned}
&\frac{\partial\lambda_U(z)}{\partial z}=\lambda_{F_a}(z)\omega^2\rho(z)A(z),\ \frac{\partial\lambda_W(z)}{\partial z}=\lambda_{F_t}(z)\omega^2\rho(z)A(z),\\
&\frac{\partial\lambda_\varphi(z)}{\partial z}=-\lambda_W(z),\\
&\frac{\partial\lambda_{F_a}(z)}{\partial z}=\frac{-\lambda_U(z)}{E(z)A(z)},\ \frac{\partial\lambda_{F_t}(z)}{\partial z}=\frac{-\lambda_W(z)}{kA(z)G(z)}-\lambda_{M_f}(z),\\
&\frac{\partial\lambda_{M_f}(z)}{\partial z}=\frac{\lambda_\varphi(z)}{E(z)sA(z)^2},
\end{aligned} \tag{11}$$

where λ_0 is an arbitrary non-positive constant. In problems of this type it is commonly taken that $\lambda_0=-1$.

The transversality conditions [26] can be represented in the form as follows:

$$\begin{aligned}
&(\lambda_U(z)\Delta U(z)+\lambda_W(z)\Delta W(z)+\lambda_\varphi(z)\Delta\varphi(z)+\lambda_{F_a}(z)\Delta F_a(z)+\\
&\lambda_{F_t}(z)\Delta F_t(z)+\lambda_{M_f}(z)\Delta M_f(z))\ |_0^L=0,
\end{aligned} \tag{12}$$

where $\Delta(\cdot)$ is an asynchronous variation. Based on initial and final conditions (8,9), the following variation dependencies are obtained at the left end:

$$
\begin{aligned}
&(M_l\omega^2 - c_{2l})\Delta U(0) + M_l\omega^2 h_l\Delta\varphi(0) + \Delta F_a(0) = 0,\\
&(M_l\omega^2 - c_{1l})\Delta W(0) - M_l\omega^2 e_l\Delta\varphi(0) + \Delta F_t(0) = 0,\\
&(J_{Cl}\omega^2 - c_l)\Delta\varphi(0) - M_f(0) + e_l\Delta F_t(0) - c_{1l}e_l\Delta W(0)\\
&-h_l\Delta F_a(0) + c_{2l}h_l\Delta U(0) = 0,
\end{aligned}
\tag{13}
$$

and at the right end:

$$
\begin{aligned}
&(M_r\omega^2 - c_{2r})\Delta U(L) + M_r\omega^2 h_r\Delta\varphi(L) - \Delta F_a(L) = 0,\\
&(M_r\omega^2 - c_{1r})\Delta W(L) + M_r\omega^2 e_r\Delta\varphi(L) - \Delta F_t(L) = 0,\\
&(J_{Cr}\omega^2 - c_r)\Delta\varphi(L) + \Delta M_f(L) + e_r\Delta F_t(L) + e_r c_{1r}\Delta W(L)\\
&+h_r\Delta F_a(L) + h_r c_{2r}\Delta U(L) = 0.
\end{aligned}
\tag{14}
$$

Substituting (13) and (14) in (12), the transversality conditions are obtained:

$$
\begin{aligned}
&-(M_l\omega^2 - c_{2l})\lambda_{F_a}(0) + M_l\omega^2 h_l\lambda_{M_f}(0) + \lambda_U(0) = 0,\\
&-(M_l\omega^2 - c_{1l})\lambda_{F_t}(0) - M_l\omega^2 e_l\lambda_{M_f}(0) + \lambda_W(0) = 0,\\
&(J_{Cl}\omega^2 - c_l)\lambda_{M_f}(0) + \lambda_\varphi(0) + e_l\lambda_W(0) + c_{1l}e_l\lambda_{F_t}(0)\\
&-h_l\lambda_U(0) - c_{2l}h_l\lambda_{F_a}(0) = 0,\\
&-(M_r\omega^2 - c_{2r})\lambda_{F_a}(L) + M_r\omega^2 h_r\lambda_{M_f}(L) - \lambda_U(L) = 0,\\
&-(M_r\omega^2 - c_{1r})\lambda_{F_t}(L) + M_r\omega^2 e_r\lambda_{M_f}(L) - \lambda_W(L) = 0,\\
&(J_{Cr}\omega^2 - c_r)\lambda_{M_f}(L) - \lambda_\varphi(L) + e_r\lambda_W(L) - e_r c_{1r}\lambda_{F_t}(L)\\
&+h_r\lambda_U(L) - h_r c_{2r}\lambda_{F_a}(L) = 0.
\end{aligned}
\tag{15}
$$

If the conjugate vector coordinates are expressed via state quantities using the scalar parameter p:

$$
\lambda_U = pF_a,\ \lambda_W = pF_t,\ \lambda_\varphi = -pM_f,\ \lambda_{M_f} = p\varphi,\ \lambda_{F_t} = -pW,\ \lambda_{F_a} = -pU, \tag{16}
$$

it can be noted that differential equations of the coupled system (11) are reduced to the governing system (6), and that the transversality conditions (15) are satisfied in the case when the conditions at the left end (8) and at the right end (9) are satisfied. This has been noted in the shape optimization problems reported by Atanacković et al. [4-8] and has significantly facilitated the application of Pontryagin's maximum principle. It is very well known that numerical difficulties related to computations of the costate variables are those that are limiting the application of maximum principle.

Optimal controls $A(z)$ are defined from the maximum condition of Pontryagin's function (10):

$$\frac{\partial H}{\partial A(z)} = 0, \qquad \frac{\partial^2 H}{\partial A(z)^2} < 0, \tag{17}$$

which, considering (16), is reduced to the conditions:

$$-\frac{pF_a(z)^2}{E(z)A(z)^2} - \frac{pF_t(z)^2}{kG(z)A(z)^2} - \frac{2pM_f(z)^2}{sA(z)^3E(z)} + \\ +2ps\omega^2 A(z)\varphi(z)^2\rho(z) + (-1 + p\omega^2 U(z)^2 + p\omega^2 W(z)^2)\rho(z) = 0, \tag{18}$$

$$2p\left(\frac{F_a(z)^2}{E(z)A(z)^3} + \frac{F_t(z)^2}{kG(z)A(z)^3} + \frac{3M_f(z)^2}{sA(z)^4E(z)} + s\omega^2 A(z)\varphi(z)^2\rho(z)\right) < 0. \tag{19}$$

Based on (19), without loss of generality, it can be taken that $p = -1\frac{s^2}{m^2}$, so that the expression for defining optimal control is reduced to the 4th degree polynomial with respect to $A(z)$:

$$\left(\frac{F_a(z)^2}{E(z)} + \frac{F_t(z)^2}{kG(z)}\right)A(z) + \frac{2M_f(z)^2}{sE(z)} - \\ -2s\omega^2 A(z)^4\varphi(z)^2\rho(z) - (1 + \omega^2 U(z)^2 + \omega^2 W(z)^2)\rho(z)A(z)^3 = 0. \tag{20}$$

The procedure of numerical solving of the two-point boundary value problem (6-9,20) consists of the three-parameter shooting that involves selecting $F_a(0), F_t(0), M_f(0)$ (where $U(0), W(0), \varphi(0)$ can be calculated from (8)) to satisfy the relations (9). If numerical solving is performed in the program package *WolframMathematica* [27] using function NDSolve[…], it is not necessary to express *A(z)* from (20) in analytical form via state quantity, because this function contains in itself the procedure for numerical solving of the system of differential and ordinary equations.

In the case of restrictions imposed on the cross-sectional area:

$$A_{\min} \le A(z) \le A_{\max} \tag{21}$$

it is necessary to check whether the values obtained from (20) satisfy the restrictions (21). If they are lower or higher compared to the permissible limit values, the cross-sectional areas are constant over those intervals, amounting to $A_{\max}$ or $A_{\min}$. As a rule, when solving such problems, the optimal shape is first determined without considering the restrictions (21). Thereafter, it is attempted to find a control that satisfies all conditions of the Maximum principle of such structure that on the segments where an area larger than $A_{\max}$ is obtained by solving (20), it is taken that in that segment a constant cross-section is of

maximum permissible area. Similarly, in the case when the area is smaller, but it is then taken $A_{\min}$.

Positions z_i where a variable cross-section joins a constant cross-section of the maximum area are determined from the conditions:

$$\left(\frac{F_a(z_i)^2}{E(z_i)}+\frac{F_t(z_i)^2}{kG(z_i)}\right)A_{\max}+\frac{2M_f(z_i)^2}{sE(z_i)} \\ -2s\omega^2 A_{\max}{}^4\varphi(z_i)^2\rho(z_i)-(1+\omega^2U(z_i)^2+\omega^2W(z_i)^2)\rho(z_i)A_{\max}{}^3=0, \tag{22}$$

however, in the case of merging with a segment of the constant cross-section of the minimum area:

$$\left(\frac{F_a(z_i)^2}{E(z_i)}+\frac{F_t(z_i)^2}{kG(z_i)}\right)A_{\min}+\frac{2M_f(z_i)^2}{sE(z_i)}- \\ -2s\omega^2 A_{\min}{}^4\varphi(z_i)^2\rho(z_i)-(1+\omega^2U(z_i)^2+\omega^2W(z_i)^2)\rho(z_i)A_{\min}{}^3=0. \tag{23}$$

4. Numerical example

The shape optimization procedure will be presented using the example of a cantilever beam of a square cross-section, length L=1m, with a rigid body placed eccentrically at the free end, as shown in Fig. 2. The rigid body has mass $M_r=10kg$ and moment of inertia $J_{Cr}=2.5kg\,m^2$. Axial and transverse eccentricities of the rigid body amount to $e_r=e=h_r=h=0.5m$. In AFG material considered herein the laws of change in density and modulus of elasticity are taken as in [24,25]:

$$\rho(z)=\rho_0(1-0.8\cos(\pi z)),\ \rho_0=7850\frac{kg}{m^3}, \\ E(z)=E_0(1-0.2\cos(\pi z)),\ E_0=2.068\cdot10^{11}\frac{N}{m^2}. \tag{24}$$

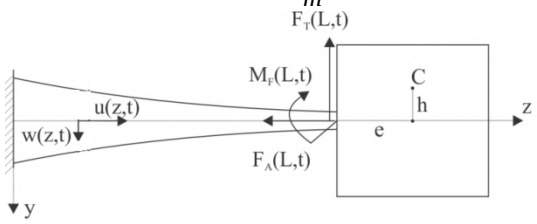

Fig. 2 [25] Cantilever beam of a variable square cross-section

For Timoshenko beams of a square cross-section, $=1/12$. The Timoshenko coefficient, in this case, amounts approximately to $k=\frac{5}{6}$. The shear modulus is

defined using the Poisson coefficient ν from the expression $G(z) = \frac{E(z)}{2(1+\nu)}$, where for its value it is taken here that $\nu = 0.3$.
Also, let the required value of the fundamental frequency be $f = 10\,Hz$ which leads to the fundamental circular frequency $\omega^* = 20\pi\,Hz$.
Let us seek a solution of the optimization problem first for the case when there are not restrictions to the cross-sectional area. When performing a three-parameter shooting in the program package *WolframMathematica* [27], three missing values of the three parameters at the left end are obtained:

$$F_a(0) = -219.631\,N, \quad F_t(0) = -451.863\,N, \quad M_f(0) = 848.826\,Nm, \qquad (25)$$

It should be noted here that from the contour conditions (8), when stiffnesses are of infinitely large values (in the case of a clamped left end), zero values of corresponding displacements U(0), W(0), φ(0) formally follow too.
Fig. 3 shows values of the optimum cross-sectional area shape and its corresponding sides of a square (red line). The dashed line denotes values corresponding to a constant cross-sectional area A^* and the side of a square a^*, respectively $A^* = 0.00207910\,m^2$, $a^* = 0.0455971\,m$ for which the fundamental circular frequency is $\omega^* = 20\pi\,Hz$, and which were obtained in paper [24].

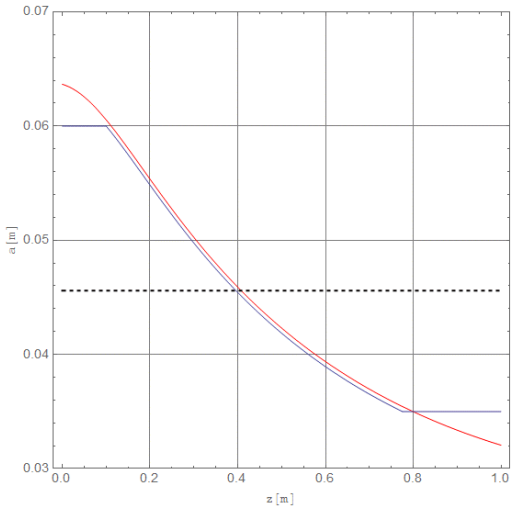

Fig. 3 Optimum cross-sectional side of a square *a(z)*

Relative material saving compared to the cantilever beam of a constant cross-section corresponding to the same circular frequency amounts to:

$$\Delta = \frac{\left(\int_0^L \rho(z) A_1 \mathrm{d}z - \int_0^L \rho(z) A(z) \mathrm{d}z \right)}{\int_0^L \rho(z) A_1 \mathrm{d}z} \text{x}100\% = 23.38\%, \tag{26}$$

where numerical integration was done in (26).

Consider the case when the cross-sectional area is limited so that a_{max}=0.06m, a_{min}=0.035m. Therefore, it can be assumed that at the initial segment the beam is of the maximum possible area and at the end segment it is of the minimum area.

Besides unknow quantities $F_a(0)$, $F_t(0)$, $M_f(0)$, it is also necessary to determine positions $z_{1,2}$ of coupling occurrence between maximum of minimum corss-section varying in area.

These five parameters are chosen so that after numerical integration of the system (6) final conditions (9) as well as conditions (22,23) are satisfied at the coupling points. The values obtained as solutions are

$$\begin{aligned} &F_a(0) = -208.038\,N, \quad F_t(0) = -446.939\,N, \quad M_f(0) = 826.645\,Nm \\ &z_1 = 0.10013m,\ z_2 = 0.77526m \end{aligned} \tag{27}$$

and optimal shape is shown in Fig. 3 (blue line). In this case, the relative percent saving of the mass (26) is slightly lower and amounts to 22.97%.

5. Conclusions

This paper demonstrates the performance of shape optimization of AFG Timoshenko beam of a square cross-section with coupled axial and bending vibrations, where the beam mass minimization is done at specified fundamental frequency. In solving this optimization problem Pontryagin's maximum principle is applied. So far, Pontryagin's maximum principle has been practically used for solving optimization problems in buckling so that in this paper its application is extended to optimization problems in oscillating body. The above procedure can be also applied to the general case of a cross-section such as circular, etc. The above procedure can be also applied to the general case of contour conditions at the beam ends, including bodies eccentrically positioned at both ends, different types of supports at beam ends, as well as clamping of the bodies with different springs. By taking infinitely large stiffnesses of appropriate springs, the model considered can be also extended to the cases when the corresponding displacements in the supports equal zero.

References

[1] S. S. Rao, *Vibration of continuous systems*, John Wiley & Sons; 2007.

[2] H. Zhang, C. M. Wang, N. Challamel and E. Ruocco, *Semi-analytical solutions for optimal design of columns based on Hencky bar-chain model*, Eng. Struc. (2017) 136.

[3] E. Ruocco, C. M. Wang, H. Zhang and N. Challamel, *An approximate model for optimizing Bernoulli columns against buckling*, Eng. Struct. (2017) 141.

[4] T. M. Atanackovic and V. B. Glavardanov, *Optimal shape of a heavy compressed column*, Struct. Multidisc. Optim. (2004) 28.

[5] T. M. Atanackovic and B. N. Novakovic, *Optimal shape of an elastic column on elastic foundation*, Eur. J. Mech. A. (2006) 25.

[6] T. M. Atanackovic, *Optimal shape of column with own weight: bi and single modal optimization*, Mecc. (2006) 41.

[7] T. M. Atanackovic and A. P. Seyranian, *Application of Pontryagin's principle to bimodal optimization problems*, Struct. Multidisc. Optim. (2008) 37.

[8] B. N. Novakovic and T. M. Atanackovic, *On the optimal shape of a compressed column subjected to restrictions on the cross-sectional area*, Struct. Multidisc. Optim. (2011) 43.

[9] M. J. Turner, *Design of minimum mass structures with specified natural frequencies*, AIAA. J. (1967) 5.

[10] J. E. Taylor, *Minimum mass bar for axial vibration at specified natural frequency.*, AIAA. J. (1967) 5.

[11] C. Y. Sheu, *Elastic minimum-weight design for specified fundamental frequency*, Int. J. Solids Struct. (1968) 4.

[12] R. M. Brach, *On the extremal fundamental frequencies of vibrating beams*, Int. J. Solids Struct. (1968) 4.

[13] R. M. Brach, *On optimal design of vibrating structures*, J. Optim. Theory Appl. (1973) 11(6).

[14] M. R. Khan and K. D. Willmert, *An efficient optimality criterion method for natural frequency constrained structures*, Comput. Struct. (1981) 14(5-6).

[15] R. V. Grandhi and V. B. Venkayya, *Structural optimization with frequency constraints*, AIAA. J. (1988) 26(7).

[16] R. Sedaghati, A. Suleman and B. Tabarrok, *Structural optimization with frequency constraintsusing the finite element force method*, AIAA. J. (2002) 40(2).

[17] R. Sedaghati, *Benchmark case studies in structural design optimization using the force method*, Int. J. Solids Struct. (2005) 42.

[18] L. Gang, R.-G. Zhou, L. Duan and W.-F. Chen, *Multiobjective and multilevel optimization for steel frames*, Eng. Struct. (1999) 21.
[19] M. M. Savković, R. R. Bulatović, M. M. Gašić, G. V. Pavlović and A. Z. Stepanović, *Optimization of the box section of the main girder of the single-girder bridge crane by applying biologically inspired algorithms*, Eng. Struct. (2017) 148.
[20] R. Falcone, C. Lima and E. Martinelli, *Soft computing techniques in structural and earthquake engineering:a literature review*, Eng. Struct. (2020) 207.
[21] S. Hanagud, A. Chattopadhyay and C. V. Smith, *Optimal design of a vibrating beam with coupled bending and torsion*, AIAA. J. (1987) 25(9).
[22] A. Obradović, S. Šalinić, D. R. Trifković, N. Zorić and Z. Stokić, *Free vibration of structures composed of rigid bodies and elastic beam segments*. J. Sound. Vib. (2015) 347.
[23] A. Obradović, S. Šalinić and A. Grbović, *Mass minimization of an Euler-Bernoulli beam with coupled bending and axial vibrations at prescribed fundamental frequency*, Eng. Struct. (2021) 228.
[24] A. Obradović, S. Šalinić and A. Tomović, *Free vibration of axially functionally graded Timoshenko cantilever beam with a large rigid body attached at its free end*, 8th Int. Serb. Con. on Theo. and App. Mech., Serbian Society of Mechanics, Kragujevac, Serbia T.1A.6 (2021)
[25] A. Obradović, S. Mitrović and N. Zorić, *Mass minimization of an AFG Timoshenko cantilever beam with a large body placed eccentrically at the beam end*, 8th Int. Serb. Con. on Theo. and App. Mech., Serbian Society of Mechanics, Kragujevac, Serbia M.2B.2 (2021)
[26] L. S. *Pontryagin*, V. G. Boltyanskii, R. V. Gamkrelidze, E. F. Mishchenko, *The mathematical theory of optimal processes*, New York: Interscience (1962).
[27] Wolfram Research Inc., *Mathematica, Version 12.0* (2019).

Self-organized bridge connecting THEORY to EXPERIMENTS*

Vladimir Skarka†
Laboratoire de Photonique d'Angers, EA 4464, Université d'Angers, 49045 Angers, France
Institute of Physics, University of Belgrade, 11000 Belgrade, Serbia
Marina Lekić ‡
Institute of Physics, University of Belgrade, 11000 Belgrade, Serbia

ABSTRACT

Laser tweezing stability is crucial for selective inactivation of viruses, bacteria, and cancer tissues preserving healthy cells in body water. However, laser beam propagates modifying the medium, simultaneously altering itself by feedback mechanisms, thus, jeopardizing the control. Using multidisciplinary synergy between theoretical, experimental, and numerical results, we demonstrate the feasibility of novel soliton-tweezers controlling nanoparticles in water suspensions. In soft matter like body water, suspended nanoparticles are aspirated inside the soliton-tweezers, if their refractive index is larger than the background one. They are expelled whenever their index is lower. In both case, the nonlinear density distribution of nanoparticles induces beam self-focusing that compensates self-defocusing effects, generating soliton-tweezer. Experimentally measured self-focusing and self-defocusing coefficients are incorporated in established novel synergetic soliton-tweezer complex intensity equation describing experiments realistically. Virus-nanoparticles with resonant frequencies higher than the one of soliton-tweezer would be possibly inactivated paraxially.

* This work has been supported by the Ministry of Education and Science of the Republic of Serbia, under Projects III 45016, OI 171038, and OI 171006. Najdan Aleksić, Vazha Berezhiani, and Stephan Rakotoarimalala are acknowledged for their contributions.
† e-mail address: vskarka@yahoo.com
‡ e-mail address: lekic@ipb.ac.rs

1. Introduction

First and second law of equilibrium thermodynamics are the foundations of physics. However, every action involves utilization, hence, loss of energy, but this is only a transformation to another energy. Macroscopic laser light, *i.e.*, electromagnetic wave is transformed into heat, *i.e.*, nanoscopic agitation of interacting atoms and molecules. Following the second low, interacting nanoparticles are trying to reach the thermodynamic equilibrium, which cannot be reached since the system cannot be isolated. However, this strong attraction to the equilibrium organizes the system, making it self-organized (harmonized). Following 1977 Nobel Prize winner Ilya Prigogine, nonlinear dissipative structures are self-organized far from thermodynamic equilibrium, due to the intake of energy and/or matter (mainly nanomatter) [1]. The self-organization is the compensation of antagonist effects. The fight and the collaboration of antagonist effects, *e.g.* yin and yang, are the universal principles of dialectic. Fortunately for us, in nature yin and yang mainly cooperate generating even the self-organized life. Living organisms are mainly composed of soft nanomatter including body cells, bacteria, viruses, and other nanoparticles in water suspensions. The total human body water volume estimated from simple anthropometric measurements is about 70% [2]. Healthy human body has ten times more bacteria than cells and countless viruses. Biomedia like blood, myosin, kinesin, ribosomes, liposomes, and varieties of living cells suspended in body water can be manipulated, tweezed, and controlled using laser beams and pulses [3-7]. The safety of any laser manipulation depends on good knowledge of its propagation in water with nanoparticles [8]. A laser beam propagates in nonlinear way through a nanosuspension modifying it. Doing this, beam is simultaneously altering itself by feedback mechanisms, thus, jeopardizing its control on nanoparticles [9]. The laser stability and robustness are of crucial importance for medical and biological applications *e.g.* photobiomodulations [7]. The laser dynamical stability and precision are of crucial importance, not only for brain

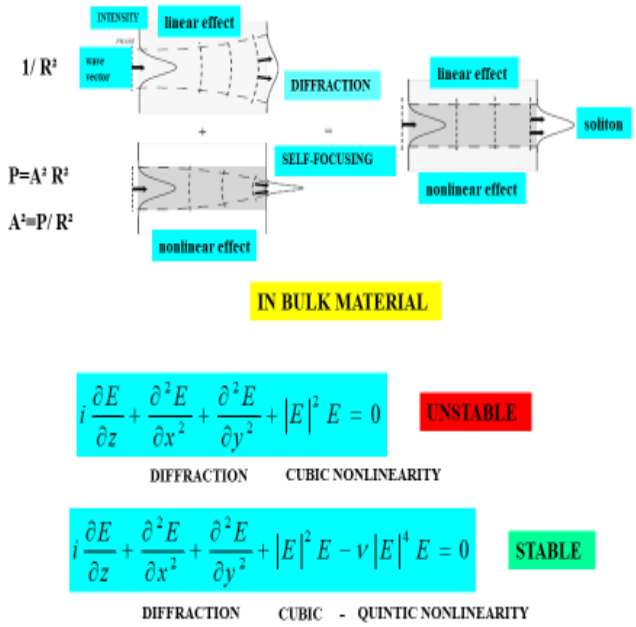

(1)

Figure 1 Self-collimated soliton becomes stable whenever the cubic self-focusing nonlinearity is compensating diffraction and quintic self-defocusing nonlinearity described by two-dimension saturating Schrödinger equation.

surgery but also for nondestructive medical diagnostics [10]. The very promising mechanism to achieve the necessary stability and control of nanoparticles is the self-organization of the laser light inside nanosuspensions into solitons localized in space and in time [11-17]. The laser beam becomes soliton whenever antagonist effects, *i.e.*, beam focusing and defocusing are balanced in self-organized dynamical equilibrium far from the thermodynamic one (cooperation of yin and yang) [18-20]. In any medium, including vacuum, laser beam is diffracting. In Kerr media, in rigid slab guides beam is confined into soliton, in the region with higher optical index of refraction due to the compensation of diffraction by cubic self-focusing (see Figure 1). Such a soliton is described by the one transverse dimension (1D) nonlinear Schrödinger equation (NLS) for electric field $E=A(r)\exp(ik_0n_0z)$ where A(r) is slowly varying amplitude envelop propagating following z

direction with wave vector k_0 and vacuum index of refraction n_0. However, 2D NLS is unstable in bulk media where both linear and nonlinear effects have the same width R dependence $1/R^2$ (see Figure 1). Indeed, initially dominating diffraction cannot be arrested by self-focusing, contrary to the 1D case where the focusing is proportional to 1/R. Therefore, amplitude decreases and soliton disappears. In opposite case, the self-focusing domination leads to increase of amplitude till the catastrophic collapse. To be stable, solitons need to be in Kerr media with quintic self-defocusing nonlinearity too. Such a reinforcement of yin, together with diffraction compensates self-focusing cubic nonlinearity self-generating a soliton described by saturable 2D NLS Eq. (1).

In contrast, the particularity of the laser propagation in soft matter is that the easily moving nanoparticles in fluid adapt their density distribution in such a way that the laser beam always propagates through the highest index of refraction. In experimental biophysics, 2018 Nobel Prize winner A. Ashkin used this property in order to tweeze bionanoparticles using lasers [3-5]. The high frequency pressure force of the laser field either attracts or repels suspended nanoparticles from the field region, depending if the nanoparticles optical index of refraction (n_p) is either larger or smaller than the background one (n_b). The tweezing laser beam collects paraxially, around its central axes, positively polarized nanoparticles having the index of refraction n_p higher than the background medium one ($n_p>n_b$). Therefore, such a redistribution of nanoparticles density following laser Gaussian intensity profile always induces the nonlinear beam self-focusing [3-5,8]. In opposite case beam is self-focusing too, taking into account that negatively polarized nanoparticles with lower index ($n_p< n_b$) are expelled from the beam. In both cases, the nanoparticles density modifications result in the nonlinear increase of effective index of refraction inside a tweezer making it always self-focusing and potentially collapsing [8,9]. Only solitons are stable and self-collimated due to the compensation of all self-defocusing effects by self-focusing in a self-created precarious guide corresponding to a dynamical equilibrium far from thermodynamic one.

In recent studies of the laser beam propagation in diluted noniteracting nanoparticles suspensions, the balance between the optical gradient force

and particles diffusion due to Brownian motion is achieved for long duration pulses [21]. For nanoparticles with positive polarizability ($n_p > n_b$) the nonlinear Schrödinger equation (NLSE) has exponentially growing nonlinearities that lead to a catastrophic collapse [21,22]. In real nanosuspensions the wave collapse cannot take place since nonlinear Rayleigh scattering losses grow dramatically with increase of nanoparticles concentration invalidating the diluted suspension model. To overcome these difficulties more realistic formalisms with particle-particle interactions were suggested [8,23-26]. In contrast to the positive polarizability, negatively polarized nanoparticles, having refractive index smaller than the background one ($n_p < n_b$), are expelled from the laser beam minimizing Rayleigh scattering losses. The corresponding nonlinearity in NLSE is saturable leading to the formation of stable self-trapped transversely localized beam, *i.e.*, spatial soliton [8,11-13, 18-20].

The usual approach to tweezing of nanoparticles in suspensions is to artificially focalize laser tweezer in order to trap few nanoparticles in its beam waist, *i.e.*, in a very small region where the beam is precariously self-collimated in a local dynamical equilibrium (see Refs. [3] and [4]). In contrast, in our innovating experiments, this tweezing self-collimation is extended paraxially along the entire beam in solitonic dynamical equilibrium, called soliton-tweezer. In this case, not only few nanoparticles but all nanoparticles are tweezed collectively. In order to establish soliton-tweezing of nanoparticles in body water, the prerequisites are synergetic multidisciplinary theoretical, numerical and experimental investigations of nanoparticles in pure water suspensions.

A very difficult task is to describe essentially nonlocal tweezing experiments measuring electric intensity I=EE, by a partial differential equation like NLSE that generally gives electric field E in one point in space and time. Therefore, in our innovating description of tweezing experiments in water suspensions of nanoparticles we introduce the nonlocality through the coupling between the heat equation and the generalized higher order NSL. Taking into account the estimated total body water volume of about 70%, the biosafety of any laser manipulation depends on good knowledge of solitons propagation in water with nanoparticles [2]. Consequently, our theoretical model in a multidisciplinary synergetic approach, needs confirmation by

experiments and numerical simulations as the prerequisite for safe medical and biological applications.

2. Nonlocal model of self-organized soliton-tweezers

Coupling light pressure and thermal self-action, we establish a nonlocal variational model of soliton-tweezers self-trapped propagation in nanoparticles suspensions. The soliton-tweezers self-organization and nonlinear guiding are investigated starting from the Helmholtz equation

$$\Delta\check{E} + k_0^2 n^2 \check{E} = 0 \qquad (2)$$

where $k_0=\omega/c$ is the wavevector and $\bar{E}$ is the amplitude of monochromatic electric field $\check{E}=\bar{E}(Z, r_\perp)$ *exp* (iωt)+cc denoting by cc complex conjugate [12,22,26]. The Laplasian $\Delta = \partial^2/\partial Z^2 + \nabla_\perp^2$ with the transverse one $\nabla_\perp^2 = \frac{\partial^2 E}{\partial x^2} + \frac{\partial^2 E}{\partial y^2}$ is associated to the field propagation variable Z and the transverse coordinate $r_\perp = \sqrt{x^2 + y^2}$. The complex medium effective index of refraction, n depends not only on refractive indices of background (n_b) and nanoparticles (n_p), but also on the volume filling factor $f=V_p\, dN_p/dV$, where N_p stands for the number of nanoparticles and $V_p=4\pi a^3/3$ is the volume of a spherical nanoparticle with radius a. The effective refractive index of composed medium reads $n = (1-f)n_b + fn_p$ [22]. Optical indices $n_b=n_{0b} + \delta n_b(J)$ and $n_p=n_{0p} + \delta n_p(J)$, as well as the filling factor $f=f_0 + \delta f(J)$ depend on the laser intensity $J=(cn_0/2\pi)|\bar{E}|^2$. Consequently, the effective index in Eq. (2) is also perturbed $n=n_0 + \delta n(J)$, where $n_0=(1-f_0)n_{0b} + f_0 n_{0p}$ and $\delta n=(n_{0p}-n_{0b})\delta f + (1-f_0)\delta n_b + f_0\delta n_p$. The filling factor reads $f=f_0$ *exp* $(-\beta|\bar{E}|^2)$ where $\beta=|\alpha|/4k_BT$ with temperature, T and k_B as Boltzmann constant [12,21]. The polarizability α of nanoparticles is given by $\alpha=3V_p n_b^2\xi/(4\pi)$ where $\xi=(n_{0p}^2 - n_{0b}^2)/(n_{0p}^2 + 2n_{0b}^2)$.

Importance of thermal nonlinear effects modifying laser beam dynamics in suspensions of nanoparticles is well recognized [22,27,28]. Indeed, the temperature of background liquid (*e.g.* body water) increases absorbing part of radiation energy, hence, the thermal nonlinearity of host medium can modify the nonlinear dynamics of soliton in a nonlocal way [17,29,30]. The electromagnetic laser waves induced temperature

change obeys the heat transport equation $C\partial\delta T/\partial t-\chi\Delta\delta T=\mu J$ where C is the heat capacity per unit volume, χ is the thermal conductivity, while the coefficient μ characterizes linear absorption losses due to the background liquid heating [17]. Such a heat transfer equation reduces to

$$\chi\Delta\delta T = -\mu J \tag{3}$$

under steady state conditions, *i.e.*, when temporal variation in laser intensity profile can be neglected [17,27]. Indeed, one of the main characteristics of solitons is their high temporal and spatial stability [11-13,18-20,31,32].

In order to elucidate experiments that have essentially a nonlocal character, we construct, starting from Eqs. (2)-(3), a novel nonlocal theoretical model of self-organized soliton-tweezers propagation in suspensions of nanoparticles. Assuming the electric field, $\bar{E}=\bar{A}(r_\perp)$ *exp* (ik_0n_0Z), the slowly varying envelop $\bar{A}(r_\perp)$ approximation is applied to both equations simultaneously. Using paraxial approximation, the following set of coupled nonlinear equations is obtained

$$i\frac{\partial\bar{E}}{\partial Z}+\frac{\nabla_\perp^2\bar{E}}{2k_0n_0}+k_0|n_{0p}-n_{0b}|f_0(1-e^{-\beta|\bar{E}|^2})\bar{E}-k_0(1-f_0)\left|\frac{\partial n_b}{\partial T}\right|\delta T\bar{E}=0 \tag{4}$$

and

$$\nabla_\perp^2\delta T=-\frac{cn_0\mu}{2\pi\chi}|\bar{E}|^2. \tag{5}$$

Besides the propagation and diffraction terms, in Eq. (4) appear the exponential focusing term as well as the defocusing one that insure the coupling with Eq. (5). In most of liquids, like body water, the thermal nonlinearity has a defocusing character $\partial n_b/\partial T<0$. Taking into account that nanoparticles are expelled from the laser beam, the Rayleigh scattering losses are neglected [8, 21]. Eqs. (4)-(5) are rewritten as

$$i\,\partial E/\partial z+\nabla_\perp^2E+(1-exp(-|E|^2))E-\Theta E=0 \tag{6}$$

and

$$\nabla_\perp^2\Theta=-K|E|^2=-K|I| \tag{7}$$

using dimensionless variables: the propagation and transverse coordinates $z=Zk_0|n_{0p}-n_{0b}|f_0$ and $r=(2k_0^2 n_0|n_{0p}-n_{0b}|f_0)^{1/2}r_\perp$, envelop electric field $E=\beta^{1/2}\bar{E}$, real intensity $|I|=|E|^2$, and generalized thermal index $\Theta=K_1(\delta T/T)$, with the coefficient $K_1=|n_{0p}-n_{0b}|^{-1}(f_0^{-1}-1)T|\partial n_b/\partial T|$ and the coupling parameter $K=K_1K_2$ where $K_2=\mu c n_0 k_B/(2\pi|\alpha|\chi k_0^2|n_{0p}-n_{0b}|f_0)$. The thermal conductivity of water at T=300 K˚ is χ=0.6071 K˚W/m and $\partial n_b/\partial T=-10^{-4}$ (K˚)$^{-1}$.

3. Nonlocal variational approach of soliton-tweezers

Starting from Eqs. (6)-(7) a novel nonlocal variational approach adapted to nonlocal experiments, is established [33,34]. The Lagrangian density corresponding to Eqs. (6)-(7) reads

$$L=\frac{i}{2}\left(\frac{\partial E^{cc}}{\partial z}E-\frac{\partial E}{\partial z}E^{cc}\right)+|\nabla_\perp E|^2-(|E|^2-1+exp[-|E|^2])-\frac{|\nabla_\perp\Theta|^2}{2K}+\Theta|E|^2 \tag{8}$$

The appropriate variations of Lagrangian, $\delta L/\delta E^{cc}=0$ and $\delta L/\delta\Theta=0$ yield Euler-Lagrange equations associated to Eqs. (6)-(7). Suitably chosen trial functions are optimized. For the laser field envelop the natural trial function is a Gaussian [8,16,18-20]

$$E=A(z)exp[-r^2/(2R(z)^2)+iC(z)r^2+i\Psi(z)], \tag{9}$$

where A, R, C, and Ψ are respectively amplitude, beam width, wave front curvature and phase [8,13,16,20]. The trial function for the nonlocal heat response of the medium reads

$$\Theta=B(z)\{Ei[-r^2/R_T(z)^2]-ln[r^2/d^2]\}, \tag{10}$$

where B is the amplitude and R_T is the width [33,34]. Here, *Ei* is the exponential integral function. The trial function Θ corresponds to radially-symmetric solution of Eq. (7) with zero boundary conditions on a circle of radius d>>R. The trial functions are substituted into Eqs. (6)-(7) and Lagrangian is averaged over radial coordinate

$$< L >= P\left[\frac{d\psi}{dz} + \left(\frac{dC}{dz} + 4C^2\right)R^2 + \frac{1}{R^2}\right] - PBln[\frac{d^2e^{\gamma}}{R^2+R_T^2}] - \frac{2\pi B^2}{K} ln[\frac{d^2e^{\gamma}}{2R_T^2}] + \pi R^2 G(A^2) \quad (11)$$

with the nonlinearity

$$\mathrm{G(A^2)} = \int_0^{\infty}(1 - \mathrm{A^2}exp[-\rho] - exp[-\mathrm{A^2}exp[-\rho]])\mathrm{d}\rho = ln[\mathrm{A^2}] - \mathrm{A^2} + \Gamma[0, \mathrm{A^2}] + \gamma, \quad (12)$$

where $\gamma \simeq 0.577216$ is Euler's constant, $\Gamma[s,w] = \int_w^{\infty} y^{s-1}exp(-y)dy$ is the incomplete gamma function, and $\rho = r^2/R^2$. The beam power is $P=\pi A^2R^2$. The following set of ordinary differential equations is obtained under the condition of zero variation with respect to each of unknown functions $Q=(A, B, R, R_T, C, \Psi)$ in trial functions, $\delta<L>/\delta Q=0$

$$dA/dz = -4\,A\,C, \quad (13)$$

$$C = 1/(4R)\,dR/dz, \quad (14)$$

$$\mathrm{d^2R/dz^2} = 4[1/\mathrm{R^3} + \mathrm{B}/2\mathrm{R} - 1/\mathrm{R}(\mathrm{G}/\mathrm{A^2} - G')] = \mathrm{F}, \quad (15)$$

$$\mathrm{d\Psi/dz} = -2/\mathrm{R^2} + \mathrm{G}/\mathrm{A^2} - 2G' + \mathrm{B}\,ln[2\mathrm{R^2}/(\mathrm{d^2}e^{\gamma+1/2})], \quad (16)$$

where $G' = \partial G(A^2)/\partial A^2$, along with two algebraic relations $B=KP/4\pi$, and $R_T = R$. The beam power conservation follows immediately from Eqs. (14)-(15). The generalized force, F is given by Eq. (15) [11]. To steady state solutions, $dA/dz=dR/dz=dC/dz=C=0$ of Eqs. (13)-(16) correspond soliton-tweezer widths $R_{\pm} = 2\left[A^2\sqrt{K}\sqrt{(G - G'A^2) \pm \sqrt{(G - G'A^2)^2 - \frac{KA^6}{2}}}\right]^{-1}$. This equation exists providing the coupling parameter $K<K_{cr}\approx 0.056$, as follows from expressions $G - A^2G' = -1 + exp[-A^2] + ln[A^2] + \Gamma[0, \mathrm{A^2}] + \gamma$ and $G' = -1 + (1 - exp[-A^2])/A^2$. The influence of thermal effects on the laser beam propagation depends on the value of the coupling parameter K that is very small [17,27]. The relation between power, P and amplitude, A, obtained solving Eqs. (13)-(15), is charted in Figure 2 for different small parameters K. Indeed, the influence of background heating is

present but small. Full curves correspond to stable steady state soliton-tweezer solutions, while the dotted ones stand for unstable solutions.

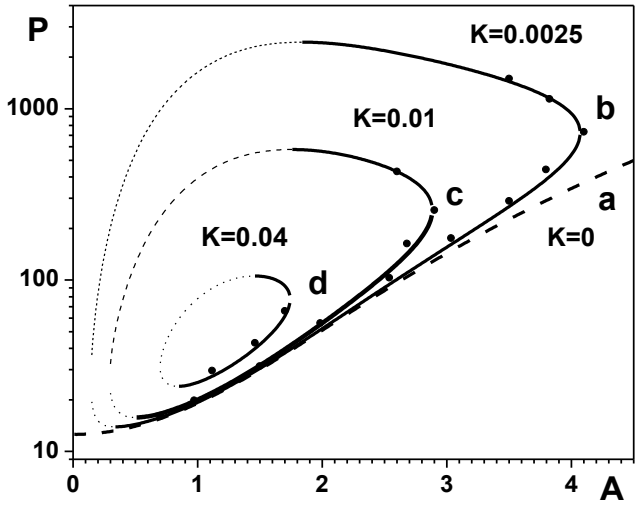

Figure 2 Power, P as a function of amplitude, A for various coupling parameters, K. For K=0 (dashed line) there are no heating effects. Full lines correspond to stable analytical solutions and dotted lines to unstable ones. Heavy dots are obtained by numerical simulations.

The soliton-tweezer stability is confirmed by numerical simulations represented by heavy dots in Figure 2. Without heating effects (K=0), the system of two coupled Eqs. (6)-(7) reduces to the one higher order NSLE corresponding to the Eq. (6) without coupling linear term. Such a case is charted in in Figure 2 by dashed strait line.

The potential, U, shown in Figure 3, is obtained integrating the generalized force F from Eq. (15)

$$U = -\int F(R)dR = \frac{2}{R^2} + \frac{2\pi R^2}{P}\left(\Gamma\left[0, \frac{P}{\pi R^2}\right] + ln\left[\frac{Pe^{\gamma}}{\pi R^2}\right]\right) - 2 - \frac{KP ln R^2}{4\pi}. \quad (17)$$

Using the analogy with a bullet in a potential well, a deeper physical understanding of "light bullet" dynamics around equilibrium width, R_{eq}, can be acquired [13,16,20]. Indeed, dynamically stable soliton-tweezers

are self-trapped in minima of U-potential well corresponding to the novel analytical stability criterion

$$\left(\frac{\partial^2 U}{\partial R^2}\right)_{R=R_{eq}} = \frac{8}{R^2}\left(\frac{2}{R^2} + \frac{KP}{8\pi} - \frac{\pi R^2}{P} + \left(1 + \frac{\pi R^2}{P}\right) exp\left[-\frac{P}{\pi R^2}\right]\right)_{R=R_{eq}} > 0 \,. \tag{18}$$

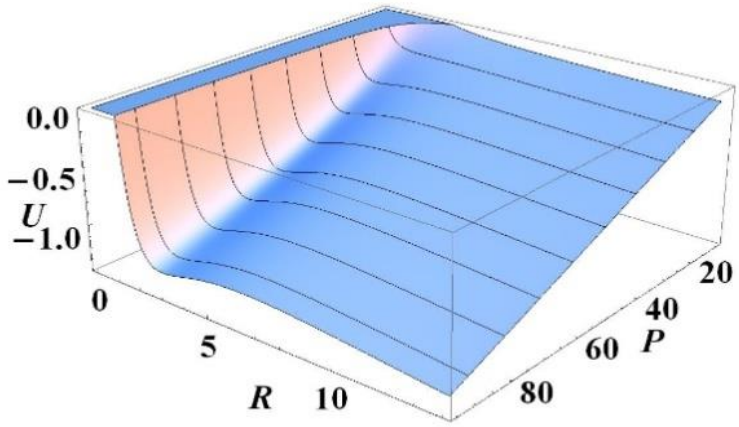

Figure 3 Stable steady state soliton-tweezer solutions are in the bottom of U-potential well for small widths, R, and self-trapping powers, P.

Therefore, the stable propagation of soliton-tweezer is analytically established for full line intervals of self-trapping in Figure 2 corresponding to the bottom of potential well in Figure 3.

In experiments only global self-focusing and self-defocusing effects are measured [32]. Therefore, the exponential of Eq. (6) is formally expanded and the dominating self-focusing cubic nonlinearity term is weighted by the coefficient σ that takes into account the formal sum of all smaller positive higher-order self-focusing terms in the expansion. Similarly, the dominating negative, self-defocusing quintic nonlinearity is weighted by the coefficient ν regrouping all smaller negative terms of higher order

$$i\,\partial E/\partial z + \nabla_{\perp}^{2}E + (\sigma|I| - \nu|I|^{2})E - \Theta E = 0. \qquad (19)$$

The established nonlocal variational model of self-organized soliton-tweezer propagation in nanosuspensions has to be confirmed by experiments.

4. Experimentally self-generated soliton-tweezers confirmed by numerical simulations

In order to establish soliton-tweezing of nanoparticles in body water, the prerequisites are synergetic multidisciplinary theoretical, numerical and experimental investigations of the suspension of nanoparticles in pure water [8,35-39]. Here we consider, as a representative example, the continuous laser interaction with negatively polarized nanoparticles ($n_b > n_p$) in pure water suspension. Without loss of generality, we investigate the self-organized propagation of a near infrared laser beam of wave length λ_0=727 nm in u-cuvette with 100 mL pure water suspension of 0.05 mg gold nanoshells. Such hybrids are surface plasmon resonant nanoparticles consisting of a nanoscale silica core surrounded by an ultra-thin gold shell [22,37,39,40]. In experiments we use gold nanoshells of 240 nm diameter that have a strong plasmon resonance at wave length λ_0=980 nm [37,41]. In laser light of lower wave length λ_0=727 nm, hence, higher frequency, these nanoparticles are negatively polarized [22]. Their capping agent is the polyethylene glycol (PEG) ligand that is covalently bound to the particles surface [37,42]. It is a safe polyether compound consisting of repeating units of ethylene oxide. The PEG is used as a stealth coating in biomedical applications in order to evade the body immune system and to reduce non-specific binding [37,42]. Its surface functionality disperses very well in water increasing biocompatibility for *in-vivo* and *in-vitro* toxicology experiments, radionanomedicine, nanobiodiagnostic, as well as photothermal applications [5,10,35,37-42]. Such a surface is very stable in buffers containing high salt concentrations found in culture media and body water like blood.

The established nonlocal variational model of soliton-tweezer self-trapped propagation controlling collectively tweezed nanoparticles in plasmonic suspensions is confirmed by experiments using appropriate

setup with Mira 900 laser of wavelength λ_0=727 nm in continuous regime. The spontaneous self-collimation of laser beam due to its self-trapped propagation in 20 cm long optically clear u-cuvette filled with pure water suspension of collectively tweezed gold nanoshells, is shown in Figure 4a. Corresponding camera captured output beam intensity profile is charted in Fig. 4b. The constant beam width during the propagation is the signature of stable soliton-tweezer self-trapping. Indeed, the beam width conservation implies the zero wave front curvature that is the main property of solitons [12,18,31,32]. In contrast to usual diffracting laser beams, the nonlinear soliton-tweezer is spontaneously self-collimated due to the compensation of self-defocusing by the self-focusing tweezing effect [8,13,16,18-20,31,32]. Therefore, experiments

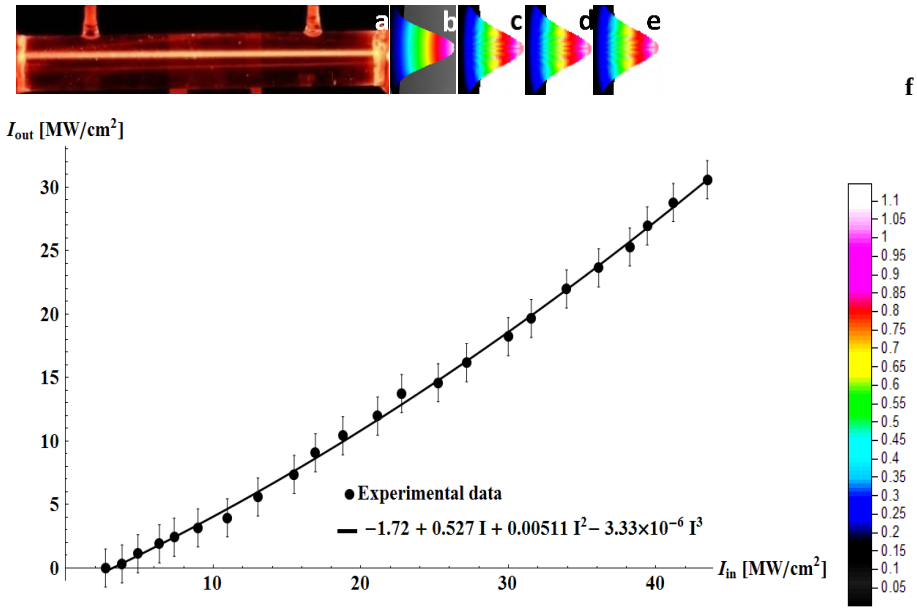

Figure 4 Matching of experimental and numerical results of soliton-tweezer propagation in u-cuvette of 20 cm. **a** Spontaneously self-trapped and self-collimated soliton-tweezer propagating through plasmonic suspension of collectively tweezed nanoshells. **f** Dots with uncertainty bars represent measured soliton-tweezer output intensities for increasing input intensities. In insert, their third order polynomial fit determines positive numerical values of coefficients **η** and **σ** in front of intensities I, and I^2 of Eq. (20), as well as the negative value of **ν** in front of I^3. **b** The soliton-tweezer output profile, camera captured in experiment, is matching numerical profiles that stay same after propagations of (**c**) z=1000, (**d**) z=20000, and (**e**) z=30000 arbitrary unit. The color scale is common.

confirm that soliton-tweezers stay in dynamical equilibrium in the bottom of the U-potential well in Figure 3, as predicted by the established analytical stability criterion, Eq. (18). Dots in Figure 4f correspond to measured values of output intensities, I_{out} as functions of gradually increasing input intensities, I_{in}. Their third order polynomial fit gives $\eta I + \sigma I^2 - \nu I^3$ with concrete values of coefficients in insert of Figure 4f. The quadratic intensity term, σI^2 corresponding to the concave part of curve for small intensities, is focusing, like the self-focusing term in usual nonlinear Schrödinger equation (NLSE) for electric field, E. The negative cubic intensity term, $-\nu I^3$ corresponding to the convex part of curve for big intensities, is defocusing, like the negative self-defocusing term in NLSE. The linear intensity term, ηI does not have a counterpart in ordinary local NLSE. It corresponds to the linear term in Eq. (19) that couple this equation with heat equation Eq. (7). As can be seen from Figure 2 the parameter K is very small. As a consequence, Eq. (7) can be formally integrated contributing a coefficient η to this coupling term in Eq. (19). Therefore, the nonlocal influence of the heat can be included in the linear term of Eq. (19) rewriting it as ηE in our model equation. Therefore, the coefficient η as well as coefficients σ and ν have to be determined from experiments by fitting measured input-output intensity $I=E^2$ curve, as in Figure 4f. Usually in theoretical approaches, laser electromagnetic wave is represented only by the electric field E, taking into account that the corresponding magnetic field is proportional to its complementary electric radiation E [6,12]. However, the experimental data force us to take into account intensity $I=E^2$ if we want to establish a realistic theoretical description of laser electromagnetic field that necessary includes complementary magnetic field. Indeed, the self-generation of laser electromagnetic light is the consequence of the universal principle of dialectic: the cooperation of electric (yang) and magnetic (yin) fields. As a consequence, rewritten Eq. (19) for complex electric field E is multiplied by the same E in order to model the experimentally measured complex intensity $I=E^2$, giving the synergetic soliton-tweezer equation

$$i\,\partial I/\partial z + \varepsilon\nabla_{\perp}^{2} I + \eta I + (\sigma|I| - \nu|I|^{2})I = 0. \qquad (20)$$

This equation model the influence of heat nonlocality, self-focusing, and self-defocusing in experiment, respectively, through the measured coefficient η, σ, and ν. Both experimental results and theoretical model

confirm the solitonic nature of soliton-tweezers. Consequently, self-focusing balances self-defocusing and diffraction, implying $\varepsilon = \sigma - \nu$. Therefore, the coefficient ε is also determined from the same experiment. This novel synergetic soliton-tweezer complex intensity equation (STCIE) establishes the missing bridge between nonlocal experiments and their direct theoretical description.

The output intensity profile after a propagation of z=1000 arbitrary units (a.u.), is obtained in Figure 4c as a numerical solution of STCIE with experimentally measured coupling, self-defocusing and tweezing self-focusing coefficients. It coincides with numerical profiles in Figures 4d and 4e after very long propagations of z=20000 a.u. and 30000 a.u. This is numerical confirmation of a spontaneous self-collimation of soliton-tweezer with conserved width. The striking similarity of experimental and numerical profiles in Figures 4b-4e helps to establish the feasibility and numerical predictability of soliton-tweezers based on the synergy of the multidisciplinary theoretical, experimental, and numerical approaches.

Soliton-tweezer robustness is also confirmed in Figures 5 by a stable behavior of its width, R, complex intensity, I, and power, P during a 30,000 a.u. long numerical evolution. The light breathing is the signature of soliton-tweezer dynamic stabilization in the bottom of U-potential well of Figure 3, through collective tweezing of nanoparticles that have inertia.

In order to see the beam profile in the center of u-cuvette of 20 cm, the same experiment is repeated with the u-cuvette of 10 cm. Obtained spontaneously self-collimated soliton-tweezer is camera captured in Figures 6a-6b. It has the same width as the one in Figs. 4a-4b. Numerical values of coefficients in Eq. (20) are extracted from the third order polynomial fit of experimentally obtained input-output dots in insert of Fig. 6f. STCIE with these values is solved numerically yielding identical soliton-tweezer output profiles after z=1000 a.u. (Figure 6c), z=20000 a.u. (Fig. 6d) and z=30000 a.u. (Fig. 6e) numerical propagations. These profiles are matching those of the 20 cm u-cuvette in Figures 4c-4e, although the fitting coefficients for STCIE in inserts of Figs. 4f and 6f are quite different. Essential is that both curves start as concave causing tweezing self-focusing with positive I^2 and finish as convex inducing self-defocusing with negative I^3, confirming the feasibility of soliton-tweezers.

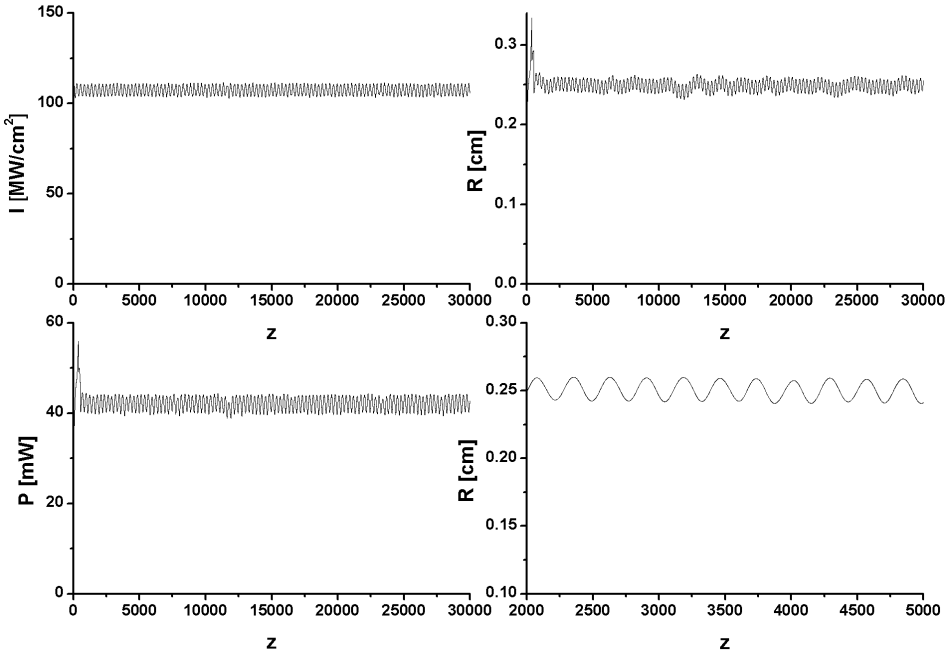

Figure 5. Numerical propagation of STCIE with fitting parameters of Figure 4f, during z=30,000 a.u. shows stable and robust regular breathing of soliton-tweezer complex intensity, **I** power, **P,** and beam width, **R** (with two different resolutions) in the dynamical equilibrium in the bottom of U-potential well of Figure 3.

Coefficients coming from insert of Figure 6f are introduced in STCIE in order to obtain stable numerical evolutions of width, R, complex intensity, I, and power, P during more than z=30,000 a.u. (see Figure 7). Their behavior

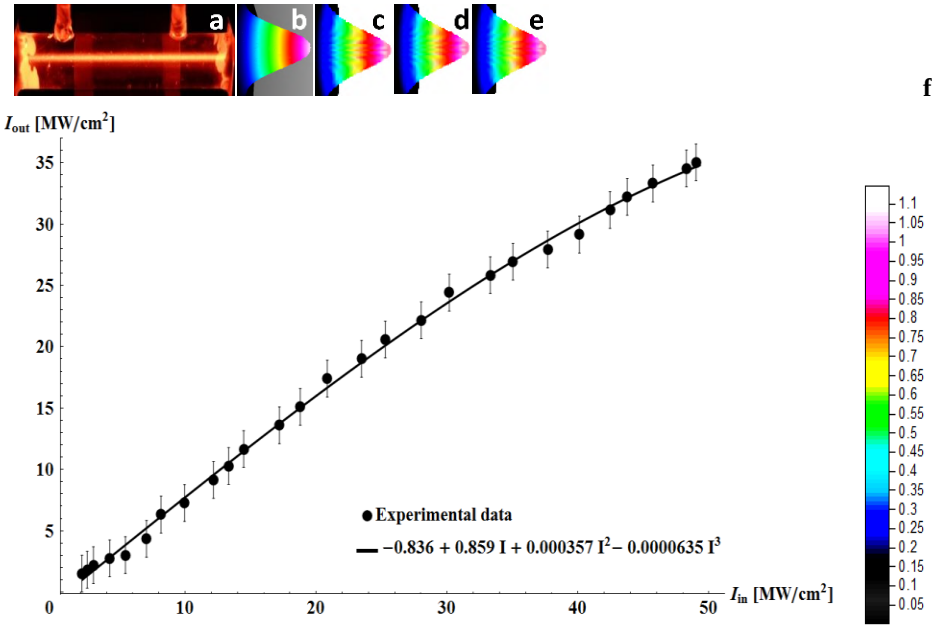

Figure 6 Spontaneously self-collimated propagation of soliton-tweezer in 10 cm u-cuvette. **a** The camera captured beam is the same as the one in 20 cm u-cuvette. **b** Its experimental output profile coincides with those obtained by numerical propagation of Eq. (20) after (**c**) z=1000, (**d**) z=20000, and (**e**) z=30000 a.u., as well as with those of Fig. 4a-4e. The color scale is common for both experiments. **f** Measured soliton-tweezer output intensities for increasing input ones are represented by dots with uncertainty bars. In insert, their third order polynomial fit gives numerical values of coefficients in front of linear and nonlinear intensities in Eq. (20).

is similar to the one in Figure 5, confirm robustness of soliton-tweezer and its predictability important for medical applications.

Therefore, identical experimental and numerical results of self-trapping in
both u-cuvettes and in theoretical model, charted in Figures 2-7, confirm the feasibility, stability, robustness, and predictability of soliton-tweezer controls of collectively tweezed nanoparticles in plasmonic suspensions.

Behavior of soliton-tweezer self-trapped in suspension of positively polarized nanoparticles is investigated using femtosecond laser of wavelength λ_0=1037 nm. In experiments we use gold nanoshells of 240 nm diameter that have a strong plasmon resonance at wave length λ_0=980

nm. Indeed, in laser light of higher wave length λ_0=1037 nm, these nanoparticles are positively polarized [22]. The experiment is of the same conception with the same cuvette of 10 cm as in previous experiments, but the soliton-tweezer is invisible at this wavelength. However, it is possible to investigate the

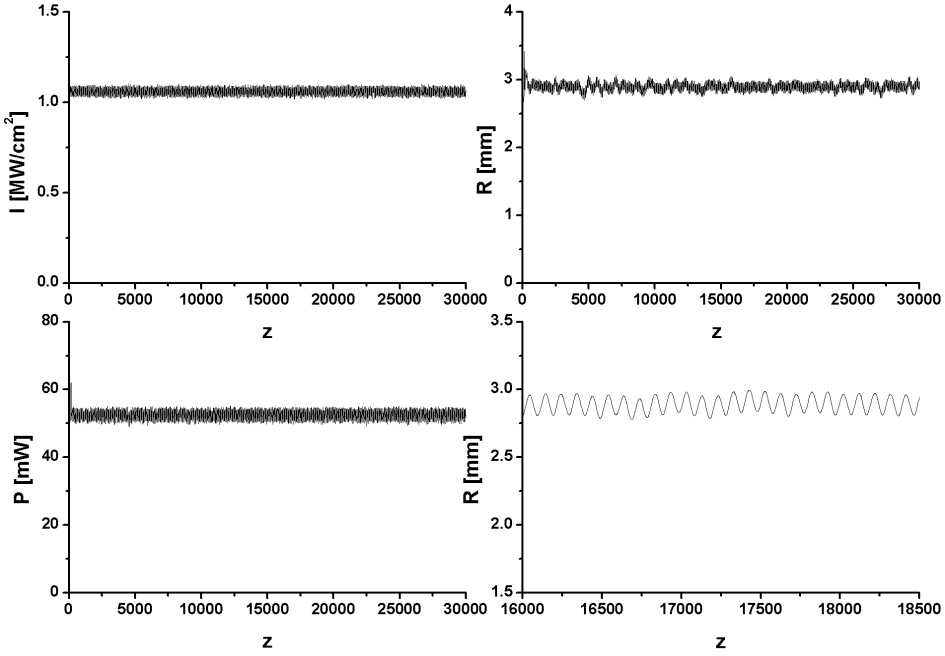

Figure 7. Soliton-tweezer stability in 10 cm cuvette is confirmed numerically. Numerical values of coefficients, obtained by fitting experimental data, are included in Eq. (20), in order to perform 30,000 steps long stable numerical propagation of complex intensity, **I**, power, **P**, and width, **R,** resulting in their conservation that confirm soliton-tweezer stability.

structure of soliton-tweezer and its propagation using our innovative approach. In Figure 8 are charted data of measured output complex intensities as function of increasing input intensities, in form of dots. Their third order polynomial fit gives $\eta I + \sigma I^2 - \nu I^3$ in inset of Figure 8 with concrete values of coefficients η, σ, and ν. As in previous examples, the positive sign of the quadratic self-focusing term implies that the first part of the curve for the smaller intensities is parabolic, *i.e.*, convex. The second part of the curve for higher intensities is concave due to negative sign of the cubic self-defocusing term. We see here the collaboration of

antagonist effects of self-focusing (yang) and self-defocusing (yin) that is responsible for the self-organization of stable soliton-tweezer in Figure 8. We have intention to investigate the universal character of convex-concave curves that appear in the increasing part of Gaussian and sinusoid too.

Obtained values of coefficients η, σ, and ν are introduced in our innovative STCIE, Eq. (20). This equation is then numerically propagated from z= 0 a.u. till z=90520 a.u. (see Figure 9). Such an exceptionally long propagation has for purpose to demonstrate the perfect stability and robustness of soliton-

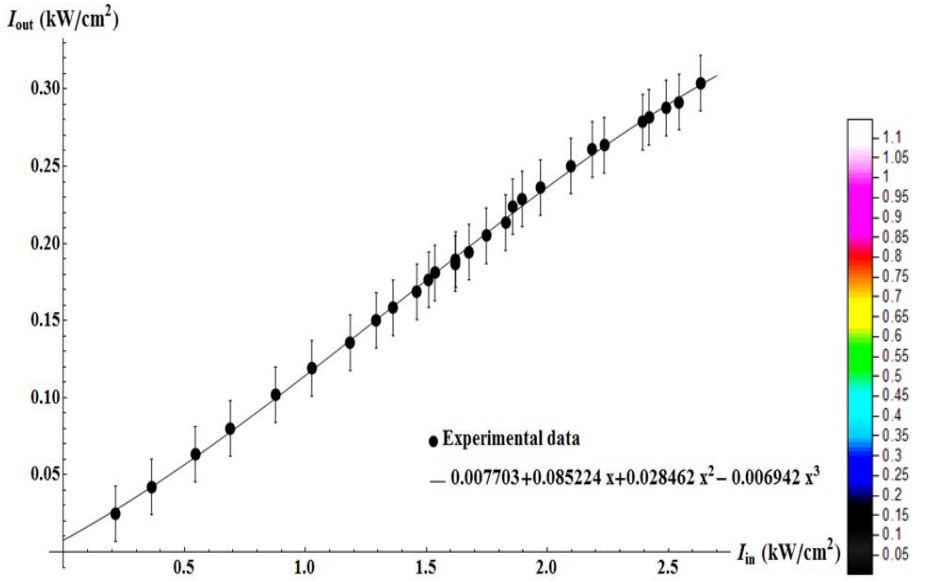

Figure 8 Soliton-tweezer self-trapped and self-collimated in suspension of positively polarized nanoparticles is investigated using femtosecond laser of wavelength λ_0=1037 nm. Heavy dots output intensities are charted in function of increasing input intensities.

tweezer. This is due to the compensation of all self-defocusing effects by self-focusing nonlinearity induced by collective modification of nanoshells density following the soliton-tweezer profile. This compensation in STCIE comes from the synergetic yin-yang self-cooperation of theory and experiments making the bridge between them. Although STCIE is local in space as any nonlinear partial differential equation, it includes, in its linear term, the essence of nonlocality through

the coefficient η that take formally into account the coupling with heat equation. The value of η comes from experimental measurements. Indeed, our synergetic STCIE is a hybrid equation with values of coefficient σ in self-focusing term and coefficient ν in self-defocusing term, come directly from the measurements too. In such a way, a realistic theoretical description of the experiment is established for the first time.

The stability and robustness as well as the predictability are demonstrated in figure 10 where the soliton-tweezer intensity, I, power, P, and width, R are constant. Nearly imperceptible breathing of intensity is seen in Figure 10 only with very big resolution of 30 a.u. This breathing appears in Figure 9 as the transformation of dome soliton-tweezer into millstone one.

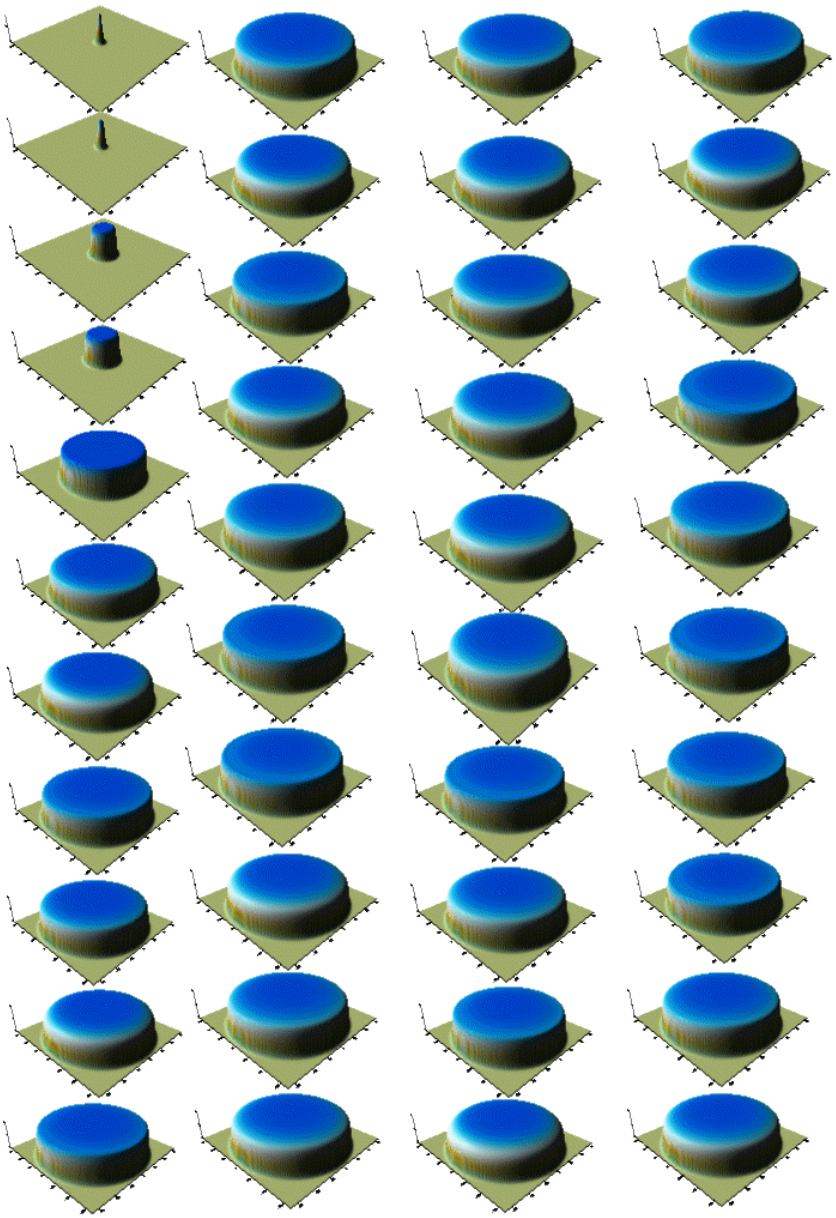

Figure 9 Exceptionally long numerical propagation of STCIE with fitting parameters of Figure 8, charted for z=0, 20, , 40, 50, 100, 300, 400, 430, 440, 450, 460, 1600, 1750, 2690, 2700, 2710, 3250, 5000, 8000, 10000, 15000, 16900, 17370, 17880, 18120, 18400, 18420, 21280,21800, 24450, 27000, 32550, 33000, 46400, 49960, 60500, 90510, and z=90,520 a.u. shows stable and robust regular breathing of soliton-tweezer consisting of the change of its shape from millstone to dome and vice versa.

5. Conclusions

As demonstrated, the self-trapped and self-collimated soliton-tweezer is perfectly stable in water suspensions of both positively and negatively polarized nanoparticles. Therefore, we established the feasibility of self-organized soliton-tweezers controlling collectively nanoshells in water suspension using multidisciplinary theoretical, experimental, and numerical results obtained synergistically. The stability, predictability and robustness of soliton-tweezers suggest the possibility of safe medical applications, *e.g.*

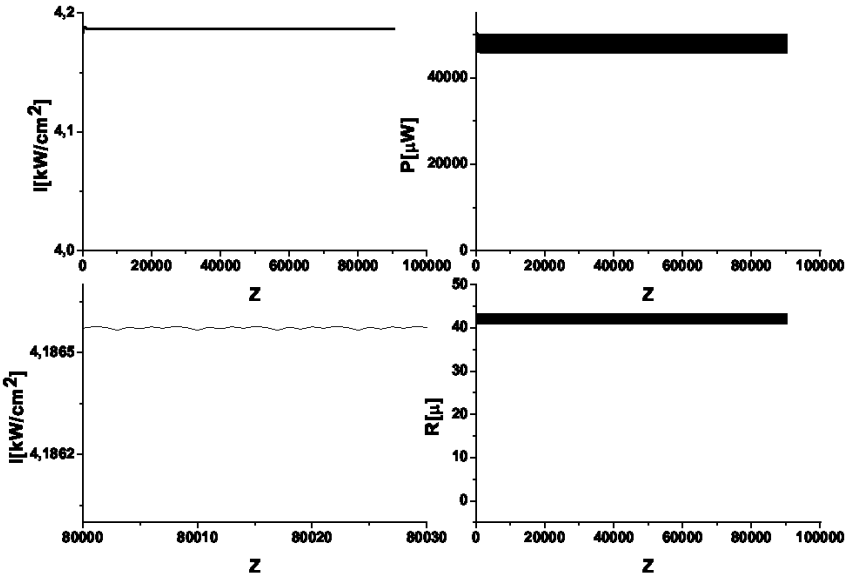

Figure 10 Numerical propagation of STCIE with fitting parameters of Figure 4f, during z=30,000 a.u. shows stable and robust regular breathing of soliton-tweezer complex intensity, **I** power, **P,** and beam width, **R** (with two different resolutions) in the dynamical equilibrium in the bottom of U-potential well of Figure 3.

selective inactivation of viruses, bacteria or cancer cells in body water without damaging healthy tissues [4,10,35-41,43,44]. Indeed, an efficient and safe inactivation of human coronaviruses by far-UVC light (222 nm) is recently demonstrated [45]. The fact that both golden nanoshells and

viruses, despite their fundamental difference, belong to the same category of nanoparticles due to their similar size, encourage us to suggest experimental studies on the possibility to inactivate SARS-CoV-2 in blood using our novel soliton-tweezers. Indeed, the presence of SARS-CoV-2 was detected recently in human blood [46]. The size of nanoparticles determines the plasmon resonance frequencies that are crucial for efficient applications of soliton-tweezers. The glycoprotein membrane of SARS-CoV-2 is rich of electric dipoles susceptible to generate some surface resonances [48,49]. In soliton-tweezer field, all nanoparticles, including virus-nanoparticles, with higher resonant frequency than laser one, behave as positively polarized as in Figures 8-10. In contrary, if their resonant frequency is lower than soliton-tweezer one, they are effectively negatively polarized as in Figures 4-7. If SARS-CoV-2 in blood filling u-cuvette is positively polarized, it would be squeezed paraxially in a soliton-tweezer. Consequently, it may be supposed that in the central part of soliton-tweezer field, viruses would be inactivated suffering simultaneously enhanced heat and resonant vibrations, [43-45]. The inactivation temperature of about 60°C can be easily achieved increasing the soliton-tweezer intensity (see Figures 4-10). Therefore, we suggest to incorporate our u-cuvette in *extracorporeal membrane oxygenation system* (ECMOS) used for medical treatment of SARS-CoV-2 by blood extraction from human body in order to provide input of oxygen and output of carbon dioxide. In order to collect all such positively polarized SARS-CoV-2, the soliton-tweezer width has to be enlarged in order to match the radius of redesigned u-cuvettes in ECMOS. Negatively polarized viruses are expelled out of beam and may be stick on the u-cuvette wall by monoclonal antibodies that have the high level capacity to bind them [47-49]. In such a way viruses are mechanically removed from the blood without need of their inactivation. SARS-CoV and MERS-CoV monoclonal antibodies can be used for binding SARS-CoV-2 in absence of specific antibodies [48,49]. Taking into account that the blood processing in ECMOS is in vitro, *i.e.*, out of human body, easily produced mouse monoclonal antibodies can be used too for binding SARS-CoV-2 without danger of inducing body immunologic reactions [47-49].

We stress that it is not necessary to know the resonant frequencies of SARS-CoV-2 in order to purify the blood efficiently. Indeed, viruses with resonant frequencies higher than the frequency of soliton-tweezer

are attracted toward its central axe and inactivated there by high intensity, heat, and vibrations [43-45]. Simultaneously, viruses with resonant frequencies lower than soliton-tweezer one, are expelled toward the wall where they stay bind by monoclonal antibodies [47-49]. Notice that viruses with the refracting index larger that blood one, are negatively polarized if their resonant frequency is below soliton-tweezer one [22].

Resonant frequencies of viruses, related to their small size, are much higher than those of other nanoparticles in body water [43-49]. This is crucial for selective and secure medical applications. In contrast to the Kerr solitons generated above an intensity threshold, soliton-tweezers always control nanoparticles concentration independently of their intensity [8,13,18]. The lack of the threshold allows use of very low intensity soliton-tweezers that do not affect other nanoparticles in blood increasing safety in medical applications [45]. However, thorough experimental studies involving SARS-CoV-2 are needed in order to confirm our hypothesis.

Soliton-tweezers exist in nature in the form of vortices as e.g. tornado. This violent meteorological event is tweezing air and water nanoparticles, hence, can be modeled as soliton–tweezer. Indeed, we generated, for the first time up to our knowledge, a self-trapped vortex soliton-tweezer in 65 cm air column, using simultaneously red, blue, and green lasers. Such a multicolor combination of lasers gives a novel white spot. Tornado and laboratory soliton-tweezer are both big solitary waves that may be considered as concrete examples of rotating rogue waves (see Figure 11). The similarity of camera captions of tornado and our soliton-tweezer encourage us to suggest safe experimental studies of tornado on the model of laboratory soliton-tweezer.

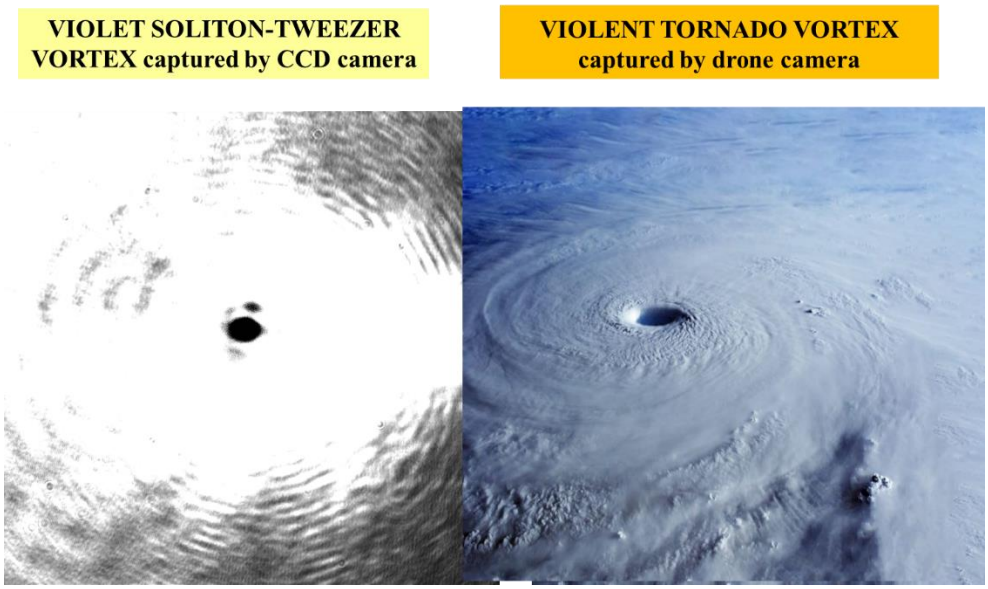

Figure 11 Vortex soliton-tweezer is realized in 65 cm of air using red, green, and blue lasers simultaneously, giving white spot. It is similar to the tornado captured by drone camera.

In conclusion, the innovative is threefold in establishing direct multidisciplinary synergetic bridge between theory and experiments via numerical simulations. 1. We established an original theoretical model of self-trapping of soliton-tweezers in suspensions of nanoparticles by extending variational approach to nonlocal systems. 2. Soliton gradient forces tweeze nanoparticles collectively inducing density gradient that produces, in turn, self-focusing and self-trapping of soliton-tweezer in a stable dynamical equilibrium that we realized experimentally in very long cuvettes. 3. Using synergy between our experimental and theoretical results, we established a direct description of soliton-tweezer self-trapping by an innovating partial differential equation for complex intensity that includes experimentally measured coefficients. Numerical simulations of this equation together with self-collimation experiments confirm feasibility, stability, robustness, and predictability of soliton-tweezers.

References

[1] G. Nicolis and I. Prigogine, *Self-organization in Nonequilibrium Systems* Wiley: New York 1977.

[2] P. E. Watson, I. D. Watson and R. D. Batt, *Am. J. Clin. Nutr.* **33** (1980) 27.
[3] A. Ashkin, *Phys. Rev. Lett.* **24** (1970) 156.
[4] A. Ashkin, J. M. Dziedzic and P. W. *Opt. Lett*. **7** (1982) 276.
[5] A. Ashkin *et al*. *Nature* **348** (1990) 346.
[6] N. N. Akhmediev, A. Ankiewicz, *Dissipative Solitons: From Optics to Biology and Medicine, Lect. Notes Phys*. 751 Springer-Verlag: Berlin, 2008.
[7] L. Santana-Blank *et al*. *Water as a Photoacceptor, Energy Transducer, and Rechargeable Electrolytic Bio-battery in Photobiomodulation*. In *Handbook of Low-Level Laser Therapy*, (2017) 119.
[8] V. Skarka *et al. Opt. Express* **25** (2017) 10090.
[9] R. El-Ganainy *et al. Opt. Express* **15** (2007) 10207.
[10] G. R. Schweinsberger *et al*. *Lasers Surg. Med*. **43** (2011) 443.
[11] C. Conti, G. Ruocco and S. Trillo, *Phys. Rev. Lett.* **95** (2005) 183902.
[12] Y. S. Kivshar and G. P. Agrawal, *Optical Solitons: From Fibers to Photonic Crystals*; Academic Press: San Diego, 2003.
[13] V. Skarka and N. B. Aleksić, *Phys. Rev. Lett*. (2006) 0139031.
[14] Z. Chen, M. Segev and D. N. Christodoulides, *Rep. Prog. Phys.* **75** (2012) 086401.
[15] F. T. Arecchi, S. Boccaletti and P. L. Ramazza, *Phys. Rep*. **318** (1999) 1.
[16] V. Skarka *et al*. *Phys. Rev. Lett.* **105** (2010) 213901.
[17] R. W. Boyd, *Nonlinear Optics*; Academic Press: San Diego, 1992.
[18] V. Skarka, V. I. Berezhiani and R. Miklaszewski, *Phys. Rev. E***56** (1997) 1080.
[19] V. Skarka, V. I. Berezhiani and R. Miklaszewski, *Phys. Rev. E***59** (1999) 1270.
[20] V. Skarka *et al. Phys. Rev. A***90** (2014) 023845.
[21] R. El-Ganainy *et al. Opt. Express* **15** (2007) 10207.
[22] S. Fardad *et al*. *Nano Lett*. **14** (2014) 2498.
[23] M. Matuszewski, W. Krolikowski and Y. S. Kivshar, *Opt. Express* **16** (2008) 1371.
[24] M. Matuszewski, W. Krolikowski and Y. S. Kivshar, *Phys. Rev. A***79** (2009) 023814.
[25] R. El-Ganainy *et al. Phys. Rev. A***80** (2009) 053805.

[26] R. Gordon and J. T. Blakely, *Phys. Rev*. *A***75** (2007) 055801.

[27] S. A. Akhmanov *et al. IEEE J. Quantum Elect*. **4** (1968) 568.
[28] Y. Lamhot, A. Barak, O. Peleg and M. Segev, *Phys. Rev. Lett.* **105** (2010) 163906.
[29] C. F. Bohren and D. R. Huffman, *Absorption and Scattering of Light by Small Particles* Wiley: New York 1983.
[30] A. I. Yakimenko, V. M. Lashkin and O. O. Prikhodko, *Phys. Rev*. *E***73** (2006) 066605.
[31] E. L. Falcao-Filho, C. B. de Araujo, G. Boudebs, H. Leblond and V. Skarka, *Phys. Rev. Lett.* **110** (2013) 0139011.
[32] V. Skarka, M. M. Lekić, A. G. Kovačević, B. Zarkov and N. Ž. Romčević, *Opt. Quant. Electron*. **50** (2018) 37.
[33] N. B. Aleksić, N. B. Petrović, M. S. Strinić and M. R. Belić, *Phys. Rev. A***85** (2015) 043832.
[34] B. N. Aleksić, N. B. Aleksić, N. B. Petrović, M. S. Strinić and M. R. Belić, *Opt. Express* **22** (2014) 31842.
[35] G. Makey *et al. Nat. Phys.* **4,** (2020) 1.
[36] C. N. Likos, *Phys. Reps.* **348** (2001) 267.
[37] A. S. Schwartz-Duval *et al. Nat Commun* **11** (2020) 4530.
[38] Kai Yang *et al. Adv. Mater*. **24** (2012) 1868.
[39] R. S. Riley and E. S. Day**,** *WIREs Nanomed Nanobiotechnol* **9** (2017) 1449.
[40] R. A. Sperling *et al. Chem. Soc. Rev.* **37** (2008) 1896.
[41] Minho Kim, Jung-Hoon Lee and Jwa-Min Nam, *Science* **6** (2019) 17.
[42] Jiang Wu *et al. J. Mater. Chem. B* **2** (2014) 2983.
[43] A. R. Singh, A. Košmrlj and R. Bruinsma *Phys. Rev. Lett.* **124** (2020) 158101.
[44] Szu-Chi Yang *et al. Sci. Rep.* **5** (2016) 18030.
[45] M. Buonanno *et al. Sci. Rep.* **10** (2020) 10285.
[46] Wenling Wang *et al. JAMA.* **10** (2020) 10285.
[47] R. G. H. Cotton and C. Milstein, *Nature* **244** (1973) 42.
[48] Lingshu Wang, *Journal of Virology* **92** (2018) e02002.
[49] S. Balamurugan, S. Konlavat, W. Kittikhun and P. Waranyoo, *Asian Pac J Allergy Immunol*. **38** (2020) 10.

W-potentials in nonlinear biophysics of microtubules

Slobodan Zdravković[*]
Institut za Nuklearne Nauke Vinča, Laboratorija za Atomsku Fiziku
(040), 11001 Beograd, Serbia

Dragana Ranković[†]
Farmaceutski fakultet, Univerzitet u Beogradu, 11221 Beograd, Serbia

ABSTRACT

In the present article we investigate the nonlinear dynamics of microtubules, the basic components of the eukaryotic cytoskeleton, and rely on the known general model. A crucial interaction among constitutive particles is modelled using W-potential. Three kinds of this potential are studied, symmetrical and two non-symmetrical. We demonstrate an advantage of the latter ones.

1. Introduction

There are two kinds of cells. These are eukaryotic, having a membrane-bound nucleus, and much simpler prokaryotic cells, without the nucleus. In the eukaryotes, an intracellular protein filament network exists. Microtubules (MTs), studied in this article, are the basic components of this cytoskeleton. They play essential roles in the shaping and maintenance of cells and in cell division. Also, MTs represent a traffic network for motor proteins moving along them.

Information about their structure and function can be found in many references [1-3]. Here, we mention some basic pieces of information only. MT is a long hollow cylinder spreading between the nucleus and cell membrane. Its surface is usually formed of 13 long structures called protofilaments (PFs), representing a series of heterodimers, as shown in Fig. 1. A key point is that the heterodimer, or dimer for short, is an electric dipole. This means that MT behaves as ferroelectric [4], which is

[*] e-mail address: szdjidji@vin.bg.ac.rs
[†] e-mail address: dragana.rankovic@pharmacy.bg.ac.rs

crucial for many models of MTs. In this paper, we rely on the so-called general model (GM) [5].

The lengths of MTs vary from a few hundred nanometers up to meters in long nerve axons [6]. For most of the models, a dimer is a constitutive unit, which means that its internal structure is not taken into consideration. Its mass and length are $m = 1.8\times10^{-22}$kg [4] and $l = 8$nm [4,7,8], respectively. The longitudinal, tangential, and radial components of the electric dipole moment are $p_z = 1.13\times10^{-27}$Cm, $p_\theta = 0.66\times10^{-27}$Cm, and $p_r = -5.57\times10^{-27}$Cm, respectively [9]. Hence, p_z is in the direction of MT.

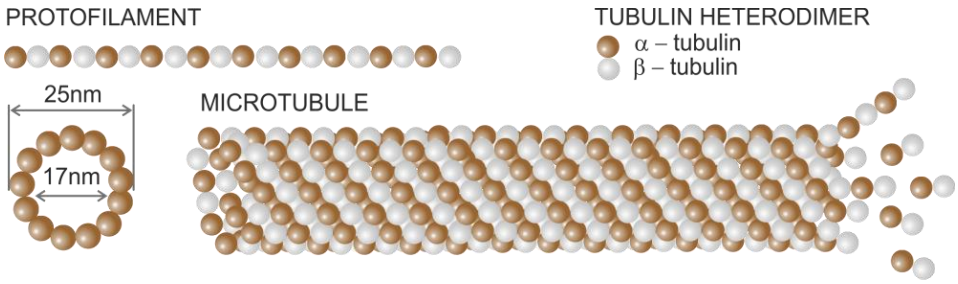

Fig. 1. Microtubule

In Section 2, we very briefly explain the used model. For one of the interactions between the dimers, we use W-potential energy, or potential for short. We study three types of them and obtain three dynamic equations of motion. These are crucial equations, solved in Section 3, while Section 4 is devoted to some concluding remarks.

2. W-potential within the general model of MTs

It was mentioned above that MT behaves like a ferroelectrics. Based on this fact is the first model [4] in a series of models describing MT nonlinear dynamics. As the used coordinate is a longitudinal one, the model belongs to the group of longitudinal models, as well as its improved ancestor [10]. There are a few degrees of freedom for each dimer, but the essential is the angular one. Hence, angular models

represent a crucial group of models describing MT dynamics. The first in this series is the so-called φ-model [11], a perhaps somewhat naive but rather important step in the evolution of the models. The next one is the general model (GM), mentioned above [5], which we rely on in this paper. We conclude the series with the model introduced recently [12]. This two-component angular model has been under active investigation and is not relevant for this work.

A starting point for all these models is Hamiltonian. For GM, it is [5]

$$H = \sum_n \left[\frac{I}{2} \dot{\varphi}_n^{\,2} + \frac{k}{2} \left(\varphi_{n+1} - \varphi_n \right)^2 + W(\varphi_n) - pE \cos \varphi_n \right], \tag{1}$$

where I is a moment of inertia of the single dimer, k is an inter-dimer stiffness parameter, $E > 0$ is the intrinsic electric field, and $p > 0$ stands for electric dipole moment. Notice that E is the internal electric field, which means that a particular dimer exists in the field of all other dimers. The angle φ_n describes the dimer`s oscillation and *n* is its position. We recognize the kinetic and potential energies of the interaction of the two neighbouring dimers belonging to the same PF. A term $W(\varphi)$ represents the interaction of a single dimer with all other ones that do not belong to the same PF. It is called W-potential as it looks like a letter W, which will be clear later on. The very last term is coming from the fact that the electric dipole is in the field of all other ones. For this paper, the most important is the W-potential. We study the following three cases:

Case 1. W-potential is a symmetric function:

$$W_1 = -\frac{A}{2} \varphi_n^{\,2} + \frac{B}{4} \varphi_n^{\,4}, \quad A > 0, \quad B > 0. \tag{2}$$

Case 2. W-potential is a non-symmetric function:

$$W_2 = -\frac{A}{2} \varphi_n^{\,2} + \frac{B}{4} \varphi_n^{\,4} - C \varphi_n. \tag{3}$$

Case 3. W-potential is a non-symmetric function:

$$W_3 = -\frac{A}{2}\varphi_n{}^2 + \frac{B}{4}\varphi_n{}^4 - \frac{D}{3}\varphi_n{}^3 . \tag{4}$$

We use Hamilton's dynamical equation $I\ddot{\varphi}_n = -\partial H/\partial\varphi_n$, a continuum approximation $\varphi_n(t) \Rightarrow \varphi(x,t)$, series expansion of the cosine term, as well as $\varphi_{n\pm1} \Rightarrow \varphi \pm \frac{\partial\varphi}{\partial x}l + \frac{1}{2}\frac{\partial^2\varphi}{\partial x^2}l^2$ [10], and obtain the following dynamical equations of motion:

Case 1.

$$I\frac{\partial^2\varphi}{\partial t^2} - kl^2\frac{\partial^2\varphi}{\partial x^2} - (A - pE)\varphi + \left(B - \frac{pE}{6}\right)\varphi^3 + \Gamma\frac{\partial\varphi}{\partial t} = 0 , \tag{5}$$

Case 2.

$$I\frac{\partial^2\varphi}{\partial t^2} - kl^2\frac{\partial^2\varphi}{\partial x^2} - (A - pE)\varphi + \left(B - \frac{pE}{6}\right)\varphi^3 - C + \Gamma\frac{\partial\varphi}{\partial t} = 0 , \tag{6}$$

Case 3.

$$I\frac{\partial^2\varphi}{\partial t^2} - kl^2\frac{\partial^2\varphi}{\partial x^2} - (A - pE)\varphi + \left(B - \frac{pE}{6}\right)\varphi^3 - D\varphi^2 + \Gamma\frac{\partial\varphi}{\partial t} = 0 , \tag{7}$$

where Γ is a viscosity parameter. Hence, we obtained partial differential equations. It is well known that, for a given wave equation, a travelling wave $\varphi(\xi)$ is a solution that depends upon x and t only through a unified variable

$$\xi = \kappa x - \omega t , \tag{8}$$

where κ and ω are constants. According to Eqs. (5)-(8), we straightforwardly obtain ordinary differential equations (ODE):

Case 1. $$\alpha\psi'' - \rho\psi' - \psi + \psi^3 = 0 , \tag{9}$$

Case 2. $$\alpha\psi'' - \rho\psi' - \psi + \psi^3 - \sigma = 0, \tag{10}$$

Case 3. $$\alpha\psi'' - \rho\psi' - \psi + \psi^3 - \delta\psi^2 = 0, \tag{11}$$

where,

$$\varphi = \sqrt{\frac{A - pE}{B - pE/6}}\,\psi \equiv K\psi, \quad \alpha = \frac{I\omega^2 - kl^2\kappa^2}{A - pE}, \quad \rho = \frac{\Gamma\omega}{A - pE}, \tag{12}$$

$$\sigma = \frac{C}{K(A - pE)}, \qquad \delta = \frac{D}{\sqrt{(A - pE)\left(B - \frac{pE}{6}\right)}}, \tag{13}$$

and $\varphi' \equiv \mathrm{d}\varphi/\mathrm{d}\xi$. Experimental values of the involved parameters do not exist but our estimations strongly suggest $A > pE$ and $B > pE/6$ [5], which was used above.

Let us point out the great importance of the parameter α. From Eqs. (1), (5)-(7), and (12), we conclude that its negative sign means that the elastic term is larger than the inertial one, and vice versa. Also, Eq. (12) can be written as

$$\alpha = \frac{I\omega^2 - kl^2\kappa^2}{A - pE} = \frac{I\kappa^2(\omega^2/\kappa^2 - kl^2/I)}{A - pE} \equiv \frac{I\kappa^2(v^2 - c^2)}{A - pE}, \tag{14}$$

where v is the velocity of the solitary wave, while c is the speed of sound. This means that the sign of α shows if the wave is subsonic or supersonic.

3. Solutions of equations (9) – (11)

There are many mathematical procedures for solving Eqs. (9)-(11). One of the simplest is a procedure that we call the tangent hyperbolic function method (THFM). According to THFM, we expect the solution ψ as [13]

$$\psi = a_0 + \sum_{i=1}^{M} \left(a_i \Phi^i + b_i \Phi^{-i} \right), \tag{15}$$

where Φ is the solution of the well-known Riccati equation

$$\Phi' = b + \Phi^2, \tag{16}$$

and the parameters a_0, a_i, b_i, and b should be determined. A solution of Eq. (16) depends on b [10,13]. The one having physical sense is

$$\Phi = -\sqrt{-b} \tanh\left(\sqrt{-b} \xi \right), \tag{17}$$

which holds for $b < 0$. The highest exponents are Φ^{M+2} and Φ^{3M}, coming from ψ'' and ψ^3, respectively. This means that $M = 1$ in Eq. (15). Also, we set $b_i = 0$ because we are not interested in diverging solutions in this work, and Eq. (15) becomes.

$$\psi = a_0 + a\Phi. \tag{18}$$

According to Eqs. (9)-(11), (16), and (18), we obtain the expression

$$K_3 \Phi^3 + K_3' \Phi^{-3} + K_2 \Phi^2 + K_2' \Phi^{-2} + K_1 \Phi + K_1' \Phi^{-1} + K_0 = 0, \tag{19}$$

which is satisfied if all the coefficients K_i are simultaneously equal to zero. Of course, for $b_1 = 0$, the system is simplified. In what follows, we solve ODEs for all three cases, i.e., Eqs. (9)-(11).

Case 1.

This case was solved in Ref. [5], where the model we rely on was introduced. Using Mathematica, we easily obtain the following two solutions:

$$a_0^{(\pm)} = \pm \frac{1}{2}, \quad a^{(\pm)} = \pm \frac{2\rho}{3}, \quad b = -\frac{9}{16\rho^2}, \quad \alpha = -\frac{2\rho^2}{9}, \tag{20}$$

which yields

$$\psi_1^{(\pm)} = \pm\frac{1}{2}\left[1-\tanh\left(\frac{3}{4\rho}\xi\right)\right]. \tag{21}$$

The functions $\psi_1^{(+)}$ and $\psi_1^{(-)}$ are kink and antikink solitons, respectively, or kinks for short. They are shown in Fig. 2 for $\rho = 1$.

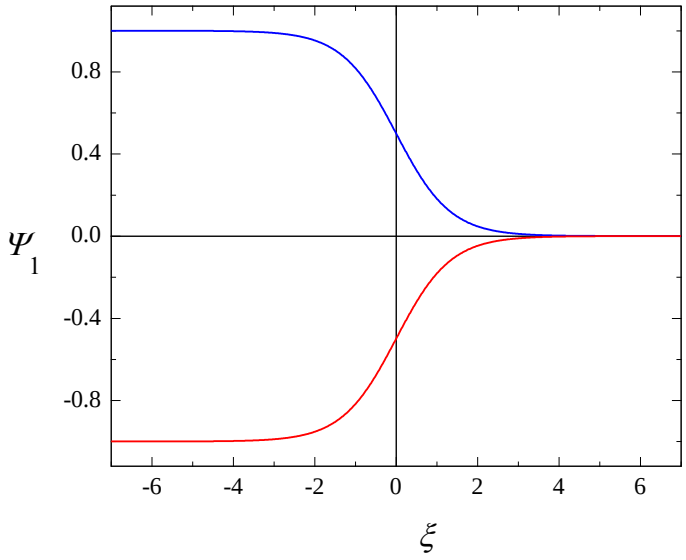

Fig. 2. Kink solitons $\psi_1^{(+)}$ (blue) and $\psi_1^{(-)}$ (red) for $\rho = 1$

If viscosity is neglected, that is for $\rho = 0$, the solution of Eq. (9) is

$$\psi_{10} = \tanh(\xi/a), \qquad \alpha = -a^2/2 < 0, \tag{22}$$

where a is an arbitrary constant introduced in Eq. (18). This function is similar to the one shown in Fig. 2 but it goes from -1 to 1, or from 1 to -1, depending on a sign of a.

To obtain Eqs. (20)-(22), $A > pE$ and $B > pE/6$ were assumed, as mentioned above. The cases $(A - pE)\left(B - \frac{pE}{6}\right) < 0$, $A = pE$ and $B \neq \frac{pE}{6}$, and $B = pE/6$ were studied in Ref. [5]. No solution having physical sense, relevant for this article, was obtained.

Case 2.

Eq. (10) exists in Ref. [10], even though different models were established. Solutions, corresponding to Eq. (20), are [10]

$$b = \frac{3{a_0}^2 - 1}{{a_1}^2}, \quad \alpha = -\frac{a^2}{2}, \quad a = \frac{\rho}{3a_0}, \quad 8{a_0}^3 - 2a_0 + \sigma = 0. \tag{23}$$

Three real solutions of Eq. (23) are [10]

$$\left.\begin{aligned} a_{01} &= -\frac{1}{2\sqrt{3}}\left(\cos F + \sqrt{3}\sin F\right) \\ a_{02} &= \frac{1}{2\sqrt{3}}\left(-\cos F + \sqrt{3}\sin F\right) \\ a_{03} &= \frac{1}{\sqrt{3}}\cos F \end{aligned}\right\}, \tag{24}$$

where

$$F = \frac{1}{3}\arccos\left(\frac{\sigma}{\sigma_0}\right), \quad \sigma_0 = \frac{2}{3\sqrt{3}}. \tag{25}$$

Figure 3 shows how the functions a_{0i} depend on σ. We notice that ${a_{01}}^2 < 1/3$. Also, according to Eqs. (24) and (25), we see that $a_{03}(\sigma_0) = 1/\sqrt{3}$. This means that three real roots of Eq. (23) exist for $\sigma < \sigma_0$, as $b < 0$. There is one real solution for $\sigma > \sigma_0$ [10]. However,

the requirement $\sigma > \sigma_0$ is nothing but $3a_0^{\,2} > 1$. This case corresponds to the positive b, which brings about the diverging solution [10].

The finite solutions, i.e., the functions ψ_{2i}, are determined by Eqs. (17), (18), and (23)-(25). They are

$$\psi_{2i}(\xi) = a_{0i} - \sqrt{1-3a_{0i}^{\,2}}\,\tanh\left(\frac{3a_{0i}}{\rho}\sqrt{1-3a_{0i}^{\,2}}\,\xi\right), \qquad i = 1,2,3, \tag{26}$$

shown in Fig. 4.

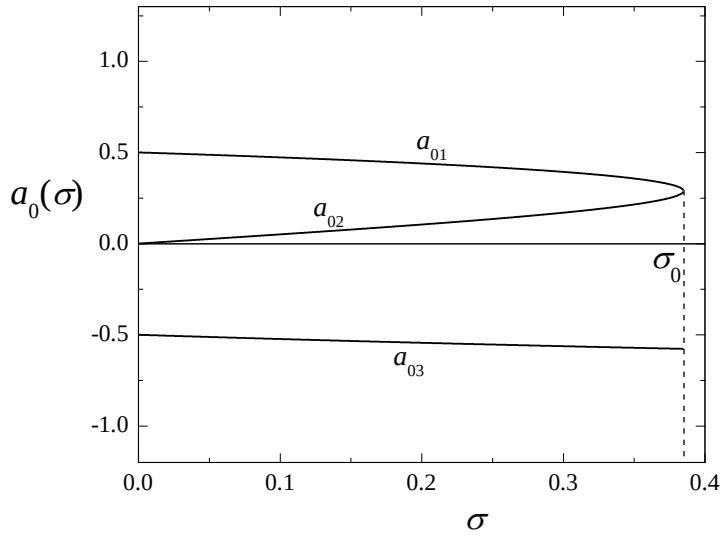

Fig. 3. The parameters a_{0i} as functions of σ

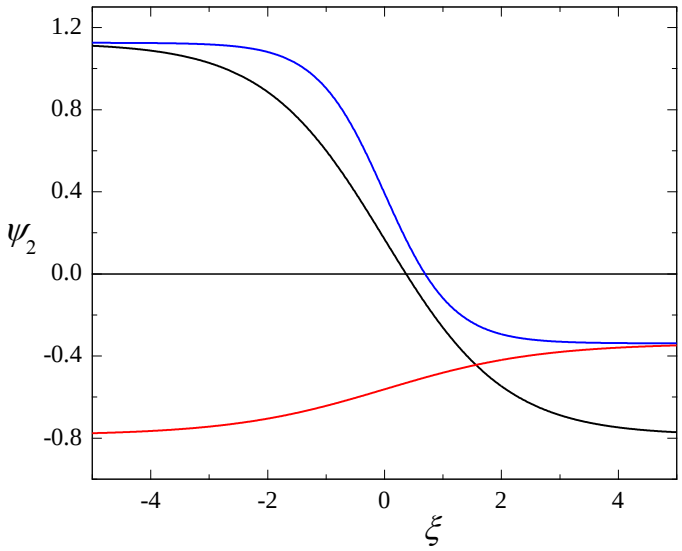

Fig. 4. Kink solitons ψ_{21} (blue), ψ_{22} (red), and ψ_{23} (black) for $\rho = 1$ and $\sigma = 0.3$

According to Eqs. (13) and (23), we see that the approximation $\rho = 0$ yields to $a_0 = 0$ and $\sigma = 0$ and, consequently, to the symmetric potential.

Case 3.

It was explained above that Eq. (19) gives a system of equations from which we obtain values of the parameters determining the function ψ. As we study the case $a_1 \equiv a \neq 0$ and $b_1 = 0$, the coefficients K_1', K_2', and K_3' disappear. Hence, we use Eqs. (11), (16), and (18) and obtain Eq. (19) for this particular case. The coefficients for ϕ^3, ϕ^2, ϕ^1, and $\phi^0 = 1$ respectively bring about the following system

$$\left.\begin{aligned} &2\alpha + a^2 = 0 \\ &3a_0 a - \rho - \delta a = 0 \\ &2\alpha b - 1 + 3{a_0}^2 - 2\delta a_0 = 0 \\ &\rho a b + a_0 - {a_0}^3 + \delta {a_0}^2 = 0 \end{aligned}\right\}. \tag{27}$$

According to Eq. (27), we obtain $\alpha = -a^2/2$, like in the previous two cases, and the three solutions for a_0, a, and b. These solutions are

$${a_0}^{(1)} = \frac{\delta}{2}, \quad a^{(1)} = \frac{2\rho}{\delta}, \qquad b^{(1)} = -\frac{\delta^2 {K_0}^2}{16\rho^2}, \tag{28}$$

$${a_0}^{(2)} = \frac{\delta - K_0}{4}, \quad a^{(2)} = -\frac{4\rho}{\delta + 3K_0}, \quad b^{(2)} = -\frac{\left(\delta + 3K_0\right)^2}{32\rho^2\left(\delta^2 + \delta K_0 + 2\right)} \tag{29}$$

$${a_0}^{(3)} = \frac{\delta + K_0}{4}, \quad a^{(3)} = -\frac{4\rho}{\delta - 3K_0}, \quad b^{(3)} = -\frac{\left(\delta - 3K_0\right)^2\left(\delta^2 + \delta K_0 + 2\right)}{128\rho^2}, \tag{30}$$

where

$$K_0 = \sqrt{\delta^2 + 4}\,. \tag{31}$$

It may be useful to keep in mind that the different analytical procedures, or different kinds of software, can bring about the expressions for the parameter that looks different from those given by Eqs. (29) and (30). For example, the alternative expressions for $b^{(3)}$ could be

$$b^{(3)} = -\frac{18 + 8\delta^2 + \delta^4 + 6\delta K_0 + \delta^3 K_0}{32\rho^2} \tag{32}$$

and

$$b^{(3)} = -\frac{\left(2\delta^2+9\right)^2\left[2\delta^4+10\delta^2+9+2\delta\left(\delta^2+3\right)K_0\right]}{\rho^2\left(\delta+3K_0\right)^4}. \tag{33}$$

Therefore, all the three expressions are identical, which might not be obvious at first glance.

The final solutions, i.e., the functions $\psi_3^{(1)}$, $\psi_3^{(2)}$, and $\psi_3^{(3)}$, can be obtained according to Eqs. (17), (18), and (28)-(31). They are

$$\psi_{31}(\xi) = \frac{\delta}{2} - \frac{K_0}{2}\tanh\left(\frac{\delta K_0}{4\rho}\xi\right), \tag{34}$$

$$\psi_{32}(\xi) = \frac{\delta - K_0}{4} + \frac{1}{\Lambda}\tanh\left(\frac{\delta+3K_0}{4\rho\Lambda}\xi\right), \tag{35}$$

$$\psi_{33}(\xi) = \frac{\delta + K_0}{4} + \frac{\Lambda}{4}\tanh\left(\frac{\left(\delta-3K_0\right)\Lambda}{16\rho}\xi\right), \tag{36}$$

where

$$\Lambda = \sqrt{2\delta^2 + 2\delta K_0 + 4}\,. \tag{37}$$

They are shown in Fig. 5 for $\delta = 0.3$.

4. Discussions and future research

Each of the three potentials given by Eqs. (2)-(4) has two minima and one maximum. In terms of the functions ψ, we can talk of the right and left minima, and of the maximum, denoted as ψ_{R}, ψ_{L}, and ψ_{M}, respectively. Let us compare Figs. 2 and 4. The solutions in Fig. 2 represent the transitions $\psi_{\mathrm{R}} \to \psi_{\mathrm{M}}$ (blue) and $\psi_{\mathrm{L}} \to \psi_{\mathrm{M}}$ (red). Both transitions can be seen in Fig. 4, but there is one more. This is $\psi_{\mathrm{R}} \to \psi_{\mathrm{L}}$ (black), representing a transition from a deeper minimum to a shallower one. An obvious conclusion is that the non-symmetric potential W_2 is

better than the symmetric one. Also, the same conclusion is suggested by the geometry of MTs.

The potentials W_2 and W_3 bring about Figs. 4 and 5. These figures are basically of the same value, i.e., describe all three transitions. This means that it is difficult to state which potential is better for MT modelling. In the case of W_3, the transition $\psi_{\mathrm{R}} \to \psi_{\mathrm{L}}$ goes slowly in comparison to W_2 (black lines), but this depends on the values of the parameters σ and δ. This might mean that W_3 is better but we are not ready for any suggestions without further research. We should notice that $\psi_{\mathrm{M}} = 0$ in cases W_1 and W_3. This indicates that the unstable orientations of the dimers are exactly in the direction of PF. Unfortunately, the orientation of the dimers has not been experimentally determined yet. We can state that the potentials W_2 and W_3 are more convenient for MT modelling than the symmetric one. This issue should be studied within a new model [12].

The equations (5)-(7) were solved using the continuum approximation. The question of whether MT is a discrete or continuum system was studied in Ref. [14].

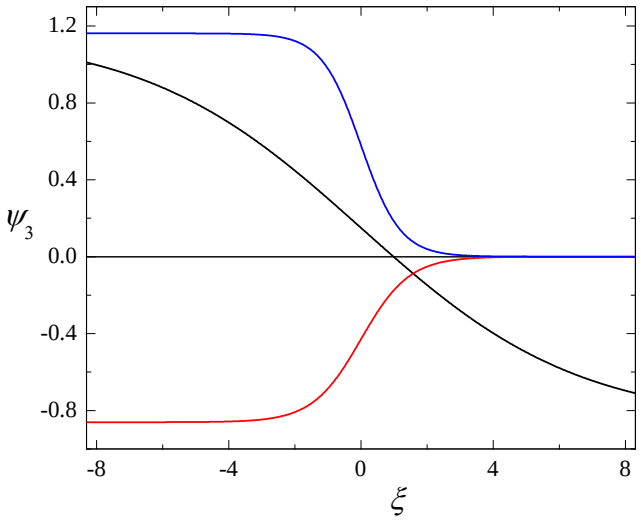

Fig. 5. Kink solitons ψ_{31} (blue), ψ_{32} (red), and ψ_{33} (black) for $\rho = 1$ and $\delta = 0.3$

References

[1] P. Dustin, *Microtubules*, Springer, Berlin, 1984.
[2] S. Zdravković, *J. Serb. Chem. Soc.* **82** (5) (2017) 469.
[3] S. Zdravković, *Mechanical Models of Microtubules*, In Complexity in Biological and Physical Systems, Edited by Ricardo Lopez-Ruiz, Chapter 1, IntechOpen, 2018.
[4] M. V. Satarić, J. A. Tuszyński and R. B. Žakula, *Phys. Rev. E* **48** (1993) 589.
[5] S. Zdravković, M. V. Satarić and V. Sivčević, *Nonlinear Dyn.* **92** (2018) 479.
[6] S. Hameroff and R. Penrose, *Phys. Life Rev.* **11** (2014) 39.
[7] S. Sahu, S. Ghosh, K. Hirata, D. Fujita and A. Bandyopadhyay, *Appl. Phys. Lett.* **102** (2013) 123701.
[8] D. Havelka, M. Cifra, O. Kučera, J. Pokorný, J. Vrba, *J. Theor. Biol.* **286** (2011) 31.
[9] J. E. Schoutens, *J. Biol. Phys.* **31** (2005) 35.
[10] S. Zdravković, L. Kavitha, M. V. Satarić, S. Zeković and J. Petrović, *Chaos Solitons Fract.* **45** (2012) 1378.
[11] S. Zdravković, M. V. Satarić, A. Maluckov and A. Balaž, *Appl. Math. Comput.* **237** (2014) 227.
[12] S. Zdravković, S. Zeković, A. N. Bugay and J. Petrović, *Chaos Soliton Fract.* **152** (2021) 111352.
[13] S. A. El-Wakil and M. A. Abdou, *Chaos Solitons Fract.* **31** (2007) 840.
[14] S. Zdravković, A. Maluckov, M. Đekić, S. Kuzmanović and M. V. Satarić, *Appl. Math. Comput.* **242** (2014) 353.

Modelling the Steel Fibre Reinforced Concrete material nonlinearity with ANSYS [*]

Stepa Paunović [†]
Mathematical institute of the Serbian Academy of Sciences and Arts, Belgrade, Serbia

ABSTRACT

In this paper the possibilities of modelling the steel fibre reinforced concrete (SFRC) in ANSYS software are explored in detail. Several available material models are analysed, and their advantages and shortcomings in describing the SFRC behaviour are discussed. Since it was shown that none of the existing material models available in ANSYS was able to produce satisfactory results, a novel modelling approach was proposed, which combined several individual material models in order to build on their strengths and overcome their disadvantages. All the models were assessed against the experiment results found in literature. The analysis showed that not even the novel modelling approach was able to simulate SFRC in all its complexity and possible improvements of the presented novel approach which would lead to more reliable results are discussed. Finally, further research and some other software alternatives are proposed.

1. Introduction

There are two types of microreinforced concrete – Microreinforced concrete in a specific sense, where the concrete element is reinforced by some highly ductile strips or ribbons (Figure 1.a) [1], and the fibre reinforced concrete, where the concrete matrix is reinforced by many relatively short and thin fibres randomly oriented, but homogeneously dispersed throughout the matrix (Figure 1.b) [2]. Fibres can be of different shapes and sizes and made from different materials, and the

[*] This work has been supported by the Ministry for Education, Science and Technological development of the Republic of Serbia, through the Mathematical institute of SASA.
[†] e-mail address: stepa.paunovic@mi.sanu.ac.rs

most commonly used ones are the steel or glass fibres, usually with hooked ends [3-6].

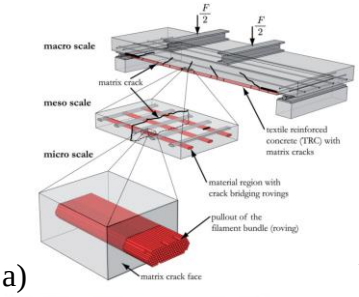

a)

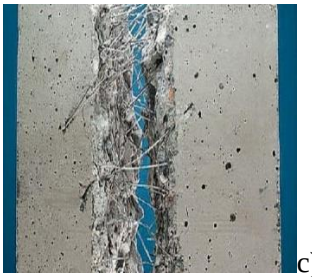

b)

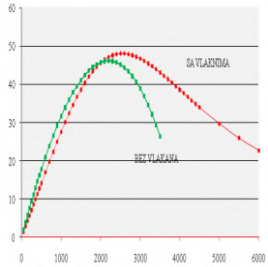

c)

Figure 1. Microreinforced concrete. Concrete reinforced a) by composite strips [1], and b) by steel fibres [2]. c) Stress-strain diagram for conventional concrete (green line) and for steel fibre reinforced concrete (red line)

In this paper, the Steel Fibre Reinforced Concrete (SFRC) will be of main interest. Adding ductile fibres to the otherwise brittle concrete matrix improves the overall strength, durability and toughness of the concrete, but the main improvement lies in its ductility [7,8], which can be readily observed by comparing characteristic stress-strain diagrams for conventional, plain concrete, and the fibre reinforced one, Figure 1c [2].

Fibre reinforced concrete is a construction material that exhibits highly nonlinear behaviour, even more so than the conventional concrete. This makes it very hard to model it numerically, and there is no one universal way of modelling it, but rather many different approaches can be found in the literature. The simplest and the most widely used approach is to model the SFRC as a homogeneous material [9-12]. However, although computationally very effective, it is very hard to capture and adequately describe all the nonlinear effects that occur in this composite material. The other approach consists in modelling the concrete matrix as a homogeneous material, and to model the added fibres discretely, while defining the appropriate interaction between these two phases of the material [13-15]. This approach produces a more precise model and it

can handle the nonlinearities better, but it requires the use of the Extended Finite Element Method (XFEM) and is computationally much more expansive. The approach next in model complexity is the Multiscale modelling [16-19], where several numerical models are produced, modelling the elements at different length scales and calculating the material characteristics for each scale on the model of the one scale below, all the way down to atoms. This approach can produce very accurate results, it requires enormous computational power which makes it suitable for in-depth research of material behaviour, but renders it inapplicable in everyday engineering practice. There are some even more complex modelling approaches involving peridynamics and molecular dynamics [20, 21], but they exceed the scope of this survey. Figure 2 shows examples of the three modelling approaches described above. In this paper, the most basic approach is considered, since it is the most commonly used one in practice and most pieces of commercial software are limited to this approach. Moreover, the aim of this paper is to explore the possibilities of using the ANSYS commercial FEM software for modelling the SFRC material.

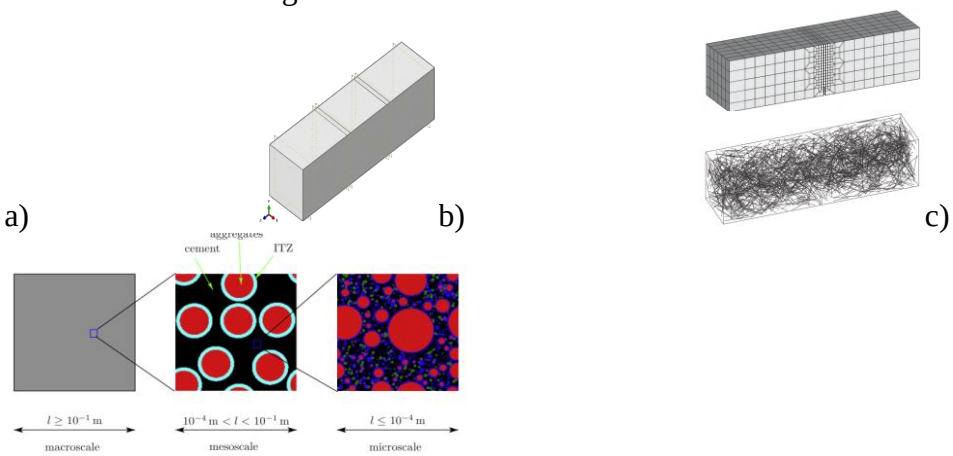

Figure 3. Different SFRC modelling approaches: a) as a homogeneous material, b) homogeneous matrix and discrete fibres [15], and c) multiscale modelling [16]

However, as it will shortly become apparent, this software, although very sophisticated, appears to be incapable to produce a SFRC model with a satisfactory accuracy by any of the predefined means and procedures provided within the software. Therefore, the second part of this paper presents a novel modelling approach that overcomes the limitations of material models provided in the software.

2. Modelling the SFRC with material models available in ANSYS

In ANSYS there are several different material models provided that can be readily used to model concrete. However, although accurate enough when modelling conventional concrete, each of them possesses some major drawbacks and disadvantages when used for SFRC modelling. In the following text all these standard models provided in ANSYS will be presented and their shortcomings when modelling SFRC will be discussed.

CONCRETE material model

The conventional concrete is much more investigated than the SFRC and, although with a quite nonlinear behaviour as well, it is much easier to model and there is a well-developed and refined model in ANSYS made for this purpose. It is called the CONCRETE material model and it is meant to be used in combination with the finite element of type SOLID65, which is a modified 8-node hexahedral FE developed specially for modelling the concrete. It provides the ability to define the "smeared" rebar reinforcement inside each element, as well as the ability to track and display the crack that appear in any of 8 integration points inside each element during the nonlinear numerical analysis, along with the crack type and crack plane orientation. Details of the SOLID65 FE are shown in Figure 3. It should be noted that this material model and FE can be used only inside the Mechanical APDL environment.

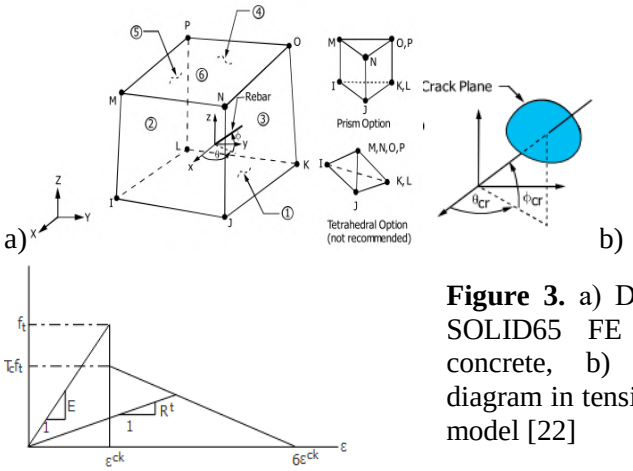

Figure 3. a) Details of the ANSYS's SOLID65 FE made for modelling concrete, b) concrete stress-strain diagram in tension for William-Warnke model [22]

In ANSYS, a more complex material model can be obtained by combining two or more elementary material models provided in the software. For instance, standard structural steel is usually modelled by combining isotropic elastic model with nonlinear plastic model with isotropic hardening, to account for the steel plastic deformations. In similar manner, the concrete material model is obtained by combining the isotropic linearly elastic material model, defined through two parameters – Young elasticity modulus and the Poisson's ratio, and the CONCRETE material model, defined through 9 constants, defining the Open shear transfer coefficient, Closed shear transfer coefficient, Uniaxial cracking stress, Uniaxial crushing stress, Biaxial crushing stress, Hydrostatic pressure, Hydrostatic biaxial crushing stress, Hydrostatic uniaxial crushing stress and the Tensile crack factor. The highly nonlinear behaviour of concrete in compression is directly defined by adding a multilinear isotropic behaviour defined through a tabular set of arbitrarily many stress-strain points of a compression stress strain diagram.
This modelling approach yields very accurate results when modelling conventional concrete and it has become a benchmark approach when dealing with such problems. It is particularly convenient for visual representation of material damage, since the cracks can be directly plotted, an example of which is given in Figure 4.

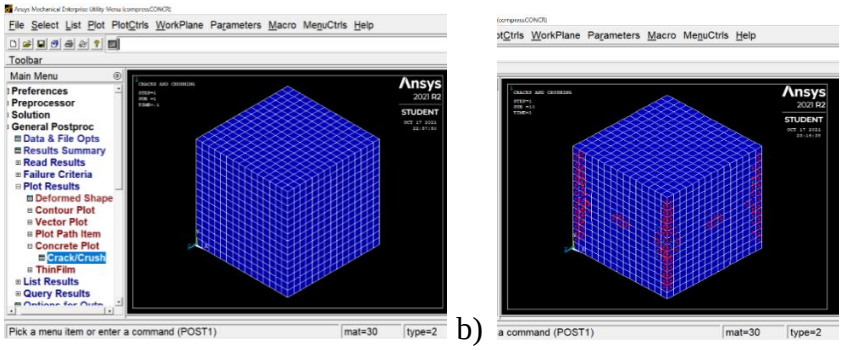

Figure 4. Numerical model of a SFRC cube in a uniaxial compression test; a) Mesh with SOLID65 Fes and CONCRETE material model, b) Plot of cracks

However, CONCRETE material model is defined based on the William-Warnke material model [23], which assumes the tri-linear concrete behaviour in tension with the relatively brittle failure mechanism, Figure 3b. For this reason, it is not suitable to describe the SFRC, since this

composite material is much more ductile and exhibits highly nonlinear behaviour in tension, as well as in compression. Therefore, another material model needs to be examined in order to obtain an appropriate SFRC model.

Manetray-William material model (MW model)

This material model is made especially to model concrete and it is available only in more recent distributions of ANSYS software, i.e. since v18.1. The main advantage of this material model is that the exact stress-strain diagram can be defined directly. This is very convenient since the stress-strain diagram can be experimentally obtained very easily in many standard test procedures, and inputting it directly means that during simulation material follows this real behaviour exactly. It should be mentioned that prior to this material model, the "negative" elastic modulus could not be given in ANSYS material models, that is, the stress-strain diagram could not account for stress relaxation when plasticity occurs. This has been improved with the Manetrey-William model.

The MW model is defined by three parts. The first part defines the plastification conditions by three parameters - Uniaxial compressive strength (R_c), Uniaxial tensile strength (R_t) and Biaxial compressive strength (R_b). The second part of the model refers to the way the material deforms after the plasticization limit is reached, and it is set through the Dilatancy angle (ψ), a parameter which shows how the elementary volume changes with the increase of plastic deformation. The third part of the model defines the post-critical behaviour of the material, i.e. the strain hardening or the strain softening of the material. If the third part is not explicitly specified, the model assumes perfectly plastic behaviour in post-critical zone. This part can be defined in various ways, and for this research a linear softening behaviour was defined, and it was done through defining six parameters - Plastic strain at uniaxial compressive strength (κ_{ci}), Ultimate effective plastic strain in compression (κ_{cr}), Relative stress at start of nonlinear hardening (Ω_{ci}), Residual relative compressive stress (Ω_{cr}), Plastic strain limit in tension (κ_{tr}) and Residual relative tensile stress (Ω_{tr}), and these parameters are graphically presented in Figure 5. It is pointed out that on the abscissa are the *plastic* strains.

Through these parameters, a desired stress-strain diagram for SFRC can be defined *exactly*, even in tension. However, this model exhibited much

convergence difficulties in the simulations done in numerical analysis of SFRC made for this research. Moreover, this model cannot show the cracks and material damage that occurs in concrete, it can only show the plastic zones, but the material remains continuous throughout the analysis. For these reasons, another material model was sought that would be more suitable for modelling the SFRC.

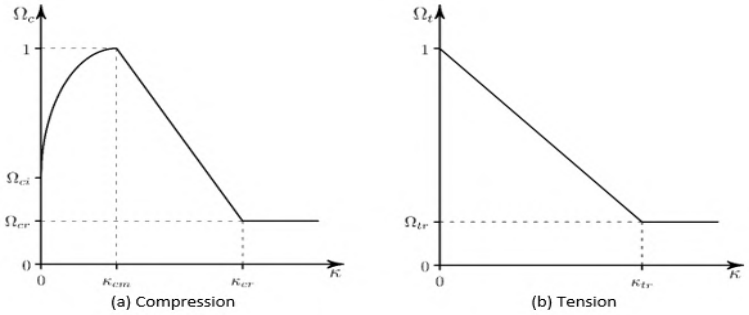

Figure 5. Parameters for post-critical behaviour for concrete in the Manetray-William model and the Drucker-Prager model – a post-critical (plastic strain)-(normalized stress) diagram in a) compression and b) tension [22]

The Drucker-Prager material model (DP model)

This material model was made primarily for modelling granular materials and concrete. It is also found only in more recent software releases, like the previously discussed Manetrey-William model, and it is also defined similarly. Namely, the Drucker-Prager model is also comprised of three parts. The first and the third part are identical as for the MW model, while the second part also defines the material behaviour at plastic deformation, but it is now defined through different two parameters – the dilatancy parameter in compression (δ_c) and the dilatancy parameter in tension (δ_t).

Similarly as with the MW model, an advantage of DP model is that all parameters have clear physical meaning and are directly measurable in experiments, and the stress-strain curve can be inputted exactly. However, while keeping the advantages of this type of input data, unlike the MW model, the DP model behaves much better in numerical analysis, it is much more stable and robust, and it yields better results when modelling SFRC. Nevertheless, it also exhibits convergence issues when the material enters the zone of residual stresses, and it also lacks the ability to visually represent the cracks in concrete and the damage of the material still limit its applicability for modelling the SFRC. So, yet another material model provided in ANSYS needed to be investigated.

However, these three models are the only ones that ANSYS provided specifically for modelling concrete. The rest of the considered material models are general purpose, but have some desired characteristics for SFRC modelling which make them suitable candidates.

The Material Damage Model (DMG model)

In ANSYS software, beside the CONCRETE model, the only other material model that can provide a direct visual insight into material damage and cracks is the Material DAMAGE model, and since it is very important to capture cracking when modelling the SFRC, this material model is the next one to be considered.

The material DAMAGE model consists of two parts. The first part describes the Damage initiation criteria (DMGI), and the other part defines how the damage propagates through the material – the Damage evolution law (DMGE). The damage initiation criteria can be described in various ways, and ANSYS provides several: maximum stress criterion, maximum strain criterion, Puck criterion, Tsai-Wu criterion and Hashin criterion, and there is also a user-defined criterion option. For this research, a maximum stress criterion was used, defined through four parameters – compression and tensile strength of concrete matrix, and compression and tensile strength of fibres. For DMGE there are two possible variants – the instant material property degradation (MPDG), and the Continuous damage model (CDM), where the material degradation progresses gradually. The input parameters for this part of the model are the viscous damping coefficient and the potential energy of deformation released until the material strength reduces to zero.

The idea was to use the DMG model to simulate the stress-strain diagram of SFRC by choosing the appropriate parameter values for CDM, while keeping the possibility of crack and material damage visualization. However, this could not be achieved due to some inherent limitations ANSYS imposes on using the DMG material model. Namely, ANSYS allows combining the material DAMAGE model only with the ideally elastic isotropic material model, which makes it impossible to input a highly nonlinear stress-strain relation needed to describe SFRC adequately. And even it was possible to input the stress-strain curve in compression, the CDM assumes linear strength degradation to zero, which is also not suitable for describing the SFRC behaviour. MPDG is even worse for modelling SFRC since it does not allow for any residual strength and material properties are instantly reduced to zero upon

damage initiation, which would correspond to a ideally elastic-perfectly brittle type of failure, and it is also not suitable for SFRC modelling. This is why another material model needed to be examined for modelling SFRC.

The MicroPLANE material model (MPLAN model)

Each of the aforementioned models was designed to model some particular material, so it has advantages when modelling that material, but also some drawbacks when being used to model other materials. This led the developers in ANSYS to include a "generalized" material model that could be used to describe any material. This "generalized" model is constituted by directly defining the constitutive relations for the material, which can be different in different directions. They are defined on an infinitesimal polyhedral element with 42 sides, so that a separate constitutive relation can be defined for each of the 21 section planes. This model is therefore called the MicroPLANE material model, and Figure 6 shows the infinitesimal polyhedron on which the model is defined.

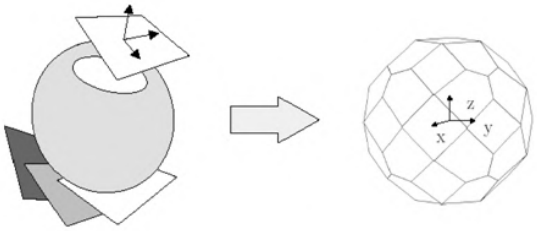

Figure 6. The infinitesimal polyhedron with 42 sides for definition of the MicroPLANE model [22]

The main idea when using this model is to rewrite the equations of Mechanics of continua such as to account for the material damage, which is done through 6 parameters. First the deformation tensor and the stress tensor are decomposed into a spherical and deviatoric parts, then the free Helmholz energy of deformation is defined on a micro scale, and then during the homogenization a material damage function is defined. Parameters that are introduced to define the material damage function include: three parameter for failure mechanics (k_0, k_1, k_2), maximum damage parameter (α^{mic}), degradation speed parameter (β^{mic}) and parameter of the equivalent strain energy at the moment of damage initiation (γ_0^{mic}). This enables MPLAN model to be used in a variety of

different problems, since that the different values of these input parameters produce different failure criteria. For instance, for $k_0 = 0$, $k_1 = 0$, $k_2 = 1$ the Huber-Hanky-Mieses plasticization criterion is obtained, $k_0 > 0$, $k_1 = 0$, $k_2 = 1$ gives the Drucker-Prager criterion, and so on.

The MicroPLANE model has already been used to model fibre reinforced concrete [24]. In the literature, the following parameter relations are proposed as suitable for SFRC modelling

$$k = f_c/f_t \ , \quad k_0 = \frac{(k-1)}{2k(1-2\nu)} \ , \quad k_1 = k_0 \ , \quad k_2 = \frac{3}{k(1+\nu)^2} \tag{1}$$

where f_c is the concrete compression strength, f_t is the concrete tensile strength, and ν is the Poisson's coefficient.

However, these relations are empirical, and values for the other three parameters ($\alpha^{mic}, \beta^{mic}, \gamma_0^{mic}$) need to be determined through calibrations by the experimental results, and the model is highly sensitive to their variations. Moreover, microplane material model cannot be combined with other material models, and it also cannot visually represent the crack and the damage of the material, which is essential for SFRC modelling. In addition, this model also showed considerable convergence difficulties. Therefore, another solution for SFRC was sought. However, this exhausts the available predefined possibilities provided in ANSYS software. Since none of the options was not accurate to a satisfactory extent, the novel approach for modelling the steel fibre reinforced concrete is proposed in this paper, by using the available programme resources and writing some user-defined subroutines.

3. A novel method for modelling the SFRC with ANSYS

As it has been pointed out in the previous text, none of the predefined material models available in ANSYS, separately, was not able to adequately model SFRC. This is why an attempt is made in this paper to find a novel modelling approach that would exploit the advantages of these models, while overcoming their limitations.

The main idea is fairly simple. Since beside the CONCRETE model, the only other material model that enables crack visualization is the Material damage model that is the one that will be used. The limitation of this

model is that it inevitably assumes linearly elastic material behaviour up until the material bearing capacity is reached. However, ANSYS also provides another command – the Material Property Change command (MPCHG) – which allows that at any point during the numerical analysis the material of any finite element be changed with another material model. In this way the material stiffness can be changed as needed.

Therefore, the idea was to define the criteria on which to reduce the material stiffness of the finite elements meeting these criteria for a certain amount, and these criteria should be checked between each step of the nonlinear analysis. By defining several such degradation limits at which the material stiffness would be reduced ever more, if defined and applied properly, this could impose that, although the material in each finite element is linear, the global material model overall follows a multilinear stress-strain relation. By choosing sufficient number of degradation limits, the nonlinear stress-strain diagram for SFRC can be closely approximated by a multilinear relation defined through a sufficiently large set of inflection points. Thus the main disadvantage of the DMG model is overcome, while keeping its main advantage – the ability to visualize crack initiation and propagation through the material. The described procedure was successfully implemented in the Mechanical APDL programming environment through the algorithm shown in Figure 7.

Preprocessor – FE type, model geometry, mesh, boundary conditions, material models:
- MAT1 – linearly elastic + DMG material model, full material stiffness (E)
- MAT2 – linearly elastic + DMG material model, reduced material stiffness (k_1*E)
- MAT3 – linearly elastic + DMG material model, zero material stiffness (k_2*E)
- Defining the criteria for MPCHG (σ_{d1}, σ_{d2}) and damage initiation criteria
- Defining the loads in the model (p)
- Defining the numerical nonlinear analysis parameters, number of analysis steps (n)
- Calculating the load increment: opt=p/n

Solver modul
- Step 1 – solve
- Step 2 - Select all nodes that satisfy the first criterion: $\sigma>\sigma_{d1}$
  - Select all elements containing these nodes (command: ESELE)
  - Change the material model for the selected elements into MAT2
  - Select the whole model
- Select all nodes that satisfy the second criterion: $\sigma>\sigma_{d2}$
  - Select all elements containing these nodes (command: ESELE)
  - Change the material model for the selected elements into MAT2
  - Select the whole model
- Increment the load (opt=opt+p/n)
- solve
- Step 3 – Repeat Step 2 until the defined load value is reached (opt=p)

Postprocessor
- Results visualization (strain, stress, damage, material models each FE)

Figure 7. Algorithm of the novel SFRC modelling approach proposed in this paper

Another advantage of the proposed approach is that all the required parameters are plain, simple, they have a clear physical meaning and are directly measurable in experiments. However, this approach requires a finer finite element mesh, which makes it numerically somewhat more expansive compared to other considered material models. On the other side, the algorithm is simple and robust so the convergence issues are avoided. Another disadvantage is that there are no options for this modelling approach that are readily available in ANSYS software, but this approach rather requires some programming skill for the user to apply it. It should also be pointed out that for demonstration purposes in this paper only a three-linear stress-strain relation is defined, with two material property change limits. However, the number of these points can be increased to achieve a better approximation.

The proposed modelling approach was validated on a benchmark problem of modelling a conventional concrete cantilever beam loaded at its free end until failure. The results were compared to the ones obtained through a standard simulation procedure with using the CONCRETE material model and SOLID65 finite element, which are routinely used for

conventional concrete modelling. The results are presented in Figure 8, and they showed a very good agreement, thus validating the proposed novel approach and encouraging its use for SFRC modelling.

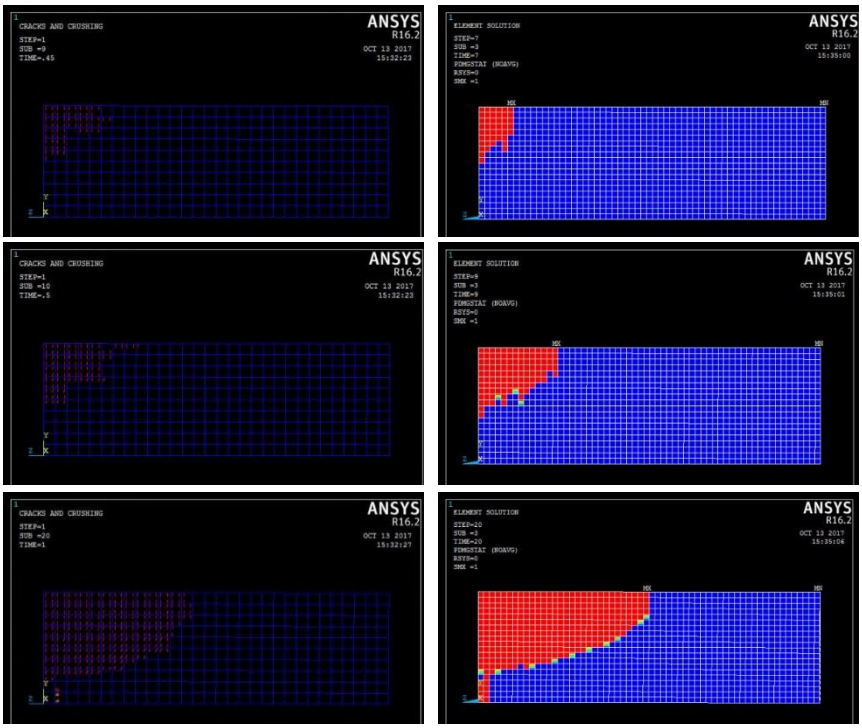

Figure 8. Validation of the proposed modelling approach on a benchmark problem. CONCRETE material model with SOLID65 FE (left) and MPCHG model (right)

4. Assessment of different SFRC modelling approaches in ANSYS

In this section the performance of all the presented material models in modelling the steel fibre reinforce beam will be assessed. All the results will be compared to the results obtained in the experiments found in the literature [2]. The experiment was a standard four-point-bending test, and specimens were made of reinforced concrete with steel hooked fibres and conventional steel rebar 2Rϕ12. Details are presented in Figure 9.

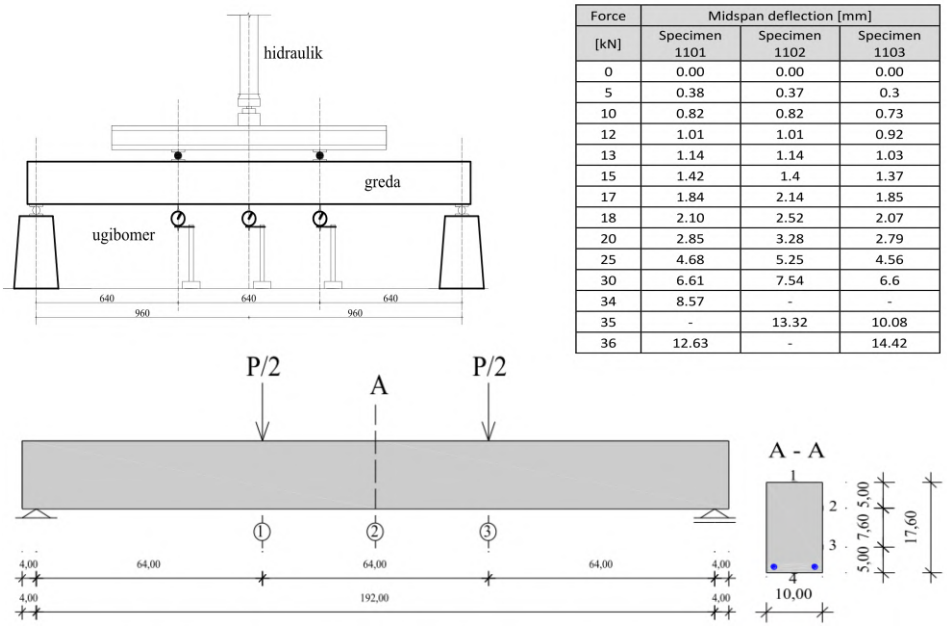

Force	Midspan deflection [mm]		
[kN]	Specimen 1101	Specimen 1102	Specimen 1103
0	0.00	0.00	0.00
5	0.38	0.37	0.3
10	0.82	0.82	0.73
12	1.01	1.01	0.92
13	1.14	1.14	1.03
15	1.42	1.4	1.37
17	1.84	2.14	1.85
18	2.10	2.52	2.07
20	2.85	3.28	2.79
25	4.68	5.25	4.56
30	6.61	7.54	6.6
34	8.57	-	-
35	-	13.32	10.08
36	12.63	-	14.42

Figure 9. Details of the experiment [2], a) the setup, b) schematic representation of the specimens, c) the experiment results

The geometry and boundary conditions were the same for all the considered numerical models and they are shown in Figure 10. For all the models the standard general purpose solid hexahedral 3D finite element SOLID185 was used, except for the CONCRETE material model where the SOLID65 FE was used. The applied material models differed from model to model accordingly.

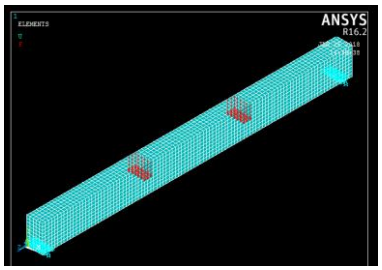

Figure 10. The geometry and used boundary conditions for the numerical models

The following material models were tested: the CONCRETE material model, the Menetrey-William model (MW), the Drucker-Prager model (DP), the material damage model (DMG), the microplane model

(MPLAN), and the novel modelling approach utilizing the material property change command (MPCHG). All the results of the numerical analysis are presented in Figure 11.

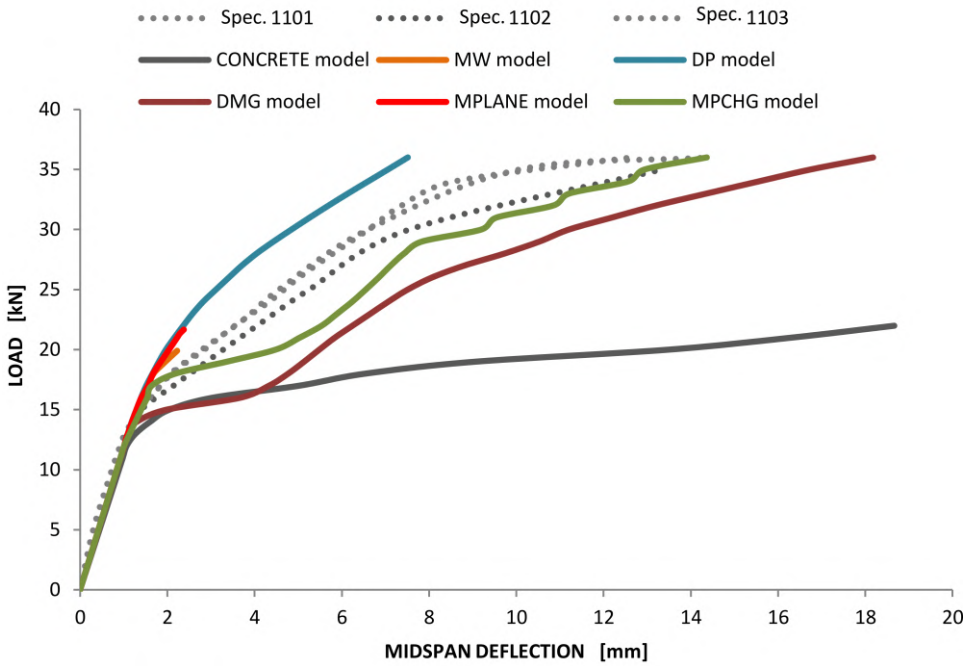

Figure 11. The results of the numerical simulations for all the considered models

Base on the results of numerical analyses, from the viewpoint of their applicability to SFRC modelling, the following assessment of the considered material models can be given.

<u>The Menetrey-William (MW) model and the Microplane (MPLAN) model</u>

It is obvious from Figure 11 that these models did not even manage to converge to the final load size, the simulation rather fails practically as soon as the model enters a nonlinear zone, that is, with the first crack openings. It can be concluded that these models are not suitable for SFRC modelling.

The CONCRETE material model

It can be clearly seen that deformations of this model are much larger than the experiment results, predicting the final specimen bearing capacity of only 22kN, whereas the real value measured in the experiment was 36.6kN. It can also be noted that the predicted post-critical curve is much steeper than the actual ones, implying much lower material strength. This was expected since the CONCRETE model does not assume any residual material strength after the crack occurs, so the model degrades more rapidly than the actual SFRC, in which the damage propagates much more slowly due to the present fibres. From all this it can be concluded that this model also isn't suitable for SFRC modelling and should not be used as such.

The Material damage (DMG) model

Form Figure 11 it is apparent that the DMG model accurately simulates the SFRC behaviour in the linear zone, but after the cracks occur the deformation increases very rapidly. Consequently, although the predicted curve follows the shape of the experimental ones quite well after stabilization, due to this initial rapid decay the predicted deformations remain larger than the real ones measured in the experiment. It can be concluded that this model could potentially be used for SFRC modelling, but further research to this end is necessary.

The Drucker-Prager (DP) model

The obtained results imply that the Drucker-Prager material model simulates the SFRC behaviour relatively well, but it still predicts material strength and model stiffness that are higher than the real ones. Further analysis revealed that this model predicts some material softening in the post-critical zone, but material degradation is not rapid enough, so the residual strength is much higher than the real one, which led to overestimated results overall. This emphasizes the main disadvantage of this material model – it does not allow for an instant stiffness reduction, which is needed to capture the opening of cracks adequately. This model is perhaps more suitable for modelling some material which is much more ductile than the SFRC, but it cannot describe the SFRC behaviour accurately enough.

The model with the Material property change command (MPCHG model)

Of all the considered material models, the MPCHG model produced the results that are the closest to the ones obtained in the experiment. However, it is obvious that not even this model predicted the SFRC behaviour accurately enough. The performance of this model could possibly be improved by including more points in stress-strain curve approximation through more material property change criteria limits, leading to a smoother stiffness reduction and more gradual transition after the crack occur. The performance could be improved still if even finer finite element mesh was used, further cushioning the material degradation and lowering the instantaneous initial deformation step. Nevertheless, in its current state of development, although it possesses some potential to be improved and produce more robust and reliable results, this model is also not quite suitable for SFRC modelling.

5. Concluding remarks

In this paper some of the issues regarding the modelling of steel fibre reinforced concrete (SFRC) in ANSYS software were pointed out. As it was shown in the text, the problem of accurate SFRC modelling is a challenging task, due to highly nonlinear material behaviour and many physical mechanisms that drive the damage initiation and evolution in the material. Several possibilities of SFRC modelling within the ANSYS software were studied in detail, and the results of all the numerical analyses were compared to the experiment results found in the literature. However, none of the predefined material models available in ANSYS was able to capture the SFRC behaviour in all its detail, so a novel modelling approach was proposed, which builds on the advantages of some of the predefined ANSYS models, and combines them to overcome the shortcomings of each individual model. Nevertheless, although producing the best predictions of all the considered models, not even the proposed novel modelling approach was accurate to a satisfactory level in approximating the actual SFRC behaviour from the experiment. The proposed approach can be improved by defining more precise material change and failure criteria or by using more material degradation stages. This, combined with a finer finite element mesh, could lead to a better representation of the SFRC post-critical behaviour. However, in its

current state of development, the proposed novel modelling approach is unable to provide sufficiently reliable results when modelling SFRC.
Overall, it can be concluded that ANSYS is not the most suitable software for modelling the SFRC as a homogeneous material. It should be noted that it may not be the case for a more detailed modelling approach such as the XFEM models for instance, but that research exceeds the scope of this paper. Still, when modelling the SFRC as a homogeneous material, some other software alternatives such as ABAQUS or OpenSEES should probably be preferred.

References

[1] Lepenies, I. G., Richter, M., & Zastrau, B. W. (2008, December). A Multi-Scale Analysis of Textile Reinforced Concrete Structures. In PAMM: Proceedings in Applied Mathematics and Mechanics (Vol. 8, No. 1, pp. 10553-10554). Berlin: WILEY-VCH Verlag.
[2] Predrag Blagojević, *PhD thesis* (2011) Faculty of Civil Engineering and Arcitecture, University of Niš, Serbia.
[3] Andrzej M. Brandt, Fibre reinforced cement-based (FRC) composites after over 40 years of developement in building and civil engi-neering, *Composite Structures* 86 (2008), pp. 3-9
[4] D. Snoeck, N. De Belie, From straw in bricks to modern use of microfibers in cemntitious composites for improved autogenous healing – A review, *Construction and Building Materials* 95 (2015) pp. 774-787
[5] Ronald F. Zollo, Fibre-reinforced Concrete: an Overview after 30 years of Developement, *Cement and Concrete Composites* 19 (1997), pp. 107-122
[6] T. Blaszczynski, M. Przybylaska-Falek, Steel fibre reinforced concrete as a structural material, *Procedia Engineering* 122 (2015), pp. 282-289
[7] B. Mobasher, Y. Yao, Ch. Soronakom, Analytical solutions for flexural design of hybrid steel fibre reinforced concrete beams, *Engineering Structures* 100 (2015), pp. 164-177
[8] H. Behbahani, B. Nematollahi, Steel Fibre Reinforced Concrete: A Review, *conference paper, December 2011*, preuzeto sa sajta Research Gate, 22. avgusta 2017. godine, internet adresa:

https://www.researchgate.net/publication/266174465_Steel_Fiber_Reinforced_Concrete_A_Review

[9] D.M. Ozcan, A. Bayraktar, A. Sahin, T. Haktanir, T. Turker, Experimental and finite element analysis on the steel fibre-reinforced concret (SFRC) beams ultimate behavior, *Construction and Building Materials* 23 (2009) pp. 1064-1077

[10] R. Cerioni, P. Bernardi, E. Michelini, A. Mordini, A general 3D approach for the analysis of multi-axial fracture behavior of reinforced concrete elements, *Engineering and Fracture Mechanics* 78 (2011), pp. 1784-1793

[11] R. Brighanti, A. Carpinteri, A. Spagnoli, D. Scorza, Crackong beahvior of fibre reinforced cementitious composites: A comparison between a continuous and a discrete computational approach, *Engineering and Fracture Mechanics* 103 (2013), pp. 103-114

[12] D. Nicolaides, G. Markou, Modelling the flexural behavior of fibre reinforced concrete beams with FEM, *Engineering Structures* 99 (2015), pp. 653-665

[13] V. M.C.F. Cunha, J. A.O. Barros, J. M. Sena-Cruz, A finite element model with descrete embedded elements for fibre reinforced composites, *Computers and Structures* 94-95 (2012), pp. 22-33

[14] J. Kang, K. Kim, Y. Mook Lim, J. E. Bolander, Modeling of fibre-reinforced cement composites: Discrete representation of fibre pullout, *International Journal of Solids and Structures* 51 (2014), pp. 1970-1979

[15] V. M.C.F. Cunha, Steel Fibre reinforced Self-Compacting Concrete (from Micro-Mechanics to Composite Behavior), *PhD thesis*, University of Minho, Portugal (2010) ISBN: 978-972-8692-44-5

[16] V.P. Nguyen, M. Stroeven, L.J. Sluys, Multiscale failure modeling of concrete: Micromechanical modeling discontinuous homogenization and parallel computations, *Computational Methods and Aplications in Mechanical Engineering* 201-204 (2012) 139-156

[17] J. Elias, M. Vorechovsky, J. Skoček, Z. P. Bažant, Stochastic discrete meso-scale simulations of concrete fracture: Comparison to experimental data, *Engineering Fracture Mechanics* 135 (2015) 1-16

[18] V. Palmieri, L. De Lorenzis, Multiscale modeling of concrete and of the FRP-concrete interface, *Engineering Fracture Mechanics* 131 (2014) pp. 150-175
[19] H. M. Jennings, J. W. Bullard, From electrons to infrastructure: Engineering concrete from bottom up, *Cement and Concrete Research* 41 (2011) pp. 727-735
[20] A. Yaghoobi, M. G. Chorzepa, Fracture analysis of fiber reinforced concrete structures in the micropolar peridynamic analysis framework, *Engineering Fracture Mechanics* 169 (2017) pp.238-250
[21] W. Gerstle, N. Sau, S. Silling, Peridynamic modeling of concrete structures, *Nuclear Engineering and Design* 237 (2007) pp. 1250-1258
[22] ANSYS 21 APDL help manual
[23] K. J. Willam, E. D. Warnke, Constitutive Model for the Triaxial Behavior of Concrete, *Proceedings*, *International Association for Bridge and Structural Engineering*, Vol. 19, ISMES, Bergamo, Italy, p. 174. 1975.
[23] J. H. P. de Vree, W. A. M. Brekelmans, M. A. J. van Gils, Comparison of nonlocal approaches in continuum damage mechanics, *Computers & Structures* 55 (1995) pp. 581-588

Bray-Liebhafsky reaction: From monotonous to chaotic evolution

Željko D. Čupić[*] and Ana Z. Ivanović-Šašić[†]

Institute of Chemistry, Technology and Metallurgy, University of Belgrade, Department of Catalysis and Chemical Engineering, Njegoševa 12, 11000 Belgrade, Serbia

ABSTRACT

Many physicochemical processes can exhibit various forms of non-linear dynamics, which have been widely investigated in the oscillatory reaction Bray-Liebhafsky, too. The stoichiometry of this reaction corresponds to the hydrogen peroxide decomposition to water and oxygen in an acidic environment, in the presence of iodate ions as a catalyst. During this reaction an oscillatory change of the intermediate species concentration, along with a cascade change in the hydrogen peroxide concentration and oxygen removal can be obtained. By selecting the experimental conditions, the simple periodic or complex chaotic concentration changes can be generated. Concentration oscillations are a consequence of alternating dominance of different reaction pathways present in the reaction mechanism. Large extent of the phenomena experimentally observed in the oscillatory reaction Bray-Liebhafsky is well explained by the mechanistic model, investigated by the Belgrade group over a many years.

Acknowledgement. The present investigations were partially supported by The Ministry of Education, Science and Technological Development of the Republic of Serbia, under Project 172015 and 45001 and contract number 451-03-68/2022-14/200026. This research was also supported by Science Fund of Republic of Serbia #Grant Number. 7743504, Physicochemical aspects of rhythmicity in neuroendocrine systems: Dynamic and kinetic investigations of underlying reaction networks and their main compounds, NES.

[*]e-mail: zcupic@nanosys.ihtm.bg.ac.rs

[†] e-mail: ana.ivanovic@nanosys.ihtm.bg.ac.rs

1. Introduction

In everyday practice of the whole of human activity, including physical chemistry, the nonlinear dynamics is represented at least equally as well as linear; actually, linear dynamics is only a limit case of the nonlinear one. [1] Probably, the human tendency toward simplification and limited capacity of the human brain to perceive and predict the nonlinear dynamics, are the only ones responsible for the long-standing dominance of linear models of natural processes. This statement is supported by the fact that the processes of nonlinear dynamics are observed in all areas that are the subject of scientific considerations, among which are the typical examples in elementary particle physics, [2] in chemical kinetics, [3]-[7] in electrochemistry [8]-[10] in cell biochemical processes [11] and at the level of multicellular organisms, [12],[13] in population processes at the level of ecosystems, [14] in the economy [15] and astrophysics. [16]

The study of homogeneous oscillatory reactions (such as: the Bray-Liebhafsky one [17]-[30] – first reported homogeneous oscillatory chemical reaction, the Belousov-Zhabotinsky [31]-[38] – the most popular one, and the Briggs-Rauscher [39]-[43] oscillatory reaction) is one of the most important contributions from physical chemistry to development of the nonlinear dynamics. In this area, oscillatory reaction Bray-Liebhafsky (BL) has a particular importance because it was first discovered homogeneous oscillatory chemical reaction, furthermore, because it is probably the simplest studied chemical oscillator, but also, because the study of this system allow the experimental and numerical analysis of a wide range of dynamic phenomena.

Multiple-time-scale behavior of the BL reaction is explored here to explain mechanistic sources of dynamic transitions. Different levels of understanding oscillatory process are described here by models with varying complexity. Hence, present paper presents results about modeling BL reaction at different levels.

2. Multi-level modeling of the BL reaction

The Bray-Liebhafsky reaction is the hydrogen peroxide decomposition in the presence of iodate and hydrogen ions, as catalysts. This, apparently simple oscillatory reaction, known as the Bray-Liebhafsky one, consists of a complex homogeneous catalytic oscillatory processes involving periodic changes in concentrations of numerous iodine intermediates such as I_2, I^-, HIO, HIO_2 and I_2O, that all oscillates in the same time-scale, but in different phases and relative intensities. [25] Periodic changes of the solution color, oxygen removal and indicator electrode potential were detected in this system, at temperatures between 20°C and 65°C. Periodicity in this system is a consequence of complex reaction mechanism which consists of a series of reaction steps with multiple feedbacks. Just like any complex process, the BL reaction may be modeled at several levels of understanding. Here, it will be described starting from the most

rudimentary, system level, where system components are defined, and then, with gradually increasing complexity, details of the process will be added to the model, making it, finally, convenient to describe even the strangest dynamic states of chaos.

2.1. System-level – components

Investigation of the BL reaction is often performed in either open or closed reactor, usually in the form of thermostated bath with some mixing device (Fig 1.). Although the system has finite phase boundary, reaction goes on within the liquid phase. The advantage of open systems over the closed ones is in the presence of inlets/outlets for continuous inflow/outflow of reactants/reaction mixture, which is the external force used to maintain this dissipative system in vicinity of the unstable steady state, far from equilibrium.

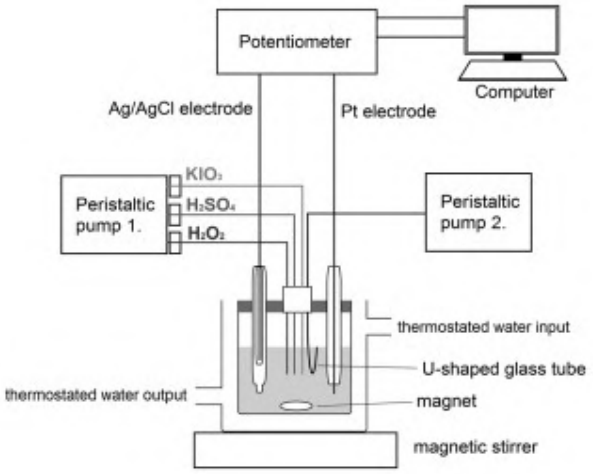

Figure 1. *Continuous Stirred Tank Reactor* (CSTR). If pumps are removed, the batch reactor is obtained.

Flow rate in open oscillating BL systems is always small against the fast reaction rates in oscillations, and mixing makes the liquid system macroscopically homogeneous. Thermostated coat ensures that rate constants have really constant values independent on extent of the reaction and its heat effects. Hence, usual approach in modeling BL reaction assumes deterministic, mean field approximation, where state of the system is represented by mean concentrations of all species. Thus, the BL reaction is described by the system of *Ordinary Differential Equations* (ODE) which depicts the changes in concentration of reaction species in time (see below).

Moreover, the first approximation of the BL reaction system would have to be nothing else, but liquid water (H_2O), since it is by far the most abundant component in the system. The water concentration is about 55 M and concentrations of other macro-components (H_2O_2, H^+, IO_3^-, K^+, SO_4^{2-}) are for about three orders of magnitude lower. Besides, ionic species K^+ and SO_4^{2-} are not involved in any significant reaction, and will not be considered further. Thus, typical concentration of hydrogen peroxide (as well as H^+ and IO_3^-) during the oscillatory state of the system is between 10^{-2} and 10^{-1} M, the concentration of iodine, I_2, is between 10^{-5} and 10^{-4} M, whereas the concentrations of other intermediary species are even much lower, between 10^{-9} and 10^{-6} M. Nonetheless, the role of water in the BL system is often neglected and underestimated, since it is not directly involved in reduction - oxidation processes. There is no doubt that water plays important role in solvation, changing all reaction rates and dynamics of the oscillating process. There is also increasing number of evidences that water is even more important, taking part in redirecting energy transfer during the delicate oxidation phase of the BL reaction. [44]-[48] However, we are still far away from clear understanding of water structure and its dynamics, and therefore, this level of modeling will here, again, be neglected. All effects of water will here be considered as included in rate constants of particular reactions.

2.2. Process-level – reaction

The most intensive effect of the BL reaction is the decomposition of the hydrogen peroxide with production of oxygen.

$$2H_2O_2 \xrightarrow{IO_3^-, H^+} 2H_2O + O_2 . \qquad \text{(D)}$$

Process is followed by the stoichiometricaly equivalent production of water, which has no noticeable effect on overall composition, since it is already present in large excess. Concentrations of two other macrocomponents (iodate and hydrogen ions) are changed during reaction, but in so small extent that we can consider them as constant, and equal to initial values during the whole process. Thus, their role is mainly catalytic. Hence, corresponding reaction (D) represents the next level model of the BL reaction. The process (D) is irreversible, since oxygen leaves liquid phase and goes to the gas phase. Consequently, the equilibrium is never reached and reaction goes until complete exhaust of the hydrogen peroxide as the only reactant. Since hydrogen peroxide decays in time, and oxygen, as the only product besides water, leaves the mixture through the phase boundary, concentrations of all species in liquid mixture are much less than the water content in all times, and hence, new model is consistent with previous one.

The BL reaction rate depends on several control parameters, such as the temperature in both reactors (closed and open) and flow rate in open reactor, or also the initial concentrations of the above mentioned reaction species (H^+ and IO_3^-) which are aproximately constant during reaction. Finally, reaction rate in BL reaction depends also on hydrogen peroxide concentration. Usually, decomposition reactions correspond to the first order reaction kinetics. In fact, within a very wide region of concentration values of the BL system constituents, hydrogen peroxide concentration really monotonously decays in time with first order kinetics. Even, during the periodic changes of iodine species concentrations, while hydrogen peroxide decays in cascades, small steps in its concentration curve could be neglected, and overall change fits well the first order kinetics (Fig. 2).

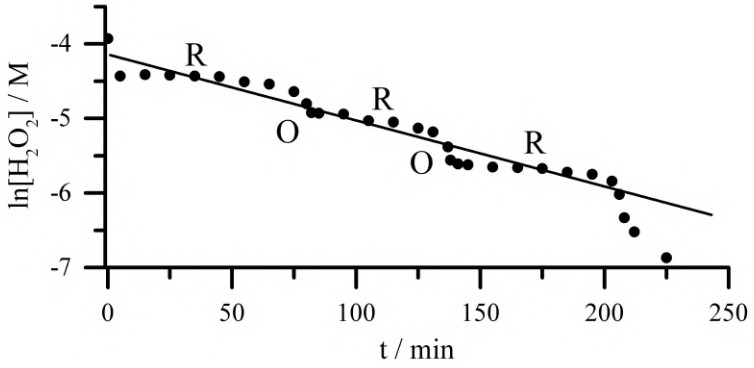

Figure 2. Changes of the hydrogen peroxide concentration with time, during oscillatory reaction BL. Solid circles designate experimentally measured values and line approximates the first order decay. The R and O branches are indicated. Results from ref. [49].

2.3. Alternate-pathways-level of modelling

Periodic changes of the solution color (connected with hydrogen peroxide concentration changes, Fig. 2) observed in the BL system are not explained either by the stoichiometry of the reaction (D) or by the simple first order reaction kinetics. The first attempt to explain these phenomena was already in the first report about the BL oscillatory reaction, [17] where Bray analyzed dual role of hydrogen peroxide as an oxidizing and reducing agent. There, he noticed that the hydrogen peroxide decomposition to water and oxygen in the presence of iodate and hydrogen ions is the result of the reduction (R) of iodate to iodine and the oxidation (O) of iodine to iodate by the following reaction scheme:

$$2IO_3^- + 2H^+ + 5H_2O_2 \rightarrow I_2 + 5O_2 + 6H_2O \quad \text{(R)}$$

$$I_2 + 5H_2O_2 \rightarrow 2IO_3^- + 2H^+ + 4H_2O \,. \quad \text{(O)}$$

Rates of the two processes are in such ratio that only small extent of the iodate is converted to iodine and *vice versa* in any moment of time. Their rates tend to become equal, and, when the two processes achieve balance, the overall process is represented by the sum of these two reactions (R) and (O), which is identical to the smooth decomposition reaction (D). Then, we usually observe only a smooth decomposition described by reaction (D) where iodine, as intermediate species, does not appear in corresponding net stoichiometric relation. Hence, the model is at present level in consistency with the previous one. However, concentration of iodine, produced in reaction pathway (R), and removed in reaction pathway (O), gives coloration to the BL system solution. Periodic changes of the color are induced by periodic changes in the domination of the processes (R) and (O). Namely, in a narrow range of initial concentrations values, the alternating domination of processes (R) and (O) occurs, resulting in alterations between periods of slower increase (R branch) and faster decrease (O branch) of the iodine concentration during stepwise decrease of the hydrogen peroxide and increase of the oxygen concentrations.

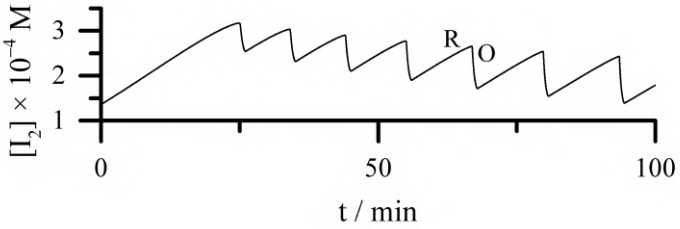

Figure 3. Changes of the iodine concentration with time, during oscillatory reaction BL. The R and O branches are indicated. The concentrations of iodate and hydrogen ions were: $[IO_3^-] = 0.0474$ M, $[H^+] = 0.0958$ M. Rate constants are taken from the ref. [50].

Nevertheless, it is obvious that the two reactions cannot be elementary processes. Their kinetics was investigated in many years and complex kinetic rates were established indicating several reaction steps with many intermediary species involved in each of the two. At the end, no rate law identified in two of the processes could successfully simulate periodic changes. Thus, stoichiometry of periodic processes was well described at the present level of model, but not the reaction kinetics. More precisely, the necessary feedback needs to be included in the model of the reaction mechanism.

2.4. Kinetic level – model capable to simulate oscillatory dynamics

In attempts to construct appropriate model able to simulate oscillating reaction, several reaction networks were synthesized with all possible reaction steps and intermediary species. However, reaction rates mainly remained unknown. Therefore, modeling based on such detailed description was still unsuccessful. Further development leaded to several approximations and model reductions, based on excluding very slow or less probable reaction pathways and condensing details of complex branches from detailed reaction network into simplified representations by single steps with empirically evaluated rate constants. This phase in the frame of modeling process is not uniquely defined and, consequently, several models occurred attempting to explain the BL system. [17]-[19],[21],[22],[50]-[60] Among the most successful results, there is a model M(1-8) represented by eight reactions or reaction steps (R1-R8 in Table 1), where three of them are reversible. It will be used in the following analysis of the process.

Summation of all reactions in model M(1-8) gives again reaction (D), making system inherently consistent with its lower level representation. Reaction (D) represents smooth decomposition steady state of the model M(1-8), in which, all reactions run with equal rate. Reactions (R) and (O) are also incorporated in the reaction network of the model M(1-8), but in less obvious way. They are manifested only as partial sums of certain reaction pathways alternately dominating during the reduction and oxidation phase in oscillations (Table 2).

Table 1. Model M(1-8) of the BL reaction used in numerical simulations under batch conditions. [57]

Reaction or Reaction step			Reaction rate[a]	No.
$IO_3^- + I^- + 2H^+$	$\rightleftharpoons$	$HIO + HIO_2$	$r_1 = k_1 [I^-]$ $r_{-1} = k_{-1} [HIO] [HIO_2]$	(R1) (R–1)
$HIO_2 + I^- + H^+$	$\longrightarrow$	$I_2O + H_2O$	$r_2 = k_2 [HIO_2] [I^-]$	(R2)
$I_2O + H_2O$	$\rightleftharpoons$	$2HIO$	$r_3 = k_3 [I_2O]$ $r_{-3} = k_{-3} [HIO]^2$	(R3) (R–3)
$HIO + I^- + H^+$	$\rightleftharpoons$	$I_2 + H_2O$	$r_4 = k_4 [HIO] [I^-]$ $r_{-4} = k_{-4} [I_2]$	(R4) (R–4)
$HIO + H_2O_2$	$\longrightarrow$	$I^- + H^+ + O_2 + H_2O$	$r_5 = k_5 [HIO]$	(R5)
$I_2O + H_2O_2$	$\longrightarrow$	$HIO + HIO_2$	$r_6 = k_6 [I_2O]$	(R6)
$HIO_2 + H_2O_2$	$\longrightarrow$	$IO_3^- + H^+ + H_2O$	$r_7 = k_7 [HIO_2]$	(R7)
$IO_3^- + H^+ + H_2O_2$	$\longrightarrow$	$HIO_2 + O_2 + H_2O$	$r_8 = k_8$	(R8)

[a] Reaction rate constants at 60°C: $k_1 = 1.383 \times 10^2$ min^{-1}; $k_{-1} = 7.91 \times 10^7$ mol^{-1} × dm^3 × min^{-1}; $k_2 = 4.79 \times 10^{10}$ mol^{-1} × dm^3 × min^{-1}; $k_3 = 5.00 \times 10^3$ min^{-1}; $k_{-3} = 3.15 \times 10^8$ mol^{-1} × dm^3 × min^{-1} ; $k_4 = 3.00 \times 10^{11}$ mol^{-1} × dm^3 × min^{-1}; $k_{-4} = 46.97$ min^{-1}; $k_5 = 2.974 \times 10^2$ mol^{-1} × dm^3 × min^{-1}; $k_6 = 1.00 \times 10^4$ mol^{-1} × dm^3 × min^{-1}; $k_7 = 4.00 \times 10^1$ mol^{-1} × dm^3 × min^{-1}; $k_8 = 4.4606 \times 10^{-6}$ min^{-1}. The concentrations of iodate and hydrogen ions, taken as constant in simulations ($[IO_3^-] = 0.0474$ mol × dm^{-3} and $[H^+] = 0.0958$ mol × dm^{-3}) are included in corresponding rate constants. Unlike the models presented in the literature, here, the concentration of hydrogen peroxide is taken as constant in simulations, too ($[H_2O_2] = 0.0200$ mol × dm^{-3}) and also included in corresponding rate constants.

Hence, reactions (R) and (O) and corresponding reaction pathways represent some new kind of steady states, other than smooth decomposition one. Corresponding steady states must be connected with balanced production and consumption of selected intermediary species, only. The hydrogen peroxide is always only consumed and therefore it cannot be balanced in present model. Besides, the iodine is also produced from iodate in process (R) and it is spent in process (O) to regenerate iodate. Hence, production and consumption are not balanced for these two species in corresponding (R) and (O) steady states. Other iodine species do not appear in the observed stoichiometry, and thus, seem to be

balanced. Similar differentiation between reaction species is usually connected with slow-fast dynamics.

Table 2. The reaction pathways derived from the model M(1-8)

1.Reaction pathways:
(R2) + (R5) + (R6)
(R1) + (R5) + (R7)
(R-1) + (R2) + (R6) + (R8)
(R7) + (R8)
Net reaction (D)
$2H_2O_2 \rightarrow 2H_2O + O_2$
2.Reaction pathways:
2x(R1) + 2x(R2) + 2x(R3) + (R4) + 5x(R5)
3x(R-1) + 2x(R2) + 2x(R3) + (R4) + 5x(R8)
2x(R2) + 2x(R3) + (R4) + 3x(R5) + 2x(R8)
Net reaction (R)
$2IO_3^- + 2H^+ + 5H_2O_2 \rightarrow I_2 + 5O_2 + 6H_2O$
3.Reaction pathways:
2x(R-1) + 3x(R2) + 2x(R-3) + (R-4) +5x(R6)
(R1) + 2x(R-3) + (R-4) + 2x(R6) + 3x(R7)
(R2) + 2x(R-3) + (R-4) + 3x(R6) + 2x(R7).
Net reaction (O)
$I_2 + 5H_2O_2 \rightarrow 2IO_3^- + 2H^+ + 4H_2O$

Slow and fast subsystem

Obvious difference between reaction species included in the model, is in the concentration levels. The concentrations of reaction species in the considered process differ for several orders of magnitudes among themselves. Thus, in oscillatory dynamic state of the BL system, typical concentration of hydrogen peroxide is between 10^{-2} and 10^{-1} M, concentration of iodine is between 10^{-5} and 10^{-4} M, whereas the concentrations of other species are much lower, between 10^{-9} and 10^{-6} M.

In systems, where concentrations of crucial species differ significantly, the *relaxation oscillations* are common. Such oscillations are generated by alternating relatively long periods of slow changes, eventually interrupted by short and sudden jumps to another state of relatively slow changes. These oscillations are connected with slow-fast dynamical systems where dynamical variables are divided in slow and fast ones, according to time scale at which they are changed. There, fast variables always quickly adjust to any change in

slow variables, which act as the parameters for the fast subsystem. Dynamics of such systems is reduced to lower dimensional subspace of the phase space.

Hydrogen peroxide, hydrogen ion and iodate concentrations are much higher than those of other species and one can approximate that they are constant. Thus, in a case where these concentrations are considered as a fixed parameters, iodine concentration is the only slow variable and concentrations of other four iodine species (I^-, HIO, HIO_2, I_2O) from the Model(1-8) are fast variables. The stationary values of fast variables are positioned on the one-dimensional curve in five-dimensional space. This curve, known as *slow nullcline*, represents steady states of the fast subsystem, which are functionally dependent on instantenous values of the slow variable, iodine concentration. There are other nullclines too, and they correspond to various combinations of four variables, among complete set of five ones. However, only the one that correspond to the set of fast variables only, attracts the trajectories from the whole phase space and it represents one form of the so-called slow manifold of the dynamical system. Starting from an arbitrary point in the phase space, the system follows its fast component dynamics and jumps to the nearest point on the slow nullcline. Once after the system reaches it, fast variables are balanced and only slow component of the dynamics governs further propagation over the nullcline, ending usually in the special point on the nullcline representing stable steady state. Therefore, this specific nullcline is named the slow nullcline, while all others are fast ones. The direction of propagation over the slow nullcline is governed by relative position of the dynamic system with respect to the fast nullclines. The steady state is positioned in the crosspoint of slow and fast nullclines.

In the domain where relaxation oscillations are present slow nullcline is folded having at least two stable and one unstable branch in one interval of slow variable values. Slow nullcline calculated for the studied model is folded, as can be seen in Fig. 4. The steady state is in that case positioned on the unstable middle branch of the slow nullcline, and this steady state is also unstable. In that case, the fast variables often alternate between two stable branches resulting in relaxation oscillatory evolution of considered dynamical system.

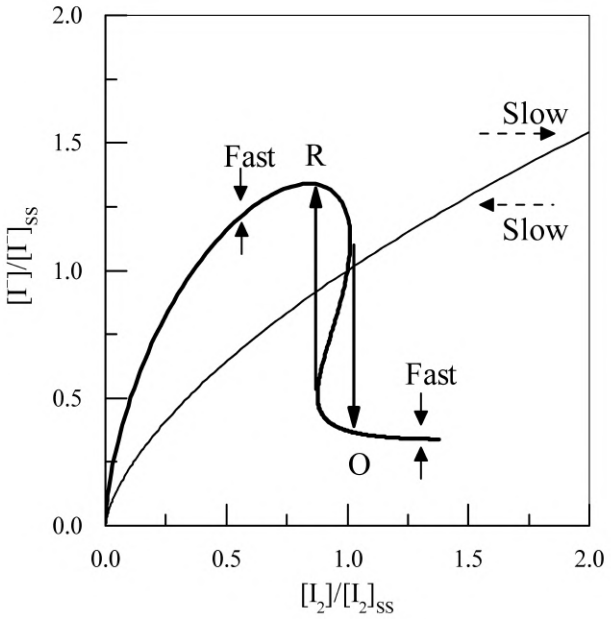

Figure 4. Slow (thick) and fast (thin) nullclines of the Model(1-8). R and O branches of the folded slow nullcline are designated. Arrows indicate directions of fast (solid line) and slow (dashed line) components of the dynamics in areas divided by nullclines.

Described two stable branches of the slow nullcline correspond to reaction pathways (R) and (O). System represented by the point on the upper branch (high iodide concentration) evolves according to (R) stoichiometry. It means that iodine concentration is increased and point is moved to right until it eventually reaches fold point delimiting stable and unstable branch. At this special point, system tends to continue increasing iodine concentration but for new higher values only lower branch values of the fast variables could satisfy fast subsystem steady state conditions. Hence, the system jumps to lower branch of the nullcline. There, it moves toward lower values of the iodine concentration according to the stoichiometry of (O) process until it comes to the other fold point. From this point, the only way is the new jump to the upper branch where cycle is closed. According to calculated nullclines Model(1-8) should be able to simulate oscillations. However, it must be confirmed by direct numerical experiment.

Numerical simulations

For final tests of oscillatory properties, the Model(1-8) must be used to generate periodic changes of concentrations. Hence, the system of ODE-s must be formed in accordance with the model. Each concentration is changed with rate which is sum of individual reaction rates multiplied by corresponding stoichiometric coefficients. Rates of individual reaction steps are given in Table 2, according to reaction stoichiometry and mass action law. Relative significance of these steps is given by rate constants multiplying concentrations of reacting species in particular step. The same rules could be used to form rate equations for each one reaction species, no matter if it is reactant, product, or intermediary species. However, some of reaction species are dynamically unimportant. Since the concentrations of iodate and hydrogen ions are significantly larger than the concentrations of other reaction species, they can be considered as constant without affecting qualitatively the results. Extending the model with two differential equations to account for the temporal evolution of these two species does not alter the dynamic structure of the system, including the highly sensitive mixed mode oscillation range, but only shifts a little the bifurcation points with respect to any control parameter values. [61] Hence the calculations presented here use $[IO_3^-] = 0.0474$ and $[H^+] = 0.0958$ mol/dm^3. [62],[63] Furthermore, in model M(1-8) hydrogen peroxide is the only reactant. The reaction kinetics depends on its concentration only parametrically. Its changes in oscillations are much slower than others, and we consider that it is not essential for occurrence of oscillations and it will be taken as constant in the first approximation. Hence, in the model under consideration, there are five independent intermediary species: I_2, I^-, HIO, HIO_2 and I_2O and only they are dynamically important.

$$\begin{aligned}
&d[I_2]/dt = r_{+4} - r_{-4} \\
&d[I^-]/dt = -r_{+1} + r_{-1} - r_2 - r_{+4} + r_{-4} + r_5 \\
&d[HIO]/dt = r_{+1} - r_{-1} + 2\,r_{+3} - 2\,r_{-3} - r_{+4} + r_{-4} - r_5 + r_6 \\
&d[HIO_2]/dt = r_{+1} - r_{-1} - r_2 + r_6 - r_7 + r_8 \\
&d[I_2O]/dt = r_2 - r_{+3} + r_{-3} - r_6.
\end{aligned} \tag{1}$$

The r_i, r_{+i} and r_{-i} denote respectively the rates of whole reactions i, its forward part and its reverse part. The values given in Table 1 are taken from ref. [64],[65] and include fixed concentrations of iodate, hydrogen ions and hydrogen peroxide.

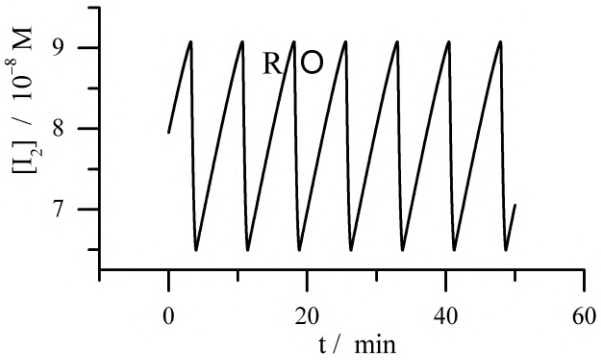

Figure 5. Numerical simulations of the Model(1-8). $[H_2O_2] = 0.02$ M.

Results in Fig. 5 confirm ability of the Model(1-8) to simulate sustained oscillations of iodine, maintaining the same type of relaxation oscillations as they are observed in experiments.

2.5. Dynamic level – model capable to simulate chaotic dynamics

In numerical simulations of batch reactor experiments, changes of hydrogen peroxide concentrations are also important, just because its parametrical influence on changes in the form of oscillograms. Hence, additional differential equation has to be added for new variable:

$$d[H_2O_2]/dt = -r_5 - r_6 - r_7 - r_8 . \quad (2)$$

Moreover, some rate equations need to be adapted since hydrogen peroxide concentration is not included in rate constants any more: $k_5 = 1.487 \times 10^4$ mol^{-1} × dm^3 × min^{-1}; $k_6 = 5.00 \times 10^5$ mol^{-1} × dm^3 × min^{-1}; $k_7 = 2.00 \times 10^3$ mol^{-1} × dm^3 × min^{-1}; $k_8 = 2.2303 \times 10^{-4}$ min^{-1}. Apropriate rate expressions are now:

$$\begin{aligned} r_5 &= k_5 [HIO] [H_2O_2] \\ r_6 &= k_6 [I_2O] [H_2O_2] \\ r_7 &= k_7 [HIO_2] [H_2O_2] \\ r_8 &= k_8 [H_2O_2]. \end{aligned} \quad (3)$$

The shape of the slow nullcline is dependent on parametrically changing hydrogen peroxide concentration. By merging slow nullclines for the range of hydrogen peroxide concentrations, one obtains folded surface that attracts all trajectories from the phase space. Since hydrogen peroxide concentration is slowly decaying in closed reactor, oscillations are evolving with time as system slowly glides over the surface (Fig. 6). After some time, system approaches the point where folded surface unfolds and oscillations disappear through the

sequence of damped, nearly harmonic oscillations. This transition corresponds to supercritical Andronov-Hopf bifurcation that occurs at critical value of hydrogen peroxide concentration.

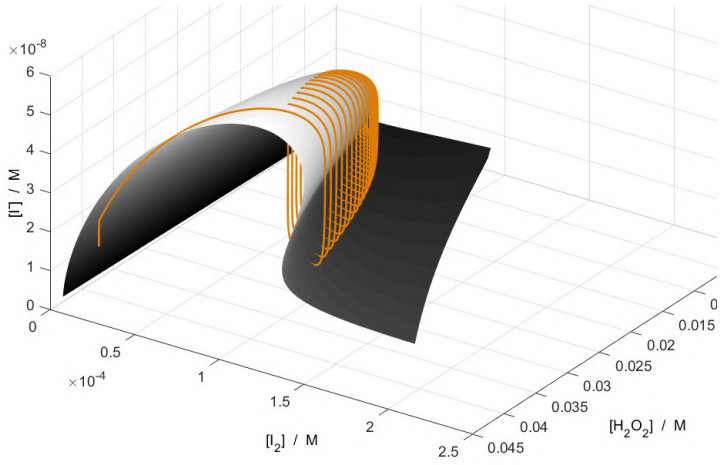

Figure 6. Surface of slow nullclines for a sequence of $[H_2O_2]$ values and trajectory of the BL reaction obtained for the Model(1-8) in the batch reactor.

Thus, at this level of modelling, damped oscillations of relaxation type, as well as nearly harmonic ones, are successfully described by model M(1-8). Even many other properties of the experimental oscillograms are simulated with given model, including pre-oscillatory period, and dependence on initial concentrations or temperature. However, complex oscillations are still not explained at this level of approximation.

Complex dynamic states like chaos, are better examined in open reactor where the selected dynamics can be sustained infinitely. Although, the first eight reactions in Table 1, are enough to describe well the mechanism of the process under batch conditions, additional ones must be taken into account in an open *continuous stirred tank reactor* (CSTR), where complex oscillations could be maintained for a very long time. Additional reactions represent only inflow and outflow of chemical species into the reaction mixture and out of it (Table 3). In this extended model only hydrogen peroxide is considered as the inflow species. (The reaction system can be open with respect to other species, too. However, in that case, the number of intermediate species and related reactions increases importantly resulting in large mathematical problems without essentially important results.) In the model under consideration, where hydrogen peroxide is taken as the only inflow species, there are now six independent species: H_2O_2,

I_2, I^-, HIO, HIO_2 and I_2O and again, they are all dynamically important. Concentrations of iodate and hydrogen ions are again considered as constant. Hence the calculations presented here use $[IO_3^-] = 0.0474$ and $[H^+] = 0.0958$ mol/dm^3 as before. [62],[63] The time evolutions of other species are described by the six following differential equations:

$$\begin{aligned}
&d[H_2O_2]/dt = -r_5 - r_6 - r_7 - r_8 + j_0([H_2O_2]_{in} - [H_2O_2])\\
&d[I_2]/dt = r_{+4} - r_{-4} - j_0[I_2]\\
&d[I^-]/dt = -r_{+1} + r_{-1} - r_2 - r_{+4} + r_{-4} + r_5 - j_0[I^-]\\
&d[HIO]/dt = r_{+1} - r_{-1} + 2r_{+3} - 2r_{-3} - r_{+4} + r_{-4} - r_5 + r_6 - j_0[HIO]\\
&d[HIO_2]/dt = r_{+1} - r_{-1} - r_2 + r_6 - r_7 + r_8 - j_0[HIO_2]\\
&d[I_2O]/dt = r_2 - r_{+3} + r_{-3} - r_6 - j_0[I_2O].
\end{aligned} \tag{4}$$

The values given in Table 3 are taken from the already published model [64],[65] and include fixed concentrations of iodate and hydrogen ions.
Thus, mathematically speaking, we are dealing with six-dimensional problem. This model is able to describe almost all features of BL reaction, including regular simple oscillatory evolution, periodic mixed-modes with *large-amplitude oscillations* (LAO-s) and *small-amplitude oscillations* (SAO-s), as well as the chaotic occurrence of LAO-s and SAO-s and their combinations. [66]

Table 3. Model M(1-15) of the BL reaction used in numerical simulations under CSTR conditions.[50]

Reaction			Reaction rate[a]	No.
$IO_3^- + I^- + 2H^+$	$\rightleftharpoons$	$HIO + HIO_2$	$r_1 = k_1 [I^-]$ $r_{-1} = k_{-1} [HIO] [HIO_2]$	(R1) (R–1)
$HIO_2 + I^- + H^+$	$\longrightarrow$	$I_2O + H_2O$	$r_2 = k_2 [HIO_2] [I^-]$	(R2)
$I_2O + H_2O$	$\rightleftharpoons$	$2HIO$	$r_3 = k_3 [I_2O]$ $r_{-3} = k_{-3} [HIO]^2$	(R3) (R–3)
$HIO + I^- + H^+$	$\rightleftharpoons$	$I_2 + H_2O$	$r_4 = k_4 [HIO] [I^-]$ $r_{-4} = k_{-4} [I_2]$	(R4) (R–4)
$HIO + H_2O_2$	$\longrightarrow$	$I^- + H^+ + O_2 + H_2O$	$r_5 = k_5 [HIO] [H_2O_2]$	(R5)
$I_2O + H_2O_2$	$\longrightarrow$	$HIO + HIO_2$	$r_6 = k_6 [I_2O] [H_2O_2]$	(R6)
$HIO_2 + H_2O_2$	$\longrightarrow$	$IO_3^- + H^+ + H_2O$	$r_7 = k_7 [HIO_2] [H_2O_2]$	(R7)
$IO_3^- + H^+ + H_2O_2$	$\longrightarrow$	$HIO_2 + O_2 + H_2O$	$r_8 = k_8 [H_2O_2]$	(R8)
$(H_2O_2)_{in}$	$\longrightarrow$	H_2O_2	$r_9 = j_0 [H_2O_2]_{in}$	(R9)
H_2O_2	$\longrightarrow$	$(H_2O_2)_{out}$	$r_{10} = j_0 [H_2O_2]$	(R10)
I^-	$\longrightarrow$	$(I^-)_{out}$	$r_{11} = j_0 [I^-]$	(R11)
HIO	$\longrightarrow$	$(HIO)_{out}$	$r_{12} = j_0 [HIO]$	(R12)
HIO_2	$\longrightarrow$	$(HIO_2)_{out}$	$r_{13} = j_0 [HIO_2]$	(R13)
I_2O	$\longrightarrow$	$(I_2O)_{out}$	$r_{14} = j_0 [I_2O]$	(R14)
I_2	$\longrightarrow$	$(I_2)_{out}$	$r_{15} = j_0 [I_2]$	(R15)

[a] Reaction rate constants at 60°C: $k_1 = 1.383 \times 10^2$ min^{-1}; $k_{-1} = 7.91 \times 10^7$ mol^{-1} × dm^3 × min^{-1}; $k_2 = 4.79 \times 10^{10}$ mol^{-1} × dm^3 × min^{-1}; $k_3 = 5.00 \times 10^3$ min^{-1}; $k_{-3} = 3.15 \times 10^8$ mol^{-1} × dm^3 × min^{-1} ; $k_4 = 3.00 \times 10^{11}$ mol^{-1} × dm^3 × min^{-1}; $k_{-4} = 46.97$ min^{-1}; $k_5 = 1.487 \times 10^4$ mol^{-1} × dm^3 × min^{-1}; $k_6 = 5.00 \times 10^5$ mol^{-1} × dm^3 × min^{-1}; $k_7 = 2.00 \times 10^3$ mol^{-1} × dm^3 × min^{-1}; $k_8 = 2.2303 \times 10^{-4}$ min^{-1}. In CSTR we distinguish inflow species $(X_i)_{in}$ and outflow species $(X_i)_{out}$. The concentrations of iodate and hydrogen ions, taken as constant in simulations ($[IO_3^-] = 0.0474$ mol × dm^{-3} and $[H^+] = 0.0958$ mol × dm^{-3}) are included in corresponding rate constants. The inflow concentration of hydrogen peroxide was $[H_2O_2]_{in} = 0.155$ mol × dm^{-3}. Flow rate as control parameter is designated as j_0.

Hydrogen peroxide is now considered as dynamical variable, but since it has largest concentration and is changed at smallest extent, it is now included in the list of slow species. Thus, now there are two slow and four fast variables. The

stationary values of fast variables are now positioned on the two-dimensional surface in six-dimensional phase space. It is known as *manifold*. It is nearly the same as the folded surface formed by merging nullclines of the smaller model M(1-8) for batch reactor. However, manifold surface is constructed from the larger extended model and this surface now consists of points representing steady states of the fast subsystem, which is functionally dependent on instantenous values of both slow variables. In the domain where relaxation oscillations are present, this surface is folded, having at least two stable and one unstable branch. Such a manifold calculated with the studied model can be seen in Fig. 7. Fast variables in that case often alternate between two stable branches resulting in relaxation oscillatory evolution of considered dynamical system.

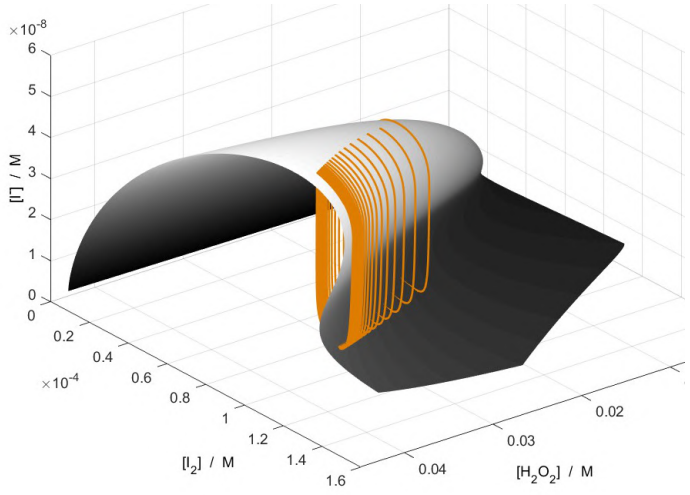

Figure 7. Surface of slow manifold and trajectory of the BL reaction obtained for the Model(1-15) in the CSTR.

In singular perturbation theory all variables are usually classified just as slow or fast ones, such that we are dealing, there, with the models having usually just two fast and one slow, or just one fast and two slow ones. These models exhibit different dynamical characteristics. Moreover, dynamical system with two slow and one fast variable can often be rescaled to system with one slow and two fast variables. [67],[68] Considered model is selforganized in such manner that its dynamical states can alternate during the course of reaction, between the ones characteristic for two slow and one fast variable to the others characteristic for one slow and two fast variables. [67]

In chemical, physicochemical and biochemical nonlinear dynamical systems the multiple-time-scale models consist commonly of three time-scale types of variables. There are, usually, several slow ones (external species, generally, reactants and products), several fast ones (internal species, intermediates) and often a middle one (the slow-fast one) having either internal or external characteristics in different regions of phase space. Necessary condition for such alternations is that some species belong to middle scale in both, concentration and time scale.

Hence, the situation in BL system is analogous to dynamical systems with two slow and several fast species. However, fast species in the BL system are all synchronized so that they oscillate either in the same phase (HIO, HIO_2 and I_2O), or in the anti-phase (I^-) with each other. Thus, they can be considered as mutually coupled variables, so that only one of them is really independent. In many ways, such a system could be considered as the system with two slow and only one fast species.

In multiple-time-scale systems with more than one slow variable, mixed-mode oscillations (MMOs) may appear within the region with simple sustained oscillations. They generally consist of two types of oscillations with distinct amplitudes: LAOs and SAOs. The LAOs are *global phenomena*, generated by the geometry of the critical manifold having an unstable branch between two stable ones. They are well known as relaxation type dynamics governed by slow sliding of the system over the stable branches of critical manifold, periodically interrupted by much faster jumps from one to another stable branch of this hyper-surface in phase space (as already described at previous level). These fast jumps usually occur at special points (*fold* points forming the *fold line*) of the critical manifold where the stable branch is connected with unstable one.

However, in mixed-mode, LAOs are mixed with SAOs of different nature. They occur at the fold points as a *local phenomena* generated by some *folded singularities*. In the mixed-mode region we can also expect the occurrence of complex dynamic phenomena known as *canards* and *tourbillion*. [67],[69]-[72]

For complex phenomena in dynamical systems on multiple time scales, the fold is an object of special importance, just as steady state is for linear systems and limit cycle for simple oscillations. Fold points are determined according to ref. [67], from the condition:

$$\mathrm{Det}(\mathrm{J}(\mathrm{X_i})) = 0\,, \tag{5}$$

where X_i denotes the fast species HIO, HIO_2, I_2O and I^- and J is the Jacobian of corresponding fast subsystem. This request must be fulfilled on the border between stable and unstable branch of the critical manifold, Fig. 8. Concentrations of slow species are treated here (in evaluation of the Jacobian for fast subsystem) as they are constant. This assumption seems to be

appropriate since they are changing on much slower time scale then the fast ones.
The singularity point on the fold line was calculated according to ref. [67], from the condition:

$$\frac{\mathrm{d}f_1}{\mathrm{d}t}\cdot\frac{\partial g}{\partial x_1}+\frac{\mathrm{d}f_2}{\mathrm{d}t}\cdot\frac{\partial g}{\partial x_2}=0, \tag{6}$$

where x_1 and x_2 are concentrations of slow species, f_1 and f_2 are their corresponding rates and g is a rate of the fast variable. In our case this gives for *e.g.* [HIO]:

$$\frac{\mathrm{d}}{\mathrm{d}t}\left(\frac{\mathrm{d}[\mathrm{H_2O_2}]}{\mathrm{d}t}\right)\cdot\frac{\partial}{\partial[\mathrm{H_2O_2}]}\left(\frac{\mathrm{d}[\mathrm{HIO}]}{\mathrm{d}t}\right)+\frac{\mathrm{d}}{\mathrm{d}t}\left(\frac{\mathrm{d}[\mathrm{I_2}]}{\mathrm{d}t}\right)\cdot\frac{\partial}{\partial[\mathrm{I_2}]}\left(\frac{\mathrm{d}[\mathrm{HIO}]}{\mathrm{d}t}\right)=0. \tag{7}$$

Furthermore, two *nullclines* were evaluated from corresponding rate equations for sets of all four fast species combined with each of two slow ones, Fig. 8. Hence, we have one nullcline that describe the steady state condition of species I_2, HIO, HIO_2, I_2O and I^- (the iodine nullcline) and the other one for the combination H_2O_2, HIO, HIO_2, I_2O and I^- (the hydrogen peroxide nullcline). Each one of two subsystems gives as a solution a line, located in the critical manifold of the fast species. Steady state of the full system is placed in the point where two nullclines intersect, and it will be shortly referred below as the *equilibrium*, keeping in mind that our system is of non-equilibrium type. More precisely, in our papers this is known as disproportionation steady-state.[50]
Finally, *Andronov-Hopf point* was identified numerically on the iodine nullcline using simple test ensuring that the real part of two complex eigenvalues (corresponding to corresponding five dimensional Jacobian) is passing through zero.
The SAO occurs when trajectory comes close to the fold line and starts spiral damped circling around nullcline which contains steady states of slow-fast subsystem including iodine with other fast species. The system becomes closest to the nullcline and amplitude of SAOs are the smallest when this spiral circling gets him nearest to the Andronov-Hopf point. From this point on, spiralling makes system go away from the Andronov-Hopf point and SAO amplitudes are raising leading finally to new global jump representing LAO excursion.

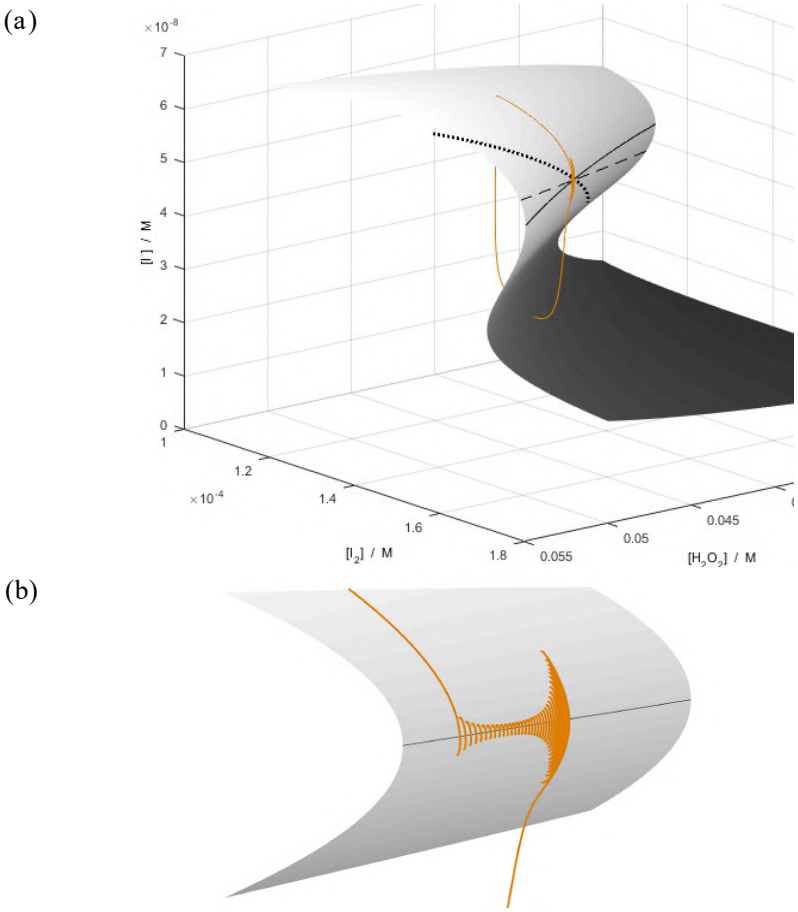

Figure 8. Slow manifold and trajectory of the MMOs for the Model(1-15). (a) The fold line (presented by solid line) and two nullclines (iodine nullcline presented by dashed line and peroxide nullcline by dotted line) are given. (b) Enlarged part showing structure of SAOs around the fold line.

Hence, observed complex mixed mode oscillations are decomposed in three segments by the properties of the analyzed model. First, in the LAOs itself, clear fast dynamic in jumps from one to another manifold branch are alternating with clear slow dynamics over the manifold surface. Then, in SAOs, the third component with mixed slow-fast dynamics leads to spiralling near the fold line. Therefore, the decisive role for the MMO appearance must be ascribed to the iodine species, due to their dynamical role changing from the slow one in LAOs to the fast one in SAOs.

Complex oscillations in the BL system, including LAO and SAO type MMO, could be periodic or aperiodic - chaotic. It depends only on specific ratio between control parameters. Continuous increase of the flow rate, with fixed all other parameters, leads to discontinuous increase (Figure 9) of so called firing number F, indicating fraction of SAOs in MMOs:

$$F = \frac{S}{S + L} \tag{8}$$

where S and L are numbers of SAOs and LAOs in one period, or more generally, total numbers of SAOs and LAOs in long enough sequence of any kind of oscillations, either periodic or aperiodic ones.

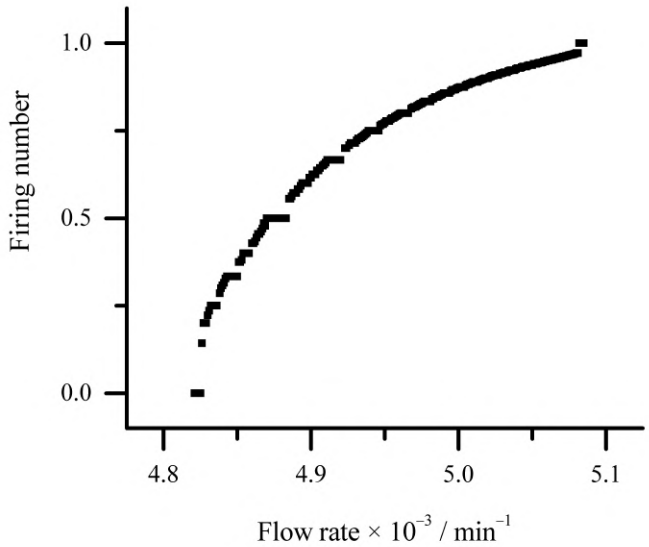

Figure 9. Devil's staircase. Firring number as a function of flow rate for the Model(1-15).

Chaotic windows occur between each pair of periodic dynamic states, Fig. 10. In chaotic dynamic states, irregular alterations of LAO and SAO cycles occur with properties typical for neighboring periodic windows. Hence, the fraction of SAOs and LAOs in MMOs is the only important factor determining if the system will be periodic or chaotic. Furthermore, we explained that this fraction is determined by the fraction of the slow-fast character of the iodine species depending on the flow rate value. Hence, our model successfully explained deterministic dynamic state shifts with controlled changes of the flow rate, Figure 11.

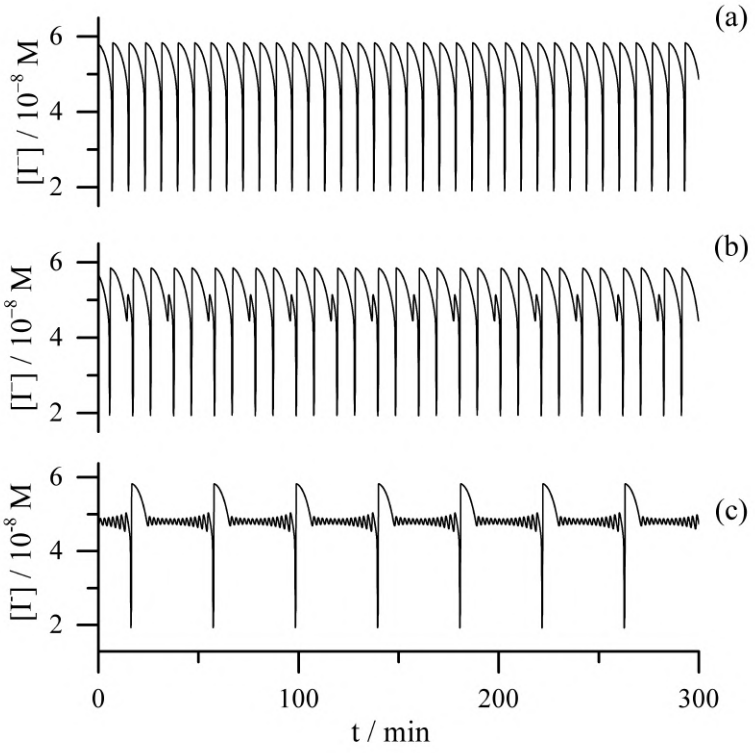

Figure 10. Numerical simulations of the oscillatory dynamics of the BL reaction realized in open reactor (segment from 0 to 300 min) presented by means of the iodide concentration (in mol × dm^{-3}). (a) Regular oscillations, k_f = 4.70×10^{-3} min^{-1}; (b) and (c) mixed-mode oscillations, k_f = 4.842200×10^{-3} min^{-1} and k_f = 5.05×10^{-3} min^{-1}, respectively.

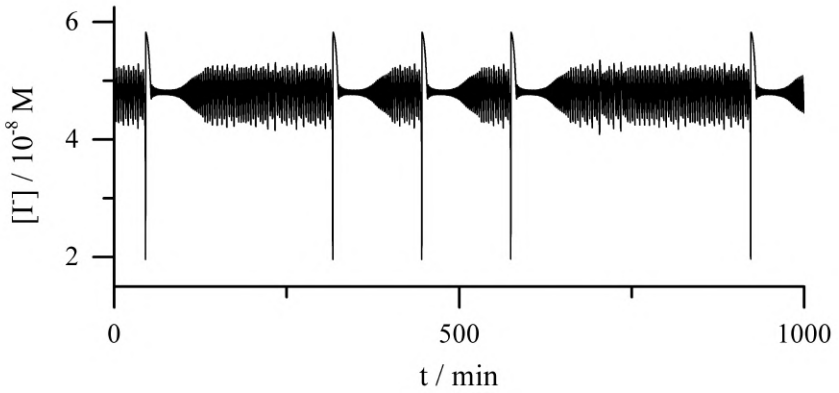

Figure11. Numerical simulations oscillatory dynamics of the BL reaction realized in open reactor (segment from 0 to 1000 min) presented by means of the iodide concentration (in mol × dm^{-3}). Deterministic chaos with chaotically distributed number of the small-amplitude oscillations between the large-amplitude ones, $k_f = 5.0815\times10^{-3}$ min^{-1}.

Generally, chaotic dynamics occurs when limit cycle loose stability with changes of the control parameter values. This kind of behavior is easier to understand through the changes in iteration maps. Two neighbouring periodic states of the BL reaction model are given in Figure 12, one of them corresponding to the dynamic of $4^1 3^1$ type, and the other of $(3^1)_2$ type.

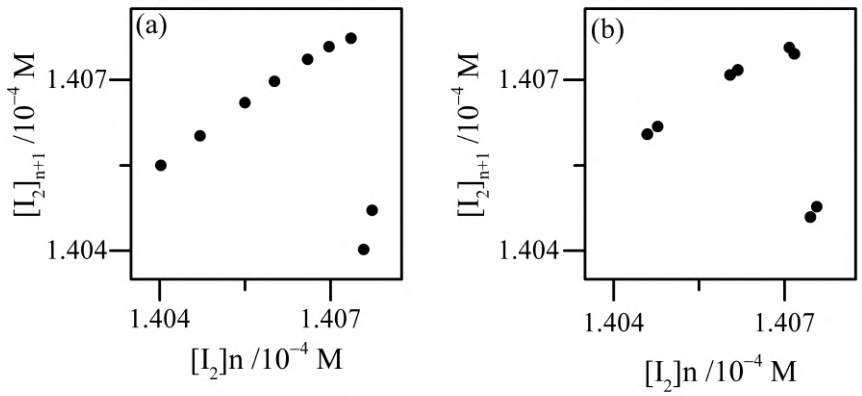

Figure 12. Poincare iteration maps: (a) for $4^1 3^1$ dynamics, and (b) for $(3^1)_2$ dynamics of the Model(1-15).

Between these two states, chaotic one was obtained and its iteration map is given in Figure 13. The position of the fixed point is identified in the crosspoint of the main diagonal (blue line) and imaginary line connecting the points on the iteration map. The fixed point corresponds to the point where the closed orbit (limit cycle) intersects the corresponding Poincare section. The slope of the tangent line (red line) in the fixed point is the criterion determining the stability of the limit cycle for the particular value of the control parameter. If the absolute value of the slope is higher than one the limit cycle is unstable and chaotic attractor is born.

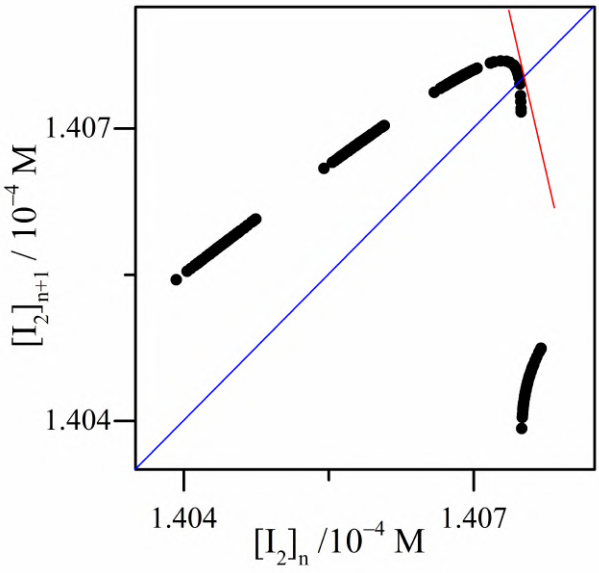

Figure 13. Poincare iteration map for chaotic dynamics of the Model(1-15) obtained with control parameter values between the ones used in Figure 11 (a) and (b).

Corresponding attractor of the iteration map given in Fig. 13 is given below, with enlarged part where Poincare section was made, Fig. 14.

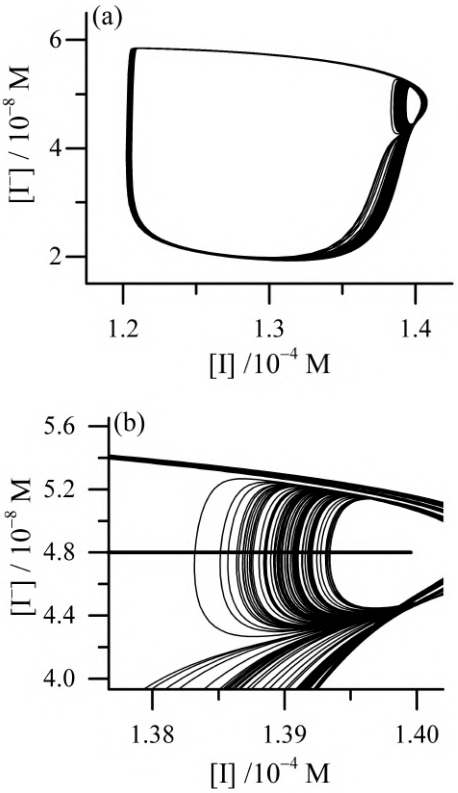

Figure 14. The chaotic attractor (a) of the Model(1-15) corresponding to the iteration map given in Fig. 13. (b) Enlarged part of the attractor with indicated position of the Poincare section.

Stability of the periodic orbit is global property of the dynamic system and its phase space. It may not be directly connected with steady state properties but rather with its manifold and trajectories over it. Hence, the transition to chaos is not generally the consequence of single dominating set of reaction steps, but rather of sequences of states laying on periodic orbit, where several sets of reactions subsequently dominate over others.

3. Summary

The stoichiometry of the Bray-Liebhafsky reaction corresponds to the hydrogen peroxide decomposition to water and oxygen in an acidic environment, in the presence of iodate ions as a catalyst. During this

reaction an oscillatory change of the intermediate species concentration, along with a cascade change in the hydrogen peroxide concentration and oxygen removal can be obtained. By selecting the experimental conditions, the simple periodic or complex chaotic concentration changes can be generated. Concentration oscillations are a consequence of alternating dominance of different reaction pathways present in the reaction mechanism. The spontaneous selforganized alteration of dominating reaction pathways was used in this paper to explain occurrence of simple and complex oscillations in this system. Fundamental importance of processes on multiple time scales was identified and demonstrated.

Keywords: Linear and nonlinear reaction system, feedback, autocatalysis, autocatalator, Bray-Liebhafsky oscillatory reaction

References:

[1] J. H. He, Nonlinear science as a fluctuating research frontier, Chaos Soliton. Fract. **41** (2009) 2533–2537.
[2] M. S. El Naschie, A review of E infinity theory and the mass spectrum of high energy particle physics, Chaos Soliton. Fract. **19** (2004) 209–236.
[3] P. Gray, S. K. Scott, Chemical oscillations and instabilities: nonlinear chemical kinetics. Oxford university press, Oxford, 1990.
[4] I. R. Epstein, K. Showalter, Nonlinear Chemical Dynamics: Oscillations, Patterns, and Chaos, J. Phys. Chem. **100** (1996) 13132-13147.
[5] Lj. Kolar-Anić, Ž. Čupić, S. Anić, Multistabilnost i nelinearni dinamički sistemi, Hem. ind. **52** (1998) 337-342.
[6] T. Bánsági Jr., M. Leda, M. Toiya, A.M. Zhabotinsky, I.R. Epstein, High-Frequency Oscillations in the Belousov-Zhabotinsky Reaction, J. Phys. Chem. A **113** (2009) 5644–5648.
[7] S. Anić, D. Stanisavljev, Ž. Čupić, M. Radenkovć, V. Vukojević, Lj. Kolar-Anić, The selforganization phenomena during catalytic decomposition of hydrogen peroxide, Sci. Sinter. **30** (1998) 49-57.
[8] I. Z. Kiss, V. Gáspár, L. Nyikos, P. Parmananda, Controlling Electrochemical Chaos in the Copper-Phosphoric Acid System, J. Phys. Chem. A, **101** (1997) 8668-8674.
[9] N. Potkonjak, Lj. Kolar-Anić, T. Potkonjak, S. N. Blagojević, S. Anić, Oscillatory Phenomena during Anodic Copper Electrodissolution in Trifluoroacetic Acid Solution, Mater. Sci. Forum **518** (2006) 301-306.
[10] J. L. Hudson, T. T. Tsotsis, Electrochemical reaction dynamics: a review, Chem. Eng. Sci. **49** (1994) 1493-1572.
[11] K. Nielsen, P. Graae Sørensen, F. Hynne, Chaos in Glycolysis, J. Theor. Biol. **186** (1997) 303-306.

[12] E. Haus, Chronobiology in the endocrine system, Adv. Drug Deliver. Rev. **59** (2007) 985–1014.
[13] S. Jelić, Ž. Čupić, Lj. Kolar-Anić, Mathematical modeling of the hypothalamic-pituitary-adrenal system activity, Math. Biosci., **197** (2005) 173-187.
[14] R. E. Ulanowicz, The dual nature of ecosystem dynamics, Ecol. Model. **220** (2009) 1886–1892.
[15] L. Oxley, D. A. R. George, Economics on the edge of chaos: Some pitfalls of linearizing complex systems, Environ. Modell. Softw. **22** (2007) 580-589.
[16] N. J. Cornish, J. J. Levin, Mixmaster universe: A chaotic Farey tale, Phys. Rev. D **55** (1997) 7489-7510.
[17] W. C. Bray, A periodic reaction in homogeneous solution and its relation to catalysis, J. Am. Chem. Soc. **43** (1921) 1262-1267.
[18] W. C. Bray, H.A. Liebhafsky, Reaction involving hydrogen peroxide, iodine and iodate ion. I. Introduction, J. Am. Chem. Soc. **53** (1931) 38.
[19] H. A. Liebhafsky, R. Furuichi, G. M. Roe, Reaction involving hydrogen peroxide, iodine, and iodate ion. 7. The smooth catalytic decomposition of hydrogen peroxide, mainly at 50°C, J. Am. Chem. Soc. **103** (1981) 51-56.
[20] M. G. Peard, C. F. Cullis, A periodic chemical reaction. The reaction between hydrogen peroxide and iodic acid, Trans. Faraday Soc. **47** (1951) 616-630.
[21] H. Degn, Evidence of a branched chain reaction in the oscillating reaction hydrogen peroxide, iodine and iodate, Acta Chem. Scand. **21** (1967) 1057-1066.
[22] K. R. Charma, R. M. Noyes, Oscillations in chemical systems. 13. A detailed molecular mechanism for the Bray-Lebhafsky reaction of iodate and hydrogen peroxide, J. Am. Chem. Soc. **98** (1976) 4345-4360.
[23] G. Schmitz, Kinetcis and mechanism of the iodate-iodide reaction ant other related reactions, Phys. Chem. Chem. Phys. **1** (1999) 1909-1914.
[24] V. A. Vavalin, A. M. Zhabotinskii, A. N. Zakain, Self-oscillation of iodide ion concentration during the iodate-catalyzed decomposition of hydrogen peroxide, Russ. J. Phys. Chem. **44** (1970) 1345-146.
[25] S. D. Furrow, Chemical oscillators based on iodate ion and hydrogen peroxide, in: R. J. Field M. Burger (Eds.), Oscillations and Traveling Waves in Chemical Systems, J. Wiley, New York, 1985, 171-192.
[26] G. Schmitz, Cinetique de la reaction de Bray, J. Chim. Phys. **84** (1987) 957-965.
[27] S. Anić, Lj. Kolar-Anić, Kinetic Aspects of the Bray-Liebhafsky oscillatory reaction, J. Chem. Soc. Faraday. Trans. I **84** (1988) 3413-3421.
[28] S. Anić, D. Stanisavljev, G. Krnajski Belovljev, Lj. Kolar-Anić, Examination of the temperature variations on the Bray-Liebhafsky oscillatory reaction, Ber. Bunsenges. Phys. Chem. **93** (1989) 488-491.
[29] L. Treindl, R. M. Noyes, A new explanation of the oscillations in the Bray-Liebhafsky reaction, J. Phys. Chem. **97** (1993) 11354-11362 and references cited therein.
[30] A. Olexova, M. Mrákavová, M. Melicherčík, L. Treindl, Oscillatory system I^-, H2O2, HClO4: The modified form of the Bray Liebhafsky reaction, J. Phys. Chem. A **114** (2010) 7026–7029.
[31] B. P. Belousov, A periodic reactions and its mechanism, Sbornik Referatov po Radiatsionnoi Meditsine, Medigz, Moskow, 1958, pp. 145.

[32] A. M. Zhabotinskii, periodic processes of the oxidation of malonic acid in solution, Biofizika **9** (1964) 306-311.
[33] A. Zhabotinskii, G. Frank, Oscillating processes in biological and chemical system, Nauka, Moskow, 1967.
[34] R. J. Field, E. Korös, R.M. Noys, Oscillations in chemical systems. II. Thorough analysis of temporal oscillation in the bromate-cerium-malonic acid system, J. Am. Chem. Soc. **94** (1972) 8649-8664.
[35] A. M. Zhabotinskii, Koncentrationnye avtokolebanya, Nauka, Moskva, 1974.
[36] R. J. Field, Experimental and mechanistic caractezitaion of bromate-ion-driven chemical oscillations and traveling waves in closed reaktor, in: R.J. Field M. Burger (Eds.), Oscillations and traveling waves in chemical systems, J. Wiley, New York, 1985, pp. 55-92.
[37] E. Korös, K. Kurin, On the behavior of chemical oscillator, in: G. Györgyi, I. Konodr, L. Sasvari, T. Tèl, (Eds), from phase transition to chaos, World Scientific, Singapure, London, 1992, pp. 128-142.
[38] S. M. Blagojević, S. R. Anić, Ž. D. Čupić, N. D. Pejić, Lj. Z. Kolar-Anić, Malonic acid concentration as a control parameter in the kinetic analysis of the Belousov-Zhabotinsky reaction under batch conditions, Phys. Chem. Chem. Phys. **10** (2008) 6658-6664.
[39] T. S. Briggs, W.C. Rausher, An oscillatory iodine clock, J. Chem. Education **50** (1973) 496-499.
[40] S. D. Furrow, Briggs-Rauscher oscillator with methylmalonic acid, J. Phys. Chem. **85** (1981) 2026-2031.
[41] S. D. Furrow, R. Cervellati, G. Amadori, New substrates for the oscillating Briggs Rauscher reaction, J. Phys. Chem. A **106** (2002) 5841-5850.
[42] S. Anić, V. Vukojević, M. Radenković, Lj. Kolar-Anić, New approach to the study of the peroxide kinetics of the Briggs-Rausher oscillatory reaction, J. Serb.Chem. Soc. **54** (1989) 521-562.
[43] V. Vukojević, P. Graae Sorensen, F. Hynne, Quenching analysis of the Briggs-Rauscher reaction, J. Am. Chem. Soc. **97** (1993) 4091-4100.
[44] D. Stanisavljev, N. Begovic, Z. Zujovic, D. Vucelic, G. Bacic, 1H NMR Monitoring of Water Behavior during the Bray-Liebhafsky Oscillatory Reaction. Journal of Physical Chemistry A **102** (1998) 6883-6886.
[45] D. Stanisavljev, V. Vukojevic, Investigation of the Influence of Heavy Water on Kinetic Pathways in the Bray-Liebhafsky Reaction. J. Phys. Chem. A **106** (2002) 5618-5625.
[46] D. Stanisavljev, A. Djordjevic, V. Likar-Smiljanic, Investigation of microwave effects on the oscillatory Bray-Liebhafsky reaction. Chem. Phys. Lett. **412** (2005) 420-424.
[47] D. Stanisavljev, A. Djordjevic, V. Likar-Smiljanic, Microwaves and coherence in the Bray-Liebhafsky oscillatory reaction. Chem. Phys. Lett. **423** (2006) 59-62.
[48] D. Stanisavljev, M. Dramicanin, Excessive Excitation of Hydrogen Peroxide during Oscillatory Chemical Evolution. J. Phys. Chem. A **111** (2007) 7703-7706.
[49] J. Ćirić, S. Anić, Ž. Čupić and Lj. Kolar-Anić: The Bray-Liebhafsky oscillatory reaction. The kinetics of overall reduction and oxidation processes analysed by hydrogen peroxide decomposition, Sci. Sinter. **32** (2000) 187-196.

[50] Lj. Kolar-Anić, Ž. Čupić, G. Schmitz, S. Anić, Improvement of the stoichiometric network analysis for determination of instability conditions of complex nonlinear reaction systems, Chem. Eng. Sci. **65** (2010) 3718-3728.
[51] G. Schmitz, Cinetic de la reaction Bray, J. Chim.Phys. **84** (1987) 957-965.
[52] H. A. Liebhafsky, L.S. Wu, Reaction involving hydrogen peroxide, iodine, and iodate ion. 5. Introduction to the oscillatory decomposition of hydrogen peroxide, J. Am. Chem. Soc. **96** (1974) 7180-7187.
[53] H. A. Liebhafsky, W.C. McGavock, R.J. Reyes, G.M. Roe, L.S. Wu, Reaction involving hydrogen peroxide, iodine, and iodate ion. 6. Oxidation of iodine by hydrogem peroxide at 50 OC, J. Am. Chem. Soc. **100** (1978) 87-91.
[54] D. Edelson, R. M. Noyes, Detailed calculations modeling the oscillatory Bray-Liebhafsky reaction, J. Phys. Chem. **83** (1979) 212-220.
[55] S. Furrow, Reaction of iodine intermediates in iodate-hydrogen peroxide oscillators, J. Phys. Chem. **91** (1987) 2129-2135.
[56] Lj. Kolar-Anić, G. Schmitz, Mechanism of the Bray-Liebhafsky reaction: Effect of the oxidation of iodous acid by hydrogen peroxide, J. Chem. Soc. Faraday Trans. **88** (1992) 2343-2349.
[57] Lj. Kolar-Anić, Đ. Mišljenović, S. Anić, G. Nicolis, Influence of the reduction of iodate by hydrogen peroxide on the model of the Bray-Liebhafsky reaction, React. Kinet. Catal. Lett. **54** (1995) 35-41.
[58] G. Schmitz, Iodine oxidation by hydrogen peroxide and Bray–Liebhafsky oscillating reaction: effect of the temperature, Phys. Chem. Chem. Phys. **13** (2011) 7102-7111.
[59] I. Valent, L. Adamčikova, P. Ševčik, Simulations of the iodine interphase transport effect on the oscillating Bray-Liebhafsky reaction, J. Phys. Chem. A **102** (1998) 7576-7579.
[60] K. Kissimonova, I. Valent, L. Adamčiková, P. Ševšik, Numerical simulations of the oxygen production in the oscillating Bray-Liebhafsky reaction, Chem. Phys. Lett. **341** (2001) 345-350.
[61] Lj. Kolar-Anić, T. Grozdić, V. Vukojević, G. Schmitz, A. Anić, 2004. Simulations of complex oscillations based on a model of the Bray-Liebhafsky reaction, in: Anić, S., Čupić, Ž., Kolar-Anić, Lj. (Eds.), Selforganization in nonequilibrium systems. Society of Physical Chemists of Serbia, Belgrade, pp. 115-118.
[62] G. Schmitz, Lj. Kolar-Anić, S. Anić, T. Grozdić, V. Vukojević, Complex and chaotic oscillations in a model for the catalytic hydrogen peroxide decomposition under open reactor conditions. J. Phys. Chem. A **110** (2006)10361-10368.
[63] G. Schmitz, Lj. Kolar-Anić, S. Anić, Ž. Čupić, Stoichiometric network analysis and associated dimensionless kinetic equations. Application to a model of the Bray-Liebhafsky reaction. J. Phys. Chem. **112** (2008) 13452-13457.
[64] Lj. Kolar-Anić, Đ Mišljenović, S. Anić, G. Nicolis, The influence of the reduction of iodate ion by hydrogen peroxide on the model of the Bray-Liebhafsky reaction. React. Kinet. Catal. Lett. **54** (1995) 35-41.
[65] Lj. Kolar-Anić, Ž. Čupić, S. Anić,G. Schmitz, Pseudo-steady states in the model of the Bray-Liebhafsky oscillatory reaction. J.Chem. Soc. Faraday Trans. **93** (1997) 2147- 2152.

[66] G. Shmitz, Lj. Kolar-Anić, S. Anić, T. Grozdić, V. Vukojević, Complex and chaotic oscillations in a model for the catalytic hydrogen peroxide decomposition under open reactor conditions, J. Phys. Chem. A **110** (2006) 10361-10368.
[67] M. Desroches, J. Guckenheimer, B. Krauskopf, C. Kuehn, H. Osinga, M. Wechselberger, Mixed-mode oscillations with multiple time-scales, SIAM Review **54** (2012) 211-288.
[68] M. Krupa, N. Popovic, and N. Kopell, Mixed-mode oscillations in three time-scale systems: A prototypical example, SIAM J. Appl. Dyn. Sys. **7** (2008) 361–420.
[69] S. K. Scott, Chemical chaos, Clarendon Press, Oxford, 1997.
[70] B. Peng, V. Gáspár, K. Showalter, False bifurcations in chemical systems: Canards, Phil. Trans. R. Soc. Lond. A **337** (1991) 275-289.
[71] V. Petrov, V. Gáspár, J. Masere, K. Showalter, Controlling chaos in the Belousov-Zhabotinsky reaction, Nature **361** (1993) 240-243.
[72] G. Wallet, Entrée-sortie dans un tourbillon, Annales de l'Institut Fourier **36** (1986) 157-184.

Auxiliary equations for solving nonlinear evolutionary equations*

Corina N. Babalic†
University of Craiova, A.I.Cuza 13, Craiova, 200585, Romania

Radu Constantinescu‡
University of Craiova, A.I.Cuza 13, Craiova, 200585, Romania

Abstract

The paper offers a monographic approach to the direct finding of travelling wave solutions. The basic tool will be the *auxiliary equation*, an equation whose known solutions are used to express solutions of more complicated models. The main question we are trying to answer is how the solutions depend on the choice of the auxiliary equations and on the solving method. To effectively find these answers, we will use the subequations that can be generated by a quite general auxiliary equation, and, as a solving method, the *functional expansion*, an approach that generalizes the G'/G technique. The investigated model will be the *Benjamin-Bona-Mahony* (*BBM*) *equation*, a model belonging to a general class of higher order PDEs with *travelling wave solutions*, and interesting classes of rational, hyperbolic or periodic solutions will be generated for it.

Keywords: travelling waves, auxiliary equation technique, functional expansion, BBM model.

1. Introduction

Since under real circumstances most of the physical phenomena are nonlinear, the nonlinear dynamics represent an important issue in understanding the most fascinating phenomena which occur in nature. The most suitable mathematical tool which allows describing such phenomena in many space-time dimensions is represented by the nonlinear partial differential equations (NPDEs). They allow modelling phenomena as wave propagation through optical fibres [1], heat or fluid diffusion [2].

* This work has been supported by ICTP through the grant offered to SEENET–MTP, in the frame of the Network Programme (NT–03).

† e-mail address: babalic.corina@ucv.ro

‡ e-mail address: rconsta@central.ucv.com

Solving NPDEs became perhaps the most challenging and the most highly promising area in modern mathematics. Numerical techniques [3] are often made use of in order to solve them, but scientists and engineers also show an increasing interest in developing analytical techniques.Therefore during the recent years some important progresses have been achieved and many powerful and effective methods have been created in order to derive explicit solutions. There are some rigorous methods, for example the inverse scattering [4], the Hirota bilinear formalism [5, 6], the super-bilinear formalism [7, 8], the Lax Pair [9] or the Lie symmetry method [10, 11, 12]. We will focus in this paper on another class of solving methods, more direct and simple to apply, methods based on the use of the auxiliary equation technique. These methods are supposed to look for solutions of complicated NPDEs in terms of the known solutions of an "auxiliary equation" and they originate from the extension of the tanh-methods [13, 14] to the whole class of solutions of the Riccati equation. This was the first auxiliary equation used, followed by the Jacobi elliptic equation [15]. As we will illustrate, other simple or more complex equations are quite often chosen as auxiliary equations.

Beyond the choice of the auxiliary equation, a second key issue in applying the auxiliary equation technique is related to the explicit mathematical expressions that we choose in order to construct the NPDEs solutions in terms of the auxiliary equation solutions. There are many proposed approaches from this perspective and we can cite: the generalized Kudryashov method [16, 17], the (G'/G)-expansion method [18], its extension to the functional expansion method [19], as well as other investigation tools [20, 21], including methods applied to mechanical models from field theory [22]. Many of the above mentioned methods do allow the construction of the *travelling wave solutions* of the NPDEs, solutions that have attracted the attention of many researchers. This is why the focus of this paper will be on how travelling waves can be obtained using a very general approach, based on the auxiliary equation technique, the functional expansion. Moreover, an important purpose will be to investigate how these solutions depend on the choice of the auxiliary equation, a question not tackled by the papers published so far. For answering, we will use a quite complex auxiliary equation that, depending on the values given to the parameters appearing in it, could reduce to many sub-equations. The BBM solutions will be pointed out and compared among them for two such sub-equations.

The paper is organized as follows: in Section 2 we present the investigated model and the whole hierarchy of equations that generalizes it. In Section 3, we outline how the auxiliary equation method can be used and we give a few examples of auxiliary equations that are used in various papers. The focus will be on the equation we are going to use. In Section 4 we effectively point out the BBM solutions in two specific cases. The paper ends with some essential facts on how the solutions are looking and what are their specificity.

2. The BBM model and its generalizations

The first equation describing travelling waves in shallow water was proposed by Boussinesq in 1877 and rediscovered by Diederik Korteweg and G. de Vries in 1895. It is known as the Korteweg-de Vries (KdV) equation and has the form:

$$u_t + u_{xxx} + 6uu_x = 0.$$

For a relatively long period of time, KdV was considered as the only equation with these peculiar solutions called solitons. Later, it was realized that a large number of equations could accept similar solutions. Among the first such equations, the Regularized Long-Wave (RLW) Equation was proposed. It is also known as *Benjamin-Bona-Mahony (BBM) Equation* and describes the small-amplitude long wave of water in a channel. The mathematical form of this equation is:

$$u_t + u_x + uu_x - u_{xxt} = 0 \tag{1}$$

The equation (1) was quickly extended towards a larger class of equations, as for example the Camassa-Holm equation, proposed for modelling the unidirectional propagation of irrotational water wave over a planar wall:

$$u_t + 2ku_x - u_{xxt} + 3uu_x - 2u_xu_{xx} - uu_{xxx} = 0$$

Here k is a constant related to gravity and to the initial undisturbed water depth.

Another equation, known as the Rosenau equation [23], was proposed for describing the wave-wave and wave-wall interactions for which KdV equation is not working:

$$u_t + u_x + uu_x + u_{xxxt} = 0. \tag{2}$$

The previous equation was upgraded to a 5th order equation, as solitonic equation, and the Rosenau-RLW equation arisen when the term $-u_{xxt}$ from BBM was included in the Rosenau Equation:

$$u_t - u_{xxt} + u_{xxxxt} + u_x + uu_x = 0. \tag{3}$$

Further extensions that are now used for describing better the behaviour of the nonlinear waves:

- the generalized Rosenau-RLW Eq. [24]:

$$u_t - u_{xxt} + u_{xxxxt} + u_x + u^m u_x = 0, \quad (m \geq 1, \textit{ positive integer})$$

- the Rosenau-KdV [25] equation includes the viscous term u_{xxx} in the Rosenau equation (2):

$$u_t + u_{xxxt} + u_{xxx} + u_x + uu_x = 0 \tag{4}$$

- the Rosenau-KdV-RLW [26] equation couples the above Rosenau-RLW and Rosenau-KdV Equations:

$$u_t - u_{xxt} + u_{xxxxt} + u_{xxx} + u_x + uu_x = 0$$

- the Kawahara equation [27] arose in the theory of shallow water waves with surface tension:

$$u_t + u_x + uu_x + u_xxx - u_{xxxxx} = 0$$

- the Rosenau-Kawahara equation [28] arose by adding another viscous term, $-u_{xxxx}$, to the Rosenau-KdV equation, (4):

$$u_t + u_x + uu_x + u_{xxx} + u_{xxxt} - u_{xxxxx} = 0$$

- the generalized Rosenau-Kawahara Equation:

$$u_t + au_x + b^m u_x + cu_{xxx} + \lambda u_{xxxxt} - vu_{xxxxx} = 0. \tag{5}$$

  Here a, b, c, λ, v are real constants; m is a positive integer, which indicates the power law nonlinearity.

- the generalized Rosenau-Kawahara-RLW equation [29]:

$$u_t + au_x + bu^m u_x + cu_{xxx} - \alpha u_{xxt} + \lambda u_{xxxxt} - vu_{xxxxx} = 0.$$

  It is obtained by coupling the generalized Rosenau-RLW equation (3) and the generalized Rosenau-Kawahara equation (5).

As we already mentioned, we will investigate the BBM model given by (1). Despite the numerous studies on the BBM equation and of the various techniques used for solving it, it seems that the model contains a much richer phenomenology.

3. The auxiliary equation techniques

The travelling waves represent an important class of solutions for mathematical models in the field of nonlinear dynamics.The algorithm for finding travelling waves supposes three important steps: (i) reduction of the investigated NPDE to an ordinary differential equation (ODE); (ii) choice of an adequate auxiliary equation, a supplementary equation with known solutions; (iii) expressing the solutions for the investigated ODE in terms of those of the auxiliary equation. In this section we will follow the first two steps from the mentioned algorithm. The third step will be presented in the next section.

Let us consider the dependent variable $u(x,t)$ defined in a $2D$ space (x,t) satisfying the PDE:

$$F(u, u_t, u_x, u_{xx}, u_{tt}, ..) = 0. \tag{6}$$

The equation (6) can be transformed into an ODE by the use of the wave variable, joining the two coordinates (x,t) with the wave velocity, V:

$$\xi = x - Vt. \tag{7}$$

The ODE we have to solve now has the generic form:

$$\Delta(u, u', u'', \cdots) = 0; \quad u' = du(\xi)/d\xi. \tag{8}$$

For solving (8), we consider that its solutions could be expressed in terms of the known solutions $G(\xi)$ of an auxiliary equation of the form:

$$\Theta(G, G', G'', \cdots) = 0. \tag{9}$$

We will write down here examples of auxiliary equations usually met in literature. The most classical example is represented by the Riccati equation:

$$G' = q_0 + q_1 G + q_2 G^2. \tag{10}$$

The Jacobi elliptic equation is also very often used, because of its general and well classified solutions:

$$G'^2 = P(G) = c_0 + c_2 G^2 + c_4 G^4 + c_6 G^6. \tag{11}$$

The both previous examples are first order differential equations. Second order equations represent very interesting cases of auxiliary equations, allowing more sophisticated choices for the solutions we are looking for. The most frequent examples met in various papers are the following:

$$G'' + \lambda G' + \mu G = 0, \tag{12}$$

$$G \cdot G'' - B \cdot G'^2 - F \cdot G \cdot G' - H \cdot G^2 = 0. \tag{13}$$

As we are interested in quite complex auxiliary equations, we decided to use here (13), containing three parameters B, F, H. This is why we will list now, for the future use, the main solutions of this equation [30]:

- If $F^2 + 4H(1-B) > 0$, the equation (13) admits hyperbolic solutions:

$$G(\xi) = \left[e^{F\xi/2} \left(C_1 e^{\sqrt{F^2+4H(1-B)}\xi/2} + C_2 e^{-\sqrt{F^2+4H(1-B)}\xi/2} \right) \right]^{\frac{1}{1-B}} \tag{14}$$

- If $F^2 + 4H(1-B) < 0$, the equation (13) admits periodic solutions:

$$G(\xi) = \left[e^{\frac{F\xi}{2}} \left(C_1 \sin \sqrt{-F^2-4H(1-B)}\frac{\xi}{2} + C_2 \cos \sqrt{-F^2-4H(1-B)}\frac{\xi}{2} \right) \right]^{\frac{1}{1-B}} \tag{15}$$

- If $F^2 + 4H(1-B) = 0$, we will have rational solutions for (13):

$$G(\xi) = \left[e^{\frac{F\xi}{2}} (C_1 \xi + C_2) \right]^{\frac{1}{1-B}}. \tag{16}$$

4. Solutions for the BBM model through the functional expansion method

The third step of the solving algorithm mentioned in the previous section asks for expressing the solutions $u(\xi)$ of (8) in terms of the solutions $G(\xi)$ of the auxiliary equation. Usually, we do that in the form:

$$u(\xi) = \sum_{i=-m}^{m} P_i(G) H^i(G, G', G'', \cdots). \tag{17}$$

Here $P_i(G)$ are $2m+1$ functionals depending on $G(\xi)$ and that have to be determined. The value of the parameter m depends on the model and it is established through a balancing procedure among the terms of higher order derivative, respectively of the higher nonlinearity.

The functional expansion method, proposed in [21], supposes to have:

$$u(\xi) = \sum_{i=0}^{M} P_i(G)(G')^i = P_0 + P_1 G' + ... + P_M (G')^M \tag{18}$$

where $G' \equiv \frac{dG}{d\xi}$. The functionals $P_i(G), \quad i = 1, ..., M$, can be found by solving the determining system generated when (18) is introduced in the ODE (8).

Let us apply the technique for finding analytic solutions for the BBM model described by the equation (1). Considering the transformation (7), this equation becomes the following ODE:

$$2V u_{\xi\xi} + u^2 + 2(1-V)u + 2C = 0, \tag{19}$$

where C is a constant of integration and V is the velocity (real constant). In this specific case, the parameter from (18) takes the value $M = 2$, and this expansion becomes:

$$u(\xi) = P_0(G) + P_1(G) G_\xi + P_2(G)(G_\xi)^2. \tag{20}$$

We will consider that $G(\xi)$ is the solution of the auxiliary equation:

$$G G_{\xi\xi} - B G_\xi^2 - F G G_\xi - H G^2 = 0. \tag{21}$$

Taking into consideration the relations (19), (20) and (21), collecting G', $(G')^2$, $(G')^3$, $(G')^4$ and putting the coefficients to zero, we get a general system of equations which should allow us to determine the functionals $\{P_i, i = 0, 1, 2\}$.

The system has the form:

$$\begin{aligned}
&2C+2P_0-2VP_0+P_0^2+2FHVGP_1+4H^2VG^2P_2+2HVGP_0{}'=0\\
&-P_1+VP_1-F^2VP_1-HVP_1-2BHVP_1-P_0P_1-6FHVGP_2-\\
&\qquad -FVP_0'-3HVGP_1'=0\\
&-6BFVP_1-GP_1^2-2GP_2+2VGP_2-8F^2VGP_2-4HVGP_2-\\
&-16BHVGP_2-2GP_0P_2-2BVP_0'-6FVGP_1'-10HVG^2P_2'-\\
&\qquad -2VGP_0''=0,\\
&-BVP_1+2B^2VP_1+10BFVGP_2+G^2P_1P_2+3BVGP_1'+\\
&\qquad +5FVG^2P_2'+VG^2P_1''=0\\
&-4BVP_2+12B^2VP_2+G^2P_2^2+10BVGP_2'+2VG^2P_2''=0
\end{aligned}\tag{22}$$

We were not able to solve (22) in its most general form. This is way, we considered the functionals P_0, P_1, P_2 having the forms

$$\begin{aligned}
P_0&=\frac{\beta_0+\beta_1G+\beta_2G^2}{\alpha_0+\alpha_1G+\alpha_2G^2},\\
P_1&=\frac{\gamma_0+\gamma_1G}{\alpha_0+\alpha_1G+\alpha_2G^2},\\
P_2&=\frac{\tau_0}{\alpha_0+\alpha_1G+\alpha_2G^2}.
\end{aligned}\tag{23}$$

Here are the main results and the most interesting BBM solutions we got for two specific cases:

Case I. $B=0, F\neq 0, H=0$
The auxiliary equation (13) becomes:

$$G_{\xi\xi}-FG_\xi=0\tag{24}$$

If the constraint from below is satisfied, the system (22) can be solved and gives the following expressions for the functionals:

$$(F^4-1)V^2+2V+2C-1=0,\tag{25}$$

$$P_0=V-1-F^2V,\quad P_1=\frac{24FV\alpha_2}{\alpha_1+2\alpha_2G},\quad P_2=-\frac{48V\alpha_2^2}{(\alpha_1+2\alpha_2G)^2}.\tag{26}$$

It is interesting to note that, for $\alpha_1\neq 0$, the solution we get is more general than the one given by the (G'/G)-approach. As we will see below, unlike α_2, the value of α_1 will influence the form of the solutions, being able to generate their translations. Note that for choosing the integration constant $C=0$, the wave velocity V is limited by the above constraint to two possible expressions. By contrary, considering a non-zero C makes V remain an arbitrary parameter.

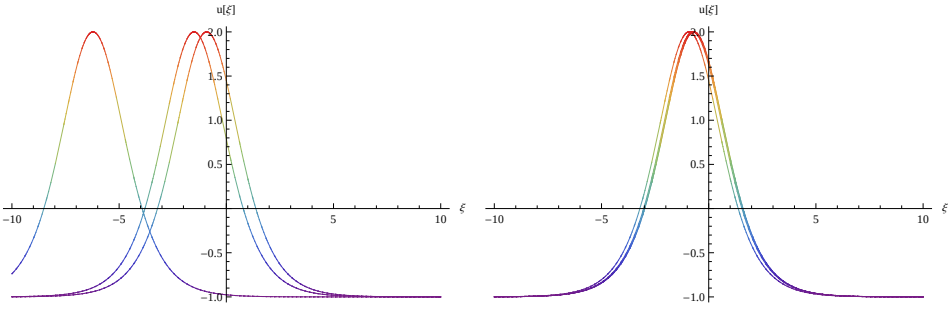

Figure 1: Plot of $u(\xi)$ given by Eq. (28) for fixed $V = 1, F = -1, \alpha_2 = 1$ and $\alpha_1 = 1, \alpha_1 = 5, \alpha_1 = 1000$ (left); for fixed $V = 1, F = -1, \alpha_1 = 1$ and $\alpha_2 = 5, \alpha_2 = 100, \alpha_2 = 1000$ (right).

Two important sub-cases have to be mentioned:
I.1 For $F^2 > 0$, the auxiliary equation (24) admits the solution:

$$G(\xi) = C_2 + C_1 e^{F\xi}. \tag{27}$$

The solution of (19) is:

$$u(\xi) = V - 1 - F^2 V + \frac{24 C_1 F^2 V \alpha_2 e^{F\xi}}{\alpha_1 + 2\alpha_2 (C_2 + C_1 e^{F\xi})} - \frac{48 C_1^2 F^2 V \alpha_2^2 e^{2F\xi}}{[\alpha_1 + 2\alpha_2 (C_2 + C_1 e^{F\xi})]^2} \tag{28}$$

For $\xi = x - Vt$ we obtain $u(x,t)$ for BBM equation in (1).

From Figure 1 we can see the influence of the constants α_1 and α_2 on the solutions. In the graph on the left, varying α_1 we get quite important translations, while, in the graph from the right, we note small effects of the variation of α_2.

I.2 For $F^2 < 0$, the auxiliary equation (24), admits the solution:

$$G(\xi) = e^{F\xi/2}(C_1 \sin \Delta\xi/2 + C_2 \cos \Delta\xi/2), \quad \Delta^2 = -F^2 > 0. \tag{29}$$

In this case the solution of (19) is:

$$\begin{aligned} u(\xi) &= V - 1 - F^2 V + \\ &+ \frac{12 F V \alpha_2 e^{F\xi/2}[(FC_1 - \Delta C_2)\sin \Delta\xi/2 + (FC_2 + \Delta C_1)\cos \Delta\xi/2]}{\alpha_1 + \alpha_2 e^{F\xi/2}(C_1 \sin \Delta\xi/2 + C_2 \cos \Delta\xi/2)} - \\ &- \frac{12 V \alpha_2 e^{F\xi}[(FC_1 - \Delta C_2)\sin \Delta\xi/2 + (FC_2 + \Delta C_1)\cos \Delta\xi/2]^2}{\alpha_1 + \alpha_2 e^{F\xi/2}(C_1 \sin \Delta\xi/2 + C_2 \cos \Delta\xi/2)^2}. \end{aligned} \tag{30}$$

For $\xi = x - Vt$ we obtain $u(x,t)$ for BBM equation in (1).

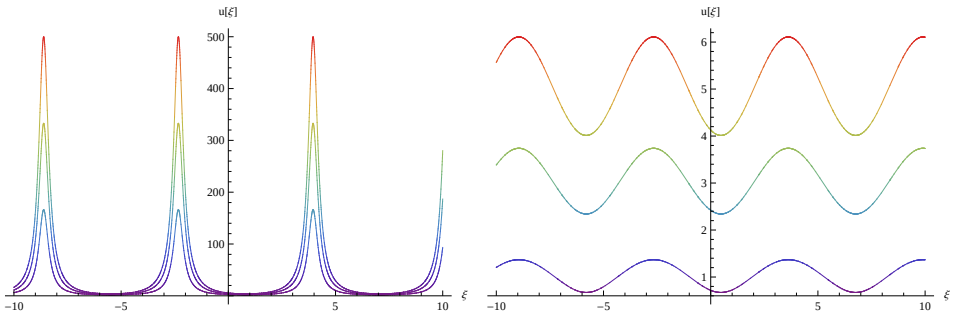

Figure 2: Plot of $u(\xi)$ given by Eq. (30) for fixed $F^2 = -1, \alpha_1 = 3, \alpha_2 = 4$, and $V = 1, V = 2, V = 3$ (left); for fixed $F^2 = -1, \alpha_1 = 300, \alpha_2 = 4$, and $V = 1, V = 2, V = 3$ (right).

Figure 2 shows that, in this case too, large values of α_1 can generate not only translations, but can change the profile of the solution.

Case II. $B \neq 0, F \neq 0, H \neq 0$

The system (22) can be solved if the following relation is satisfied:

$$[(F^2 + 4(1-B)H)^2 - 1]V^2 + 2V - 1 + 2C = 0. \tag{31}$$

If we consider the integration constant $C = 0$, the condition for real velocities is $(F^2 + 4(1-B)H)^2 > 0$. Solving (31), we obtain two possible expressions for velocities in terms of F, B, H, from the auxiliary equation:

$$V_1 = \frac{1}{F^2 + 4(1-B)H + 1}, \quad V_2 = \frac{1}{-F^2 - 4(1-B)H + 1}.$$

The auxiliary equation (13) takes now its most general form:

$$G_{\xi\xi}G - BG_\xi^2 - FGG_\xi - HG^2 = 0,$$

and the functionals from (22) are:

$$P_0 = V - 1 - F^2V + 8HV(1-B), \;\; P_1 = \frac{12FV(1-B)}{G}, \;\; P_2 = -\frac{12V(1-B)^2}{G^2}$$

II.1 For $F^2 + 4H(1-B) > 0$, the auxiliary equation (21) admits the solution (14). Using it, we get a solution of (19) in the form:

$$\begin{aligned} u(\xi) &= V - 1 - F^2V - 4HV(1-B) + \\ &+ \frac{12C_2V(F^2 + 4H(1-B)}{C_2 + C_1e^{\sqrt{F^2+4H(1-B)}\xi}} - \frac{12C_2^2V(F^2 + 4H(1-B)}{[C_2 + C_1e^{\sqrt{F^2+4H(1-B)}\xi}]^2} \end{aligned} \tag{32}$$

For $\xi = x - Vt$ we obtain $u(x,t)$ for BBM equation in (1).

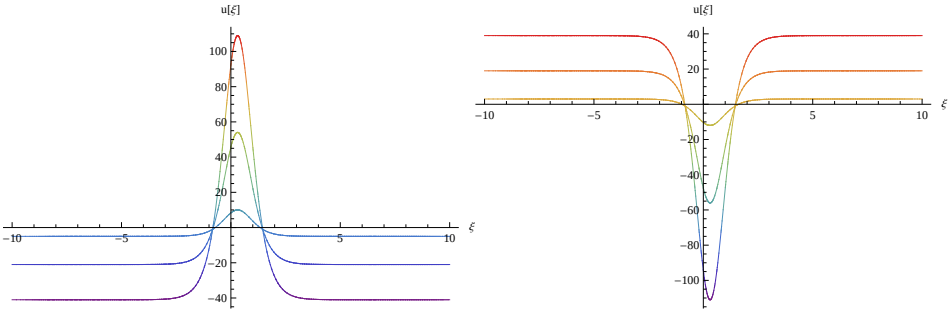

Figure 3: Plot of $u(\xi)$ given by Eq. (32) for $H = -1, F = -1, B = 2$ and positive velocities $V = 1, V = 5, V = 10$ (left); negative velocities $V = -1, V = -5, V = -10$ (right).

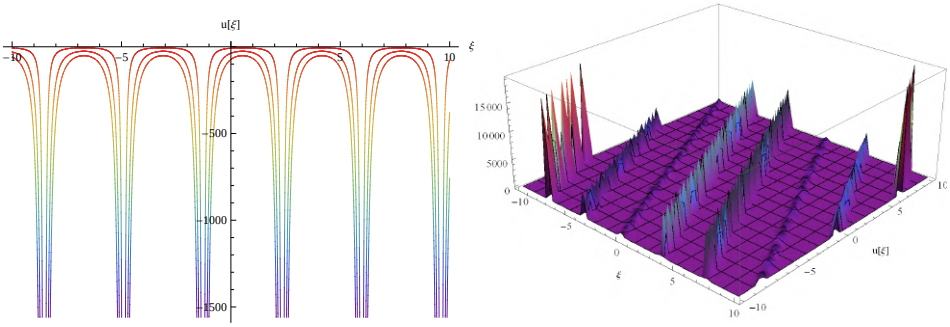

Figure 4: Plot of $u(\xi)$ given by Eq. (33) for $H = 1, F = 1, B = 2$ and positive velocities $V = 1, V = 5, V = 10$ (left); Plot of $u(x,t)$ where $\xi = x + V/2$, so for negative velocity $V = -1/2$ (right).

For fixed F, H, B, the increasing positive velocity leads to increasing positive amplitude as shown in Figure 3. For negative velocities the bright solitons become dark solitons.

II.2 For $F^2 + 4H(1-B) < 0$, the equation (21) admits the solution (15). In this case the solution of (19) is, after simplification:

$$u(\xi) = V - 1 - F^2V - 4HV(1-B) + \tag{33}$$
$$+\frac{3V(C_1^2 + C_2^2)(F^2 + 4H(1-B))}{[C_1 \sin\sqrt{-F^2 - 4H(1-B)}\xi/2 + C_2 \cos\sqrt{-F^2 - 4H(1-B)}\xi/2]^2}.$$

For $\xi = x - Vt$ we obtain $u(x,t)$ for BBM equation in (1) (Fig. 4 (right).

As Figure 4 shows, for fixed F, H, B , we get periodic solutions with negative or positive amplitudes. Depending on the values taken by the velocities the solutions change the amplitude and the period.

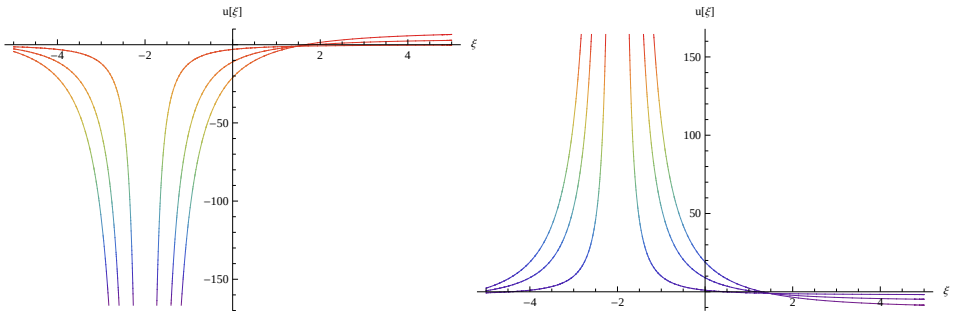

Figure 5: Plot of $u(\xi)$ given by (34) for any H, F, B that satisfy $F^2 + 4H(1-B) = 0$ and positive velocities $V = 1, V = 5, V = 10$ (left); negative velocities $V = -1, V = -5, V = -10$ (right).

II.3 For $F^2 + 4H(1-B) = 0$, the auxiliary equation (21) admits the solution (16). In this case the solution of (19) is, after simplification:

$$u(\xi) = V - 1 - \frac{12VC_1^2}{[C_1\xi + C_2]^2}. \tag{34}$$

Coming back to the initial variables (x, t), we obtain $u(x, t)$ for BBM equation in (1). As in the previous case, for fixed F, H, B, we get unbounded solutions whose amplitudes depend on the values of velocity (see Figure 5).

5. Conclusions

The paper pointed out travelling wave solutions for the BBM model, using the auxiliary equation and the functional expansion techniques. The main aim was to investigate how the travelling waves depend on the form of the auxiliary equation. The conclusion is that, usually, the travelling waves inherit important characteristics of the solutions accepted by the auxiliary equation. It was possible to get hyperbolic or periodic solutions of BBM starting from similar solutions of the considered auxiliary equation. With the help of various chosen values for the parameters appearing both in BBM and in the auxiliary equations, some kinds of exact travelling wave solutions were represented. We illustrated how the parameters influence the type and the shape of the solutions. In Case I. we considered the dependency on the parameters α_1 and α_2 appearing in the functionals (26). In Case II. we considered different values of the wave velocity which is in fact expressed through the parameters B, F, H as shown in Eq. (31). The graphical representations show a quite important dependency of the waves amplitude on the propagation velocity. More general solutions than those of the form (G'/G) were pointed out in Case I, with a reduced form of the auxiliary equation.

References

[1] J. P. Gordon, *Optics Letters* **8**(11) (1983) 596.

[2] E. Infeld and G. Rowlands, *Nonlinear waves, solitons and chaos*, Cambridge University Press, Second Ed. 2000.

[3] N. Sirendaorejia and S. Jiong, *Phys. Lett. A* **309** (5–6) (2003) 387.

[4] M. J. Ablowitz and P.A. Clarkson, *Solitons, Nonlinear Evolution Equations and Inverse Scattering*, Cambridge University Press, 1991.

[5] C. N. Babalic, *Rom. J. Phys.* **63** (2018) 114.

[6] C. N. Babalic, *Int. J. Mod. Phys. B* **34** (29) (2020) 2050274.

[7] C. N. Babalic and A. S. Carstea, *J. Phys. A: Math. Theor.* **51** (2018) 225204.

[8] C. N. Babalic and A. S. Carstea, *Theoretical and Mathematical Physics* **188** (2) (2016), 1172.

[9] C. N. Babalic, R. Constantinescu and V. S. Gerdjikov, *J. Geom. and Symm. in Phys.* **37** (2015) 1.

[10] N. Ibragimov, *Elementary Lie group analysis and ordinary differential equations*, Wiley Series in Mathematical Methods in Practice, vol. 4, *John Wiley & Sons Ltd.*, Chichester, 1999.

[11] R. Cimpoiasu, *Rom. J. Phys.* **58** (5-6) (2013) 519.

[12] R. Cimpoiasu, V. Cimpoiasu and R. Constantinescu, *Rom. J. Phys.* **55** (1-2) (2010) 25.

[13] E. J. Parkes and B. R. Duffy, *Comput. Phys. Commun.* **98** (1996) 288.

[14] R Constantinescu, *Rom. Rep. Phys.* **69** (2017) 112.

[15] E. M. E. Zayed and K. A. E. Alurrfi, *Chaos Soliton Fract.* **78** (2015) 148.

[16] N. A. Kudryashov, *Commun. Nonlinear Sci. Numer. Simul.* **17** (6) (2012) 2248.

[17] R. Cimpoiasu and A. S. Pauna, Open Phys.16(1) 2018 419.

[18] M. L. Wang, X. Z. Li and J. L. Zhang, *Phys. Lett. A* **372** (2008) 417.

[19] R. Constantinescu and A. Florian, *Symmetry* **12** (11) (2020) 1819.

[20] J. Weiss, *J. Math. Phys.* **24** (1983) 1405.

[21] J. H. He and X. H. Wu, *Chaos Solitons Fractals* **30** (2006) 700.

[22] A. Babalean, R. Constantinescu and C. Ionescu, *J.Phys A-Math Gen.* **31** (43) (1998) 8653.

[23] P. Rosenau, *Phys. Scr.* **34** (1986) 827.

[24] X. Pan and L. Zhang, *Appl. Math. Model.* **36** (2012) 3371.

[25] A. Esfahani, *Commun. Theor. Phys.* **63** (2013) 1.

[26] P. Razborova, B. Ahmed and A. Biswas, *Appli. Math. Info. Sci.* **8** (2014) 485.

[27] T. Kawahara,*J. Phys. Soc. Japan* **33** (1972) 260.

[28] J.-M. Zuo, *Appl. Math. Comput.* **215** (2) (2009) 835.

[29] J.-M. Zuo, Y.-M. Zhang, T.-D. Zhang and F. Chang, *Boundary Value Prob.* **2010** (2010) 516260.

[30] H. Naher and F. A. Abdullah, *J. Egypt. Math. Soc.* **22** (2014) 390.

Fluid theory of coherent magnetic vortices in high-β space plasmas

Dušan Jovanović[*]
Institute of Physics, University Belgrade, Pregrevica 118, Belgrade, Serbia

Olga Alexandrova[†], **Milan Maksimović**[‡]
LESIA, Observatoire de Paris, 5 place Jules Janssen, 92195 Meudon, France

Milivoj Belić[§]
Texas A&M University at Qatar, P.O. Box 23874 Doha, Qatar

Abstract

Observations in planetary magnetosheaths and in the solar wind reveal the presence of Alfvén vortices as intermittent structures whose scales range from fluid lengths down to few ion lengths, whose density and magnetic are compressible for higher plasma β's. We develop a hydrodynamic model of compressible magnetic vortices in high-β plasmas with anisotropic temperature, with the size ranging from fluid to ion scales. At magneto-fluid scales we find non-propagating field-aligned cylindrical monopoles and inclined propagating dipoles, whose transverse magnetic and velocity fluctuations are aligned, but not identical, and they have finite density and compressible magnetic field fluctuations localized inside the vortex core. In the presence of thermal anisotropy and acoustic effects, they may be correlated or anti-correlated $\delta n/\delta B_{\|} = \text{constant} \gtrless 0$; fluctuations whose velocity along the magnetic field is below the ion thermal speed are always correlated. At ion or kinetic scales (with the smallest radii $\sim c/\omega_{pi}, \rho_{Li}$) and in the absence of acoustic perturbations, only dipolar Alfvén vortices may exist, whose properties are similar as those at fluid scales. We also find pressure balanced kinetic slow magnetosonic dipoles, possessing finite $E_{\|}$ and purely compressional magnetic field perturbation, whose existence is facilitated by a strong ion temperature anisotropy.

PACS numbers: 52.35.Ra, 52.35.We, 94.05.Lk, 94.30.cj, 96.50.Ci

1. Introduction

Magnetic structures at ion break scale, commonly in the form of Alfvén vortices with the diameter $10 - 30$ times longer than the ion scales, have

[*] e-mail address: dusan.jovanovic@ipb.ac.rs
[†] e-mail address: olga.alexandrova@obspm.fr
[‡] e-mail address: milan.maksimovic@obspm.fr
[§] e-mail address: milivoj.belic@qatar.tamu.edu

been observed in the solar wind and in the magnetosheaths of the Earth and Saturn [1, 2, 3, 4]. Similar structures with the diameter comparable to ion-acoustic Larmor radius, identified as drift-Alfvén vortices, were observed in the Earth's magnetospheric cusp [5] where plasma β (ratio of thermal and magnetic pressures, $\beta = 2p/c^2\epsilon_0 B^2$) is much smaller. A statistical analysis of magnetic fluctuations in the turbulent cascade at the ion spectral break, detected in the slow and fast solar wind by the multi-spacecraft Cluster mission [3, 6], showed that the intermittency of the magnetic turbulence is due to the presence of various coherent structures. Compressible structures in the slow wind are predominantly parallel perturbations of the magnetic field ($\delta B_\parallel \gg \delta B_\perp$) in the form of magnetic holes, solitons and shock waves. Coherent shear Alfvénic perturbations have been observed both in the slow and the fast solar wind with $\beta_i \gtrsim 1$ and $\beta_i \lesssim 1$. They appear either as the current sheets or the vortex-like structures. Vortices with a larger compressional magnetic field component, $\delta B_\perp \gtrsim \delta B_\parallel$, have been observed only in the slow wind. The compressible component $\delta B_\parallel$ is localized within the structure, while the torsional $\delta B_\perp$ extends outside of the vortex core.

Shear Alfvén vortices were predicted theoretically by [7], who showed that structures bigger than ion inertial length c/ω_{pi}, $\omega_{pi} = (n_0 e^2/m_i\epsilon_0)^{1/2}$, could exist in plasmas with incompressible density (when $\beta \ll 1$), when nonlinear solutions are described by the Kadomtsev-Pogutse-Strauss' reduced MHD (magnetohydrodynamic) equations [8, 9]. Solutions can be nontravelling monopoles or propagating structures. A vortex moving relative to the plasma is always a dipole, but a monopole can be superimposed to it.

We present a hydrodynamic theory of coherent vortices in space plasmas with anisotropic electron and ion temperatures and arbitrary plasma β. We generalize the shear-Alfvén description [7] by including the diamagnetic and finite Larmor radius effects via Braginskii's collisionless stress tensor, and the compressional magnetic component via a generalized pressure balance. We find a general reduced MHD vortex, whose torsional magnetic field leaks outside of the vortex core while the compressional magnetic field is restricted to its interior, which is why the latter may remain undetected by a spacecraft. They possess also a finite density perturbation and parallel fluid velocity that are proportional to the vorticity and the compressional magnetic field. Conversely, in plasmas with $\beta \lesssim 1$ and on a characteristic length that on the ion-scale, we find two different particular dipole vortex solutions that can be regarded as the generalizations of the Kadomtsev-Pogutse-Strauss' structures to smaller scales and of the nonlinear drift-mode structures to the large-β plasmas, respectively. Generalized K-P-S dipoles possess three components of the magnetic field and their phase velocity along the ambient magnetic field lies in the Alfvén and the acoustic ranges, $u_\parallel \sim (c_A, c_S)$. The slow magnetosonic dipoles that we are able to study analytically propagate much slower, $u_\parallel \ll c_A$ (the range of permitted $u_\parallel \ll$ is broadened in the presence of ion temperature anisotropy), and their

magnetic field perturbation is mostly compressional, viz. $\vec{B}_\perp \to 0$.

2. Fluid theory of slow, weakly z-dependent nonlinear phenomena in a warm plasma $\boldsymbol{\beta_{i_\perp} \sim \beta_{e_\perp} \sim 1}$

We consider a collisionless plasma with the unperturbed density n_0 immersed in the homogeneous magnetic field $\vec{e}_z B_0$. We assume that the electron and ion temperatures can be anisotropic, i.e. that the temperatures associated with the particles' random motions along and perpendicularly to the magnetic field may be different, $T_{j_\parallel} \neq T_{j_\perp}$, where $j = e, i$ and the subscripts $\parallel$ and $\perp$ denote the components parallel and perpendicular to the magnetic field, respectively. The hydrodynamic equations of continuity and momentum for each of the species have the form

$$\left(\frac{\partial}{\partial t} + \vec{U}\cdot\nabla\right) n + n\nabla\cdot\vec{U} = 0, \tag{1}$$

$$\left(\frac{\partial}{\partial t} + \vec{U}\cdot\nabla\right)\vec{U} = \frac{q}{m}\left(\vec{E} + \vec{U}\times\vec{B}\right) - \frac{1}{mn}\nabla\cdot(\boldsymbol{P} + \boldsymbol{\pi}), \tag{2}$$

where, for simplicity, we have omitted the subscripts e and i referring to the electrons and ions, respectively. In the above, n, $\vec{U}$, q, and m are the number density, fluid velocity, charge, and mass, respectively. The pressure $\boldsymbol{P}$ and the stress $\boldsymbol{\pi}$ are diagonal and off-diagonal tensors. Using the standard shorthand notation, the pressure tensor in the case of an anisotropic temperature is given by $\boldsymbol{P} = p_\perp(\boldsymbol{I} - \vec{b}\,\vec{b}) + p_\parallel \vec{b}\,\vec{b}$ where $\boldsymbol{I}$ is a unit tensor, viz. $I_{\alpha,\beta} = \delta_{\alpha,\beta}$ and $\delta_{\alpha,\beta}$ is the Kronecker delta, and $\vec{b}\,\vec{b}$ stands for the dyadic product, whose components are given by $(\vec{b}\,\vec{b})_{\alpha,\beta} = b_\alpha b_\beta$. Here $\vec{b}$ is the unit vector parallel to the magnetic field, $\vec{b} = \vec{B}/B$, B is the intensity of the magnetic field, $B = |\vec{B}|$, $p_\parallel = nT_\parallel$, and $p_\perp = nT_\perp$. Likewise, the stress tensor is written as $\boldsymbol{\pi} = \vec{e}_\alpha\vec{e}_\beta\,\pi_{\alpha,\beta}$. These enable us to use the standard formula from the tensor algebra $\nabla\cdot\vec{q}\,\vec{r} = (\nabla\cdot\vec{q} + \vec{q}\cdot\nabla)\vec{r}$, and to write the divergence of the pressure and the stress tensors as

$$\nabla\cdot\boldsymbol{P} = \nabla p_\perp + \vec{b}\left(\vec{b}\cdot\nabla\right)(p_\parallel - p_\perp) + (p_\parallel - p_\perp)\left(\nabla\cdot\vec{b} + \vec{b}\cdot\nabla\right)\vec{b}, \tag{3}$$

$$\nabla\cdot\boldsymbol{\pi} = \vec{e}_\beta\,(\vec{e}_\alpha\cdot\nabla)\,\pi_{\alpha,\beta} + \pi_{\alpha,\beta}\,(\nabla\cdot\vec{e}_\alpha + \vec{e}_\alpha\cdot\nabla)\,\vec{e}_\beta. \tag{4}$$

The endmost terms on the right-hand-sides in the abov arise from the curvature of magnetic field lines. For convenience, we introduce the notation $(\nabla\cdot\boldsymbol{\pi})_{curv} = \pi_{\alpha,\beta}\,(\nabla\cdot\vec{e}_\alpha + \vec{e}_\alpha\cdot\nabla)\,\vec{e}_\beta$. The chain of hydrodynamic equations is truncated by using the Braginskii's collisionless (nongyrotropic) stress tensor [10], which is appropriate for perturbations that are weakly varying both on the timescale of the gyroperiod and on the perpendicular

scale of the Larmor radius. Within the adopted large scale limit, Braginskii's stress tensor has been generalized to plasmas with anizotropic temperature [11, 12]. Following these, we neglect the heat flux and use instead generic equations of state

$$dp_\perp/p_\perp = \gamma_\perp\, dn/n, \qquad dp_\parallel/p_\parallel = \gamma_\parallel\, dn/n, \tag{5}$$

in which the multipliers $\gamma_\parallel$ and $\gamma_\perp$ are some functionals of the plasma density, see [13]where polytropic indices for collisionless plasmas were derived. We consider regimes in which the perturbations of the density and of the magnetic field are not too large, see Eq. (10), which permits us to make an estimate of the functionals $\gamma_\parallel$ and $\gamma_\perp$ from the linearized Vlasov equation. These are further simplified under the drift scaling and for weak dependence along magnetic field lines, (10), when $\gamma_\parallel$ reduces to a constant, viz. $\gamma_\parallel = 3$ if $u_z > v_{T_\parallel}$ and the process can be considered as adiabatic, and to $\gamma_\parallel = 1$ when $u_z \ll v_{T_\parallel}$, i.e. the process is isothermal. Likewise, the perpendicular functional reduces to $\gamma_\perp = 1$ for arbitrary $u_z/v_{T_\parallel}$ if the characteristic perpendicular size of the solution is much bigger than the Larmor radius. Conversely, for solutions whose transverse scale approaches the ion scales, $\gamma_\perp$ can be approximated by a constant only in a limited number of cases. These include the shear Alfvén solution with zero parallel electric field, $E_\parallel = 0$, decoupled from acoustic perturbations, $u_z > v_{Ti_{\parallel,\perp}}$, for which $\gamma_{i_\perp} = 2$, and the kinetic slow magnetosonic mode solution whose torsion of the magnetic field is absent, $\delta\vec{B}_\perp = 0$, realized in the regime $c_A > u_z > v_{Ti_{\parallel,\perp}}$ in which the coupling with acoustic perturbation is negligible and we also have $\gamma_{i_\perp} = 2$.

The system of equations is closed by the Faraday's and Ampere's laws

$$\nabla \times \vec{E} = -\frac{\partial \vec{B}}{\partial t}, \qquad \nabla \times \vec{B} = \frac{1}{c^2}\left(\frac{\partial \vec{E}}{\partial t} + \frac{\vec{j}}{\epsilon_0}\right). \tag{6}$$

The latter is simplified on temporal scales that are slow compared to the electron plasma frequency $\omega_{pe} = \sqrt{n_0 e^2/m_e\epsilon_0}$ and spatial scales that are long compared to the electron Debye length $\lambda_{De} = v_{Te}/\omega_{pe}$, when we can neglect both the charge separation and the displacement current, yielding

$$n_e = n_i \equiv n, \qquad \frac{n}{n_0}\left(\vec{U}_i - \vec{U}_e\right) = \frac{e}{m_e}\frac{c^2}{\omega_{pe}^2}\,\nabla \times \vec{B}. \tag{7}$$

We consider single-charged ions, viz. $q_i = -q_e = e$.

For later reference, we write also the parallel momentum equation, that

is obtained when we multiply the momentum equation with $\vec{b}\cdot$, viz.

$$\left(\frac{\partial}{\partial t}+\vec{U}\cdot\nabla\right)U_{\parallel}-\frac{q}{m}\,\vec{b}\cdot\left(\vec{E}-\frac{1}{qn}\,\nabla p_{\parallel}+\frac{p_{\parallel}-p_{\perp}}{qnB}\,\nabla B\right)+\frac{1}{mn}\left[\frac{\partial\pi_{\alpha,b}}{\partial x_{\alpha}}+\vec{b}\cdot\left(\nabla\cdot\boldsymbol{\pi}\right)_{curv}\right]=\vec{U}_{\perp}\cdot\left(\frac{\partial}{\partial t}+\vec{U}\cdot\nabla\right)\vec{b},\tag{8}$$

where $U_{\parallel}=\vec{b}\cdot\vec{U}$. Likewise, the perpendicular momentum equation for the plasma fluid has the form

$$\nabla_{\perp}\left(c^2\epsilon_0\frac{B^2}{2}+p_{e_{\perp}}+p_{i_{\perp}}\right)=\epsilon_0\left[\vec{E}_{\perp}\left(\nabla\cdot\vec{E}\right)+B\vec{b}\times\frac{\partial\vec{E}}{\partial t}\right]+\vec{b}\times\left\{\vec{b}\times\left[m_en_e\left(\frac{\partial}{\partial t}+\vec{U}_e\cdot\nabla\right)\vec{U}_e+m_in_i\left(\frac{\partial}{\partial t}+\vec{U}_i\cdot\nabla\right)\vec{U}_i\right]\right\}+\left(c^2\epsilon_0B^2-p_{e_{\parallel}}-p_{i_{\parallel}}+p_{e_{\perp}}+p_{i_{\perp}}\right)\left(\vec{b}\cdot\nabla\right)\vec{b}-\nabla\cdot\left(\pi_{e_{\alpha,\beta}}+\pi_{i_{\alpha,\beta}}\right).\tag{9}$$

In the quasineutrality regime (i.e. on the adopted scales bigger than the Debye length λ_{De}), Eq.(7) is simplified by setting $\nabla\cdot\vec{E}=e(n_i-n_e)/\epsilon_0=0$. Eqs. (1), (2), (8), and (9) are vastly simplified under the drift scaling and in the regime of small perturbations of the density and of the magnetic field, and of the weak dependence along the magnetic field line

$$\frac{1}{\Omega}\frac{\partial}{\partial t}\sim\frac{1}{\Omega}\,\vec{U}\cdot\nabla\sim\epsilon\ll1,\qquad\text{and}\qquad\frac{\delta n}{n}\sim\frac{|\delta\vec{B}|}{|\vec{B}|}\sim\frac{\vec{b}\cdot\nabla}{\nabla_{\perp}}\sim\epsilon.\tag{10}$$

Here, Ω is the gyrofrequency, $\Omega=qB/m$, and δ denotes the deviation of a quantity from its unperturbed value. The explicit form of the collisionless stress tensor $\boldsymbol{\pi}$ in a plasma with anisotropic temperature can be seen e.g. in Refs. [11]where it has been calculated under the scaling (10), with the accuracy to the the first order in the FLR (finite-Larmor-radius) corrections, and expressed in the local orthogonal coordinate system with the curvilinear b-axis along the magnetic lines of force

$$\begin{aligned}
&\pi_{m,m}=-\pi_{l,l}=\left(p_{\perp}/2\Omega\right)\left(\partial U_l/\partial x_m+\partial U_m/\partial x_l\right),\\
&\pi_{l,m}=\pi_{m,l}=\left(p_{\perp}/2\Omega\right)\left(\partial U_l/\partial x_l-\partial U_m/\partial x_m\right),\\
&\pi_{l,b}=\pi_{b,l}=-\left(p_{\perp}/\Omega\right)\left(\partial U_b/\partial x_m\right)-\left[\left(2p_{\parallel}-p_{\perp}\right)/\Omega\right]\left(\partial U_m/\partial x_b\right),\\
&\pi_{m,b}=\pi_{b,m}=\left(p_{\perp}/\Omega\right)\left(\partial U_b/\partial x_l\right)+\left[\left(2p_{\parallel}-p_{\perp}\right)/\Omega\right]\left(\partial U_l/\partial x_b\right),\\
&\pi_{b,b}=0.
\end{aligned}\tag{11}$$

Here $\vec{b}$, $\vec{e}_l$, and $\vec{e}_m$ are three mutually perpendicular unit vectors and $\partial/\partial x_{\alpha}\equiv\vec{e}_{\alpha}\cdot\nabla$, where $\alpha=l,m,b$. We adopt the last two vectors as

$\vec{e}_l = \vec{b} \times (\vec{e}_x \times \vec{b})/|\vec{e}_x \times \vec{b}|$ and $\vec{e}_m = \vec{b} \times \vec{e}_l$. In the regime of a weak curvature of magnetic field lines, Eq. (10), these unit vectors are properly approximated by the expressions given in Eq. (26) below.

The perpendicular component of the fluid velocity is obtained after we multiply Eq. (2) with $\vec{b}\times$, and can be readily written as the sum of the $\vec{E} \times \vec{B}$, diamagnetic, anisotropic-temperature, and polarization drifts, together with the leading part and the curvature correction of the stress-related (or the FLR) drift, $\vec{U}_\perp = \vec{U}_E + \vec{U}_D + \vec{U}_A + \vec{U}_p + \vec{U}_\pi + \delta\vec{U}_\pi$, where

$$\vec{U}_E = -\frac{\vec{b}}{B} \times \vec{E}, \quad \vec{U}_D = \frac{\vec{b}}{qnB} \times \nabla_\perp p_\perp, \quad \vec{U}_A = \left(p_\parallel - p_\perp\right) \frac{\vec{b}}{qnB} \times \left(\vec{b} \cdot \nabla\right) \vec{b},$$
$$\vec{U}_B = \frac{p_\perp \vec{b}}{qnB^2} \times \nabla_\perp B, \quad \vec{U}_p = \frac{\vec{b}}{\Omega} \times \left(\frac{\partial}{\partial t} + \vec{U} \cdot \nabla\right) \vec{U},$$
$$\vec{U}_\pi = \frac{\vec{b}}{qnB} \times \vec{e}_\beta \frac{\partial \pi_{\alpha,\beta}}{\partial x_\alpha}, \quad \delta\vec{U}_\pi = \frac{\vec{b}}{qnB} \times (\nabla \cdot \boldsymbol{\pi})_{curv}\,. \tag{12}$$

For completeness, in the above list we have added also the grad-B drift velocity $\vec{U}_B$. Using Eq. (11), the stress-related drift and the leading contribution of the stress to the parallel momentum equation (8) take the form:

$$\vec{U}_\pi = -\frac{T_\perp}{2m\Omega^2} \nabla_\perp^2 \vec{U}_\perp -$$
$$\frac{1}{qnB} \left\{ \left[\left(\vec{b} \times \nabla_\perp \frac{p_\perp}{2\Omega} \right) \cdot \nabla_\perp \right] \vec{b} \times \vec{U}_\perp + \left(\nabla_\perp \frac{p_\perp}{2\Omega} \cdot \nabla_\perp \right) \vec{U}_\perp + \right. \tag{13}$$
$$\left. \left(\vec{b} \cdot \nabla\right) \left[\frac{p_\perp}{\Omega} \nabla_\perp U_\parallel + \frac{2p_\parallel - p_\perp}{\Omega} \left(\vec{b} \cdot \nabla\right) \vec{U}_\perp \right] \right\}, \tag{14}$$
$$\frac{\partial \pi_{\alpha,b}}{\partial x_\alpha} = \vec{b} \cdot \left\{ \nabla_\perp U_\parallel \times \nabla_\perp \frac{p_\perp}{\Omega} - \nabla_\perp \times \left[\frac{2p_\parallel - p_\perp}{\Omega} \left(\vec{b} \cdot \nabla\right) \vec{U}_\perp \right] \right\}. \tag{15}$$

In the regime of slow variations (compared to Ω), weak dependence along the magnetic field lines, and small perturbations of the magnetic field in all spatial directions, that is described by the scalings Eqs. (10), we can neglect the last term in Eq. (14) that contains the second parallel derivative $(\partial/\partial x_b)^2$. The contribution of the magnetic curvature to the divergence of the stress tensor is a small quantity of the order $\epsilon^2 \rho_L^2 \nabla^2$, viz.

$$(\nabla \cdot \boldsymbol{\pi})_{curv} = \pi_{\alpha,b} \left(\partial\vec{b}/\partial x_\alpha\right) - \vec{b}\, \pi_{\alpha,\beta} \left[\vec{e}_\beta \cdot \left(\partial\vec{b}/\partial x_\alpha\right) \right] + \mathcal{O}\left(\epsilon^3\right), \tag{16}$$

and using Eqs. (11) and the approximations in Eq. (26), we obtain the following leading-order expressions:

$$\delta\vec{U}_\pi = \vec{e}_{\alpha_\perp} \rho_L^2 \left(\frac{\partial \vec{b}}{\partial x_{\alpha_\perp}} \cdot \nabla U_\parallel \right), \qquad \vec{b} \cdot (\nabla \cdot \boldsymbol{\pi})_{curv} = q n_0 \rho_L^2 \frac{\partial \vec{U}_\perp}{\partial x_{\alpha_\perp}} \cdot \nabla_\perp \frac{\partial A_z}{\partial x_{\alpha_\perp}}, \tag{17}$$

where $\rho_L = \sqrt{T_\perp/m\Omega_0^2}$ is the (unperturbed) Larmor radius and $\alpha_\perp = x, y$.

The leading order (in ϵ) stress-related drift $\vec{U}_\pi + \delta\vec{U}_\pi$ is given by the first term on the right-hand-side of Eq. (14). As the polarization drift $\vec{U}_p$ and the curvature related drifts $\vec{U}_A$ and $\delta\vec{U}_\pi$ are small compared to the $\vec{E}\times\vec{B}$ and diamagnetic drifts and noting that $\nabla\cdot(\vec{U}_E + \vec{U}_D) = \mathcal{O}\left(\epsilon^2\right)$, see Eq. (20), to leading order in ϵ we can write $\vec{U}_\perp \approx \vec{U}_E + \vec{U}_D - \rho_L^2\nabla_\perp^2\vec{U}_\perp/2$, that is formally solved as $\vec{U}_\perp \approx \vec{U}_\perp^{apr}$, where

$$\vec{U}_\perp^{apr} \equiv \left(1 + \rho_L^2\nabla_\perp^2/2\right)^{-1}\left(\vec{U}_E + \vec{U}_D\right). \tag{18}$$

Within the adopted accuracy, this expression for $\vec{U}_\perp$ can be used on the right-hand-sides of Eqs. (12)–(15) and (19). Likewise, in the convective derivatives we use $\vec{U}\cdot\nabla \approx \vec{U}_\perp\cdot\nabla_\perp \approx \vec{U}_\perp^{apr}\cdot\nabla_\perp$. Under scaling (10) we can also neglect the right-hand-side of Eq. (8). On the right-hand-side of Eq. (9) we neglect the second-order terms coming from the polarizaton, charge separation, displacement current and the curvature of the magnetic field. Only the leading part of the last term remains and the equation simplifies:

$$\nabla_\perp\left(\frac{c^2\epsilon_0 B^2}{2} + p_{e_\perp} + p_{i_\perp}\right) = -\vec{b}\times\left(\frac{p_{i_\perp}}{2\Omega_i}\nabla_\perp^2\vec{U}_{i_\perp} + \frac{p_{e_\perp}}{2\Omega_e}\nabla_\perp^2\vec{U}_{e_\perp}\right), \tag{19}$$

which reduces to the equation of pressure balance when the Larmor radius corrections can be neglected. Now, using

$$\nabla\cdot\left(\vec{U}_E + \vec{U}_D\right) \approx -\left[\frac{\partial}{\partial t} + \left(\vec{U}_E + \vec{U}_D\right)\cdot\nabla_\perp\right]\log B - \left(\vec{U}_E + \vec{U}_D\right)\cdot\left(\vec{b}\cdot\nabla\right)\vec{b} - \left(\vec{b}\times\nabla p_\perp\right)\cdot\frac{\nabla n}{qn^2B}, \tag{20}$$

$$\nabla\cdot\vec{U}_A \approx \left(\vec{b}\cdot\nabla\right)\left[\frac{p_{\parallel_0} - p_{\perp_0}}{qn_0B_0}\ \nabla\cdot\left(\vec{e}_z\times\vec{b}\right)\right], \tag{21}$$

and Eqs. (14), (16) for $\nabla\cdot\vec{U}_\pi$, we evaluate continuity and parallel momentum equations to leading order in ϵ setting $\vec{U}\cdot\nabla \approx \vec{U}_\perp^{apr}\cdot\nabla_\perp$ and $\vec{U}_\perp \approx \vec{U}_\perp^{apr}$, and dropping the last term on the right hand side of Eq. (20) that vanishes

if $p_\perp$ is a function of n, described by Eq. (5) when $\gamma_\perp = \gamma_\perp(n)$. We obtain:

$$\left(\frac{\partial}{\partial t} + \vec{U}_\perp^{apr} \cdot \nabla_\perp\right) \log\frac{n}{B} + \left(\vec{b}\cdot\nabla\right)\left[U_\parallel + \frac{p_{\parallel_0} - p_{\perp_0}}{qn_0B_0}\ \nabla\cdot\left(\vec{e}_z\times\vec{b}\right)\right] + \frac{1}{\Omega_0}\nabla_\perp\cdot\left\{\left[\frac{\partial}{\partial t} + \left(\vec{U}_\perp^{apr} + \vec{U}_B - \vec{U}_D\right)\cdot\nabla_\perp\right]\vec{e}_z\times\vec{U}_\perp^{apr}\right\} + \rho_L^2\left(\nabla_\perp^2\vec{b}\cdot\nabla U_\parallel - \vec{b}\cdot\nabla\nabla_\perp^2 U_\parallel\right) = 0, \tag{22}$$

$$\left[\frac{\partial}{\partial t} + \left(\vec{U}_\perp^{apr} + \vec{U}_B - \vec{U}_D\right)\cdot\nabla\right]U_\parallel = \frac{q}{m}\left(\vec{b}\cdot\vec{E} - \rho_L^2\,\frac{\partial\vec{U}_\perp^{apr}}{\partial x_{\alpha_\perp}}\cdot\nabla_\perp\frac{\partial A_z}{\partial x_{\alpha_\perp}}\right) - \frac{\vec{b}}{n_0m}\cdot\nabla\left[p_\parallel - \left(p_{\parallel_0} - p_{\perp_0}\right)\frac{B}{B_0} + \frac{2p_{\parallel_0} - p_{\perp_0}}{\Omega_0}\,\nabla_\perp\cdot\left(\vec{b}\times\vec{U}_\perp^{apr}\right)\right]. \tag{23}$$

Momentum equation for the plasma fluid is obtained by multiplying the electron and ion momentum equations respectively by m_e and m_i and adding, which in the limit of massless electrons $m_e \to 0$ gives

$$\left[\frac{\partial}{\partial t} + \left(\vec{U}_{i_\perp}^{apr} + \vec{U}_{i_B} - \vec{U}_{i_D}\right)\cdot\nabla\right]U_{i_\parallel} = -\rho_{Li}^2\,\frac{q_i}{m_i}\,\frac{\partial\vec{U}_{i_\perp}^{apr}}{\partial x_{\alpha_\perp}}\cdot\nabla_\perp\frac{\partial A_z}{\partial x_{\alpha_\perp}} - \frac{1}{n_0m_i}\left(\vec{b}\cdot\nabla\right)\left[p_{i_\parallel} + p_{e_\parallel} - \left(p_{i_{\parallel_0}} - p_{i_{\perp_0}} + p_{e_{\parallel_0}} - p_{e_{\perp_0}}\right)\frac{B}{B_0} + \frac{2p_{i_{\parallel_0}} - p_{i_{\perp_0}}}{\Omega_{i_0}}\,\nabla_\perp\cdot\left(\vec{b}\times\vec{U}_{i_\perp}^{apr}\right)\right]. \tag{24}$$

Within the drift- and small-but-finite FLR scalings, Eq. (10), and taking that $\delta\vec{B}_\parallel \not> \delta\vec{B}_\perp$, the electromagnetic field can be expressed in terms of the electrostatic potential and of the z-components of the vector potential and magnetic field, ϕ, A_z, and δB_z, viz.

$$\vec{E} = -\nabla\phi - \frac{\partial}{\partial t}\left(\vec{e}_zA_z + \vec{e}_z\times\nabla\,\nabla_\perp^{-2}\delta B_z\right), \quad \vec{B} = \vec{e}_z\left(B_0 + \delta B_z\right) - \vec{e}_z\times\nabla A_z, \tag{25}$$

which yields the following expressions, accurate to first order:

$$\vec{b} = \vec{e}_z - \frac{1}{B_0}\,\vec{e}_z\times\nabla_\perp A_z, \quad \vec{e}_l = \vec{e}_x - \frac{\vec{b}}{B_0}\frac{\partial A_z}{\partial y}, \quad \vec{e}_m = \vec{e}_y + \frac{\vec{b}}{B_0}\frac{\partial A_z}{\partial x}, \tag{26}$$

$$B = |\vec{B}| = B_0 + \delta B_z, \quad \vec{b}\cdot\vec{E} = -\vec{b}\cdot\nabla\phi - \frac{\partial A_z}{\partial t}, \quad \vec{b}\times\vec{E} = -\vec{e}_z\times\nabla\phi, \tag{27}$$

We conveniently rewrite our basic equations in a dimensionless form using

the following scaled variables and parameters

$$t' = \omega\, t, \quad x' = k\, x,\ y' = k\, y,\ z' = (\omega/c_A)\, z,\ \phi' = \frac{k^2\phi}{B_0\omega}, \quad A'_z = \frac{k^2 c_A A_z}{B_0\omega},$$
$$B'_z = \frac{\Omega_{i_0}}{\omega}\frac{\delta B_z}{B_0}, \quad n' = \frac{\Omega_{i_0}}{\omega}\frac{\delta n}{n_0}, \quad U'_\parallel = \frac{\omega_{pi}}{\omega}\frac{U_\parallel}{c}, \quad p' = \frac{k^2}{\Omega_{i_0}\omega}\frac{\delta p}{n_0 m_i},$$
$$\beta = \frac{2p_0}{c^2\epsilon_0 B_0^2}, \quad d'_e = \frac{c\,k}{\omega_{pe}}, \quad d'_i = \frac{c\,k}{\omega_{pi}}, \quad \rho'_i = k\,\rho_{Li} = d'_i\sqrt{\frac{\beta_{i_\perp}}{2}}, \tag{28}$$

where k and ω are some characteristic wavenumber and characteristic frequency, i.e. the inverse characteristic spatial and temporal scales, such as the width of the structure r_0 and the transit time $r_0/u_\perp$, $u_\perp$ being the speed of its propagation in the plasma frame transversely to the magnetic field. The normalization through k, ω is used for convenience and does not infer any presence of wave phenomena. Other notations are standard.

The dimensionless versions of the charge continuity (the difference of the ion and electron continuity equations with electron polarization and FLR effects neglected), the electron continuity and parallel momentum equations, Eqs. (22) and (23), and of the parallel and perpendicular fluid momentum equations (24) and (19), can be written as follows (for simplicity, here and in the rest of the paper, we omit the primes):

$$\left[\vec{e}_z \times \nabla_\perp \left(\frac{p_{i_\perp} - \rho_i^2\nabla_\perp^2\phi/2}{1+\rho_i^2\nabla_\perp^2/2} + p_{e_\perp}\right)\right]\cdot\nabla_\perp(n - B_z) -$$
$$\left[\frac{\partial}{\partial z} - (\vec{e}_z\times\nabla_\perp A_z)\cdot\nabla_\perp\right]\left(1 - \frac{\beta_{i_\parallel} - \beta_{i_\perp} + \beta_{e_\parallel} - \beta_{e_\perp}}{2}\right)\nabla_\perp^2 A_z -$$
$$\nabla_\perp\cdot\left(\left\{\frac{\partial}{\partial t} + \left[\vec{e}_z\times\nabla_\perp\left(\frac{\phi - \rho_i^2\nabla_\perp^2 p_{i_\perp}/2}{1+\rho_i^2\nabla_\perp^2/2} + \frac{\beta_{i_\perp}}{2}\, d_i^2 B_z\right)\right]\cdot\nabla_\perp\right\}\times\right.$$
$$\left.\nabla_\perp\frac{\phi + p_{i_\perp}}{1+\rho_i^2\nabla_\perp^2/2}\right) - \rho_i^2\left(\vec{e}_z\times\nabla_\perp\nabla_\perp^2 A_z\right)\cdot\nabla_\perp U_{i_\parallel} -$$
$$\rho_i^2\left[\frac{\partial}{\partial z} - (\vec{e}_z\times\nabla_\perp A_z)\cdot\nabla_\perp\right]\nabla_\perp^2 U_{i_\parallel} = 0, \tag{29}$$

$$\left\{\frac{\partial}{\partial t} + [\vec{e}_z\times\nabla_\perp(\phi - p_{e_\perp})]\cdot\nabla_\perp\right\}(n - B_z) + \tag{30}$$
$$\left[\frac{\partial}{\partial z} - (\vec{e}_z\times\nabla_\perp A_z)\cdot\nabla_\perp\right]\left(U_{e_\parallel} - \frac{\beta_{e_\parallel} - \beta_{e_\perp}}{2}\nabla_\perp^2 A_z\right) = 0, \tag{31}$$

$$\left[\frac{\partial}{\partial z} - (\vec{e}_z\times\nabla_\perp A_z)\cdot\nabla_\perp\right]\left(\phi - p_{e_\parallel} + \frac{\beta_{e_\parallel} - \beta_{e_\perp}}{2}\, d_i^2 B_z\right) + \frac{\partial A_z}{\partial t} = 0, \tag{32}$$

$$\left\{\frac{\partial}{\partial t}+\left[\vec{e}_z\times\nabla_\perp\left(\frac{\phi-\rho_i^2\nabla_\perp^2 p_{i_\perp}/2}{1+\rho_i^2\nabla_\perp^2/2}+\frac{\beta_{i_\perp}}{2}\,d_i^2 B_z\right)\right]\cdot\nabla_\perp\right\}\,d_i^2 U_{i_\parallel}=$$
$$-\left[\frac{\partial}{\partial z}-(\vec{e}_z\times\nabla_\perp A_z)\cdot\nabla_\perp\right]\times$$
$$\left[p_{i_\parallel}+p_{e_\parallel}-\frac{\beta_{i_\parallel}-\beta_{i_\perp}+\beta_{e_\parallel}-\beta_{e_\perp}}{2}\,d_i^2 B_z-\left(\frac{2\beta_{i_\parallel}}{\beta_{i_\perp}}-1\right)\frac{\rho_i^2\nabla_\perp^2\,(\phi+p_{i_\perp})}{1+\rho_i^2\nabla_\perp^2/2}\right]-$$
$$\rho_i^2\left(\vec{e}_z\times\nabla_\perp\,\frac{\partial}{\partial x_{\alpha_\perp}}\frac{\phi+p_{i_\perp}}{1+\rho_i^2\nabla_\perp^2/2}\right)\cdot\nabla\frac{\partial A_z}{\partial x_{\alpha_\perp}},\tag{33}$$

$$d_i^2 B_z+p_{i_\perp}+p_{e_\perp}-\frac{\rho_i^2\nabla_\perp^2\,(\phi+p_{i_\perp})\,/2}{1+\rho_i^2\nabla_\perp^2/2}=0,\tag{34}$$

where we neglected the charge separation ($n_e=n_i=n$) and the displacement current ($U'_{e_\parallel}-U'_{i_\parallel}=\nabla'^2_\perp A'_z$), and we considered the electrons to be massless (i.e. we took $m_e\to 0$ and accordingly $\omega/\Omega_e=\rho'_e=d'_e=0$).

Pressure perturbations are expressed in terms of density via dimensionless versions of the equations of state (5) viz.

$$p'_{j\,\zeta}=\gamma_{j\,\zeta}\;(\beta_{j\,\zeta}/2)\;d_i'^2 n',\quad\text{where}\quad j=e,i\quad\text{and}\quad\zeta=\parallel,\perp.\tag{35}$$

The acoustic perturbations, associated with the parallel plasma motion described by the momentum equation (33), are coupled with the rest of the system only through the last term in Eq. (29) that has come from the divergence of the curvature correction to the FLR drift, $\nabla\cdot\delta\vec{U}_{i\pi}$. It will be shown below that in the regimes of our interest this term is small, so that the acoustic perturbations are fully decoupled. Eqs. (29)–(32) and (34) constitute our basic set of equations for the functions ϕ, A_z, B_z, and n.

Finding a general solution of the above equations is a formidable task, but suitable particular solutions have been found in a number of relevant cases. In our earlier papers we studied in electron-scale nonlinear structures in plasmas with cold electrons and very cold ions, $\beta_{e_\perp}\ll 1$ and $\beta_{i_\perp}\ll m_e/m_i$ on the MHD temporal scale [14, 15]. In the warm plasma, mostly electron scale structures were considered, such as whistler-frequency perturbations in the regime $\beta_{e_\perp}\gtrsim 1$ with immobile ions [16].

3. Vortex solutions approaching ion scales

When the plasma β is close to, or or bigger than, unity the dimensionless ion Larmor radius becomes comparable and even bigger than the dimensionless ion inertial length, when the reduced MHD equations do not provide an accurate description. Below we construct a localized, stationary, 2-d solution of the full system (29)-(34), assuming that its spatial extent is comparable

with ion scales but much larger than the electron skin depth, $d_e' \to 0$. We seek a solution that is travelling with the (non scaled) velocity $\vec{u}_\perp = \vec{e}_y\, k/\omega$ and is tilted to the z-axis by a small angle $\theta = \omega/ku_z$, dependent only on the variables x' and $y' + (c_A/u_z)\, z' - t'$. Then, the equations of parallel electron momentum (32), electron continuity (31), parallel fluid momentum (33), charge continuity (29), and pressure balance (34) can be cast as:

$$[\vec{e}_z \times \nabla_\perp (\psi - x)] \cdot \nabla_\perp \left[\phi - p_{e_\parallel} - x + (1/2)\left(\beta_{e_\parallel} - \beta_{e\perp}\right)\, d_i^2 B_z\right] = 0, \quad (36)$$

$$\begin{aligned}&[\vec{e}_z \times \nabla_\perp (\phi - p_{e_\perp} - x)] \cdot \nabla_\perp (n - B_z) - \\ &[\vec{e}_z \times \nabla_\perp (\psi - x)] \cdot \nabla_\perp \left\{V_\parallel + \left(c_A^2/u_z^2\right)\left[1 - (1/2)\left(\beta_{e_\parallel} - \beta_{e_\perp}\right)\right]\nabla_\perp^2 \psi\right\} = 0,\end{aligned} \quad (37)$$

$$\begin{aligned}&\left[\vec{e}_z \times \nabla_\perp \left(\Phi - p_{i_\perp} + \rho_i^2 B_z - x\right)\right] \cdot \nabla_\perp d_i^2 V_\parallel - \\ &\left(c_A^2/u_z^2\right)[\vec{e}_z \times \nabla_\perp (\psi - x)] \cdot \nabla_\perp \Big[p_{e_\parallel} + p_{i_\parallel} - \\ &\left(\beta_{e_\parallel} - \beta_{e_\perp} + \beta_{i_\parallel} - \beta_{i_\perp}\right)\left(\rho_i^2/\beta_{i_\perp}\right) B_z - \left(2\beta_{i_\parallel}/\beta_{i_\perp} - 1\right)\rho_i^2 \nabla_\perp^2 \Phi\Big] = \\ &\quad -\rho_i^2 \left(c_A^2/u_z^2\right)\left(\vec{e}_z \times \nabla_\perp\, \partial\Phi/\partial x_i\right) \cdot \nabla_\perp \partial\psi/\partial x_i,\end{aligned} \quad (38)$$

$$\begin{aligned}&\left[\vec{e}_z \times \nabla_\perp \left(-\rho_i^2 \nabla_\perp^2 \Phi/2 + p_{i_\perp} + p_{e_\perp}\right)\right] \cdot \nabla_\perp (n - B_z) + \\ &\left(c_A^2/u_z^2\right)\left[1 - (1/2)\left(\beta_{e_\parallel} - \beta_{e_\perp} + \beta_{i_\parallel} - \beta_{i\perp}\right)\right][\vec{e}_z \times \nabla_\perp (\psi - x)] \cdot \nabla_\perp \nabla_\perp^2 \psi + \\ &\rho_i^2 \left(\vec{e}_z \times \nabla_\perp V_\parallel\right) \cdot \nabla_\perp \nabla_\perp^2 \psi - \left[\vec{e}_z \times \nabla_\perp \left(\Phi - p_{i_\perp} + \rho_i^2 B_z - x\right)\right] \cdot \nabla_\perp \nabla_\perp^2 \Phi + \\ &\rho_i^2 [\vec{e}_z \times \nabla_\perp (\psi - x)] \cdot \nabla_\perp \nabla_\perp^2 V_\parallel = \\ &\quad \left[\vec{e}_z \times \nabla_\perp (\partial/\partial x_i)\left(\rho_i^2 B_z - p_{i_\perp}\right)\right] \cdot \nabla_\perp\, \partial\Phi/\partial x_i,\end{aligned} \quad (39)$$

$$d_i^2 B_z + p_{i_\perp} + p_{e_\perp} - \rho_i^2 \nabla_\perp^2 \Phi/2 = 0, \quad (40)$$

where, as before, we have omitted the primes and used the notations:

$$\Phi = \left(1 + \rho_i^2 \nabla_\perp^2/2\right)^{-1}\left(\phi + p_{i_\perp}\right), \quad \psi = \left(u_z/c_A\right)\, A_z \quad \text{and} \quad V_\parallel = \left(c_A/u_z\right)\, U_{i_\parallel}. \quad (41)$$

Electron and ion pressures are related with the density by the equation of state (35), $p_{j\,\zeta} = \gamma_{j\,\zeta}\left(\beta_{j\,\zeta}/2\right)\, d_i^2 n$, where $j = e, i$ and $\zeta = \parallel, \perp$. It is worth noting that the linearized version of our basic equations (36)-(40) in the regime of small but finite ion Larmor radius corrections, $\rho_i^2 \nabla_\perp^2 \sim \sqrt{\epsilon} < 1$, $\rho_i^4 \nabla_\perp^4 \sim \epsilon \to 0$, and in the absence of acoustic perturbations that occurs when $u_z > \max\left(v_{Ti_\perp},\, \sqrt{\gamma_{Ti_\parallel}}\, v_{Ti_\parallel}\right)$, reduces to

$$\left(\nabla_\perp^2 - \kappa^2\right)\nabla_\perp^2 \psi = 0, \quad (42)$$

where

$$\kappa^2 = \frac{2}{\rho_i^2}\left(1 - \frac{2\,u_z^2/c_A^2}{2 - \beta_{e_\parallel} + \beta_{e_\perp} - \beta_{i_\parallel} + \beta_{i_\perp}}\right) \times \left\{1 - \frac{\beta_{e_\parallel} - \beta_{e_\perp}}{2} + \left[1 + \frac{\left(2 - \beta_{e_\parallel} + \beta_{e_\perp}\right)(4/\beta_{i_\perp})}{2 - \beta_{e_\parallel} + \beta_{e_\perp} - \beta_{i_\parallel} + \beta_{i_\perp}}\right] \left[\frac{\beta_{e_\perp} + \beta_{e_\parallel}\left(\gamma_{e_\parallel} - 1\right) + \beta_{i_\perp}\gamma_{i_\perp}}{2 + \beta_{e_\perp}\gamma_{e_\perp} + \beta_{i_\perp}\gamma_{i_\perp}} + \frac{\beta_{e_\parallel} - \beta_{e_\perp}}{2}\right]\right\}^{-1}. \tag{43}$$

The linear response has the form of waves when $\kappa^2 < 0$. It consists of two modes of waves, whose wavenumbers are equal to zero and to $i\kappa$. These are identified as the large-β versions of the shear Alfvén wave (actually, it features a finite perpendicular wavenumber on the electron scale, for a simple example in the case of a very-low-β plasma see [14, 15]) and of the kinetic slow mode, respectively. We expect that in the nonlinear regime there may exist two nonlinear vortex modes analogous to these.

A simple analysis shows that the last term in Eq. (44) is strictly positive when the ion temperature is anisotropic with $\beta_{i_\parallel} \leq \beta_{i_\perp}$, if the parallel electron temperature is not too high, $\beta_{e_\parallel} \leq 2 + \beta_{e_\perp}$, i.e. a kinetic slow wave is evanescent ($\kappa^2 > 0$) when its parallel phase velocity is sufficiently small,

$$u_z^2/c_A^2 < 1 - \left(\beta_{e_\parallel} - \beta_{e_\perp} + \beta_{i_\parallel} - \beta_{i_\perp}\right)/2 \sim \mathcal{O}(1). \tag{44}$$

For larger u_z we have a propagating wave. Temperature anisotropies are common in space plasmas - in the solar wind and Earth's magnetosheath.

Seeking travelling/tilted solutions it is possible to integrate also the parallel electron momentum equation (36), viz.

$$\phi - x = p_{e_\parallel} - (1/2)\left(\beta_{e_\parallel} - \beta_{e\perp}\right) d_i^2 B_z + F(\psi - x), \tag{45}$$

where F is an arbitrary function of the nonlinear characteristic $\psi - x$.

It is difficult to proceed further because solving Eq. (37) in a general case is a formidable task. Likewise, Eqs. (38) and (39) contain higher derivatives of unknown functions on their right hand sides and are practically impossible to integrate. In particular, the coupling with acoustic perturbation increases the complexity of our equations and makes an analytic solution virtually impossible. For this reason, we will restrict our study to the perturbations whose parallel phase velocity satisfies the conditions $(c_a^2/u_z^2)(\beta_{i\perp}/2) \lesssim (c_a^2/u_z^2)(\gamma_{i\|}\beta_{i\|}/2) \sim \epsilon \to 0$ or equivalently $u_z > \max\left(v_{Ti_\perp},\ \sqrt{\gamma_{i_\parallel}}\ v_{Ti_\parallel}\right)$ when, according to Eq. (38), we can neglect the parallel fluid velocity and set $V_\parallel \to 0$.

3.1. Large-β shear Alfvén, with $\delta n/n_0 = \delta B_z/B_0$ and $E_\parallel = 0$

First, we adopt $u_z > \max\left(v_{Ti_\perp}, \sqrt{\gamma_{i_\parallel}}\, v_{Ti_\parallel}\right) \;\Rightarrow\; V_\parallel \to 0$, cf. Eq. (38), and exclude acoustic waves from our analysis. In such regime, $\gamma_{i_\perp} = 2$ and $\gamma_{e_\perp} = 1$, see Eq. (5) and the subsequent discussion. An analytic solution can be by the standard Larichev&Reznik procedure only in the special case when the relative perturbations of density and compressional magnetic field are equal (i.e. $n = B_z$ in dimensionless units), when both continuity equations (37) and (39) simplify to 2-D Euler equations, viz.

$$[\vec{e}_z \times \nabla_\perp (\psi - x)] \cdot \nabla_\perp \nabla_\perp^2 \psi = 0, \quad \text{and} \quad [\vec{e}_z \times \nabla_\perp (\Phi - x)] \cdot \nabla_\perp \nabla_\perp^2 \Phi = 0, \tag{46}$$

that can be readily integrated as

$$\nabla_\perp^2 \psi = G(\psi - x), \qquad \nabla_\perp^2 \Phi = H(\Phi - x). \tag{47}$$

G and H are arbitrary function of their argument, which we take to be part-by-part linear, viz. $G(\xi) = (\xi - \xi_0)\, G_1$, with the constants ξ_0 and G_1 taking different values ξ_0^{in}, G_1^{in} and ξ_0^{out}, G_1^{out} inside and outside, respectively, of a (moving) vortex core defined by $x^2 + [y + (c_A/u_z)\, z - t]^2 = r_0^2$. Obviously, for a spatially localized solution we must have $G_1^{out} = 0$, while G_1^{in} will be determined from the smoothness of the vector potential ψ (i.e. from the absence of the z-component of the surface current) at the edge of the vortex core. The function $G(\psi - x)$, and consequently the parallel current $-\nabla_\perp^2 \psi$, can have a finite jump for some value of $\psi - x$. Now we can readily write the solution of the 2-d Euler equation (47) as a Chaplygin vortex, viz.

$$\psi(r, \varphi) = \begin{cases} \cos\varphi \;\left(r_0^2/r\right), & r \geq r_0, \\ \cos\varphi \;\{r - (2r_0/j_1)\,[J_1(j_1\, r/r_0)/J_1'(j_1)]\} + \\ \qquad \psi_0\,[J_0(j_1\, r/r_0) - J_0(j_1)], & r < r_0, \end{cases} \tag{48}$$

The density n and the compressional magnetic field B_z are calculated from the generalized pressure balance (40), viz.

$$n = B_z = (1 + \beta_{i_\perp} + \beta_{e_\perp}/2)^{-1}\, (\beta_{i_\perp}/4)\; \nabla_\perp^2 \Phi, \tag{49}$$

which after substitution into the parallel electron momentum equation (36) and using (47) yields $\Phi - x = F(\psi - x)$ where ψ is given by Eq. (48). Obviously, for $r > r_0$ the slope of the function F is given by $F_1 = 1$, which yields $n = 0$ outside of the vortex core. The definition of the streamfunction Φ further implies that outside of the vortex core we also have $\phi = \psi$. As these potentials satisfy the same continuity conditions at the core edge, we must have $\phi = \psi$ on the entire x, y plane, which corresponds to $E_\parallel = 0$, i.e. $\phi = u_z A_z$ in dimensional units. The dipolar components of the potentials ϕ and ψ (that are $\propto \cos\varphi$) are continuous and smooth functions and that the corresponding density n and compressional magnetic field B_z are continuous

at $r = r_0$. Conversely, the monopolar component of the compressional magnetic field has a finite jump $\Delta B_z^{(0)}$ at the edge of the vortex core, where

$$\Delta B_z^{(0)} = \psi_0 \, \beta_{i_\perp} \left(j_1^2 / 4 r_0^2 \right) \left[1 + \beta_{i_\perp} + \beta_{e_\perp}/2 + (1 + \beta_{e_\perp}/2) \, \left(\rho_i^2 j_1^2 / 2 r_0^2 \right) \right]^{-1} . \tag{50}$$

Such discontinuity corresponds to a surface current (with zero thickness and infinite density) located at $r = r_0$, flowing in the poloidal direction. The latter is regarded as nonphysical and it probably gives rise to an instability of the Chaplygin's monopolar component. In other words, the monopolar Chaplygin component may exist only when the compressional magnetic field is negligible, that is usually the case when the plasma β is small. The ion-scale shear Alfvén vortex (48)-(49) is displayed in Fig. 1.It has a vanishing parallel electric field, corresponding to $\phi = (u_z/c_A) \, A_z$ and outside of the vortex core it has $\nabla_\perp^2 \phi = \nabla_\perp^2 A_z = n = B_z = 0$. Inside the core, large-scale structures feature $n/B_z = \text{constant} \neq 1$, while on the ion-scale we have been able to find analytically only vortices with $n/B_z = 1$.

3.2. Large-β kinetic slow magnetosonic solution, with $u_z < c_A$, $\vec{B}_\perp = 0$, and $\delta n/n_0 \neq \delta B_z/B_0$

In the regime with negligible contribution of acoustic perturbation defined above, when $V_\parallel \to 0$, $\gamma_{i_\perp} = 2$, $\gamma_{e_\perp} = 1$, and $u_z > \max\left(v_{Ti_\perp}, \sqrt{\gamma_{i_\parallel}} v_{Ti_\parallel}\right)$, we seek a travelling solution whose perturbations of density and compressional magnetic field are not fully correlated, i.e. with $n \neq B_z$. As outside of the vortex core the localized nonlinear solution is essentially a linear evanescent response to the nonlinearities located within the core, we ascertain from Eq. (44) that in the plasma regimes of interest, featuring ion temperature anisotropy, $\beta_{i_\parallel} \leq \beta_{i_\perp}$ and a moderate parallel electron temperature, $\beta_{e_\parallel} \leq 2 + \beta_{e_\perp}$, the parallel phase velocity of kinetic slow mode vortices can not be much bigger than the Alfvén speed, see Eq. (44). We adopt a somewhat more rigorous restriction for u_z, viz. $c_A > u_z > \max\left(v_{Ti_\perp}, \sqrt{\gamma_{i_\parallel}} v_{Ti_\parallel}\right)$ that permits us to simultaneously set $V_\parallel \ll 1$ and $\psi \sim u_z^2/c_A^2 \ll 1$. The corresponding kinetic slow wave is localized, $\kappa^2 > 0$ see Eq. (44), and it can be realized when the perpendicular ion temperature is of the order $\beta_{i_\perp} \lesssim 1$ and the parallel ion temperature is sufficiently small, $v_{Ti_\parallel}^2/c_A^2 = \beta_{i_\parallel}/2 \ll 1$. Such ordering is easy to achieve in the Earth's magnetosphere downstream of a quasi-perpendicular bow shock, possibly also in the fast solar wind, but more difficult in the slow solar wind where the separation between c_A and $v_{Ti_\parallel}$ is smaller. Besides, if the parallel electron temperature is not extremely small, $T_{e_\parallel}/T_{i_\parallel} \geq m_e/m_i$, the electrons are isothermal along the magnetic field, too. In such regime we have $\gamma_{e_\parallel} = \gamma_{e_\perp} = 1$, and making use

of Eq. (45) we can rewrite the electron continuity equation (37) as

$$\begin{aligned}&[\vec{e}_z \times \nabla F(\psi - x)] \cdot \nabla (n - B_z) - \\ &\frac{c_A^2}{u_z^2}\left(1 - \frac{\beta_{e_\parallel} - \beta_{e_\perp}}{2}\right)[\vec{e}_z \times \nabla(\psi - x)] \cdot \nabla \nabla_\perp^2 \psi = \\ &-\left[\vec{e}_z \times \nabla\left(p_{e_\parallel} - p_{e_\perp} - \frac{\beta_{e_\parallel} - \beta_{e_\perp}}{2}\, d_i^2 B_z\right)\right] \cdot \nabla (n - B_z)\,. \end{aligned} \quad (51)$$

From the isothermal equation of state (35) we have $p_{e_\parallel} - p_{e_\perp} = (1/2)(\beta_{e_\parallel} - \beta_{e_\perp})\, d_i^2\, n$ and the right-hand-side of Eq. (51) reduces to zero as a mixed product of two colinear vectors, which enables it to be integrated as

$$n - B_z = \frac{c_A^2}{u_z^2}\left(1 - \frac{\beta_{e_\parallel} - \beta_{e_\perp}}{2}\right)\frac{\nabla_\perp^2 \psi}{F'(\psi - x)} + H(\psi - x)\,, \quad (52)$$

where H is an arbitrary function. It can be shown that solutions with arbitrary u_z/c_A can meet all physical continuity conditions at the core's edge only if they contain both the shear- and the kinetic slow mode components described in Eq. (44). However, in such a case the nonlinear term on the right hand side Eq. (39) is finite on the entire $x - y$ plane, which presents a formidable obstacle for an analytic treatment and requires extensive numerical calculations that are outside the scope of the present paper. To proceed, we restrict ourselves to the phase velocities that are much smaller than the Alfvén speed, $c_A \gg u_z > v_{Ti_\parallel}$, when a solution involving only one Alfvén mode becomes possible (in the solar wind event recorded by Cluster [3] such strong constraint might not be fulfilled, and those structures are likely to be coupled either with the ion sound or with the torsional magnetic field). In such regime, the electron continuity (37) gives $\psi \sim (u_z^2/c_A^2)\,\phi \to 0$, which in turns yields that the arguments of the functions F and G reduces to $\xi \equiv \psi - x \to -x$. Same as before, these functions are adopted to be part-by-part linear, $F(\xi) = (\xi - \xi_0)\, G_1$, where the parameter ξ_0 and the slope G_1 take different constant values ξ_0^{in}, G_1^{in} and ξ_0^{out}, G_1^{out} inside and outside,, where the slopes F_1 and H_1 take different constant values F_1^{in}, H_1^{in}, and F_1^{out}, H_1^{out} inside and outside of the vortex core determined by $\xi(r_0) = \xi_0$. We note the separatrix $r = r_0$ is not an isoline of the functions F and H, whose argument is given by $\xi = \psi - x \to -x = -r\cos\varphi$, which obviously is not constant at the separatrix $r = r_0$. This prohibits the slopes to jump at the circle $r = r_0$ and implies that $F_1^{in} = F_1^{out} = 1$ and $H_1^{in} = H_1^{out} = 0$. Thus, Eq. (52) is decoupled from the rest, while from Eq. (36) we have

$$\phi - p_{e_\parallel} + (1/2)\left(\beta_{e_\parallel} - \beta_{e\perp}\right)\, d_i^2 B_z = 0. \quad (53)$$

The quantities n, B_z, and ϕ can now be expressed from Eqs. (40), (41), and (45) as follows (for easier reading, here and below we use the `mathcal`

font to denote true constants, such as $\mathcal{N}, \mathcal{B}, \mathcal{F}, \mathcal{Q}, \mathcal{A}$, and $\mathcal{U}$, that depend only on the plasma parameters and NOT on the slopes G_1^{in} and G_1^{out})

$$n = \mathcal{N}_0\Phi + \mathcal{N}_2\nabla_\perp^2\Phi \equiv \frac{1}{\rho_i^2\mathcal{Q}}\ \Phi\ +\ \frac{2+\beta_{e_\parallel}-\beta_{e_\perp}}{4\mathcal{Q}}\ \nabla_\perp^2\Phi, \tag{54}$$

$$B_z = \mathcal{B}_0\Phi + \mathcal{B}_2\nabla_\perp^2\Phi \equiv -\frac{\beta_{i_\perp}+\beta_{e_\perp}}{2\rho_i^2\mathcal{Q}}\ \Phi\ +\frac{\beta_{e_\parallel}-\beta_{e_\perp}}{4\mathcal{Q}}\ \nabla_\perp^2\Phi, \tag{55}$$

$$\phi = \mathcal{F}_0\Phi + \mathcal{F}_2\nabla_\perp^2\Phi \equiv \frac{\mathcal{Q}-1}{\mathcal{Q}}\ \Phi\ +\ \frac{\mathcal{Q}-1-\left(\beta_{e_\parallel}-\beta_{e_\perp}\right)/2}{2\mathcal{Q}}\ \rho_i^2\ \nabla_\perp^2\Phi, \tag{56}$$

$$\mathcal{Q} = \frac{\beta_{e_\parallel}+\beta_{i_\perp}}{\beta_{i_\perp}} + \frac{\beta_{i_\perp}+\beta_{e_\perp}}{2}\ \frac{\beta_{e_\parallel}-\beta_{e_\perp}}{\beta_{i_\perp}}, \qquad \mathcal{U} = 1 - \frac{\beta_{i_\parallel}-\beta_{i\perp}}{2-\beta_{e_\parallel}+\beta_{e_\perp}} \tag{57}$$

It is worth noting that, due to the ions' FLR effects, our equation (55) implies that the stream function Φ is not proportional to the magnetic field B_z, which essentially decouples the velocity and magnetic fields. After some simple manipulations, the above expressions permit us to rewrite the charge continuity equation (39) as follows

$$\begin{aligned}
&\left[\vec{e}_z\times\nabla\left(n-B_z\right)\right]\cdot\nabla\left[\Phi-\mathcal{U}\,x-\mathcal{A}_1\,\rho_i^2\left(n-B_z\right)\right]+\\
&\left\{\vec{e}_z\times\nabla\left[\Phi-x-\rho_i^2\left(n-B_z\right)+\mathcal{A}_2\,\rho_i^2\,\nabla_\perp^2\Phi\right]\right\}\cdot\nabla\nabla_\perp^2\Phi=\\
&\left[\vec{e}_z\times\nabla_\perp\left(\partial/\partial x_i\right)\rho_i^2\left(n-B_z\right)\right]\cdot\nabla\left(\partial\Phi/\partial x_i\right),
\end{aligned} \tag{58}$$

where $\mathcal{A}_1$ and $\mathcal{A}_2$ are arbitrary constants introduced for algebraic convenience. Adopting these in the following way

$$\mathcal{A}_1 = \mathcal{U} - \frac{\mathcal{U}-1}{\rho_i^2\left(\mathcal{N}_0-\mathcal{B}_0\right)}, \qquad \mathcal{A}_2 = \frac{\mathcal{U}-1}{\mathcal{U}}\ \frac{\mathcal{N}_2-\mathcal{B}_2}{\rho_i^2\left(\mathcal{N}_0-\mathcal{B}_0\right)}, \tag{59}$$

using Eqs. (54) and (55), we can cast Eq. (58) in a simple form, viz.

$$\left[\vec{e}_z\times\nabla\left(\Phi+\mathcal{V}\,x\right)\right]\cdot\nabla\left(\nabla_\perp^2\Phi+\kappa^2\mathcal{V}\,x\right) = 2\,\mathcal{C}\left(\vec{e}_z\times\nabla\ \partial\Phi/\partial x_i\right)\cdot\nabla\nabla_\perp^2\partial\Phi/\partial x_i, \tag{60}$$

where :
$$\kappa^2 = \frac{\mathcal{U}\left(\mathcal{N}_0-\mathcal{B}_0\right)}{1-\mathcal{U}\left(\mathcal{N}_2-\mathcal{B}_2\right)}, \qquad \mathcal{V} = -\frac{1-\mathcal{U}\left(\mathcal{N}_2-\mathcal{B}_2\right)}{1-\rho_i^2\left(\mathcal{N}_0-\mathcal{B}_0\right)-\left(\mathcal{N}_2-\mathcal{B}_2\right)},$$
$$\mathcal{C} = \frac{\rho_i^2\kappa^2}{2}\ \frac{\mathcal{V}}{\mathcal{U}}\ \frac{\mathcal{N}_2-\mathcal{B}_2}{\mathcal{N}_0-\mathcal{B}_0}.$$

In the regime of small but finite FLR corrections $\mathcal{C}\nabla_\perp^2 \ll 1$, the right-hand-side of Eq. (60) is a small correction that can be approximated by using

the leading order solution of Eq. (60) $\nabla_\perp^2 \Phi \approx -\kappa^2 \mathcal{V}\, x + G(\Phi + \mathcal{V}\, x)$, where G is an arbitrary function of its argument. Then, using the identity

$$2\,\nabla_\perp \cdot \{[(\vec{e}_z \times \nabla_\perp f)\cdot \nabla_\perp]\,\nabla_\perp G\,(f)\} = (\vec{e}_z \times \nabla_\perp f)\cdot \nabla_\perp \nabla_\perp^2 G\,(f) - \left[\vec{e}_z \times \nabla_\perp \nabla_\perp^2 f\right]\cdot \nabla_\perp G\,(f)\,. \quad (61)$$

With the accuracy to first order in the small $\mathcal{C}\nabla_\perp^2$, we rewrite Eq. (60) as:

$$\left[\vec{e}_z \times \nabla \left(1 + \mathcal{C}\nabla_\perp^2\right)(\Phi + \mathcal{V}\, x)\right]\cdot \nabla \left[\left(1 + \mathcal{C}\nabla_\perp^2\right)\left(\nabla_\perp^2 \Phi + \kappa^2 \mathcal{V}\, x\right)\right] = 0, \quad (62)$$

and is readily integrated one time, viz.

$$\left(1 + \mathcal{C}\,\nabla_\perp^2\right)\left(\nabla_\perp^2 \Phi + \kappa^2 \mathcal{V}\, x\right) = G\left[\left(1 + \mathcal{C}\,\nabla_\perp^2\right)(\Phi + \mathcal{V}\, x)\right]. \quad (63)$$

We adopt $G(\xi)$ in the form of a continuous part-by-part linear function, $G(\xi) = G_1 \xi$, whose constant slope G_1 takes different values G_1^{in} and G_1^{out} inside and outside of the circle $r = r_0$. Remarkably, with such choice of $G(\xi)$, the parameter $\mathcal{C}$ coming from the nonlinear term on the right-hand-side of Eq. (60) and (39), cancels out in Eq. (63).As the function $G(\xi)$ must be continuous, a jump is permitted only if the argument vanishes at such circle, $\xi(r_0, \varphi) = 0$. Noting that for a localized solution we must have $G_1^{out} = \kappa^2$, and setting $G_1^{in} = -\lambda^2$, we obtain the following equations for the stream function Φ outside and inside the circle $r = r_0$,

$$\begin{aligned} &\left(\nabla_\perp^2 - \kappa^2\right)\Phi^{out} = 0, && r > r_0, \\ &\left(\nabla_\perp^2 + \lambda^2\right)\left[\Phi^{in} + \left(1 + \frac{\kappa^2}{\lambda^2}\right)\mathcal{V}\, x\right] = 0, && r < r_0. \end{aligned} \quad (64)$$

These separate variables in cylindrical coordinates, $\Phi = \sum_k \Phi_k \exp(ik\varphi)$; amplitude of the k-th harmonic is given by

$$\Phi_k^{out} = c_k^{out}\, K_k\,(\kappa r)\,, \qquad \Phi_k^{in} = c_k^{in}\, J_k\,(\lambda r)\,, \quad (65)$$

where c_k^{in} and c_k^{out} are arbitrary constants. It can be argued that the stream function Φ must be a dipole, i.e. that it may contain only the dipole component $k = 1$ (for a discussion, see the paragraph at the end of this Section). Then, the continuity of the function G readily yields

$$\left(\Phi^{out} + \mathcal{V}\, x\right)_{r=r_0} = \left(\Phi^{in} + \mathcal{V}\, x\right)_{r=r_0} = \left(\nabla_\perp^2 \Phi^{out} + \kappa^2 \mathcal{V}\, x\right)_{r=r_0} = \left(\nabla_\perp^2 \Phi^{in} + \kappa^2 \mathcal{V}\, x\right)_{r=r_0} = 0, \quad (66)$$

which from Eqs. (54)-(56) provides also the continuity of the functions n, B_z, and ϕ. Finally, matching the above "in" and "out" solutions at $r = r_0$ we obtain a standard Larichev& Reznik-type dipole [17]

$$\Phi\,(r, \varphi) = \mathcal{V}\, r_0\ \cos\varphi \times \begin{cases} -\frac{K_1(\kappa r)}{K_1(\kappa r_0)}, & r > r_0 \\ -\left(1 + \frac{\kappa^2}{\lambda^2}\right)\frac{r}{r_0} + \frac{\kappa^2}{\lambda^2}\frac{J_1(\lambda r)}{J_1(\lambda r_0)}, & r < r_0 \end{cases}, \quad (67)$$

while the plasma density, compressional magnetic field and the electrostatic potential are expressed from Eqs. (54)-(56). Obviously, this solution is localized in space only if the '*out*' e-folding length κ defined in Eq. (61) or, equivalently obtained from Eq. (44) in the limit $u_z \ll c_A$ and $\gamma_{e_\parallel} = 1$, is a real quantity, i.e. for $\kappa^2 > 0$ which yields the condition for the existence of kinetic slow mode vortices with a complicated dependence on the values of plasma β_{j_ζ}, with $j = e, i$ and $\zeta = \parallel, \perp$. In contrast to its shear Alfvén counterpart, Eq. (48) that, being a MHD nonlinear mode does not possess a spatial scale, the kinetic slow mode vortex Eq. (67) has a scale comparable the ion Larmor radius $1/\kappa \sim \rho_i$. The remaining free parameter λ is determined from the condition that the radial electric field is continuous at the edge of the core, $(\partial\phi^{in}/\partial r)_{r=r_0} = (\partial\phi^{out}/\partial r)_{r=r_0}$, i.e. of the absence at $r = r_0$ of any surface charges. This gives rise to the following nonlinear dispersion relation

$$\left(\mathcal{F}_0 + \mathcal{F}_2\kappa^2\right)\frac{\kappa r_0\, K_1'\left(\kappa r_0\right)}{K_1\left(\kappa r_0\right)} = \mathcal{F}_0\left(1 + \frac{\kappa^2}{\lambda^2}\right) - \left(\mathcal{F}_0 - \mathcal{F}_2\lambda^2\right)\frac{\kappa^2}{\lambda^2}\frac{\lambda r_0\, J_1'\left(\lambda r_0\right)}{J_1\left(\lambda r_0\right)}. \tag{68}$$

The Chaplygin's monopole component of the solution can exist only when the function $G(\Phi + \mathcal{V}x)$ jumps at the core edge, producing also a jump in the vorticity $\nabla_\perp^2\Phi$. However, approaching the ion scales and including FLR terms, in the kinetic slow mode branch we obtain Eq. (63) that contains also the Laplacian of vorticity, $\nabla_\perp^4\Phi$ that becomes singular when $\nabla_\perp^2\Phi$ has a jump. This is clearly prohibited for physical reasons and indicates that (quasi)monopolar Chaplygin structures (48) cannot develop on the ion scale, in the kinetic slow mode branch. As this singularity arises in Eq. (62) due to the expansion in the small-but-finite FLR inherent in the stress tensor Eq. (11), one may expect that it vanishes in a plasma description that involves all orders in FLR, such as the gyrofluids, that would reveal a sharp peak of charge density and/or a thin current layer that may affect the stability of a slow magnetosonic Chaplygin vortex. A numerical study would require extensive calculations and is beyond the scope of this paper.

4. Discussions and concluding remarks

We have studied fluid plasma vortices in a high-β plasma, on the spatial scale comparable to the ion inertial length and approaching the ion Larmor radius, including the effects of the compression of the magnetic field and of the finite ion Larmor radius, in the regime when the acoustic perturbations are small. The vortices have the form of infinitely long filaments, slightly tilted to the magnetic field. Our basic Eqs. (36)-(40) possess also a trivial stationary solution that is fully aligned with the z-axis, $\partial/\partial t = \partial/\partial z = 0$ and circularly symmetric $\partial/\partial\varphi = 0$, i.e. strictly monopolar. However, water tank experiments [18], in which perturbations evolve according to the 2-d Euler equation (46) but involve also a small but finite viscosity of the

fluid (non existent in our plasma regime!), revealed that such stationary monopoles either disperse or slowly transform into dipolar or tripolar vortices, depending on the amount of shielding in the initial state. This may be related also with the jumps in the vorticity, $\nabla_\perp^2 \Phi$, at the edge of a monopole. Conversely, the propagating Lamb dipole, corresponding to a shear-Alfvén vortex with $\psi_0 = 0$ in Eq. (48), was remarkably stable and could easily survive collisions with other dipoles [19]. A propagating quasi-monopolar vortex, i.e. a Chaplygin's structure with a relatively small dipolar component is much more stable than the stationary monopoles. In an ordinary fluid it may propagate over a distance that is an order of magnitude bigger than its diameter, as suggested by the weak nonlinear theory, numerical simulations, and experiments in non-rotating water tanks [20, 21].

In a high-β plasma, we found two distinct types of coherent vortices propagating in the perpendicular direction. The first is identified as a generalized shear-Alfvén structure that possesses both the torsional and the compressional component of the magnetic field perturbation. It has a zero parallel electric field and, being homogeneous along its axis that is inclined to the ambient magnetic field, it sweeps along the z-axis with a velocity u_z that is in the Alfvén speed range; the transverse phase velocity is equal to $u_z \tan\theta$, where θ is the (small) pitch angle between the structure and the background magnetic field. While in a sufficiently incompressible plasma $\delta n/n_0 \to 0, \delta B_z/B_0 \to 0$ it has the structure of a moving Chaplygin's vortex with a monopole superimposed on a dipole, in plasmas with $\beta \sim 1$ its monopolar component is likely to be unstable and short-lived due to the emergence of a thin current layer and/or a sharp peak of charge density at its edge. The compressible magnetic field associated with such vortex is restricted to the interior of the vortex core, while the transverse perturbation "leaks out" from the core to larger distances. The second type of propagating structures obtainable analytically, possesses finite compressional magnetic field and parallel electric field, as well as the perpendicular fluid velocity and the density perturbation, but vanishing parallel ion fluid velocity and the transverse perturbations of the magnetic field. It is identified as a nonlinear kinetic slow magnetosonic structure. Its parallel phase velocity is much smaller than the Alfvén speed which also yields a thermalized electron distribution. The transverse fluid velocity of the kinetic slow mode vortex is better localized than that of its shear-Alfvén counterpart, while its compressional magnetic field extends outside the core. Purely kinetic slow magnetosonic structure exists only if $v_{Ti_\parallel}^2/c_A^2 = \beta_{i_\parallel}/2 \ll 1$, otherwise it is coupled with ion sound or torsional magnetic field.

References

[1] O. Alexandrova, A. Mangeney, M. Maksimovic, et al, JGR **109**, 5207 (2004).
[2] O. Alexandrova and J. Saur, Geophys. Res. Lett. **35**, L15 102 (2008).
[3] D. Perrone, O. Alexandrova, A. Mangeney, et al, Astrophys. J. **196**, 826 (2016).
[4] S. Lion, O. Alexandrova, and A. Zaslavsky, Astrophys. J. **824**, 47 (2016).

[5] D. Sundkvist, V. Krasnoselskikh, P. K. Shukla, et al Nature **436**, 825 (2005).

[6] D. Perrone, O. Alexandrova, O. W. Roberts, et al, Astrophys. J. **849**, 49 (2017).

[7] V. Petviashvili and O. Pokhotelov, *Solitary waves in plasmas and in the atmosphere.* (Gordon and Breach, Philadelphia, PA (USA), 1992).

[8] B. B. Kadomtsev and O. P. Pogutse, Zh. Eksp. Teor. Fiz. **65**, 575 (1973).

[9] H. R. Strauss, Phys. Fluids **20**, 1354 (1977).

[10] S. I. Braginskii, Rev. Plasma Phys. **1**, 205 (1965).

[11] N. Yajima, Prog. Theor. Phys. **36**, 1 (1966).

[12] T. Passot, P. L. Sulem, and E. Tassi, J. Plasma Phys. **83**, 715830 402 (2017).

[13] G. Belmont and C. Mazelle, J. Geophys. Res. **97**, 8327 (1992).

[14] D. Jovanovic, H. L. Pecseli, J. J. Rasmussen, et al, J. Plasma Phys. **37**, 81 (1987).

[15] D. Jovanovic and W. Horton, Phys. Plas. **1**, 2614–2622 (1994).

[16] D. Jovanović, O. Alexandrova, and M. Maksimović, Phys. Scr. **90**, 088 002 (2015).

[17] V. Larichev and G. Reznik, Rep. U.S.S.R. Acad. Sci. **231**, 1077 (1976).

[18] M. Beckers, H. J. H. Clercx, G. J. F. van Heijst, et al, Phys. Fluids **15**, 1033 (2003).

[19] G. J. F. van Heijst and J. B. Flor, Nature **340**, 212 (1989).

[20] M. E. Stern and T. Radko, J. Phys. Ocean. **28**, 22 (1998).

[21] S. I. Voropayev, G. B. McEachern, D. L. Boyer, and H. J. S. Fernando, J. Phys. Ocean. **29**, 2741 (1999).

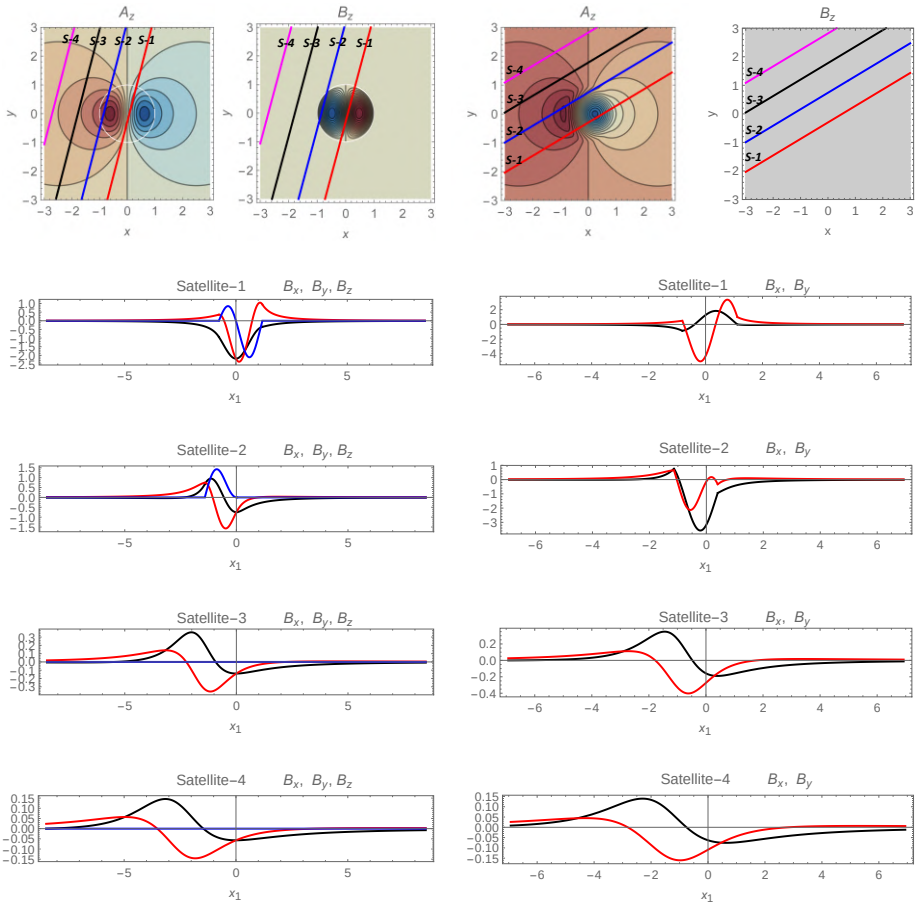

Figure 1:
Left column: Dipolar Lamb vortex with $\psi_0 = 0$; B_z is of the same order as B_x, B_y.
Right column: Quasi-monopolar Chaplygin vortex with $\psi_0 \neq 0$ and $B_z \to 0$.
Top to bottom:
Row 1: Contour plots of the vector potential A_z and of the compressional magnetic field B_z; in the case of the Chaplygin's vortex the compressional magnetic field is negligibly small. In the figure, vortices propagate in the vertical direction.
Four typical trajectories of the spacecraft, S-1, S-2, S-3, and S-4 are displayed as red, blue, black and magenta parallel lines. On the 'black and 'magenta' trajectories no compressional magnetic field B_z is recorded, but the 'detected signals' of the perpendicular magnetic field on 'blue' and 'black' trajectories are of a similar intensity as B_z.
Rows 2–5: Three components of the dimensionless magnetic field, as they would be observed by the four spacecrafts on red, blue, black, and magenta trajectories, respectively. The coordinate system is rotated with respect to that used in the calculations, so that the B_x component (black line) is now in the direction of the projection of the spacecraft's velocity to the perpendicular plane, B_y (red) is perpendicular both to it and to the magnetic field, and B_z (blue) is parallel to the ambient magnetic field. Vanishing $E_\parallel$ implies that the dimensionless electric field components are given by $E_x = -B_y$, $E_y = B_x$ and $E_z = 0$. Density is given by $n/B_z = \text{constant}$, where for the large scale RMHD vortex $n/B_z \neq 1$, and $n/B_z = 1$ for the ion-scale vortex. Normalizations are defined in Eq. (28) and we have chosen $k = 1/r_0' = 1$ and $\psi_0 = 1.75$.

Graviton mass and Yukawa-like nonlinear correction to the gravitational potential: constraints from stellar orbits around the Galactic Center*

Predrag Jovanović†
Astronomical Observatory, Volgina 7, P.O. Box 74, 11060 Belgrade, Serbia

Vesna Borka Jovanović‡
Department of Theoretical Physics and Condensed Matter Physics (020), Vinča Institute of Nuclear Sciences - National Institute of the Republic of Serbia, University of Belgrade, P.O. Box 522, 11001 Belgrade, Serbia

Duško Borka§
Department of Theoretical Physics and Condensed Matter Physics (020), Vinča Institute of Nuclear Sciences - National Institute of the Republic of Serbia, University of Belgrade, P.O. Box 522, 11001 Belgrade, Serbia

Alexander F. Zakharov¶
Bogoliubov Laboratory for Theoretical Physics, JINR, 141980 Dubna, Russia

Abstract

Here we present a short overview of our investigations in which we considered a Yukawa-like modification of the Newtonian gravitational potential in the weak field approximation and its applications for obtaining the graviton mass bounds from the observed stellar orbits around the central supermassive black hole (SMBH) of our Galaxy. For that purpose we first derived the corresponding equations of motion which appeared to be highly nonlinear due to the Yukawa correction term in the potential, and used them to perform two-body simulations of the stellar orbits. The simulated orbits were then fitted to the observed orbit of S2 star around the Galactic Center (GC) in order to constrain the parameters of Yukawa gravity (the range of Yukawa interaction Λ and universal constant δ). It was found that the range of Yukawa interaction was on the order of several

* This work has been supported by Ministry of Education, Science and Technological Development of the Republic of Serbia. PJ wishes to acknowledge the support by this Ministry through the project contract No. 451-03-68/2022-14/200002.

† e-mail address: pjovanovic@aob.rs
‡ e-mail address: vborka@vinca.rs
§ e-mail address: dusborka@vinca.rs
¶ e-mail address: alex.fed.zakharov@gmail.com

thousand astronomical units (AU), and assuming that this parameter corresponds to the Compton wavelength of graviton, we estimated the upper bound for graviton mass to $m_g < 2.9 \times 10^{-21}$ eV. This estimate was not only consistent with the LIGO estimate obtained from the first gravitational wave (GW) signal GW150914, but also it was obtained in an independent way. We also discussed the possible influence of the bulk distribution of matter around GC on this estimate. The obtained results demonstrated that such analyses of the observed stellar orbits around GC in the frame of the massive gravity theories represent a very powerful tool for constraining the graviton mass and probing the predictions of General Relativity (GR).

1. Introduction

As the carrier of the gravitational interaction, graviton is considered to be spin-2 (tensor) boson, electrically uncharged, as well as massless since, according to GR, it travels along null geodesics at the speed of light c (like photon). However, according to some alternative theories, gravity is propagated by a massive field, i.e. by a graviton with some small, nonzero mass m_g (for detailed reviews on massive gravity see [1, 2]). This approach was first introduced in 1939 by Fierz and Pauli [3]. Later, Boulware and Deser [4] found a presence of ghosts in massive gravity theories, therefore this feature was treated as a pathology and these theories were considered as non-realistic. However, de Rham et al. [5] discovered a breakthrough opportunity to create a ghost-free massive gravity theory and, as a consequence, an interest to these theories was significantly increased. In particular, these theories of massive gravity have gained a significant attention due to their ability to provide a possible explanation for the accelerated expansion of the Universe without dark energy (DE) hypothesis (earlier it was considered in the framework of the relativistic theory of gravity [6, 7, 8]), and due to important predictions that the velocity v_g of gravitational waves (gravitons) should depend on their frequency f as: $v_g^2/c^2 = 1 - c^2/(f\lambda_g)^2$, as well as that the effective gravitational potential should include a nonlinear (exponential) correction of Yukawa form: $\propto r^{-1}\exp(-r/\lambda_g)$, depending on the Compton wavelength of graviton: $\lambda_g = h/(m_g\, c)$ [9, 10].

Different techniques for constraining the Compton wavelength and mass of graviton are reviewed in e.g. [2], and the latest experimental limits can be found in [11] and references therein. Currently, the most robust estimates were obtained by LIGO Scientific and Virgo Collaborations from their analysis of the first GW signal GW150914, assuming a Yukawa type correction to the gravitational potential with characteristic length scale λ_g [12]. This analysis resulted with the following bound on the Compton wavelength of graviton: $\lambda_g > 10^{13}$ km at 90% confidence, which corresponded to the graviton mass of $m_g \leq 1.2 \times 10^{-22}$ eV$/c^2$ [12]. Consequent observations of gravitational waves by Advanced LIGO and Advanced Virgo detectors gave an opportunity to update significantly the graviton mass bound to

$m_g \leq 1.27 \times 10^{-23}$ eV/c^2 [13].

Recently, it was demonstrated that the observed stellar orbits around the central SMBH of the Milky Way, and their analysis in the frame of Yukawa gravity, can be also used for constraining the Compton wavelength and mass of graviton [14, 15, 16, 17, 18, 19, 20, 21, 22]. These bright, so called S-stars, move around the compact radio source Sgr A* in the center of our Galaxy, which is recently confirmed to be a SMBH. The orbits of S-stars around Sgr A* are monitored for about 30 years by two large observational facilities: New Technology Telescope and Very Large Telescope (NTT/VLT) in Chile [23, 24], as well as Keck telescope in Hawaii, USA [25]. Particularly, these two groups performed the precise astrometric observations of S2 star, one of the brightest members of the S-star cluster with high orbital eccentricity, which revealed a deviation from Keplerian orbit of this star, and which therefore were used to evaluate parameters of the SMBH, probe GR predictions and search for new physics beyond GR [26, 27, 28, 29]. Both Keck and GRAVITY (VLT) found that observations of S2 star trajectory are consistent with the assumption that SMBH with mass around 4×10^6 $M_\odot$ is located at GC. Moreover, an analysis of observations showed that GR predictions about relativistic redshift near the S2 pericenter passage in May 2018 have been confirmed by both collaborations [30, 31, 32]. In 2020 a presence of relativistic precession for S2 star trajectory has been reported by the GRAVITY collaboration [33].

In spite of a great success of the conventional model of GC which consists of SMBH, other approaches have been considered in the literature. For instance, it was proposed to substitute SMBH with dense dark matter (DM) concentration where there is a ball with a constant density [34] (later this approach for DM model was called the RAR-model). Recently, it was declared that RAR-model provides a better fit for the S2 star trajectory [35], however, a detailed analysis of the RAR model and SMBH for GC showed that the conventional model with SMBH is preferable [36]. Analyzing the observational data for the S2 trajectory, the GRAVITY collaboration found stringent constraints on the SMBH mass at GC and on extended mass distribution inside S2 star orbit [37]. An opportunity to distinguish between the RAR-model and the conventional approach, by selecting the RAR-model parameters where the significant part of DM mass is concentrated inside a ball with radius less than the S2 star pericenter, was discussed in [38].

In our investigations we used the previously mentioned observations of S2 star orbit, obtained by NTT/VLT and Keck groups, in order to evaluate the gravitational potential at GC and to to test and constrain different theories of modified gravity at mpc scales [39, 40, 41, 42, 43]. However, nowadays there are more recent and precise observations not only of S2 star, but also of several other members of the S-star cluster, such as S38, S55 and S62 [44, 45, 46], and thus it is possible to perform the multi-orbit fits of these stars (see e.g. [47, 48, 49, 50]), which could be then used to further improve previous constraints from the two-body orbital fits.

In this paper we give a short overview of our most important results about constraining the parameters of Yukawa gravity using the mentioned observations of S2 star orbit around the central SMBH of the Milky Way, as well as about our new and independent bounds on graviton mass (also obtained from these observations), which are since 2019 accepted by the Particle Data Group (PDG) and included in their "Gauge and Higgs Boson Particle Listings" [11].

The paper is organized as follows: in §2 we present the procedure for obtaining the gravitational potential with a Yukawa-like correction in the Newtonian limit of any analytic $f(R)$ gravity model, in §3 we review and discuss some of our most important results regarding the obtained constraints on the Compton wavelength and graviton mass from analysis of the observed stellar orbits around the SMBH at GC in the frame of Yukawa gravity, and finally in §4 we point out the most important conclusions of our study.

2. Yukawa-like correction to the gravitational potential

Gravitational potential with a Yukawa correction can be obtained in the Newtonian limit of any analytic $f(R)$ gravity model which action is given by [16]:

$$\mathcal{S} = \int d^4x\sqrt{-g}\,[f(R) + \mathcal{X}\mathcal{L}_m]\,, \quad \mathcal{X} = \frac{16\pi G}{c^4}, \tag{1}$$

where f is a generic function of Ricci scalar curvature R and $\mathcal{X}$ is the coupling constant. The resulting 4^{th}-order field equations are:

$$f'(R)R_{\mu\nu} - \frac{1}{2}f(R)g_{\mu\nu} - f'(R)_{;\mu\nu} + g_{\mu\nu}\Box f'(R) = \frac{\mathcal{X}}{2}T_{\mu\nu}, \tag{2}$$

which trace is given by:

$$3\Box f'(R) + f'(R)R - 2f(R) = \frac{\mathcal{X}}{2}T. \tag{3}$$

Yukawa-like corrections naturally emerge in the weak field limit in the case of analytic Taylor expandable $f(R)$ functions with respect to the value $R = 0$ (i.e. around the Minkowskian background):

$$f(R) \;=\; \sum_{n\,=\,0}^{\infty} \frac{f^{(n)}(0)}{n!}\,R^n \;=\; f_0 + f_1 R + \frac{f_2}{2}R^2 + \ldots \tag{4}$$

One can deal with the Newtonian limit of $f(R)$ gravity by adopting the spherical symmetry, and then the metric can be recast as follows [51]:

$$ds^2 = \left[1 + \frac{2\Phi(r)}{c^2}\right]c^2dt^2 - \left[1 - \frac{2\Psi(r)}{c^2}\right]dr^2 - r^2d\Omega^2, \tag{5}$$

where $\Phi(r)$ and $\Psi(r)$ are two potentials. As a result, the gravitational potential $\Phi(r)$, obtained in the weak field limit from g_{00} component of the metric tensor, is found to have a Yukawa-like nonlinear correction [16, 51]:

$$\Phi(r) = -\frac{GM}{(1+\delta)r}\left(1+\delta e^{-\frac{r}{\Lambda}}\right), \tag{6}$$

where $\Lambda^2 = -f_1/f_2$, Λ being an arbitrary parameter (usually referred to as the range of interaction), depending on the typical scale of a gravitational system, and $\delta = f_1 - 1$ is a universal constant (sometimes referred to as the strength of interaction). The second potential is then given by:

$$\Psi(r) = \frac{GM}{(1+\delta)r}\left[\left(1+\frac{r}{\Lambda}\right)\delta e^{-\frac{r}{\Lambda}} - 1\right]. \tag{7}$$

2.1. Nonlinear equations of motion

Since it is difficult to derive the geodesic equations of motion associated to the line element of Yukawa gravity (see e.g. an approximate derivation for $|\delta| \ll 0.1$ in [52]), and taking into account that S2 star moves around the central SMBH of our Galaxy at a sufficiently large distance where the space-time can be considered to be practically flat, we studied the classical equations of motion: $\dot{\vec{r}} = \vec{v}$, $\mu\ddot{\vec{r}} = -\nabla\Phi(\vec{r})$, corresponding to the gravitational potential given by expression (6). In that way, one can obtain the following nonlinear equations of motion in Yukawa gravity:

$$\ddot{\vec{r}} = -\frac{G(M+m)}{1+\delta}\left[1+\delta\left(1+\frac{r}{\Lambda}\right)e^{-\frac{r}{\Lambda}}\right]\frac{\vec{r}}{r^3}, \tag{8}$$

which can be then integrated numerically to obtain the orbital motion and precession of a two-body system. In such a case, the nonlinearity of the additional term with respect to the corresponding Keplerian equations of motion, caused by Yukawa type correction in the gravitational potential (6), plays a crucial role since it is responsible for inducing the precession of the resulting integrated orbits.

Besides, it is important to mutually compare the orbits simulated in Yukawa gravity and in GR, and thus we also used the following parameterized post-Newtonian (PPN) equations of motion for two-body problem, in order to calculate the simulated orbits in GR (for more details see [21] and references therein):

$$\begin{aligned}\ddot{\vec{r}} &= -G(M+m)\frac{\vec{r}}{r^3} + \frac{GM}{c^2 r^3}\left\{\left[2(\beta+\gamma)\frac{GM}{r} - \gamma\left(\dot{\vec{r}}\cdot\dot{\vec{r}}\right)\right]\vec{r}\right. \\ &+ \left. 2(1+\gamma)\left(\vec{r}\cdot\dot{\vec{r}}\right)\dot{\vec{r}}\right\},\end{aligned} \tag{9}$$

where β and γ are the PPN parameters, which are both equal to 1 in the case of GR. As it can be seen from the above expression (9), the PPN equations of motion are also highly nonlinear.

3. Results: bounding the Compton wavelength and mass of graviton by stellar orbits around GC

We used the observed stellar orbits around GC to derive constraints on the Compton wavelength and mass of graviton in two ways:

1. by fitting the simulated orbits of S2 star in Yukawa gravity into its astrometric observations, and then by using chi-square test of goodness of these fits in order to obtain the bounds on parameter Λ at 90% confidence;
2. by equating the precession angles of S-stars in Yukawa gravity to the corresponding values of their Schwarzschild precession, in order to find the values of Λ which satisfy this condition. This is done under an assumption that GR predictions for orbital precession of the S-stars will be successfully confirmed in future.

Here we will briefly describe both methods and illustrate the influence of bulk distribution of mass on the obtained estimates (for more details see [15, 21, 17]).

3.1. Bounds from the observed orbit of S2 star

As previously mentioned, we developed a novel and an independent method for obtaining the graviton mass bounds from analysis of the observed orbit of S2 star in the frame of Yukawa gravity [15]. For that purpose, we first performed two-body simulations of S2 star orbit in the gravitational potential (6), in which we varied the parameters Λ and δ over a parameter space of Yukawa gravity. For each (Λ, δ) pair, the simulated orbits were fitted into the astrometric observations of S2 star, in order to obtain the coordinates of initial position and initial velocity in the orbital plane. The best fits are obtained by minimizing the χ^2 statistics. An example of such a fit for $\Lambda = 3030$ AU and $\delta = 1/3$ is presented in the left panel of Fig. 1, from which it can be seen that Yukawa gravity induces orbital precession in the same direction as in GR.

The χ^2 values of the fits which are better than the fit by the Keplerian orbit (i.e. where $\chi^2 < \chi^2_{\rm Kepler}$) were then plotted as function of the parameters Λ and δ. In that way, the corresponding χ^2-map over the $\Lambda - \delta$ parameter space of Yukawa gravity is obtained (see the right panel of Fig. 1). It can be seen from this χ^2-map that very good fits may be obtained for almost all values of universal constant δ, ranging from 10^{-2} up to 10^6. However, the situation with the parameter Λ is different, since the fits which are much better than in the Keplerian case (represented by the region enclosed within the white contour on the χ^2-map in the right panel of Fig. 1), can

be obtained for relatively narrow range of $\Lambda \approx 5000 - 6000$ AU. This result indicated that, in the case of S2 star, the range of Yukawa interaction Λ is most likely on the order of several thousand AU. Assuming that Λ corresponds to the Compton wavelength λ_g of graviton, this constraint could be then used to estimate the lower bound for λ_g, and thus the upper bound for mass m_g of graviton.

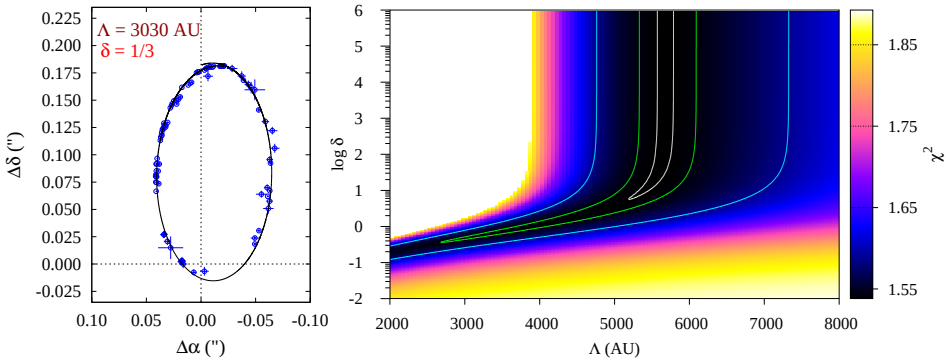

Figure 1: *Left:* An example of fitting a simulated orbit in Yukawa gravity (black solid line) into the astrometric observations of S2 star (blue circles with error bars), obtained by NTT/VLT and Keck telescopes. *Right:* An example of χ^2-map over the $\Lambda - \delta$ parameter space of Yukawa gravity, obtained from the fits like the one shown in the left panel. The color shades represent the values of the reduced χ^2 which are less than the corresponding value in the case of Keplerian orbit, while the contours enclose three regions around the χ^2 minimum, from which the one enclosed by the white contour is the closest to the minimum.

In order to estimate these bounds, we used the obtained χ^2 values to test the null hypothesis that Λ should be at least on the order of 10^3 AU. For that purpose we assumed the significance level of $\alpha = 0.1$ and calculated the critical value $\chi^2_{\nu,\alpha}$, where $\nu = 66$ was the number of degrees of freedom for the above orbital fits. By comparing the χ^2 values of these fits with the critical value $\chi^2_{\nu,\alpha}$, it was found that there was a limit for Λ, below which χ^2 is always greater than $\chi^2_{\nu,\alpha}$ (see Fig. 1 in [15]). Therefore, such cases could be then rejected with high probability of $1 - \alpha = 90\%$, leaving only those cases with Λ above this limit. This limit thus represented the lower bound on Λ and we estimated it for two different values of universal constant δ. In the case of $\delta = 1$ this bound was $\Lambda = 2900$ AU (or 4.3×10^{11} km), while in the case of $\delta = 100$ it was $\Lambda = 4300$ AU (or 6.4×10^{11} km).

Under an assumption that the above lower bounds on the range of Yukawa gravity Λ also represent, at the same time, the lower bounds on the Compton wavelength of graviton λ_g, we found the corresponding upper bounds on its mass with 90% probability: $m_g = 2.9 \times 10^{-21}$ eV for $\delta = 1$

and $m_g = 1.9 \times 10^{-21}$ eV for $\delta = 100$. Both of our estimates were slightly weaker, but consistent with LIGO bounds obtained from the first GW signal GW150914 [12]. However, they were evaluated using a novel and an independent method based on analysis of the observed orbit of S2 star in the frame of Yukawa gravity.

3.2. Bounds from Schwarzschild precession of S-stars

Recently, GRAVITY Collaboration detected the orbital precession of the S2 star and showed that it is close to the GR prediction [33]. Taking this into account, we also derived bounds on the Compton wavelength and mass of graviton under an assumption that the orbital precession of S-stars in Yukawa gravity is equal to the Schwarzschild precession in GR.

For that purpose, we first derived the approximate expression for apocenter shift in Yukawa gravity $\Delta\varphi_Y$, assuming that Yukawa gravity induces a small perturbation to the Newtonian gravitational potential [15]. The obtained expression is in the form of power series over a/Λ ratio, where a is the semi-major axis of the orbital ellipse. Taking into account that $a \ll \Lambda$ in the case of S-stars, the higher order terms in this power series expansion could be neglected. The remaining first order term then yields the following approximate formula for the orbital precession in Yukawa gravity [15]:

$$\Delta\varphi_Y^{rad} \approx \frac{\pi\delta\sqrt{1-e^2}}{1+\delta}\frac{a^2}{\Lambda^2}, \tag{10}$$

where e is orbital eccentricity.

By equating the above expression with the well known formula for Schwarzschild precession [10]:

$$\Delta\varphi_{GR}^{rad} \approx \frac{6\pi GM}{c^2 a(1-e^2)} \tag{11}$$

it was found that Λ has to satisfy the following condition in order to produce the same precession angle:

$$\Lambda \approx \sqrt{\frac{\delta c^2 (a\sqrt{1-e^2})^3}{6\,(1+\delta)\,GM}}. \tag{12}$$

Using the above expression (12), we estimated the Compton wavelength and mass of graviton for a sample of S-stars, presented in [44] (see Table 2 in [15]). The obtained results showed that the range of Yukawa gravity Λ could be indeed constrained in such a way to induce the same orbital precession of stellar orbits as in GR. In the case of S-stars with smaller orbital eccentricities and orbital periods of around a several decades, if observed, such precession could provide constraints on the mass of graviton of $m_g \approx 8 \times 10^{-23}$ eV, which is stronger than the constraints from S2 star orbital fits, presented in the previous paragraph.

3.3. Influence of bulk distribution of mass

Stellar orbits around central SMBH of our Galaxy may be influenced by other stars in the S-stellar cluster, interstellar gas and DM, which consequently may also affect the obtained constraints on the Compton wavelength and mass of graviton. Therefore, we also calculated these constraints in the case of a bulk distribution of mass $M(r) = M_{BH} + M_{ext}(r)$, consisting of SMBH mass $M_{BH} = 4.3 \times 10^6\ M_\odot$ [23] and an extended distribution of matter $M_{ext}(r)$, enclosed within some radius r, which describes the contribution from the stellar cluster, interstellar gas and DM. We modeled $M_{ext}(r)$ by a power-law mass density profile (see [17] and references therein):

$$\rho(r) = \rho_0 \left(\frac{r}{r_0}\right)^{-\alpha}, \tag{13}$$

where $\alpha = 1.4$ and $r_0 = 10''$. In that way we obtained the following expression for the extended mass distribution [17]:

$$M_{ext}(r) = \frac{4\pi\rho_0 r_0^\alpha}{3-\alpha} r^{3-\alpha}, \tag{14}$$

which corresponds to the following gravitational potential [17, 53]:

$$\Phi_{ext}(r) = \frac{-4\pi G\rho_0 r_0^\alpha}{(3-\alpha)(2-\alpha)} \left({r_\infty}^{2-\alpha} - r^{2-\alpha}\right), \tag{15}$$

where r_∞ is the outer radius for extended mass distribution of matter. The total gravitational potential $\Phi_{total}(r)$ can be then obtained as a sum of Yukawa potential $\Phi(r)$ for central SMBH with mass M_{BH} and potential Φ_{ext} for the extended mass distribution [17]:

$$\Phi_{total}(r) = \Phi(r) + \Phi_{ext}(r). \tag{16}$$

Fig. 2 shows three comparisons between the simulated orbits of S2 star in GR (using previously described PPN approach) and in the gravitational potential $\Phi_{total}(r)$ for bulk distribution of mass. Here we assumed the following three ranges of Yukawa gravity: $\Lambda = 2500$, 2547 and 2600 AU, and extended mass distribution of matter for $\rho_0 = 5 \times 10^8\ M_\odot\ \mathrm{pc}^{-3}$. As it can be seen from Fig. 2, range of Yukawa gravity Λ can significantly affect the simulated orbits of S2 star, especially its orbital precession, which is in the same direction as in GR. Moreover, as it can be seen from the middle panel of Fig. 2 which corresponds to $\Lambda = 2547$ AU, even in the case of bulk distribution of mass it is possible to constrain Λ so that the resulted orbital precession becomes very close to the Schwarzschild precession in GR, which in the case of S2 star is $\approx 0^\circ.20$ [23].

The dependence of the precession angle per orbital period of S2 star on both Λ and δ parameters of Yukawa gravity with extended mass distribution is presented in Fig. 3. Here we assumed the following two cases of

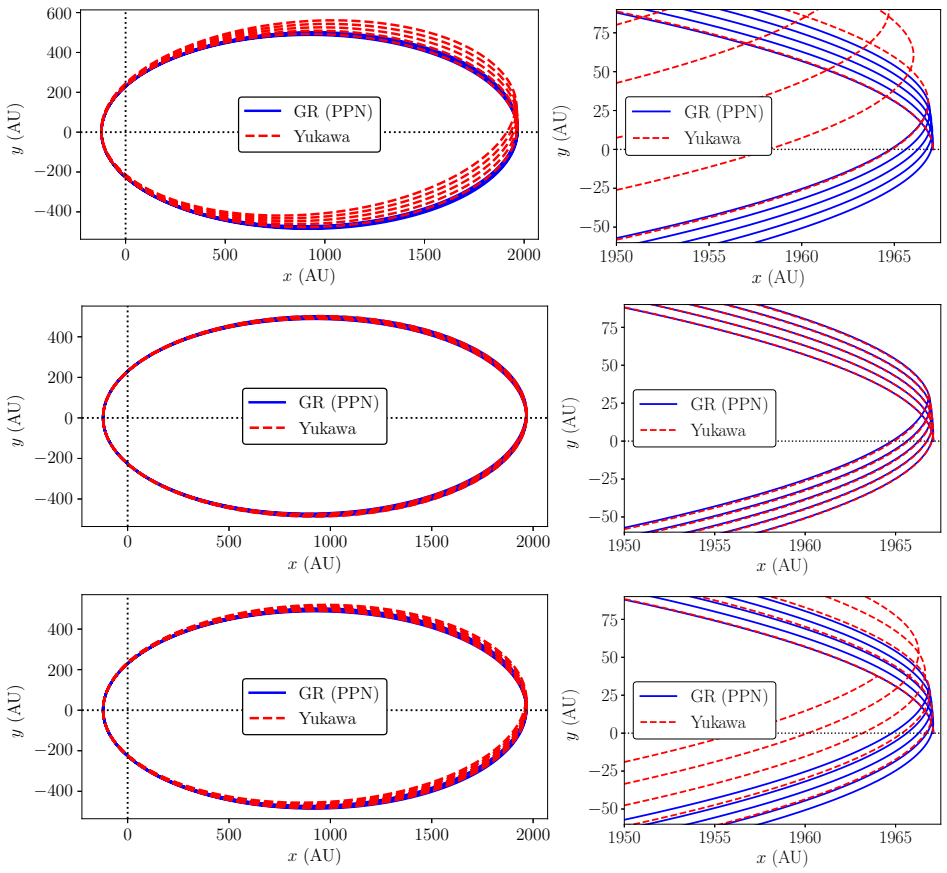

Figure 2: Comparison between the simulated orbits of S2 star, during five orbital periods, in GR (blue solid line) and in Yukawa gravity for $\delta = 10$ and with the mass density distribution of extended matter for $\rho_0 = 5 \times 10^8\ M_\odot\ \mathrm{pc}^{-3}$ (red dashed line). The left panels show full S2 star orbit, while the region around its apocenter is zoomed in the right panel for better insight. The panels, from top to bottom, correspond to $\Lambda = 2500$, 2547 and 2600 AU, respectively.

mass density distribution of extended matter: $\rho_0 = 5 \times 10^8\ M_\odot\ \mathrm{pc}^{-3}$ and $\rho_0 = 1 \times 10^9\ M_\odot\ \mathrm{pc}^{-3}$. The locations in the $\Lambda - \delta$ parameter space where the precession angle is the same as in GR are also presented in Fig. 3 by white dashed line. It can be seen from Fig. 3 that the mass density distribution of extended matter ρ_0 could have significant influence on the value of precession angle per orbital period of S2 star. Namely, although orbital precession in the case of Yukawa gravitational potential $\Phi(r)$ is in the same direction as in GR, extended mass distribution in $\Phi_{total}(r)$ induces an ad-

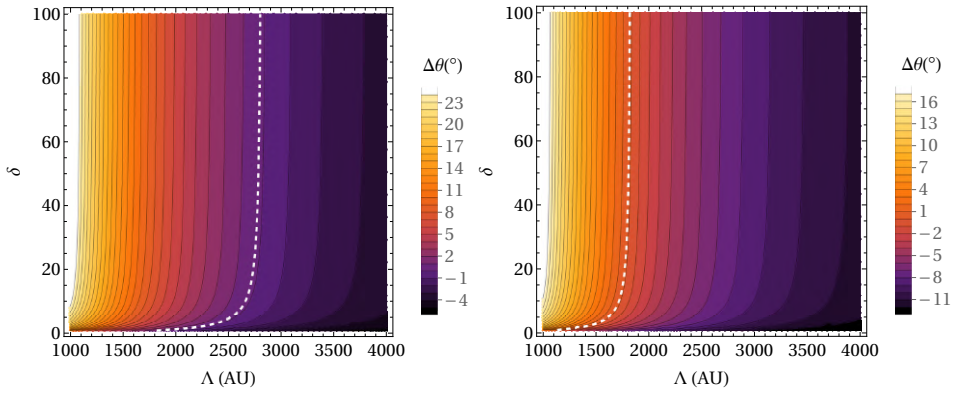

Figure 3: The precession angle (denoted by color shades) per orbital period of S2 star over $\Lambda - \delta$ parameter space of Yukawa gravity with extended mass distribution. The mass density distribution of extended matter is obtained for $\rho_0 = 5 \times 10^8\ M_\odot\ \mathrm{pc}^{-3}$ (left panel) and $\rho_0 = 1 \times 10^9\ M_\odot\ \mathrm{pc}^{-3}$ (right panel). The locations in the parameter space where the precession angle is the same as in GR (i.e. $0^\circ.20$) are designated by white dashed line.

ditional precession in opposite direction, due to which the total precession is then reduced. By comparing the left and right panels of Fig. 3, it can be also seen that the values of parameter Λ, which correspond to the same orbital precession as in GR, are smaller for larger mass density distribution of extended matter ρ_0. Therefore, the corresponding estimates for graviton mass are slightly larger, but still remain in the expected interval, as demonstrated in [17].

4. Conclusions

Here we presented a short overview of our main results concerning the constraints on the Compton wavelength and mass of graviton, obtained from analysis of the observed stellar orbits around GC in the frame of Yukawa gravity. These results were obtained in two ways: by a statistical analysis of the fits of the observed orbit of S2 star by its simulated orbits in Yukawa gravity, and by requirement that the precession angles of S-stars in Yukawa gravity should be equal to their precession angles due to the Schwarzschild precession in GR. These results showed that:

- Investigations of the observed stellar orbits around GC in the frame of the massive gravity theories represent a powerful tool for constraining the graviton mass and probing the predictions of GR;
- The nonlinearity of equations of motion, caused by Yukawa type correction to the gravitational potential, plays a very important role in such analyses, since it is responsible for inducing the precession of the

resulting integrated orbits;

- The constraint for graviton mass of $m_g < 2.9 \times 10^{-21}$ eV, obtained from the orbital fits of S2 star, is slightly weaker but consistent with the LIGO estimate from the first GW signal GW150914 [12];
- Since it was evaluated in a completely new way and independently from other existing estimates, the above bound on graviton mass was in 2019 included in the "Gauge and Higgs Boson Particle Listings" published by PDG [11];
- The second studied method, when applied to S-stars with smaller orbital eccentricities and orbital periods of around a several decades, could provide even stronger constraints of $m_g \approx 8 \times 10^{-23}$ eV;
- Bulk distribution of mass can induces an additional precession in opposite direction with respect to Yukawa gravity, due to which the corresponding estimates for graviton mass could be slightly larger for larger mass density distributions of the extended matter, but they would still remain in the expected range.

References

[1] C. de Rham, *Living Reviews in Relativity* **17** (2014) 7.

[2] C. de Rham, J. T. Deskins, A. J. Tolley, and S.-Y. Zhou, *Rev. Mod. Phys.* **89** (2017) 025004.

[3] M. Fierz and W. Pauli, *Proceedings of the Royal Society of London Series A* **173** (1939) 211.

[4] D. G. Boulware and S. Deser, *Phys. Rev. D* **6** (1972) 3368.

[5] C. de Rham, G. Gabadadze, and A. J. Tolley, *Phys. Rev. D* **106** (2011) 231101.

[6] S. S. Gershtein, A. A. Logunov, and M. A. Mestvirishvili, *Doklady Phys.* **48** (2003) 282.

[7] S. S. Gershtein, A. A. Logunov, M. A. Mestvirishvili, and N. P. Tkachenko, *Phys. Atomic Nucl.* **67** (2004) 1596.

[8] S. S. Gershtein, A. A. Logunov, and M. A. Mestvirishvili, *Phys. Usp.* **49** (2006) 1179.

[9] C. M. Will, *Phys. Rev. D* **57** (1998) 2061.

[10] C. M. Will, *Living Reviews in Relativity* **17** (2014) 4.

[11] P. A. Zyla et al. (Particle Data Group), "Review of particle physics", *Progress of Theoretical and Experimental Physics*, vol. 2020, no. 8, 083C01–1–2093, 2020.

[12] B. P. Abbott et al. (LIGO Scientific and Virgo Collaborations), *Phys. Rev. Lett.*, **116** (2016) 221101.

[13] The LIGO Scientific Collaboration, the Virgo Collaboration, and the KAGRA Collaboration; R. Abbott, H. Abe, F. Acernese et al., arXiv:2112.06861v1 [gr-qc].

[14] D. Borka, P. Jovanović, V. Borka Jovanović, and A. F. Zakharov, *Journal of Cosmology and Astroparticle Physics* **2013** (2013) 050.

[15] A. F. Zakharov, P. Jovanović, D. Borka, and V. Borka Jovanović, *Journal of Cosmology and Astroparticle Physics* **2016** (2016) 045.

[16] S. Capozziello, D. Borka, P. Jovanović, and V. Borka Jovanović, *Phys. Rev. D* **90** (2014) 044052.

[17] P. Jovanović, D. Borka, V. Borka Jovanović, and A. F. Zakharov, *European Physical Journal D* **75** (2021) 145.

[18] A. Zakharov, P. Jovanović, D. Borka, and V. Borka Jovanović, *European Physical Journal Web of Conferences* **125** (2016) 01011.

[19] A. F. Zakharov, P. Jovanović, D. Borka, and V. Borka Jovanović, *Journal of Physics Conference Series* **798** (2017) 012081.

[20] A. Zakharov, P. Jovanović, D. Borka, and V. Borka Jovanović, *European Physical Journal Web of Conferences* **138** (2017) 01010.

[21] A. F. Zakharov, P. Jovanović, D. Borka, and V. Borka Jovanović, *Journal of Cosmology and Astroparticle Physics* **2018** (2018) 050.

[22] A. F. Zakharov, P. Jovanović, D. Borka, and V. Borka Jovanović, *International Journal of Modern Physics Conference Series* **47** (2018) 1860096.

[23] S. Gillessen, F. Eisenhauer, T. K. Fritz et al., *Astrophys. J.* **707** (2009) L114.

[24] S. Gillessen, F. Eisenhauer, S. Trippe, T. Alexander, R. Genzel, F. Martins, and T. Ott, *Astrophys. J.* **692** (2009) 1075.

[25] A. M. Ghez, S. Salim, N. N. Weinberg, J. R. Lu, T. Do, J. K. Dunn, K. Matthews, M. R. Morris, S. Yelda, E. E. Becklin, T. Kremenek, M. Milosavljevic, and J. Naiman, *Astrophys. J.* **689** (2008) 1044.

[26] A. Hees, T. Do, A. M. Ghez, G. D. Martinez, S. Naoz, E. E. Becklin, A. Boehle, S. Chappell, D. Chu, A. Dehghanfar, K. Kosmo, J. R. Lu, K Matthews, M. R. Morris, S. Sakai, R. Schödel, and G. Witzel, *Phys. Rev. Lett.* **118** (2017) 211101.

[27] D. S. Chu, T. Do, A. Hees, A. Ghez, S. Naoz, G. Witzel, S. Sakai, S Chappell, A. K. Gautam, J. R. Lu, and K. Matthews, *Astrophys. J.*, **854** (2018) 12.

[28] A. Amorim et al. (GRAVITY Collaboration), *Mon. Not. R. Astron. Soc.* **489** (2019) 4606.

[29] A. Hees, T. Do, B. M. Roberts, A. M. Ghez, S. Nishiyama, R. O. Bentley, A. K. Gautam, S. Jia, T. Kara, J. R. Lu, H. Saida, S. Sakai, M. Takahashi, and Y. Takamori, *Phys. Rev. Lett.* **124** (2020) 081101.

[30] GRAVITY Collaboration: R. Abuter, A. Amorim, N. Anugu et al., *Astron. Astrophys.* **615** (2018) L15,

[31] GRAVITY Collaboration: R. Abuter, A. Amorim, M. Bauböck et al., *Astron. Astrophys.* **625** (2019) L10.

[32] T. Do, A. Hees, A. Ghez et al., Science **365** (2019) 664.

[33] R. Abuter et al. (GRAVITY Collaboration), *Astron. Astrophys.* **636** (2020) L5.

[34] R. Ruffini, C. R. Argüelles, J. A. Rueda, *Mon. Not. R. Astron. Soc.* **451**, (2015) 622.

[35] E. A. Becerra-Vergara, C. R. Argüelles, A. Krut, J. A. Rueda, R. Ruffini, *Mon. Not. R. Astron. Soc. Lett.* **505** (2021) L64.

[36] A. F. Zakharov, *Mon. Not. R. Astron. Soc. Lett.* **513** (2022) L6.

[37] The GRAVITY Collaboration: R. Abuter, N. Aimar, A. Amorim et al., *Astron. Astrophys.* **657** (2022) L12.

[38] C. R. Argüelles, M. F. Mestre, E. A. Becerra-Vergara, V. Crespi, A. Krut, J. A. Rueda, and R. Ruffini, *Mon. Not. R. Astron. Soc. Lett.* **511** (2022) L35.

[39] D. Borka, P. Jovanović, V. Borka Jovanović, and A. F. Zakharov, *Phys. Rev. D* **85** (2012) 124004.

[40] A. F. Zakharov, D. Borka, V. Borka Jovanović, and P. Jovanović, *Advances in Space Research* **54** (2014) 1108.

[41] D. Borka, S. Capozziello, P. Jovanović, and V. Borka Jovanović, *Astroparticle Physics* **79** (2016) 41.

[42] K. F. Dialektopoulos, D. Borka, S. Capozziello, V. Borka Jovanović, and P. Jovanović, *Phys. Rev. D* **99** (2019) 044053.

[43] V. Borka Jovanović, P. Jovanović, D. Borka, S. Capozziello, S. Gravina, and A. D'Addio, *Facta Universitatis* **17** (2019) 11.

[44] S. Gillessen, P. M. Plewa, F. Eisenhauer, R. Sari, I. Waisberg, M. Habibi, O. Pfuhl, E. George, J. Dexter, S. von Fellenberg, T. Ott, and R. Genzel, *Astrophys. J.* **837** (2017) 30.

[45] M. Parsa, A. Eckart, B. Shahzamanian, V. Karas, M. Zajaček, J. A. Zensus, C. Straubmeier, *Astrophys. J.* **845** (2017) 22.

[46] F. Peißker, A. Eckart, and M. Parsa, *Astrophys. J.* **889** (2020) 61.

[47] S. Kalita, *Astrophys. J.* **893** (2020) 31.

[48] P. C. Lalremruati and S. Kalita, *Mon. Not. R. Astron. Soc.* **502** (2021) 3761.

[49] P. C. Lalremruati and S. Kalita, *Astrophys. J.* **925** (2022) 126.

[50] A. D'Addio, *Physics of the Dark Universe* **33** (2021) 100871.

[51] A. Stabile, and S. Capozziello, *Phys. Rev. D* **87** (2013) 064002.

[52] M. De Laurentis, I. De Martino, and R. Lazkoz, *Phys. Rev. D* **97** (2018) 104068.

[53] A. F. Zakharov, A. A. Nucita, F. De Paolis, G. Ingrosso, *Phys. Rev. D* **76** (2007) 062001.

Scanning band topology by the modulation instability*

[1,2]**A. Maluckov**†, [3]**D. Leykam**, [2]**Sergej Flach**
[1]Vinča Institute of Nuclear Sciences, University of Belgrade, Serbia
[2]Center for Theoretical Physics of Complex Systems, Institute for Basic Science Daejeon 34126, Korea
[3]Centre for Quantum Technologies, National University of Singapore, 3 Science Drive 2, Singapore 117543

[4]**A. Mančić**, [5]**E. Smolina**, and [5,6]**D. Smirnova**
[4]Faculty of Sciences and Mathematics, University of Niš, Serbia
[5]Institute of Applied Physics, Russian Academy of Science, Nizhny Novgorod 603950, Russia
[6]Nonlinear Physics Centre, Research School of Physics, Australian National University, Canberra ACT 2601, Australia

Abstract

Synergy of topology and nonlinearity in photonics opens new prospects for fundamental science and device functionalities. We consider the sensitivity of the band topology to the modulation instability and vice versa, related bulk-edge correspondence, and nonlinearity driven topological phase transitions in photonic lattices. Here, we briefly review our first findings in this emerging field and discuss some topics of ongoing research.

1. Introduction

"The thing's hollow – it goes on forever – and – oh my God! – it's full of stars!"[1] - to start with words we are 'forced' to use so often in our journey towards the place where topology meets nonlinearity and vice versa through photonics.

* This research was supported by the Ministry of Education, Science and Technological Development of the Republic of Serbia (451-03-9/2022-14/ 200017; 451-03-68/2022-14/200124), Institute for Basic Science in Korea (IBS-R024-Y1, IBS-R024-D1), the National Research Foundation, Prime Minister's Office, Singapore, the Ministry of Education, Singapore and the Australian Research Council Early Career Researcher Award (DE190100430)

† e-mail address: sandram@vin.bg.ac.rs

[1] From 'A Space Odyssey', Arthur C. Clarke.

There are a few comprehensive review papers which provide surveys of the combination of topology, nonlinearity, dissipation, and quantum effects in atomic and photonic systems [1, 2, 3]. We will omit detailed introduction, challenging the readers to find their own route to this unique place, just mentioning that, nowadays, there are a variety of methods to combine nontrivial topological properties with nonlinear interactions using platforms ranging from exciton-polariton condensates in microcavities [4, 5], waveguide arrays [6], metasurfaces [7], and resonator lattices [8, 9]. Interest in nonlinear topological photonic systems arises from their potential to exhibit novel phenomena without any analogue in electronic topological materials. For example, they offer new approaches for designing robust localized modes giving rise to new types of lasers [10, 11] and frequency combs [12]. The focus of theoretical investigations have been positioned on the self-focusing of unidirectional edge states [13, 14, 15], solitary bulk modes [16, 17, 18], as well as the interaction between the two [19]. The possibility of chaos and extreme sensitivity to initial conditions arising in complex nonlinear wave systems is one of the main issues that must be tackled when considering applications of nonlinear topological systems.

The problem we were initially interested in was to understand the nonlinear dynamics of Bloch waves in topological bands, specifically their sensitivity (if any) to a band's topological properties. We demonstrated that the modulational instability could lead to the spontaneous formation of wave fields characterized by non-trivial Chern numbers inherited from the linear Bloch bands [20, 21, 22, 23, 24] owing to the energy-dependent parametric gain exhibited by unstable Bloch waves. The can result in the selective population of a single Bloch band by injecting a simple plane wave as the initial condition. This is a precondition for efficient measuring of the bulk Chern number, which is generally a difficult task for classical waves [25, 26, 27, 28, 29, 30, 31]. Our approach is based on the generic phenomenon of modulational instability and is thus insensitive to the type and precise form of the nonlinearity. In addition, we have recently shown the ability of modulation instability to study the anomalous topological phases in driven photonic lattices [32].

In the following we will stay in the limit of non-driven topological lattices and briefly summarize the main findings, considering the example of π-flux square lattice model [33]. We consider the modulational instability of nonlinear Bloch waves, by employing linear stability analysis to characterize the dynamics at short evolution times and numerical simulations to establish the formation of a quasi-equilibrium wave field at longer times. At low intensities the instability remains confined to the initially-excited band [34]-[39], giving the possibility of extracting the band's Chern number from the wave Fourier spectrum [40]-[42]. We associate this stage with prethermalization phase. Interestingly, with increasing intensities, we have seen the re-emergence of stability at a critical intensity associated with a nonlinearity-induced closure of the band gap [43].

2. Overview of model

We introduce the two-dimensional nonlinear Schrödinger equation describing the wave propagation dynamics in photonic lattices,

$$i\partial_t \psi_{\mathbf{r}} = (\hat{H}_L + \hat{H}_{NL})\psi_{\mathbf{r}}, \tag{1}$$

where $\hat{H}_L$ and $\hat{H}_{NL}$ are linear and nonlinear parts of the Hamiltonian, respectively, and $\mathbf{r} = (\mathbf{x}, \mathbf{y})$ indexes the lattice sites. We take $\hat{H}_L$ to be the chiral-π-flux model [44], Fig. 1(a), which presents a two dimensional Chern insulator. The underlying square lattice is composed of two sublattices a and b, with $\psi_{\mathbf{r}} = (\psi_{\mathbf{r}}^{(a)}, \psi_{\mathbf{r}}^{(b)})^T$, and is described by the Bloch wave Hamiltonian

$$\begin{gathered} \hat{H}_L(\mathbf{k}) = \mathbf{d}(\mathbf{k}) \cdot \hat{\sigma}, \quad \mathbf{d_z} = \mathbf{\Delta} + \mathbf{2J_2}(\cos \mathbf{k_x} - \cos \mathbf{k_y}) \\ d_x + i d_y = J_1[e^{-i\pi/4}(1 + e^{i(k_y - k_x)}) + e^{i\pi/4}(e^{-ik_x} + e^{ik_y})], \end{gathered} \tag{2}$$

where $\mathbf{k} = (\mathbf{k_x}, \mathbf{k_y})$ is the wavevector inside the first Brillouin zone, $k_{x,y} \in [-\pi, \pi]$, $\hat{\sigma} = (\hat{\sigma}_\mathbf{x}, \hat{\sigma}_\mathbf{y}, \hat{\sigma}_\mathbf{z})$ are Pauli matrices, $J_{1,2}$ are nearest and next-nearest neighbour hopping strengths, and Δ is a detuning between the sublattices. In the following we scale all energies with respect to J_1 (i.e. setting $J_1 = 1$) and present the results for $J_2 = J_1/\sqrt{2}J_1$ for convenience.

Fig. 1(b) shows the energy spectrum of the Bloch eigenstates $\hat{H}_L(\mathbf{k})\mathbf{u_n}(\mathbf{k}) = \mathbf{E_n}(\mathbf{k})\mathbf{u_n}(\mathbf{k})$, which form two bands $n = 1, 2$ separated by a gap. The gap closes at $\Delta/J_1 = \pm 2\sqrt{2}$, which corresponds to a change in the quantized Chern number [1],

$$C = \frac{1}{2\pi i} \int_{BZ} \mathrm{Tr}\left[\hat{P}(\mathbf{k})[\partial_{\mathbf{k_x}} \hat{\mathbf{P}}(\mathbf{k}), \partial_{\mathbf{k_y}} \hat{\mathbf{P}}(\mathbf{k})]\right] d\mathbf{k}, \tag{3}$$

where $\hat{P}(\mathbf{k}) = \mathbf{u_1}(\mathbf{k})\mathbf{u_1^\dagger}(\mathbf{k})$ is the projection operator onto the first band's Bloch functions.

For the nonlinear part of the Hamiltonian, $\hat{H}_{NL}$, we consider an on-site nonlinearity of the form

$$\hat{H}_{NL} = \Gamma \mathrm{diag}[f(|\psi_\mathbf{r}|^2)], \tag{4}$$

where Γ is the nonlinear interaction strength and f is the nonlinear response function. We analyze the nonlinear mode dynamics for the case of the saturable nonlinarity, used to model effects such as multi-photon absorption and material damage, which limit the practical strength of the Kerr effect [45]. In the low intensity limit, however, the saturable nonlinearity reduces to the standard Kerr nonlinearity.

To characterize the complex multi-mode dynamics, we compute the participation number in the lattice and k-space: $P_R = \mathcal{P}^2/(2N^2 \sum_\mathbf{r} |\psi_\mathbf{r}|^4)$

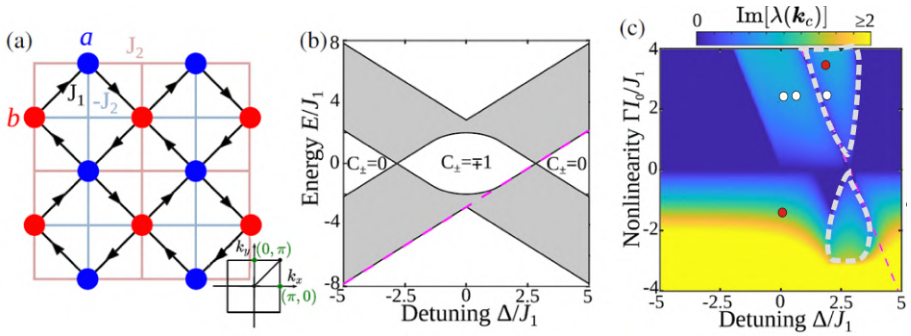

Figure 1: (a) Schematic of the lattice, consisting of two sublattices (a, b) with detuning Δ and inter- (intra-) sublattice couplings J_1 (J_2). (b) Linear band structure as a function of the sublattice detuning Δ. (c) Growth rate of the most unstable wavevector $\mathbf{k_c}$ of the $\mathbf{k} = \mathbf{0}$ nonlinear Bloch wave. Dashed red line denotes the band inversion produced by nonlinearity. Dark blue areas correspond to stablity, encircled areas (dashed white lines) correspond to oscillatory instability and the rest to exponential instability of nonlinear Bloch wave.

and $P_K = \heartsuit^2/(2N^2\sum_{\mathbf{k}}|\psi_{\mathbf{k}}|^4)$, respectively, where $\mathcal{P}$ and $\heartsuit$ are the mode powers in lattice and k-spaces; the field's Chern number $\mathcal{C}(t)$; the band population ratio $R(k) = u_1^\dagger(\mathbf{k})\psi(\mathbf{k})/(\mathbf{u_2^\dagger}(\mathbf{k})\psi(\mathbf{k}))$, and the purity gap which indicates the minimum distance between bands. In the following, we will show the results for $\mathcal{C}(t)$ measured by summing the charges of the phase singularities of the polarization azimuth $\theta = \frac{1}{2}\tan^{-1}(n_x/n_z)$ weighted by $\mathrm{sgn}(n_y)$, where $\mathbf{n} = (n_x, n_y, n_z)^T$ is polarization vector. It is worth mentioning the diversity of approaches that are being used to determine the band Chern number [26, 27, 28, 46].

3. Nonlinear dynamics senses band topology

Here we briefly introduce the numerical approach. The nonlinear extension of the $\mathbf{k_0} = (\pi, \mathbf{0})$ Bloch wave [47, 48], $\phi_{\mathbf{r}} = (\sqrt{I_0}, 0)^T e^{i\pi x}$ with energy $E_{NL} = \Delta - 4J_2 + \Gamma f(I_0)$ is our starting point. This mode bifurcates from the lower band when $\Delta < 4J_2$ and from the upper band when $\Delta > 4J_2$. We construct the initial condition for the numerical beam propagation simulations by perturbing the nonlinear Bloch wave with a random complex perturbation with amplitude not exceeding $0.01\sqrt{I_0}$ [33]. This random perturbation serves to seed any instabilities exhibited by the nonlinear Bloch wave.

3.1. The short time dynamics: Linear stability analysis

The initial phase of the MI development is investigated adopting the linear stability analysis (LSA) combining analytical and numerical tools. It consists in tracking the evolution of the small perturbation of the nonlinear Bloch mode. The first step was to add the small complex perturbation $|p| \ll 1$ to the Bloch mode: $\psi(t) = (\phi(\mathbf{k}_0)e^{i\mathbf{k}_0\cdot\mathbf{r}} + p(\mathbf{k},t)e^{i\mathbf{k}\cdot\mathbf{r}})e^{-iEt}$ and substitute this expression into the system equation (1). The second step was linearization of the equation with respect to the small perturbation, which resulted in the linear evolution equation of small perturbation. And the final step consisted in solving this equation which can be interpreted as an eigenequation of perturbation. The corresponding solutions – the instability eigenvalues λ – reveal the stability properties. Perturbation modes are exponentially or oscillatory unstable if corresponding eigenvalues are purely imaginary or complex with finite both real and imaginary part, respectively. Further details are given in the supplement of our paper [33].

In Fig. 1(c) we re-plot (see our paper [33] for details) the growth rate of the most unstable perturbation wavevector $\mathbf{k_c}$. Contour white dashed lines separate parameter areas with different types of instability: exponential and oscillatory outside and inside the contours, respectively. When the nonlinear Bloch wave bifurcates from the band edge, it exhibits a long wavelength instability for weak self-focusing nonlinearity ($\Gamma m_{\text{eff}} < 0$, where m_{eff} is the wave effective mass at $\mathbf{k_0}$), similar to the scalar nonlinear Schrödinger equation. On the other hand,the mid-band nonlinear Bloch waves are unstable for weak Γ regardless of its sign. A second long wavelength instability emerges at a stronger critical value of Γ, corresponding to the nonlinear potential $\hat{H}_{NL} = \frac{\Gamma I_0}{2}(\hat{\sigma}_0 + \hat{\sigma}_z)$ inducing a band crossing at $\mathbf{k_0}$, i.e. $\Delta + \Gamma I_0/2 = 4J_2$ [dashed red line in Figs. 1(c)].

The possibility of the nonlinearity induced band inversion was the first significant finding of our research.

3.2. The high symmetry points of the Brillouin zone

To understand the long wavelength instabilities, we considered the continuum limit of Eq. (1), which can be rewritten in a form of the effective Dirac model. By taking $\mathbf{k} = \mathbf{k_0} + \mathbf{p}$ with $\mathbf{p} \ll \mathbf{1}$, the Dirac Hamiltonian is obtained:

$$\hat{H}_D = -J_1\sqrt{2}(p_x\hat{\sigma}_y + p_y\hat{\sigma}_x) + (\Delta - 4J_2 + J_2[k_x^2 + k_y^2])\hat{\sigma}_z. \tag{5}$$

The corresponding nonlinear Bloch wave solutions of Eq. 5 we derived analytically in [33]. Here, we extract the main findings regarding the mode dynamics in the close neighborhood of the critical point by re-plotting Fig. 2(a-c) from our paper [33]. Below the critical line, for example for $\Gamma I_0 = 1$, the Bloch wave spectrum in the trivial (red dashed line) and nontrivial (blue solid line) phases consists of two gapped bands. The critical line coincides with the formation of a nonlinear Dirac cone at $\mathbf{k_0}$ [43], i.e.

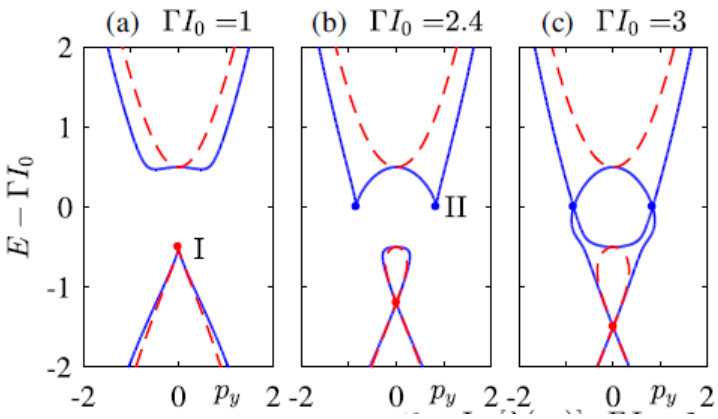

Figure 2: (a-c) The transition in the nonlinear Bloch wave spectrum across the critical line in the nontrivial (blue solid line) and trivial phases (red dashed line) of the effective Dirac model Eq. 5, respectively.

a symmetry-breaking bifurcation of the nonlinear Bloch waves. At the bifurcation, new modes $|\phi(\mathbf{r})\rangle = (\sqrt{I_a}e^{i\varphi}, \sqrt{I_b})e^{i\pi x}$ emerge, with the relative phase between the two sublattice φ forming a free parameter. Moreover, in the non-trivial phase, an additional bifurcation occurs at higher intensities at $|\mathbf{p}| = \sqrt{\mathbf{4} - \boldsymbol{\Delta}/\mathbf{J_2}}$, corresponding to $d_z(\mathbf{p}) = \mathbf{0}$, Fig. 2(b). The new branches emerging from this bifurcation merge with the lower band as ΓI_0 is increased ($\Gamma I_0 = 3$ in Fig. 2(c)) producing a gapless nonlinear Bloch wave spectrum, while in the trivial phase the nonlinear Bloch wave spectrum remains gaped [33].

We showed that the modes' stability in the vicinity of the bifurcation point was sensitive to the linear band topology [33]. In the non-trivial phase, the perturbation modes' polarization rotated away to the opposite pole of the Bloch sphere with respect to the injected nonlinear Bloch mode opposite to the case in the trivial phase. Therefore the overlap between the nonlinear Bloch wave and the perturbed mode is reduced, weakening the efficiency of the nonlinear wave mixing responsible for the emergence of instabilities.

From these considerations we concluded that the modulational instability is sensitive to the geometrical properties of the Bloch waves, i.e. their polarization and the band topology.

3.3. The long time dynamics

Next, we carried out numerical simulations of Eq. 1 to study the development of the instability beyond the initial linearized dynamics, considering a system of size $N = 32 \times 32$ unit cells and periodic boundary conditions.

Fig. 3 illustrates the dynamics of the $\mathbf{k_0} = (\pi, \mathbf{0})$ nonlinear Bloch wave with intensity $I_0 = 1$. We fixed the value of Δ and averaged the observables

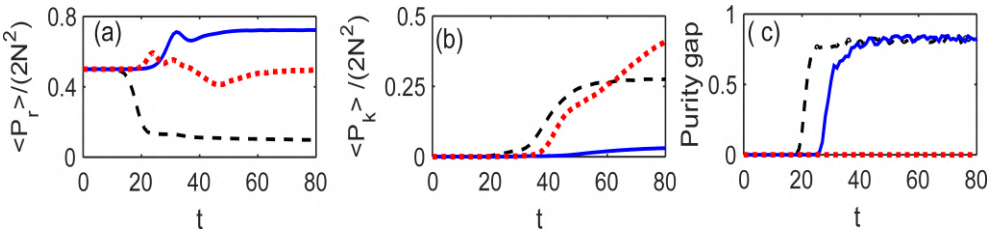

Figure 3: The evolution of $< P_R >$, $< P_K >$ and the purity gap. The parameters correspond to different types of nonlinearity: focusing ($\Gamma > 0$) and defocusing ($\Gamma < 0$). Black dashed and blue solid line denote the exponential type of instability developed for $\Gamma = -1.5$, $\Delta = 0$, and $\Gamma = 2.2$, $\Delta = 0$, respectively, while red dotted line denotes the oscillatory type of instability developed for $\Gamma = 3$, $\Delta = 2.5$. These cases are marked in Fig. 1(c) by white circles.

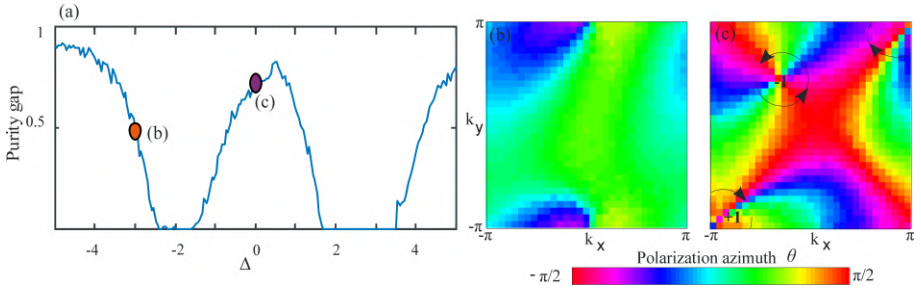

Figure 4: (a) Purity gap time $t = t_f = 40/J_1$ as a function of Δ. (b,c) Field polarization textures at t_f in the (b) trivial ($\Delta = -3$) and (c) non-trivial ($\Delta = 0$) phases. The Chern number is obtained by summing the charges of the polarization azimuth vortices (indicated by arrows) weighted by $\mathrm{sgn}(n_y)$ at the vortex core (indicated by ± 1) [40]. This figure is taken from our paper [33].

over an ensemble of 100 random initial perturbations.

In the regime with focusing instability a collection of localized solitons is generated, responsible for decrease in $\langle P_{\mathbf{r}} \rangle$ in Fig. 3(a). On the other hand, the defocusing nonlinearity spreads the energy over both sublattices, resulting in a small increase in $\langle P_{\mathbf{r}} \rangle$. In all the cases, the increase of $\langle P_{\mathbf{k}} \rangle$ is due to the nonlinear wave mixing, which caused the excitation of other Fourier modes. This is accompanied by the purity gap opening and emergence of a well-defined Chern number in the case with exponential instabilities. Interestingly, the purity gap opens prior to $\langle P_{\mathbf{r},\mathbf{k}} \rangle$ reaching a steady state. Under the oscillatory instability, the purity gap remains negligible due to the competition between pairs of instability modes with the same growth rates.

In Fig. 4(a) the value of the purity gap at $t = t_f = 40J_1$ as a function of Δ is shown. It follows the instability growth rate behaviour in Fig. 1 for $\Delta > 0$, it vanishes when the Bloch wave is linearly stable or exhibits an oscillatory instability and closes at $\Delta \approx -2$ despite no change in the fastest growing instability mode. This corresponds to a nonlinearity-induced closure of the band gap at the other high symmetry point $\mathbf{k} = (\mathbf{0}, \pi)$.

Further enlightening of the band topology is provided by measuring the field polarization $\langle \hat{\mathbf{n}}(\mathbf{k}) \rangle$ at long times, Fig.4(b,c). Details are presented in our paper [33]. In the trivial phase (large Δ) the field is predominantly localized to a single sublattice, such that n_z remains nonzero and there are no phase singularities in θ, hence $C = 0$. In the non-trivial phase, $\langle \hat{\mathbf{n}}(\mathbf{k}) \rangle$ spans the entire Bloch sphere, corresponding to a pair of opposite charge phase singularities with opposite weights $\mathrm{sgn}(n_y) = \pm 1$, and hence $C = 1$.

To summarize, we proved that the long time instability dynamics can be used to measure the band Chern number.

3.4. Band relaxation triggered by the modulation instability

The convergence of participation number P and Chern number $\mathcal{C}$ to constant values suggests the formation of an equilibrium state at long evolution times t [33]. Since $\mathcal{C}(t)$ is a function of the $\mathbf{k}$-dependent band populations, we treat the k-space field components at a particular wavevector $\mathbf{k}$ as two level systems that can exchange energy with other wavevectors (the environment) via the nonlinearity. Here, we attempt to use it in order to understand the wave thermalization process in the presence of nonlinearity [49, 50]. Regarding this, assuming that the system can reach some effective thermal equilibrium, we adopt the grand-canonical (Gibbs) approach [51]. From this point of view, we present the occupation probability for the single particle state $u_n(\mathbf{k})$ in a form: $\rho_n(\mathbf{k}) = \frac{\mathbf{1}}{\mathcal{Z}} \exp(-\beta_{\mathrm{eff},\mathbf{n}} \mathcal{P}_{\mathbf{n}}(\mathbf{k}))$, where $\mathcal{Z}$ is the partition function, $\beta_{\mathrm{eff,n}} = \beta[E_n(\mathbf{k}) - \mu]$, β is the inverse temperature, $n = 1, 2$, $\mathcal{P}_n(\mathbf{k})$ is the mode occupation number, and μ is the chemical potential.

Consequently, the mode in band n and with wavevector $\mathbf{k}$ should have an average occupation $\rho_n(\mathbf{k}) = \mathbf{1}/\beta_{\mathrm{eff,n}}$, from which we obtained the ex-

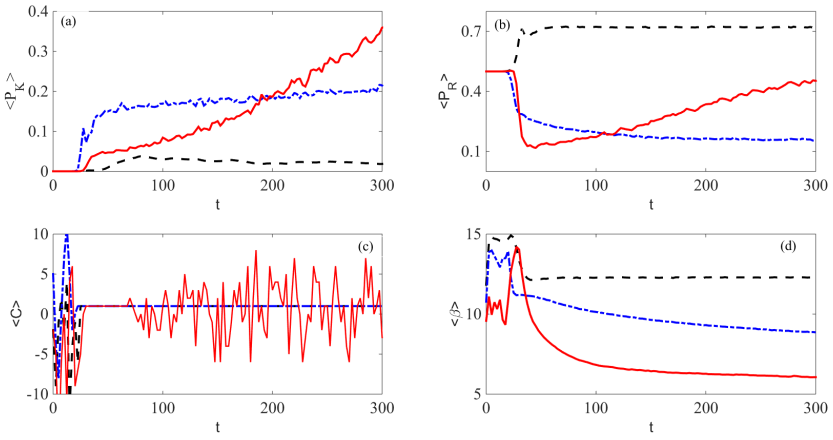

Figure 5: Dynamics of averaged P_K, P_R, C, β for $\Gamma = 2.2$ and $\Delta = 0$, 1, 2 are presented by black dashed, red solid, and blue dash-dotted lines, respectively. The inverse temperature is presented in logarithm scale for the convenience. The parameters from this figure are denoted by red circles in Fig. 1 (c).

pressions for β and μ as functions of occupation probabilities:

$$\beta = \frac{\rho_1 - \rho_2}{2\rho_1\rho_2\omega(\mathbf{k})}, \ \mu = -\frac{(\rho_1 + \rho_2)\omega(\mathbf{k})}{\rho_1 - \rho_2}, \tag{6}$$

where $\omega(\mathbf{k}) = -\mathbf{E_1}(\mathbf{k}) = \mathbf{E_2}(\mathbf{k}) > \mathbf{0}$.

In Fig. 5 we plot the dynamics of averaged participation numbers $< P_R >$ and $< P_K >$, Chern number and β for three sets of parameters $\Gamma = 2.2$ and $\Delta = 0, 1, 2$. While the average of C converges to unity in first two cases, there are significant fluctuations for $\Gamma = 2.2$ and $\Delta = 2$ after short transient time. On the other hand, $< P_r >$ and $< P_k >$ saturate to finite values only in the case with $\Delta = 0$, which together with the $< \beta >$ dynamics indicates that the system is not reaching a thermal equilibrium in the cases with $\Delta = 1$ and 2; β does not approach a constant value, but remains dependent on the wavevector $\mathbf{k}$. By increasing the propagation time, we have seen the tendency of saturation in all observables for selected values of parameters, i.e. the system is in a some kind of the "pre-thermalization" regime in which $\beta = \beta(\mathbf{k})$. We correlated the relaxation tendencies to the type of MI in the initial phase of the instability development in Fig. 1(c): the exponential instability is a necessary but not a sufficient condition for thermalization.

In order to explore the pre-thermalization more systematically, we considered in Fig. 6 the observables $< P_R >$, $< R >$, $< C >$, $< \beta >$ taken

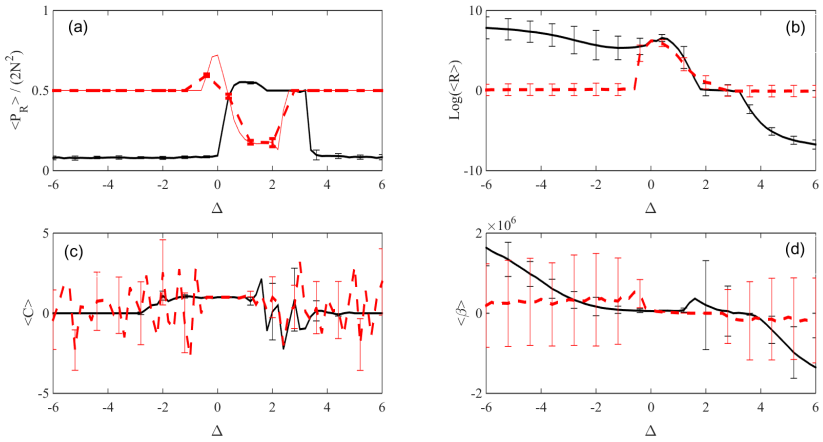

Figure 6: Effect of the sublattice detuning, Δ, on observables (a) the averaged participation number in the lattice space, (b) the averaged population ratio, (c) the averaged Chern number, and (d) the averaged inverse temperature at time $t = t_f = 100J_1$. The averaging is done over the ensemble of 100 initial conditions (see the text). Black solid and red dashed lines correspond to the nonlinearity strengths $\Gamma = -1.5$ and $\Gamma = 2.2$, respectively. Vertical bars denote the standard deviations from the averaged (mean) values.

at $t = t_f = 100J_1$ as a function of the sublattice detuning, Δ, which is related to the band flatness and width of the bands gap. It is found that, in the area corresponding to $|\Delta| < 2\sqrt{2}$, which is situated between two band-crossing points, the system is topologically nontrivial, as sketched in the Fig. 1(b). The calculated value of $C = 1$ is caught by the excitation of the whole gaped band triggered by the MI in the corresponding areas, Fig. 6 (c), for both selected values of Γ at $t = 100$. Recalling Fig. 3, we see that in both cases, at $\Delta = 0$, all quantities converged to fixed values. On the other hand, in Fig. 5, for $\Gamma = 2.2$, thermalization is reached for $\Delta = 0$, while for $\Delta = 1$ and 2 the long time behaviour of observables indicates not unfinished thermalization. So, the prethermalization phase is detected for $\Delta = 1$ while for $\Delta = 2$, the system is out of it.

4. Conclusions

Here, we reviewed the main findings of our investigation, which is still in progress, of the ability to scan the topological band properties by inducing the modulational instability of nonlinear Bloch waves. In the non-driven photonic Chern inuslator we proved the MI sensitivity to geometrical properties of Bloch waves, i.e. their polarization, and provided the tool to

measure the band Chern number by utilizing the long time instability dynamics. In other words, we established that the topological properties of the band are imprinted on the MI at small and large times and nonlinearity scales. This, together with our recent achievements regarding the driven topological photonic lattices [32], gives us the confidence to proceed with a search for new capabilities of the modulation instability in the word of topological photonics.

References

[1] T. Ozawa et al., *Topological photonics*, Rev. Mod. Phys. **91**, 015006 (2019).

[2] D. Smirnova, D. Leykam, Y. D. Chong, and Y. Kivshar, *Nonlinear topological photonics*, Appl. Phys. Rev. **7**, 021306 (2020).

[3] A. Saxena, P. G. Kevrekidis, and J. Cuevas-Marave, *Nonlinearity and Topology*, Nonlinear Systems and Complexity **32**, 25 (2020).

[4] S. Klembt et al., *Exciton-polariton topological insulator*, Nature **562**, 552 (2018).

[5] F. Baboux et al., *Unstable and stable regimes of polariton condensation*, Optica **5**, 1163 (2018).

[6] S. Mukherjee and M. C. Rechtsman, *Observation of Topological Band Gap Solitons*, Science **368**, 856 (2010).

[7] D. A. Smirnova et al., *Third-harmonic generation in photonic topological metasurfaces*, Phys. Rev. Lett. **123**, 103901 (2019).

[8] D. A. Dobrykh, A. V. Yulin, A. P. Slobozhanyuk, A. N. Poddubny, Y. S. Kivshar, *Nonlinear control of electromagnetic topological edge states*, Phys. Rev. Lett. **121**, 163901 (2018).

[9] S. Mittal, E. A. Goldschmidt, and M. Hafezi. *A topological source of quantum light*, Nature **561**, 502 (2018).

[10] G. Harari et al., *Topological insulator laser: Theory*, Science **359**, 1230 (2018).

[11] M. A. Bandres et al., *Topological insulator laser: Experiment*, Science **359**, 1231 (2018).

[12] S. Mittal et al, *Topological frequency combs and nested temporal solitons'*, Nature Physics **17**, 1169-1176 (2021).

[13] Y. Lumer, M. C. Rechtsman, Y. Plotnik, and M. Segev, *Instability of bosonic topological edge states in the presence of interactions*, Phys. Rev. A **94**, 021801(R) (2016).

[14] Y. V. Kartashov and D. V. Skryabin, *Modulational instability and solitary waves in polariton topological insulators*, Optica **3**, 1228 (2016).

[15] D. Leykam and Y. D. Chong, *Edge Solitons in Nonlinear Photonic Topological Insulators*, Phys. Rev. Lett. **117**, 143901 (2016).

[16] Y. Lumer, Y. Plotnik, M. C. Rechtsman, and M. Segev, *Self-Localized States in Photonic Topological Insulators*, Phys. Rev. Lett. 111, 243905 (2013).

[17] A. N. Poddubny and D. A. Smirnova, *Ring Dirac solitons in nonlinear topological systems*, Phys. Rev. A **98**, 013827 (2018).

[18] J. L. Marzuola, M. Rechtsman, B. Osting, and M. Bandres, *Bulk soliton dynamics in bosonic topological insulators*, arXiv:1904.10312.

[19] D. A. Smirnova, L. A. Smirnov, D. Leykam, and Y. S. Kivshar, *Topological edge states and gap solitons in the nonlinear Dirac model*, Laser Photon. Rev. **13**, 1900223 (2019).

[20] V. E. Zakharov and L. A. Ostrovsky, *Modulation instability: The beginning*, Physica D **238**, 540 (2009).

[21] R. W. Boyd, *Nonlinear Optics*, Academic Press, New York (2008).

[22] Y. S. Kivshar and M. Peyrard, *Modulational instabilities in discrete lattices*, Phys. Rev. A **46**, 3198 (1992).

[23] P. J. Everitt et al., *Observation of a modulational instability in Bose-Einstein condensates*, Phys. Rev. A **96**, 041601(R) (2017).

[24] J. H. V. Nguyen, D. Luo, and R. G. Hulet, *Formation of matter-wave soliton trains by modulational instability*, Science **356**, 422 (2017).

[25] C.-E. Bardyn, S.D. Huber, and O. Zilberberg, *Measuring topological invariants in small photonic lattices*, New J. Phys. **16**, 123013 (2014).

[26] M. Aidelsburger, M. Lohse, C. Schweizer, M. Atala, J. T. Barreiro, S. Nascimbene, N. R. Cooper, I. Bloch, and N. Goldman, *Measuring the Chern number of Hofstadter bands with ultracold bosonic atoms*, Nature Phys. **11**, 162 (2015).

[27] M. Wimmer, H. M. Price, I. Carusotto, and U. Peschel, *Experimental measurement of the Berry curvature from anomalous transport*, Nature Phys. **13**, 545 (2017).

[28] M. Tarnowski, F. N. Ünal, N. Fläschner, B. S. Rem, A. Eckardt, K. Sengstock, and C. Weitenberg, *Measuring topology from dynamics from obtaining the Chern number from a linking number*, Nature Commun. **10**, 1728 (2019).

[29] A. V. Poshakinskiy, A. N. Poddubny, and M. Hafezi, *Phase spectroscopy of topological invariants in photonic crystals*, Phys. Rev. A **91**, 043830 (2015).

[30] W. Hu, J. C. Pillay, K. Wu, M. Pasek, P. P. Shum, and Y. D. Chong, *Measurement of a topological edge invariant in a microwave network*, Phys. Rev. X **5**, 011012 (2015).

[31] S. Mittal, S. Ganeshan, J. Fan, A. Vaezi, and M. Hafezi, *Measurement of topological invariants in a 2D photonic system*, Nature Photon. **10**, 180 (2016).

[32] A. Maluckov, E. Smolina, D. Leykam, S. Gundogdu, D. G. Angelakis, and D. A. Smirnova, *Nonlinear signatures of Floquet band topology*, arXvix:2111:10229.

[33] D. Leykam, E. Smolina, A. Maluckov, S. Flach and D. A. Smirnova, *Probing band topology using modulational instability*, Phys. Rev. Lett. **126** 073901 (2021).

[34] E. Small, R. Pugatch, and Y. Silberberg, *Berezinskii-Kosterlitz-Thouless crossover in a photonic lattice*, Phys. Rev. A **83**, 013806 (2011).

[35] P. Buonsante, R. Franzosi, and A. Smerzi, *Phase transitions at high energy vindicate negative microcanonical temperature*, Phys. Rev. E **95**, 052135 (2017).

[36] T. Mithun, Y. Kati, C. Danieli, and S. Flach, *Weakly Nonergodic Dynamics in the Gross-Pitaevskii Lattice*, Phys. Rev. Lett. **120**, 184101 (2018).

[37] S. A. Derevyanko, *Thermalized polarization dynamics of a discrete optical-waveguide system with four-wave mixing*, Phys. Rev. A **88**, 033851 (2013).

[38] M. Hafezi, P. Adhikari, and J. M. Taylor, *Chemical potential for light by parametric coupling*, Phys. Rev. B **92**, 174305 (2015).

[39] F. O. Wu, A. U. Hassan, and D. N. Christodoulides, *Thermodynamic theory of highly multimoded nonlinear optical systems*, Nature Photon. **13**, 776 (2019).

[40] T. Fösel, V. Peano, and F. Marquardt, *L lines, C points and Chern numbers: understanding band structure topology using polarization fields*, New J. Phys. **19**, 115013 (2017).

[41] D. Leykam and D. A. Smirnova, *Probing bulk topological invariants using leaky photonic lattices*, Nature Phys. **17**, 632 (2021).

[42] T. Fukui, Y. Hatsugai, H. Suzuki, *Chern numbers in discretized Brillouin zone: Efficient method of computing (spin) Hall conductances*, J. Phys. Soc. Jpn. **74**, 1674 (2005).

[43] R. W. Bomantara, W. Zhao, L. Zhou, and J. Gong, *Nonlinear Dirac cones*, Phys. Rev. B **96**, 121406(R) (2017).

[44] T. Neupert, L. Santos, C. Chamon, and C. Mudry, *Fractional Quantum Hall States at Zero Magnetic Field*, Phys. Rev. Lett. **106**, 236804 (2011).

[45] R. W. Boyd, *Nonlinear Optics*, Academic Press (2007).

[46] R. Bianco and R. Resta, *Mapping topological order in coordinate space*, Phys. Rev. B **84**, 241106(R) (2011).

[47] D. Träger et al., *Nonlinear Bloch modes in two-dimensional photonic lattices*, Opt. Exp. **14**, 1913 (2006).

[48] Y. V. Kartashov, B. A. Malomed, and L. Torner, *Solitons in nonlinear lattices*, Rev. Mod. Phys. **83**, 247 (2011).

[49] M. Ueda, *Quantum equilibration, thermalization and prethermalization in ultracold atoms*, Nature reviews: Physics **2**, 669 (2020).

[50] K. G. Makris, F. O. Wu, P. S. Jung, and D. N. Christodoulides, *Statistical mechanics of weakly nonlinear optical multimode gases*, Opt. Lett. **45**, 1651 (2020).

[51] T. Mithun, Y. Kati, C. Danieli, and S. Flach, *Weakly Nonergodic Dynamics in the Gross-Pitaevskii Lattice*, Phys. Rev. Lett. **120**, 184101 (2018).

Exact traveling and solitary wave solutions to the generalized Gross-Pitaevskii equation with cylindrical potential*

Nikola Petrović†
Institute of Physics, Pregrevica 118, 11080 Belgrade,
University of Belgrade, Serbia

Abstract

In our paper we modify the Jacobi Elliptic function (JEF) expansion method to obtain solutions to the Gross-Pitaevskii equation with a cylindrical potential, in which case the three transverse dimensions are no longer symmetric. The solutions end up combining the features of the solutions for the spherical potential and the solutions of the ordinary Nonlinear Schrödinger equation (NLSE). Solutions which have an oscillating amplitude and modulational stability can be found.

PACS numbers: 05.45.Yv, 42.65.Tg

1. Introduction

Gross-Pitaevskii equation (GPE) is of the extreme importance in the study of the Bose-Einstein condensates (BEC), where it describes the behavior of the condensate wavefunction [1]. It has been introduced independently by Gross [2] and Pitaevskii [3] for an unrelated problem, but has since been found of great use in the study of BEC. Solitary wave solutions [4] have been discovered in GPE. One of the main methods of finding approximate solutions to the GP equation and related equations such as the Ginzburg-Landau equation is using the variational approximation [5, 6, 7]. Such an approach uncovered various complicated forms of solutions such as vortices [5], dipoles [6], tripoles [6] and various oscillating structures [7]. In [8] exact analytic solutions for the (1-1)D solutions to the GPE were found. The gain function was used in the diffraction coefficient to produce stable oscillating solitary wave solutions. The paper introduces many novel ideas, such as the chirp function for which in order to obtain it one must solve a Ricatti

* Work at the Institute of Physics is supported by project OI 171006 of the Serbian Ministry of Education and Science. Work in Qatar was done under the Qatar National Research Fund (QNRF) project: NPRP 8-028-1-001.

† e-mail address: nzpetr@ipb.ac.rs

differential equation. The paper obtains stable oscillating solutions for constant potential, but a complicated form for the nonlinearity coefficient.

Recently, a new class of solutions based on the Jacobi Elliptic Function (JEF) expansion [9, 10, 11] for the Nonlinear Schrödinger Equation (NLSE) and the methods used have been generalized in [12, 13] for the GPE. Unlike in [8], in [9, 10, 11, 12, 13] the dispersion/diffraction coefficient is no longer a constant and the gain function is factored differently into the formula for the nonlinearity coefficient, among other differences in the parameters of the solution. Having a non-constant dispersion/diffraction coefficient allows the use of dispersion [14] and diffraction management [15]. The modulational stability of the solutions in [9, 10, 11, 12, 13] for both the NLSE and the GPE was analyzed in [16] and also [13] for both dark/bright and spatial/temporal solitary waves, under both normal and anomalous dispersion. It was determined that in all three possible combinations the solitary waves achieve either unconditional stability or stability under dispersion management.

All the obtained solutions for the GPE have so far been for a potential with spherical symmetry. However, other forms of the potential are possible including ones that use trigonometric functions [17]. For many practical situations, confining potentials with cylindrical symmetry are used. In other words, there is a confining potential only in two transverse dimensions, reminiscent of an infinitely long cylinder [18, 19]. The elongated cylindrical form of the potential allows experimental physicists to analyze the Bose-Einstein condensate in a regime close to the 1D case [20]. In this paper we extend the results in [12, 13] to the case of the cylindrical potential.

2. Method

We consider GPE in (3+1)D with distributed coefficients [1]:

$$i\partial_t u + \frac{\beta(t)}{2}\Delta u + \chi(t)|u|^2 u + \alpha(t)(x^2+y^2)u = i\gamma(t)u. \tag{1}$$

Here t is time, $\Delta = \partial_x^2 + \partial_y^2 + \partial_z^2$ is the 3D Laplacian and $\alpha(t)$ stands for the strength of the quadratic potential as a function of time. The functions β, χ, and γ stand for the diffraction, nonlinearity, and gain coefficients, respectively. All coordinates in Eq. (1) are made dimensionless by the choice of coefficients. It is worth noting that the transverse variable z is no longer symmetric with respect to the other two transverse variables x and y.

As described in Ref. [12], we separate the real and imaginary part of u:

$$u(x,y,z,t) = A(x,y,z,t)\exp\left(iB(x,y,z,t)\right). \tag{2}$$

and, after plugging in Eq. (2) into Eq. (1), divide Eq. (1) into the real and

imaginary part. We now assume the following form for A and B:

$$\begin{aligned} A &= f_1(t)F(\theta) + f_2(t)F(\theta)^{-1}, && (3)\\ \theta &= k(t)x + l(t)y + m(t)z + \omega(t), && (4)\\ B &= a_1(t)(x^2+y^2) + a_2(t)z^2 + b_1(t)(x+y) + b_2(t)z + e(t), && (5) \end{aligned}$$

where f_1, f_2, k, l, m, ω, a_1, a_2, b_1, b_2 and e are functions of t to be determined, and F is an arbitrary Jacobi elliptic function (JEF) satisfying:

$$\left(\frac{dF}{d\theta}\right)^2 = c_0 + c_2F^2 + c_4F^4, \qquad (6)$$

where c_0, c_2 and c_4 are constants that depend on the form of the JEF and the parameter of the JEF M. For $F = cn$, the JEF we will be using in this paper, we have $c_0 = 1-M$, $c_2 = 2M-1$ and $c_4 = -M$. The JEFs are well suited as an ansatz for nonlinear partial differential equations with terms containing the third degree of the original function. Function f_2 may be set to 0. In contrast to Ref. [12], the functions next to the quadratic and linear terms in the phase have been split into two pairs of functions, a_1, a_2, b_1 and b_2 to account for the asymmetry between z and the other transverse variables.

Applying the F-expansion method and the principle of harmonic balance [9] we obtain the following system of algebraic and first order differential equations for f_i $(i = 1, 2)$, a_1, a_2, b_1, b_2, k, l, m and ω:

$$\begin{aligned} \frac{df_j}{dt} + (2a_1 + a_2)\beta f_j - \gamma f_j &= 0, && (7)\\ \frac{dk}{dt} + 2ka_1\beta = 0, \quad \frac{dl}{dt} + 2la_1\beta = 0, \quad \frac{dm}{dt} + 2ma_2\beta &= 0, && (8)\\ \frac{da_1}{dt} + 2\beta a_1^2 - \alpha = 0, \quad \frac{da_2}{dt} + 2\beta a_2^2 &= 0, && (9)\\ \frac{db_1}{dt} + 2\beta a_1 b_1 = 0, \quad \frac{db_2}{dt} + 2\beta a_2 b_2 &= 0, && (10)\\ \frac{d\omega}{dt} + \beta((k+l)b_1 + mb_2) &= 0, && (11)\\ \frac{de}{dt} + \frac{\beta}{2}(2b_1^2 + b_2^2 - (k^2+l^2+m^2)c_2) - 3\chi f_1 f_2 &= 0, && (12)\\ f_1\left(\beta(k^2+l^2+m^2)c_4 + \chi f_1^2\right) &= 0, && (13)\\ f_2\left(\beta(k^2+l^2+m^2)c_0 + \chi f_2^2\right) &= 0, && (14) \end{aligned}$$

3. Results

Now we need to classify solutions based on the forms of the functions α and β. For the spherically symmetric form of α, the case where α and β

are constant was covered in Ref. [12], while the case where α and β are sinusoidal was covered in Ref. [13].

Following the notation established in [13], we obtain the following most general results:

$$f_1 = f_{10} p_1 \sqrt{p_2} \exp\left(\int_0^t \gamma dt\right), \qquad f_2 = \epsilon \sqrt{\frac{c_0}{c_4}} f_1, \tag{15}$$

$$k = p_1 k_0, \quad l = p_1 l_0, \quad m = p_2 m_0, \tag{16}$$

$$\omega = \omega_0 - \left((k_0 + l_0) b_{10} q_1 + m_0 b_{20} q_2\right), \tag{17}$$

$$a_2 = p_2 a_{20}, \tag{18}$$

$$b_1 = p_1 b_{10}, \qquad b_2 = p_2 b_{20}, \tag{19}$$

$$e = e_0 + \frac{1}{2}\left((k_0^2 + l_0^2)(c_2 - 6\epsilon\sqrt{c_0 c_4}) - 2b_{10}^2\right) q_1 + \frac{1}{2}\left(m_0^2 (c_2 - 6\epsilon\sqrt{c_0 c_4}) - b_{20}^2\right) q_2, \tag{20}$$

with a different formula for a_1, p_1, p_2, q_1 and q_2 in each case. Here, $\epsilon = 0, \pm 1$ and p_2 corresponds to the chirp function in [10]. The index '0' represents the value of the given parameter at $t = 0$. The results in this section are not for an arbitrary χ, but one subject to an integrability condition:

$$\chi = -\beta(k^2 + l^2 + m^2) c_4 f_1^{-2}. \tag{21}$$

For the case where α and β are constants we obtain the following results:

$$a_1 = \sqrt{\frac{\alpha}{2\beta}} \frac{Ce^{pt} - 1}{Ce^{pt} + 1}, \tag{22}$$

$$p_1 = \frac{e^{pt/2}(1 + C)}{1 + Ce^{pt}}, \quad p_2 = \frac{1}{1 + 2a_{20}\beta t}, \tag{23}$$

$$q_1 = \frac{(1 + C)(e^{pt} - 1)}{p(1 + Ce^{pt})}, \tag{24}$$

$$q_2 = \frac{\beta t}{1 + 2a_{20}\beta t}, \tag{25}$$

where $C = (\sqrt{\frac{\alpha}{2\beta}} + a_{10})/(\sqrt{\frac{\alpha}{2\beta}} - a_{10})$ and $p = 2\sqrt{2\alpha\beta}$.

For the case where α and β are sinusoidal we obtain the following results, i.e. $\alpha(t) = \alpha_0 \cos(\Omega t)$, $\beta(t) = \beta_0 \cos(\Omega t)$ or $\alpha(t) = \alpha_0 \sin(\Omega t)$, $\beta(t) = \beta_0 \sin(\Omega t)$ (in this case, α_0 and β_0 stand for amplitudes, not initial values)

we have the following results:

$$a_1 = \sqrt{\frac{\alpha_0}{2\beta_0}}\tanh(\tau(t)), \tag{26}$$

$$p_1 = \sqrt{\frac{\alpha_0}{\alpha_0 - 2a_{10}^2\beta_0}}\operatorname{sech}(\tau(t)), \quad p_2 = \frac{1}{1 + 2a_{20}\int_0^t \beta(t)dt}, \tag{27}$$

$$q_1 = \frac{\sqrt{\alpha_0\beta_0}}{\sqrt{2}(\alpha_0 - 2a_{10}^2\beta_0)}\tanh(\tau(t)) - \frac{a_0\beta_0}{\alpha_0 - 2a_{10}^2\beta_0}, \tag{28}$$

$$q_2 = \frac{\int_0^t \beta(t)dt}{1 + 2a_{20}\int_0^t \beta(t)dt}, \tag{29}$$

where:

$$\tau(t) = \operatorname{arctanh}\left(a_{10}\sqrt{\frac{2\beta_0}{\alpha_0}}\right) + \sqrt{\frac{2\alpha_0}{\beta_0}}\int_0^t \beta(t)dt. \tag{30}$$

For $\beta(t) = \beta_0\cos(\Omega t)$ we have $\int_0^t \beta(t)dt = \beta_0\frac{\sin(\Omega t)}{\Omega}$ and for $\beta(t) = \beta_0\sin(\Omega t)$ we have $\int_0^t \beta(t)dt = \beta_0\left(\frac{1-\cos(\Omega t)}{\Omega}\right)$.

For this case we can perform a stability analysis similar to one in Section 5 of [16]. The key difference is that now we analyze stability for solitary waves along the z direction as a separate case, and thus have two distinct cases: $k_0 = m_0 = 0$, $l_0 = 1$ and $k_0 = l_0 = 0$, $m_0 = 1$. We also must specify up front whether $k_0 = m_0 = 0$, $l_0 = 1$ or $k_0 = l_0 = 0$, $m_0 = 1$ due to the fact that the formula for χ now contains multiple terms, each with different form of the chirp function. In Eqs. (50) of [16] we must take $p = \sqrt{p_1^2 p_2}$ instead of $p^{3/2}$. For $k_0 = m_0 = 0$, $l_0 = 1$ we must take $p = p_1$ in Eqs. (51)-(54) of [16], while for $k_0 = l_0 = 0$, $m_0 = 1$ we must take $p = p_2$ in Eqs. (51)-(54) in order to obtain the form of the GPE with constant coefficients given in Eq. (55) of [16]. We have thus shown that the same stability analysis given in [16] can also be performed on the solutions in this paper. The detailed calculations pertaining to this analysis are beyond the scope of the paper, but one obtains similar conclusions to those in [16] for the NLSE and GPE with spherical potential (the latter also covered in [13]). In any case, it can be concluded that the solutions in this paper are either unconditionally stable or stable under the regime of dispersion management. Computer simulations were performed on the solutions to the NLSE in [10] and the solutions preserved their shape after long runs.

4. Solutions

In this section we analyze the forms of the obtained solutions. As in [12], the solutions cannot be made to be of stable amplitude unless an external

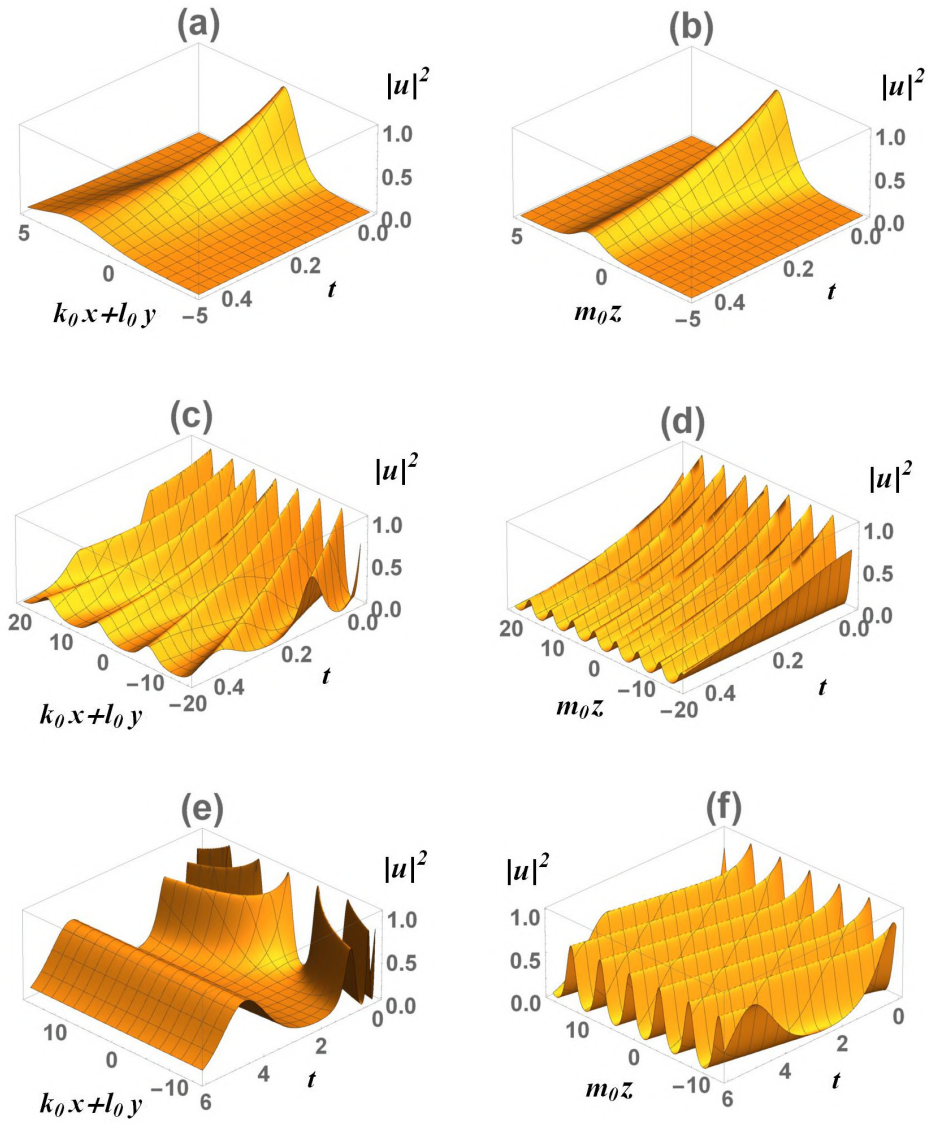

Figure 1: (Color online) Solitary and traveling wave solutions for $F = \mathrm{cn}$ as functions of time for $\alpha = \beta = 1$. Intensity $|u|^2$ is presented as a function of: $k_0x + l_0y$ for (a), (c) and (e) and m_0z for (b), (d) and (f). The main parameters are: (a), (b): $M = 1$, $\gamma = 0$; (c), (d): $M = 0.9$, $\gamma = 0$; (e), (f): $M = 0.9$, $\gamma = p/2$. The other parameters are: $k_0 = l_0 = m_0 = 1$, $a_{10} = 1$, $a_{20} = 0$, $b_{10} = b_{20} = 1$, $\epsilon = 0$ and $\omega_0 = 0$.

gain is added, even in the absence of chirp. Due to the specific form of the function, the dependencies of the function on $k_0x + l_0y$ and m_0z are no longer qualitatively the same, hence these cases must be analyzed and presented separately. The parameters p_1 and p_2 are qualitatively similar for the case of constant α and β, so there is not much of a physical difference apparent when both are present. A more noticeable difference between them occurs when $a_{20} = 0$.

In Fig. (1) we see the results for the case where α and β is constant. We see in Fig. (1)(a) and (b) the difference in the two solitary waves, where we have used $M = 1$ and $F = \mathrm{cn}$. In both plots, the function decays, i.e. spreads out, relatively quickly. The slight rightward bend is due to parameters b_{10} and b_{20} being positive.

In Fig. (1)(c) and (d) we see the difference for traveling wave solutions, i.e. when $M < 1$. We see that in Fig. (1)(c) the wave front spreads out, as is the case in [12], while in Fig. (1)(d) the distance between the traveling waves remains the same.

Finally, in Fig. (1)(e) and (f), we see the effects of adding artificial gain. Unlike in [12], the value of γ for stable solutions is $\gamma = p/2$, due to the change in the number of transverse variables. In order for the stabilization to work, we must have $a_{20} = 0$. In Fig. (1)(e), we see the dramatically different effect in comparison with similar plots in [12]. Instead of a wave front of stable intensity growing wider, we have a radical divergence of initial waves, which are replaced by a giant oscillating wave whose first period can be seen on Fig. (1)(e) and which repeats infinitely. On the other hand, in Fig. (1)(f), we obtain a wave front that doesn't spread out and whose intensity converges to a certain value. The result in Fig. (1)(e) indicates that the artificial addition of gain might not lead to stable solutions in the case of the 2D potential.

In Fig. (2) we see the solutions for $\alpha = \alpha_0 \cos(\Omega t)$ and $\beta = \beta_0 \cos(\Omega t)$, where $\alpha_0 = \beta_0 = \Omega_0 = 1$. We see that the oscillatory solutions resemble those in [13] and, as in Ref. [13], the chirp functions modulate the intensity and the overall shape of the solutions. Here, each form of chirp affects both solutions. This suggest that as in the case of the 3D potential, the dispersion management might be a good approach towards finding stable solutions.

5. Conclusion

To sum up, we have analyzed the problem of the GP equation for the 2D potential, a scenario relevant for practical applications. We have determined that the factors corresponding to the NLSE and the GP equation interact with each other to produce novel and interesting solutions. We established that the artificial gain approach in [12] does not give the same effect as for the 3D potential. We also studied the solutions for the sinusoidal variation of α and β, in other words, the case under dispersion management, and found that as in [13] one obtains stable solutions. Finally, while the

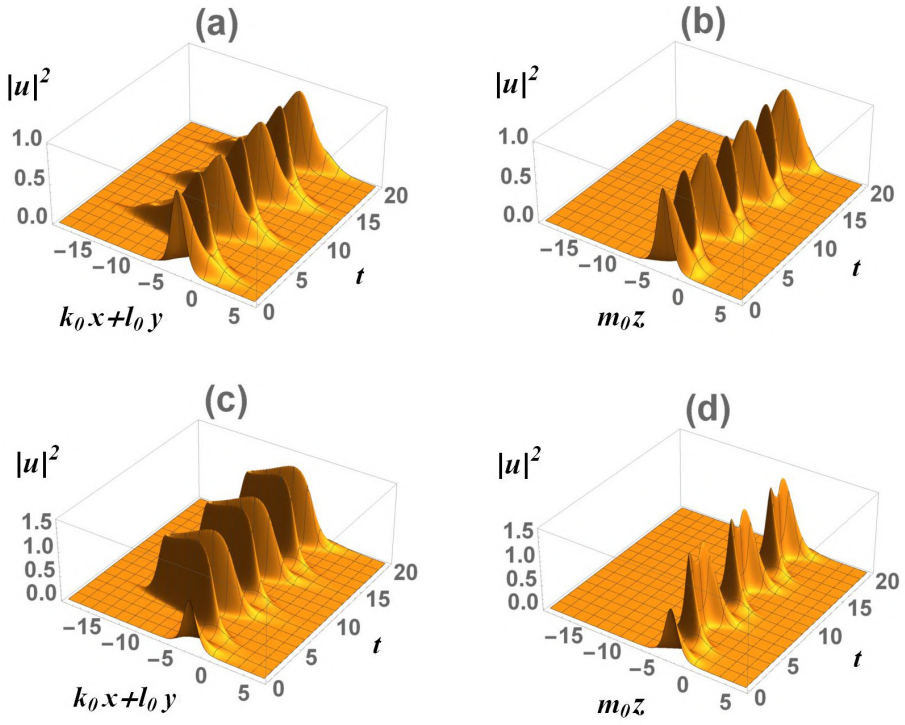

Figure 2: (Color online) Solitary wave solutions for $F = \mathrm{cn}$ as functions of time for $\alpha = \alpha_0 \cos(\Omega t)$ and $\beta = \beta_0 \cos(\Omega t)$, where $\alpha_0 = \beta_0 = \Omega_0 = 1$. Intensity $|u|^2$ is presented as a function of: $k_0 x + l_0 y$ for (a) and (c) and $m_0 z$ for (b) and (d). For (a), (b): $a_{10} = a_{20} = 0$, and for (c), (d): $a_{10} = a_{20} = 0.3$. Other parameters are the same as in Fig. (1)(a).

modulational-stability analysis of these solutions is beyond the scope of this paper, work done in [13] and [16] is strongly indicates that these forms of solutions are also modulationally stable.

References

[1] Dalfovo F *et al.*, *Rev. Mod. Phys.* **71** (1999) 463; L. P. Pitaevskii, and S. Stringari, *Bose-Einstein Condensation,* (Oxford University Press, Oxford, 2003)

[2] Gross E, *Phys. Rev.* **106**(1957) 161

[3] Ginzburg V L and Pitaevskii L P, *Sov. Phys. JETP* **7** (1958) 858 ; Pitaevskii L P, *Zh. Eksp. Teor. Fiz.* **40** (1961) 646 .

[4] Akhmediev N and Ankiewicz A *Solitons* (Chapman and Hall, London, 1997)

[5] Skarka V *et al.*, *Phys. Rev. Lett.* **105** (2010) 213901

[6] Mihalache D *et al.*, *Phys. Rev. A* **82** (2010) 023813

[7] Skarka V *et al.*, *Phys. Rev. A* **90** (2014) 023845

[8] Atre R *et al.*, *Phys. Rev. E* **73** (2006) 056611

[9] Zhong W *et al.*, *Phys. Rev. A* **78** (2008) 023821

[10] Belić M *et al.*, *Phys. Rev. Lett.* **101** (2008) 0123904

[11] Petrović N *et al.*, *Opt. Lett.* **34** (2009) 1609

[12] Petrović N *et al.*, *Phys. Rev. E* **81** (2010) 016610

[13] Petrović N *et al.*, *Phys. Rev. E* **83** (2011) 036609

[14] Eiermann B *et al.*, *Phys. Rev. Lett.* **91** (2003) 060402

[15] Eisenberg S *et al.*, *Phys. Rev. Lett.* **85** (2000) 1863

[16] Petrović N *et al.*, *Opt. Exp.* **23** (2015) 10616

[17] Leblond H *et al.*, *Phys. Rev. E* **76** (2007) 026604

[18] Salasnich L *et al.*, *Phys. Rev. A* **65** (2002) 043614

[19] Zaremba E *Phys. Rev. A* **57** (1998) 518

[20] Burger S *et al.*, *Phys. Rev. Lett.* **83** (1999) 5198

[21] Kivshar Y and Agrawal G, *Optical solitons, from fibers to photonic crystals*, (Academic, New York, 2003)

[22] Hasegawa A and Matsumoto M, *Optical Solitons in Fibers* (Springer, 2003)

[23] Malomed B, *Soliton Management in Periodic Systems* (Springer US, 2006)

[24] Petrović N *et al.*, *Phys. Rev. E* **83** (2011) 026604 .

[25] Hong-Yu W *et al.*, *Commun. Theor. Phys. (Beijing, China)* **54** (2010) 55

[26] Malomed B *et al.*, *J. Opt. B* **7** (2005) R53

[27] Petrović M *et al.*, *Laser & Photonics Reviews* **5** 2 (2009) 214

[28] Chen H *et al.*, *Phys. Rev. Lett.* **37** (1976) 0110693

[29] Li Z *et al.*, *Annals of Physics*, **322** (2007) 2545 (2007)

[30] Li Q *et al.*, *Opt. Comm.* **282** (2009) 1676

[31] Yang Q and Zhang J, *Opt. Comm.* **258** (2006) 35

Reduction methods and travelling wave solutions for nonlinear evolutionary phenomena*

Rodica Cimpoiasu†
University of Craiova, A.I.Cuza 13, Craiova, 200585, Romania

Radu Constantinescu‡
University of Craiova, A.I.Cuza 13, Craiova, 200585, Romania

Gabriel Florian§
University of Craiova, A.I.Cuza 13, Craiova, 200585, Romania

Alina Pauna¶
University of Craiova, A.I.Cuza 13, Craiova, 200585, Romania

Abstract

The paper focuses on two quite different reduction methods used for investigating models of nonlinear dynamics. The first one, the similarity reduction, is obtained through the generalized conditional symmetry approach and consists in a space-time reduction. The second approach generates a reduction of the differentiability order and is achieved by a change of variable. The first method is more general, appropriate for investigating the integrability, too, while the second method is very effective in generating classes of solutions for the model. How the two methods are functioning will be illustrated by applying them on the generalized Boussinesq equation, a mathematical model used for describing the propagation of the nerve pulses through biomembranes. The solutions of the investigated equation generated through the two reduction methods are compared and interpreted from the perspective of traveling waves.

Keywords: reductions techniques, travelling waves, generalized conditional symmetry, attached flow, generalized Boussinesq equation.

* Part of the authors acknowledges the support given by ICTP, through the grant offered to SEENET–MTP, in the frame of the Network Programme (NT–03).

† e-mail rodica.cimpoiasu@edu.ucv.ro

‡ e-mail address: rconsta@ucv.ro

§ e-mail address: gabiflorian@gmail.com

¶ e-mail address: alina.pauna@edu.ucv.ro

1. Introduction

Despite that nonlinearity is the most widespread behavior in the natural world, the investigation of nonlinear phenomena is far from coming to an end. Neither physics nor the other scientific fields dealing with nonlinear evolutionary processes offer complete theories about this important category of phenomena or, more precisely, have not formulated a general approach to study the equations modeling nonlinear evolutionary processes. They are mainly described by nonlinear differential equations and there are no clear algorithms for solving these equations. Moreover, the complexity of the nonlinear phenomenology asks for complicated mathematical models, with higher degrees both in nonlinearity and in the differentiability order. Faced with rather complex equations, scientists must give two fundamental answers: are the equations integrable and, if so, how can they be solved? The integrability of equations is a problem in itself, but solving them becomes an even more challenging task [1]. The key word seems to be "*reduction*". The equations must be reduced, both in terms of the order of differentiability and of the space (number of degrees of freedom) in which evolution takes place. The presentation of two methods by which such reductions can be obtained in a consistent way, and how they can be used for solving nonlinear differential equations are the main purposes of this paper.

As we mentioned, a first step in approaching the nonlinear phenomena consists in investigating the integrability of the differential equations describing them. There are many methods allowing a conclusion on this issue, as for example: the inverse scattering [2], the Hirota bilinear method [3], applied both as symmetric and as supersymmetric formalisms [4, 5, 6], the Lax pair operators [7], or the Lie symmetry theory [8, 9]. After having an answer to the question if and when an equation is integrable, the next step consists in solving it. Unlike the linear differential equations, the nonlinear equations do not have a single general solution, but can admit several classes that depend on the values of the parameters appearing in the equation, as well as on the initial conditions. Finding possible classes of solutions is essential in a better understanding of the phenomena. Such an important class is represented by the so-called traveling wave solutions. They can be accepted by a large class of nonlinear partial differential equations (NPDEs), but there does not exist a single and clear algorithm for finding them. Many methods have been proposed in the literature. Part of them, as for example: the tanh method [10], the tanh-coth method [11], the F-expansion method [12], the exp-function method [13], are direct solving methods. Other approaches ask for intermediate tools, as for example auxiliary equations with known solutions. This second category includes methods such as: the elliptic function method [14], the extended trial equation method [15], the functional expansion [16, 17], etc. More sophisticated and rigorous techniques use the BRST technique defined on cohomological structures [18, 19], and they are very efficient when constrained dynamical

systems are concerned [20]. Combined investigations, targeting the integrability but also the finding of solutions are offered by approaches based on dressing method [21], on imposing specific integrability conditions [22], or on symmetry group [23].

This paper will refer to two of the mentioned approaches for getting reduced equations and finding traveling wave solutions. The first one is the *generalized conditional symmetry* (GCS) [24, 25], a version of the group symmetry method providing the invariant solutions of equations on the base of the similarity reduction. The second approach is a direct solving method consisting in a reduction, too. The similarity reduction diminishes the space-time dimension, while this last procedure reduces the differentiability order of the investigated equation. More specifically, the second approach tackled here is a quite classical method recommended for solving autonomous ordinary differential equations (ODEs) that is supposed to define the derivative of the unknown variable as a new independent variable [26]. Due to the fact that this change of variable is expressed by an equation similar to the one that expresses the flow attached to dynamical systems, we call the method the *attached flow method*. Despite its apparent simplicity, the method sometimes leads to unsolvable or difficult to solve equations. Our contribution is related exactly to how to deal with such situations and how to use the method for solving important equations.

The equation we chose as a toy model in this paper is the generalized Boussinesq equation (GBE), important due to its application in describing waves in shallow water, but also the propagation of nerve pulses through biomembranes. Our aims are to show how the equation can be solved through this direct method and to compare those got through other approaches. Results related to the soliton propagation through biomembranes were reported in [27] and in other papers. The equation was also investigated from the perspective of its symmetries, in paper as [28] and [29]. The GCS method was also applied to GBE in [30]. In fact, the results obtained in this last paper will be considered as a reference and they will be compared with what we will get by the attached flow method.

The paper is structured as follows: after this section of Introduction, in section 2 we will present the generalized Boussinesq equation as a model of nerve pulse propagation; section 3 will review the main results from the paper [30], with focus on the GBE invariant solutions; section 4 will contain the novelty this paper is bringing: GBE will be solved through the attached flow approach and the solutions will be compared with those presented in the previous section. Some concluding remarks will end the paper.

2. The Generalized Boussinesq Equation and nerve pulse propagation

The Generalized Boussinesq Equation (GBE) was first formulated in order to describe the waves generated in shallow waters. Later on the specialists have realized that the equation can also model neural activity, in the

sense that the propagation of nerve flow can be assimilated with the sound propagation in biomembranes [27]. The propagation generates significant changes of the membrane's density, and the elastic constants become sensitive functions of density. If we consider the one-dimensional propagation, along the axis Ox, and we denote by $\Delta\rho$ the variation of the density, the suitable equation has the form:

$$\frac{\partial^2\Delta\rho}{\partial t^2} = \frac{\partial}{\partial x}\left(c^2(\Delta\rho)\frac{\partial\Delta\rho}{\partial x}\right) - h\frac{\partial^4\Delta\rho}{\partial x^4} \tag{1}$$

In the previous relation c^2 represents the square of the pulse velocity in the membrane and the notation $c^2(\Delta\rho)$ express its dependency of the density variation. The last term in (1) , proportional with the fourth-order derivative of the density variation, describes the dispersion that accompanies the propagation and that makes possible soliton-type solutions. With simplified notation, the previous equation can be rewritten as:

$$\frac{\partial^2 u}{\partial t^2} = \frac{\partial}{\partial x}(A(u)\frac{\partial u}{\partial x}) - h\frac{\partial^4 u}{\partial x^4} \tag{2}$$

By making few computations, and putting $A'(u)$ as the derivative in respect to u, we get:

$$u_{2t} - A'(u)u_x^2 - A(u)u_{2x} + hu_{4x} = 0 \tag{3}$$

It is a fourth order partial differential equation with variable coefficients, known as the Generalized Boussinesq Equation. We remember that $A(u)$ denotes the square of the pulse velocity. If, in the first approximation, we consider $A(u) = c_0^2 = const.$, $A'(u) = 0$, we get the case of waves propagating with the constant velocity c_0. The usual Boussinesq equation is obtained in the case when $Au)$ has a linear dependency on u: $A(u) = c_0^2 + \beta u$, and $A'(u) = \beta = const.$ In [30] it was considered the case of a quadratic dependency:

$$c^2(u) \equiv A(u) = \alpha u^2 + \beta u + c_0^2. \tag{4}$$

The parameters α, β describe the nonlinear elastic properties of the membrane. The case $\alpha = 0$ brings us back to the already known Boussinesq equation.

3. Symmetry reduction and Invariant solutions for the generalized Boussinesq equation

3.1. The generalized conditional symmetry method

The generalized conditional symmetries represent an extension of the classical Lie-type symmetries. The symmetry generators can include now derivatives of the dependent variable. Let us consider a general (1+1)-dimensional

partial differential equation of the form (3), to which we attach the vector field X and its prolongation of order n:

$$X = \eta(t, x, u, u_x, u_{2x}, ...)\frac{\partial}{\partial u} \tag{5}$$

$$\widetilde{X}^{(n)} = \sum_{k=0}^{n} D_x^k \eta \frac{\partial}{\partial u_{kx}} + D_t \eta \frac{\partial}{\partial u_t} + D_t^2 \eta \frac{\partial}{\partial u_{2t}}, \tag{6}$$

As (3) is a 4-order differential equation, we say that (5) is a Lie–Bäcklund symmetry for it if:

$$\widetilde{X}^{(4)}[u_{2t} - A'(u)u_x^2 - A(u)u_{2x} + hu_{4x}]\,|_L = 0,$$

where L is the set of all the differential consequences of the concerned equation. The vector field (5) is said to be a GCS of Eq. (3) if

$$\widetilde{X}^{(4)}[u_{2t} - A'(u)u_x^2 - A(u)u_{2x} + hu_{4x}]\,|_{L\cap M} = 0, \tag{7}$$

where M denotes the manifold defined by the set of all the differential consequences of the equation $\eta = 0$, that is to say:

$$D_t^\mu D_x^\nu \eta = 0,\ \mu + \nu \leq m. \tag{8}$$

These general definitions can be used for finding the generalized conditional symmetry operators of the Eq. (3) and for generating invariant solutions for the model. A few of the results presented there will be reviewed in the next subsection and will be compared with what we will get through the attached flow method in section 4 from below.

3.2. Invariant solutions for pulse velocities depending on the density variation

As we have announced, we will review now the main invariant solutions obtained in [30], when the equation (3) was investigated using the generalized conditional symmetry (GCS) technique. Four cases that differ in how the propagation velocity depends on the variation of the membrane density will be considered:

Case 1. For $A(u) = c_0^2 = const.$, one of the possible Lie symmetry operator generated by imposing the GCS requirements is:

$$X_1 = (u_{2x} - p)\,\frac{\partial}{\partial u}. \tag{9}$$

The corresponding solution for (3) is in fact a 5-parameter family of solutions, described by the parameters $p,\ q_j,\ j = \overline{1,4}$ and with the expression:

$$u_1(t, x) = \frac{p}{2}x^2 + (q_1 t + q_2)x + \frac{p}{2}c_0^2\ t^2 + q_3 t + q_4. \tag{10}$$

Case 2. Again for $A(u) = c_0^2 = const.$, another possible symmetry operator is:

$$X_2 = [u_{2x} - ku_x - p]\,\frac{\partial}{\partial u}. \tag{11}$$

The reduced equation arising from (3) in this case accepts the following 8-parameters family of periodic solutions, defined by the arbitrary constants p, h, k, c_0, (with $hk^2 \rangle\, c_0^2 \,\rangle\, 0$), and r_i, $i = \overline{1,4}$:

$$u_2(t,x) = r_1 t + r_2 + \frac{r_3 \sin\left[k\sqrt{hk^2 - c_0^2}\ t\right] + r_4 \cos\left[k\sqrt{hk^2 - c_0^2}\ t\right]}{k} e^{kx} - \frac{p}{k}x. \tag{12}$$

Case 3. A more general symmetry operator corresponding to the same case, when $A(u) = c_0^2 = const.$, has the form:

$$X_3 = [u_{2x} - ku_x - mu - p]\,\frac{\partial}{\partial u}. \tag{13}$$

Solving the invariance surface condition, that in this case has the form $\eta = u_{2x} - ku_x - mu - p = 0$, many solutions of the reduced GBE can be generated. We mention here only two of them:

$$\begin{aligned} u_{31}(t,x) = -\frac{p}{m} + \varphi(t) \exp\left[\left(\frac{k + \sqrt{k^2 + 4m}}{2}\right)x\right] \\ + \psi(t) \exp\left[\left(\frac{k - \sqrt{k^2 + 4m}}{2}\right)x\right], \end{aligned} \tag{14}$$

$$\begin{aligned} u_{32}(t,x) = -\frac{p}{m}. + \left[\mu \exp\left(i\sqrt{M}t\right) + \nu \exp\left(-i\sqrt{M}t\right)\right] \\ \exp\left[\left(\frac{k - \sqrt{k^2 + 4m}}{2}\right)x\right]. \end{aligned} \tag{15}$$

Depending of the values of the parameters p, m, k, and, respectively, p, m, M, μ, ν, these general solutions lead to periodic or hyperbolic solutions of (3).

Case 4. Consider now that $A(u)$ is quadratic, of the form given by (4). The symmetry operators from the previous case take now simpler expressions, and, as a result, the GBE solutions will become simpler. For example, the operator X_1 takes in this case the form:

$$X_4 = u_{2x}\frac{\partial}{\partial u}. \tag{16}$$

The 5-parameters family of solutions from the Case 1 takes now the form:

$$u_4(t,x) = \pm\frac{\sqrt{2}}{\sqrt{a}(t - n_1)}x + n_2(t - n_1)^2 - \frac{bt}{a(t - n_1)} + \frac{n_3}{(t - n_1)}. \tag{17}$$

3.3. Traveling waves with the auxiliary equation technique

Obtaining traveling wave solutions for a $(1+1)$-dimensional PDE supposes a standard algorithm with two steps: (i) reducing the PDE to an ODE, by introducing the wave variable $\xi \equiv x - vt$; (ii) solving the reduced equation by an adequate method, as we mentioned in Introduction. For (3) the algorithm leads to the following:

(i) Denoting by $U(\xi)$ the new variable and by $U' = dU/d\xi$, the resulting ODE will take the form:

$$(A(U) + v^2)U'' + A'_U(U)\ (U')^2 - hU^{(4)} = 0. \tag{18}$$

(ii) If we consider, as second step, the auxiliary equation technique, the simplest choice is to use the Riccati equation:

$$G' = \beta G + \delta G^2, \tag{19}$$

which accepts a solution of the form:

$$G(\xi) = \pm \frac{\beta \exp(\beta\xi)}{1 \mp \delta \exp(\beta\xi)} \tag{20}$$

A specific balancing procedure shows that the solution of (18) can be expressed in terms of the Riccati solutions $G(\xi)$ in the form:

$$U(\xi) = k_0 + k_1 G(\xi)$$

Let us supplementary suppose that we look to solutions of (18) in the form of low-amplitude waves with the frequency ω,propagating with a velocity v which depends on the frequency as:

$$v^2 \approx c_0^2 + \frac{h\omega^2}{c_0^2}. \tag{21}$$

Combining all these relations, we find that, for real parameters a, b, h, β, δ, possible solutions of GBE (18) have the form:

$$U(\xi) = \frac{-b \pm \beta\sqrt{6ah}}{2a} \pm \frac{\delta\sqrt{6ah}}{a} \frac{\beta \exp(\beta\xi)}{1 \mp \delta \exp(\beta\xi)} \tag{22}$$

Similar solutions will be generated in the next section, using the more simple and direct approach of the attached flow.

4. The reduction method through attached flows

4.1. What attached flow means?

We mentioned above the two steps algorithm allowing us to find traveling wave solutions for nonlinear PDEs as the generalized Boussinesq equation is. Moreover, we effectively followed the algorithm and, after the first step, we got the reduced equation (18). For the second step, we applied the auxiliary equation technique and we get a general form of the traveling wave solutions as (22). Now, we want to see if using auxiliary equations or other auxiliary tools is the only way to solve the equation. A specific possibility of direct solving an autonomous ODE, as it is the case of (18), mentioned in almost all mathematics textbooks as for example in [26], consists in the reduction of the differentiability order by considering the first derivative of the unknown variable as a new independent variable. In our case we should define:

$$U'(\xi) = V(U). \tag{23}$$

The initial equation in $U(\xi)$ turns into a system consisting of equation (23) and a new differential equation, with the unknown $V(U)$ and the order of differentiation reduced by one unit. We should find $V(U)$ solving this new equation, and, then, find $U(\xi)$ solution of (23). As this equation suggests the flow equation attached to the dynamical systems, we proposed to call this solving method the attached flow method.

Despite the apparent simplicity of the procedure, it seems that system integration is not always easy, usually the reduced equation falling, it too, into the class of equations difficult to solve. Additional considerations and improvements are needed. Here are our contributions, in establishing, after an exhaustive investigation, of "go" or "not go" rules and special algorithms to be followed in each specific case. We do not insist too much on the theoretical aspects here, focusing instead on illustrating how the method can be effectively applied to solve the GBE equation. The two cases that we analyzed in the previous section will be addressed here as well. It is about the case when the propagation of the neural flow is done with constant velocity, c_0, and the case when there is a quadratic dependence on the density variation, as described by the relation (4).

4.2. Attached flow for the Boussinesq equation

As we mentioned in section 2, the usual Boussinesq equation is obtained from (3) in the case when we consider that the square of velocity depends linearly from the variation of density. This means that we have to consider:

$$\alpha = 0 \Rightarrow A(u) = c_0^2 + \beta u;\ A'(u) = \beta.$$

The equation (3) takes the form:

$$u_{2t} - \beta u_x^2 - (c_0^2 + \beta\, \mathrm{u})u_{2x} - h u_{4x} = 0 \tag{24}$$

The ODE resulting when the wave variable is used in (24) can be integrated twice and leads to the following second order ODE:

$$hU'' + \frac{\beta}{2}U^2 + (c_0^2 - v^2)U = 0 \tag{25}$$

It is here where the attached flow appears. By considering that $U' = V(U)$, we obtain a new, first order, equation for V:

$$hV(U)V'(U) + \frac{\beta}{2}U^2 + (c_0^2 - v^2)U = 0 \tag{26}$$

This equation can be integrated and leads to:

$$V(U) = \pm\frac{\sqrt{-3hU[\beta U + 3(c_0^2 - v^2)]}}{3h} \tag{27}$$

Coming back to the flow equation (23), by integration we get the traveling wave solution of Boussinesq equation:

$$U(\xi) = -\frac{3\left(c_0^2 - v^2\right)}{\beta\cosh\left(\frac{\xi\sqrt{-h\left(c_0^2 - v^2\right)}}{2h}\right)} \tag{28}$$

The corresponding solution expressed in the initial (1+1)-dimensional space will have the form:

$$u(x,t) = -\frac{3\left(c_0^2 - v^2\right)}{\beta\cosh\left(\frac{(x-vt)\sqrt{-h\left(c_0^2 - v^2\right)}}{2h}\right)} \tag{29}$$

4.3. Attached flow for the generalized Boussinesq equation

We consider now the general case, when $A(u)$ is quadratic as in the relation (4). The equation (3) becomes:

$$u_{2t} - (2\alpha u + \beta)u_x^2 - (\alpha u^2 + \beta u + c_0^2)u_{2x} - hu_{4x} = 0 \tag{30}$$

Using the wave transformation and adopting the notation $u(x,t) = U(\xi)$, the above equation becomes:

$$\left(\alpha U^2 + \beta U + c_0^2 - v^2\right)U'' + (2\alpha U + \beta)U'^2 + hU^{(4)} = 0 \tag{31}$$

By integrating twice with respect to ξ, we will get the following second order equation:

$$hU'' + \frac{\alpha}{3}U^3 + \frac{\beta}{2}U^2 + (c_0^2 - v^2)U = 0 \tag{32}$$

Now, using the flow equation, $U' = V(U)$, we obtain the reduced equation for the new variable V:

$$hV(U)\frac{dV(U)}{dU} + \frac{\alpha}{3}U^3 + \frac{\beta}{2}U^2 + (c_0^2 - v^2)U = 0 \tag{33}$$

By chance, (33) can be integrated and gives the solutions:

$$V(U) = \pm\frac{\sqrt{-6hU[\alpha U^2 + 2\beta U + (c_0^2 - v^2)]}}{6h} \tag{34}$$

Considering these solutions for $V(U)$, we integrate (23) and we get the solution U of the ODE:

$$U(\xi) = \frac{144h(c_0^2 - v^2)(\cosh B + \sinh B)}{(24h\beta + 1)(\cosh B + \sinh B) + 144h^2[\beta^2 - 6\alpha(c_0^2 - v^2)]} \tag{35}$$

where

$$B = \frac{\xi\sqrt{-h(c_0^2 - v^2)}}{h}. \tag{36}$$

5. Concluding remarks

The complexity of the nonlinear evolutionary phenomena asks for the formulation of increasingly complex mathematical models and requires the processing of increasingly complicated equations. To deal with these models, to check the integrability and solvency of the equations that describe them, there is, as a way out, the use of various reductions and simplifications methods. All these have to be consistent, in the sense that the reduced equations must retain all the dynamic characteristics of the initial model. Two types of reductions are essential: (i) reducing the number of independent variables, leading from PDEs to ODEs, equations easier to solve, and (ii) reducing the order of differentiation of equations, which also facilitates their solving. The present paper considers these two reductions in relation to the generalized Boussinesq equation (3), a 4-order PDE defined in the (1+1)-dimensional space-time. Its reduction to an ODE can be obtained directly, by the use of the wave variable, when traveling waves are the only solutions we look for, or it can be achieved through a more general approach based on the symmetry group theory. This approach allows, on the one hand to determine the invariants and to decide on the integrability, and on the other hand to generate solutions of the investigated equations that do not belong to the class of traveling waves. We applied here the generalized conditional symmetry approach and, starting from a few symmetry operators, we generated non-traveling wave solutions, as for example the solutions (10) and (12). When, in section 3.3, the space-time reduction was obtained with the wave variable, and the auxiliary equation method was used to solve the ODE, the solution obtained, (22), was of the traveling

wave type. It was expressed through exponentials, and, depending on the parameters from the equation, can become periodic, hyperbolic or rational solutions.

Quite similar solutions were generated in section 4 of the paper, when the ODE generated by the use of the wave variable was solved directly, using a sort of constraint, the flow equation (23). The presentation of this approach was important due to the fact that, despite its simplicity and almost unanimous consideration in mathematical textbooks, the actual application is not always very direct and requires case-by-case analysis. In the GBE case for example, the reduction generated by the attached flow led to the Abel-type equations, (26) and (33), whose solving sometimes raises problems.Here we pointed out that, fortunately, both classical and generalized Boussinesq equations could be fully integrated, and the solutions obtained are compatible with the solutions of the same equations, generated by alternative methods. For example, the solution (35), up to the level of constants, has the same mathematical form as the solution (22), generated somewhat more complicatedly, using Riccati as an auxiliary equation. As a conclusion, given the simplicity and efficiency of the attached flow method, we believe that it deserves a closer investigation to which we have committed ourselves. The results will be presented in forthcoming papers.

References

[1] E. Fan, *J. Phys. A: Math. Gen.* **36** (2003), 7009.

[2] M. J. Ablowitz and P.A. Clarkson, *Solitons, Nonlinear Evolution Equations and Inverse Scattering*, Cambridge University Press, 1991.

[3] J. Hietarinta, *Physics AUC*, **15** (1) (2005), 31.

[4] C. N. Babalic, Rom. J. Phys. **63** (2018) 114.

[5] C. N. Babalic and A. S. Carstea, J. Phys. A: Math. Theor. **51** (2018) 225204.

[6] C. N. Babalic, Int. J. Mod. Phys. B, **34**(29), (2020) 2050274.

[7] W. X. Ma and W. Strampp, Phys. Lett. A **1**85(3) (1994) 277.

[8] G. W. Bluman and S. Kumei, *Symmetries and Differential Equations*, Springer, New York, 1989.

[9] N. K. Ibragimov, *Transformation Groups Applied to Mathematical Physics*, Boston, Reidel, 1985.

[10] W. Malfliet, *Am. J. Phys.*, **60** (1992), 650.

[11] A.M. Wazwaz, *Appl. Math. Comput.*, **188** (2007), 1467.

[12] M.L. Wang and X.Z. Li, *Chaos Solitons Fractals*, **24** (2005), 1257.

[13] J.H. He and X. H. Wu, *Chaos Solitons Fractals,* **30** (2006), 700.

[14] S. Liu, Z. Fu, S. Liu and Q. Zhao, *Phys. Lett. A*, **289** (2001), 69.

[15] R. Cimpoiasu and A. S Pauna, *Open Phys.* **16** (2018), 419.

[16] R.Constantinescu, C. Ionescu and M. Stoicescu, *J. Appl. Anal. Comput.*, **10**(2) (2020), 569.

[17] R. Constantinescu and A. Florian, *Symmetry* **12**(11) (2020) 1819.

[18] M.Henneaux and C.Teitelboim, *Quantization of gauge systems*, Princeton University Press, 1992.

[19] R.Constantinescu, *J. Math. Phys.* **38** (1997) 2786

[20] A. Babalean, R. Constantinescu and C. Ionescu, J.Phys A-Math Gen., **31**(43) (1998), 8653.

[21] C. N. Babalic, R. Constantinescu and V. S. Gerdjikov, *J. Geom. and Symm. in Phys.* **37** (2015), 1.

[22] T. Harko and M. K. Mak, *J.Math.Phys.* **56** (2015), 111501.

[23] R. Cimpoiasu, V. Cimpoiasu and R. Constantinescu, *Rom. J. Phys.* **55** (1-2) (2010), 25.

[24] M. Kunzinger, Michael and R. O. Popovych, *J. Math. Anal. Appl.* **379** (2011), 444

[25] R.Constantinescu, *Rom. J. Phys.* **61** (2016), 77.

[26] A. D. Polyanin and V. F. Zaitsev, *Handbook of Exact Solutions for Ordinary Differential Equations*, 2nd ed., Chapman & Hall/CRC Press, Boca Raton, 2003.

[27] T. Heimburg and A. D. Jackson, *Proc. Natl. Acad. Sci. USA* 102 (2005), 9790.

[28] Q.M. Liu and A.S. Fokas, *J. Math. Phys.* **37** (1996), 3241.

[29] P. A. Clarkson and M. D. Kruskal, *J. Math. Phys.* **30** (1989), 2201.

[30] R.Cimpoiasu, *Int. J. Biomath*, **09** (05) (2016), 1650075.

On p-adic scalar matter[*†]

Branko Dragovich[‡]
Institute of Physics, Pregrevica 118, Belgrade, Serbia

Mathematical Institute, Serbian Academy of Sciences and Arts,
Belgrade, Serbia

I dedicate this article to my friends and colleagues Igor V. Volovich and Irina Ya. Aref'eva, corresponding members of the Russian Academy of Sciences and foreign members of the Serbian Academy of Nonlinear Sciences, with whom I started my research in p-adic string theory, and on the occasion of their 75th birthday in 2021.

Abstract

In this paper, we consider a new type of scalar matter that could have its origin in p-adic strings, i.e., strings with a p-adic world-sheet. In particular, we explore some cosmological properties of this p-adic matter. We start with crossing symmetric scattering amplitudes for p-adic open strings and proceed with related effective nonlocal Lagrangian which describes dynamics of the corresponding tachyon at the tree level. Then, we make a slight modification of this Lagrangian to obtain a new Lagrangian for non-tachyonic scalar field. Using this new Lagrangian in the weak field approximation as a matter sector in Einstein gravity with the cosmological constant, one obtains an exponentially expanding FLRW closed universe. Also one obtains the connection between mass of this scalar particle, the cosmological constant and prime numbers. For small prime numbers, mass $m = \sqrt{\frac{\Lambda}{3}} \sim 10^{-66}$g. At the end, we discuss the obtained results, and conjecture that this scalar particle can be a candidate for dark energy and dark matter.

1. Introduction

Recall that p-adic numbers were discovered by K. Hansel in 1897. Their first use in modeling physical systems was started by I. V. Volovich [2] in 1987,

[*] Written on the basis of a lecture given at the 2nd Conference on Nonlinearity (Belgrade, 18–22.10.2021) and article [1].

[†] **Citation**: B. Dragovich, On p-adic scalar matter, *Proceedings of the 2nd Conference on Nonlinearity*, pp. 280–296 (Serbian Academy of Nonlinear Sciences, Belgrade, Serbia, 2022).

[‡] e-mail address: dragovich@ipb.ac.rs

when he was constructed some string scattering amplitudes, see also [3]. This was the beginning in p-adic string theory and also in many other parts of modern mathematical physics — now known as *p-adic mathematical physics*. As reviews, we refer to [4, 5, 6, 7].

Note that classical theoretical physics and quantum theory use mathematical methods based on real and complex numbers, respectively. Quantum mechanics combined with general relativity predicts the Planck length as the smallest one that can be measured [5]. This practically means breakdown of the Archimedean axiom and the problem with employment of real and complex numbers at the Planck scale. Thus, the following question arises: are there some other numbers that could be relevant when approaching to the Planck scale? A possible answer could be related to Volovich's hypothesis [8] which assumes that space–time, at very short distances, may be non-Archimedean and p-adic numbers should play some significant role. Then string worldsheet may be not only real but also p-adic. Replacing the real worldsheet by its analog with p-adic numbers some new string amplitudes where constructed. Strings with p-adic-valued worldsheet are called *p-adic strings*.

The mainstream in p-adic string theory was along an effective Lagrangian [9, 10] for the scalar field, that describes all scattering amplitudes on the tree level, see [4, 5, 6, 7] as a review. This Lagrangian does not contain p-adic ingredients, but only real terms. Hence there is no need to know and use p-adic analysis, what simplifies further elaboration of p-adic string theory. The Lagrangian (10) is exact at the tree level and contains a scalar tachyon field with a nonlocal kinetic term and nonlinear potential. The research presented in this paper is based on this effective Lagrangian.

As one of the several connections of p-adic strings with ordinary strings is an adelic product formula of ordinary and p-adic crossing symmetric Veneziano amplitudes [13, 14] (see next section). Despite interesting connections, p-adic strings have been mainly treated as auxiliary ones with respect to ordinary strings. Since there is belief that ordinary matter has its origin in ordinary strings, then why p-adic strings could not generate p-adic matter? In this paper, we consider how non-tachyonic matter can be obtained from Lagrangian for p-adic tachyons and demonstrate that this new matter makes sense.

This article is organized as follows. In Section 2, some basic facts about p-adic numbers, adeles, scattering amplitudes of open p-adic strings and an effective nonlocal Lagrangian with the corresponding equation of motion are presented. Section 3 is devoted to the Lagrangian for p-adic strings which is slightly modified to obtain the well-defined new one. The dynamics of p-adic scalar particles is considered in weak field approximation and a cosmological solution is found and presented in the case of a closed universe fulfilled by p-adic matter with the cosmological constant. Some concluding remarks are the subject of Section 4.

2. On mathematical background and p-adic strings

To have this article comprehensive and self-contained, we are now recalling some basic facts about p-adic numbers, adeles, their functions and p-adic strings.

2.1. p-Adic numbers, adeles and their functions

For those who are not familiar with p-adic numbers, adeles and their functions, here are some basic introductory facts. To this end, it is useful to start with the field of rational numbers $\mathbb{Q}$, since $\mathbb{Q}$ is important from a physical and mathematical point of view. In physics, all numerical results of measurements are rational numbers. In mathematics, $\mathbb{Q}$ is a simple infinite number field. For a given prime number p, any non-zero rational number x can be presented as $x = \frac{a}{b}p^{\nu}$, where $a, \nu \in \mathbb{Z}$ and $b \in \mathbb{N}$, also a and b are not divisible by p. Then, by definition, the p-adic norm (also called p-adic absolute value) is $|x|_p = p^{-\nu}$ and $|0|_p = 0$. One can easily show that $|a|_p \leq 1$, for any $a \in \mathbb{Z}$ and any prime p. From the above definition, it follows the strong triangle inequality $|x+y|_p \leq \max\{|x|_p, |y|_p\}$, i.e., the p-adic norm is an example of ultrametric (non-Archimedean) norm. The p-adic distance between $x, y \in \mathbb{Q}$ is $d_p(x,y) = |x-y|_p$. In the same manner, as the field $\mathbb{R}$ of real numbers obtains from $\mathbb{Q}$ by completion with respect to the real distance $d(x,y) = |x-y|$, so the completion of $\mathbb{Q}$ using a p-adic distance gives the field $\mathbb{Q}_p$ of p-adic numbers, for any prime number p.

Any non-zero p-adic number $0 \neq x \in \mathbb{Q}_p$ has unique representation in the following form:

$$x = p^{\nu}\big(x_0 + x_1 p + x_2 p^2 + ...\big), \quad \nu \in \mathbb{Z}, \quad x_0 \neq 0, \quad x_n \in \{0, 1, ..., p-1\}, \tag{1}$$

where x_n are digits. For instance, $-1 = p - 1 + (p-1)p + (p-1)p^2 + ...$ for any given prime number p.

There are mainly two kinds of functions with p-adic argument, (i) p-adic-valued functions and (ii) complex-valued functions. For example, p-adic-valued elementary functions are defined by the same power series as in the real case, but their convergence is subject to the p-adic distance. There are three typical complex-valued functions of the p-adic argument x:

- multiplicative character: $\pi_p(x) = |x|_p^c, \quad c \in \mathbb{C}$;
- additive character: $\chi_p(x) = \exp(2\pi i\{x\}_p)$, where $\{x\}_p$ is a fractional part of x;
- characteristic function: $\Omega(|x|_p) = \begin{cases} 1 & \text{if} \quad |x|_p \leq 1, \\ 0 & \text{if} \quad |x|_p > 1. \end{cases}$

There is a well-defined integration of complex-valued functions with the Haar measure, see [5]. For example, $\int_{|x|_p \leq 1} |x|_p^{a-1} = \frac{1-p^{-1}}{1-p^{-a}}$, where x is a p-adic variable and a is a complex number, with $\Re a > 0$.

According to the Ostrowski theorem, real and p-adic numbers are all possible numbers that can be obtained by completion of $\mathbb{Q}$ with respect to any nontrivial norm on $\mathbb{Q}$. $\mathbb{Q}$ is a common subfield of $\mathbb{R}$ and all $\mathbb{Q}_p$.

Adeles are a concept that takes together real and p-adic numbers. By definition, an adele is the following infinite sequence:

$$\alpha = (\alpha_\infty, \alpha_2, \alpha_3, ..., \alpha_p, ...), \tag{2}$$

where $\alpha_\infty \in \mathbb{Q}_\infty \equiv \mathbb{R}$ and, for all but a finite set $\mathcal{P}$ of primes p, it must be satisfied that $x_p \in \mathbb{Z}_p \equiv \{x \in \mathbb{Q}_p : |x|_p \leq 1\}$. $\mathbb{Z}_p$ is called a ring of p-adic integers. The set $A_\mathbb{Q}$ of all adeles over $\mathbb{Q}$ can be defined as

$$A_\mathbb{Q} = \bigcup_{\mathcal{P}} \mathcal{A}(\mathcal{P}), \quad \mathcal{A}(\mathcal{P}) = \mathbb{R} \times \prod_{p \in \mathcal{P}} \mathbb{Q}_p \times \prod_{p \notin \mathcal{P}} \mathbb{Z}_p. \tag{3}$$

$A_\mathbb{Q}$ is called an adele ring, since it satisfies component-wise addition and multiplication. Note that the components of an adele can be a rational numbers; thus, $\mathbb{Q}$ is naturally embedded in $A_\mathbb{Q}$. Hence, adeles can be viewed as a generalization of rational numbers that takes simultaneously into consideration all their completions.

There are many useful adelic product formulas which connect real and all p-adic constructions of the same form; e.g., see [5]. Some simple cases are:

- $\pi_\infty(x) \prod_p \pi_p(x) = |x| \prod_p |x|_p = 1 \ , \quad 0 \neq x \in \mathbb{Q}$;
- $\chi_\infty(x) \prod_p \chi_p(x) = e^{-2\pi i x} \prod_p e^{2\pi i \{x\}_p} = 1, \quad x \in \mathbb{Q}$.

In the next subsection, we present adelic product formulas for string amplitudes.

Above, some very basic properties of p-adic numbers and adeles are presented. For more information, we refer to books [5, 15, 16].

2.2. p-Adic open string amplitudes

Note that string theory started with the Veneziano amplitude. By definition, the crossing symmetric Veneziano amplitude for the scattering of two ordinary open strings is

$$A_\infty(a,b) = g_\infty^2 \int_\mathbb{R} |x|_\infty^{a-1} |1-x|_\infty^{b-1} \, d_\infty x \tag{4}$$

$$= g_\infty^2 \, \frac{\zeta(1-a)}{\zeta(a)} \, \frac{\zeta(1-b)}{\zeta(b)} \, \frac{\zeta(1-c)}{\zeta(c)}, \tag{5}$$

where $a, b, c \in \mathbb{C}$ are related to kinematical quantities with a condition $a+b+c=1$, $|\cdot|_\infty$ denotes the usual absolute value and ζ is the Riemann

zeta function. Then, the analogous p-adic Veneziano amplitude is defined as follows [3]:

$$A_p(a,b) = g_p^2 \int_{\mathbb{Q}_p} |x|_p^{a-1}\, |1-x|_p^{b-1}\, d_p x \tag{6}$$

$$= g_p^2\, \frac{1-p^{a-1}}{1-p^{-a}}\, \frac{1-p^{b-1}}{1-p^{-b}}\, \frac{1-p^{c-1}}{1-p^{-c}}, \tag{7}$$

where a, b and c are the same quantities as in the above real case. It is obvious that the amplitude in (7) is symmetric under any interchange among a, b and c. Note that the form of expressions (4) and (6) is the same and contains analogous ingredients. Only the integration is different–along a real axis in (4) and over $\mathbb{Q}_p$ in (6). On the integration of the p-adic integral in (6), one can see [4, 5]. Finally, one can say that the difference between p-adic and ordinary strings is in their world-sheets, i.e., p-adic and real world-sheets, respectively. Both these kinds of strings are related to tachyons [4].

Taking the product of (7) over all primes and using the Euler expression of the Riemann ζ function, one obtains the Freund–Witten formula [13] for the above Veneziano amplitudes:

$$A(a,b) = A_\infty(a,b) \prod_p A_p(a,b) = g_\infty^2 \prod_p g_p^2 = const. \tag{8}$$

Formula (8) tells us: (a) that the amplitudes of the above p-adic and ordinary strings are connected on equal footing, (b) that they may be different faces of an adelic string and (c) that complicate ordinary amplitude with the Riemann zeta function can be expressed as the infinite product of inverse p-adic amplitudes, which are simpler and elementary functions.

By a similar procedure one can define the amplitudes for p-adic closed strings and the corresponding adelic formula also exists; as a review, see [4].

2.3. Effective field theory for p-adic open strings

It is very important that there is an effective field theory model which can reproduce the p-adic string amplitudes in (7). The corresponding action [9, 10] for the scalar field $\varphi(x)$ in D-dimensional Minkowski space is

$$S_p = \sigma_p \int d^D x \, \Big(-\frac{1}{2} \varphi \; p^{-\frac{1}{2m^2}\Box} \; \varphi + \frac{1}{p+1} \; \varphi^{p+1} \Big), \tag{9}$$

where $\sigma_p = \frac{m^D}{g_p^2} \frac{p^2}{p-1}$, p is any prime number and $\Box = -\frac{\partial^2}{\partial t^2} + \sum_{i=1}^{D-1} \frac{\partial^2}{\partial x^{i\,2}}$ is the d'Alembert operator ($c = 1$) in D-dimensional space-time. Note that action (9) is invariant (symmetric) under discrete transformation $\varphi \to -\varphi$ if the prime number $p \geq 3$ and is asymmetric when $p = 2$. Field φ and mass

parameter m can also depend on the prime p, but, for simplicity, we omit index p. A similar, effective field theory was also constructed for closed p-adic strings. This model (9) describes not only four-point scattering amplitudes (7) but also all higher (Koba-Nielsen) ones at the tree-level.

The corresponding Lagrangian

$$\mathcal{L}_p = \sigma_p \Big(-\frac{1}{2}\varphi\, p^{-\frac{1}{2m^2}\Box}\, \varphi + \frac{1}{p+1}\, \varphi^{p+1}\Big), \tag{10}$$

contains a nonlocal kinetic term with infinitely many space-time derivatives in the form $p^{-\frac{1}{2m^2}\Box}$ and nonlinear potential with φ^{p+1} self-interaction.

The equation of motion (EoM) related to Lagrangian (10) is

$$p^{-\frac{1}{2m^2}\Box}\varphi \equiv e^{-\frac{\ln p}{2m^2}\Box}\varphi = \varphi^p. \tag{11}$$

There are trivial solutions $\varphi = 0, +1$ for any p as well as $\varphi = -1$, when $p \neq 2$. In the Minkowski space, there is a nontrivial homogeneous and isotropic time-dependent solution

$$\varphi(t) = p^{\frac{1}{2(p-1)}} \exp\Big(\frac{p-1}{2p\ln p} m^2 t^2\Big) \tag{12}$$

and also an inhomogeneous solution in any spatial direction x^i

$$\varphi(x^i) = p^{\frac{1}{2(p-1)}} \exp\Big(-\frac{p-1}{2p\ln p} m^2 (x^i)^2\Big). \tag{13}$$

In D-dimensional space-time, the solution is [12]

$$\varphi(x) = p^{\frac{D}{2(p-1)}}\, \exp\Big(-\frac{p-1}{2\,p\ln p}\, m^2\, x^2\Big), \quad x^2 = -t^2 + \sum_{i=1}^{D-1} (x^i)^2. \tag{14}$$

The solution in (12) can be obtained employing the identity

$$e^{A\partial_t^2}\; e^{Bt^2} = \frac{1}{\sqrt{1-4AB}} e^{\frac{Bt^2}{1-4AB}}, \quad 1-4AB > 0. \tag{15}$$

All the above solutions of EoM (11) are unstable [17].

The corresponding potential $\mathcal{V}_p(\varphi) = -\mathcal{L}_p(\Box = 0)$ of Lagrangian (10) is

$$\mathcal{V}_p(\varphi) = \sigma_p\Big[\frac{1}{2}\varphi^2 - \frac{1}{p+1}\varphi^{p+1}\Big], \tag{16}$$

which has local minimum $\mathcal{V}_p(0) = 0$ for all p and local maxima $\mathcal{V}_2(1) = \frac{\sigma_2}{6}$ and $\mathcal{V}_p(\pm 1) = \sigma_p \frac{p-1}{2(p+1)}$, when $p \neq 2$. When $p = 2$ and $p = 3$, these

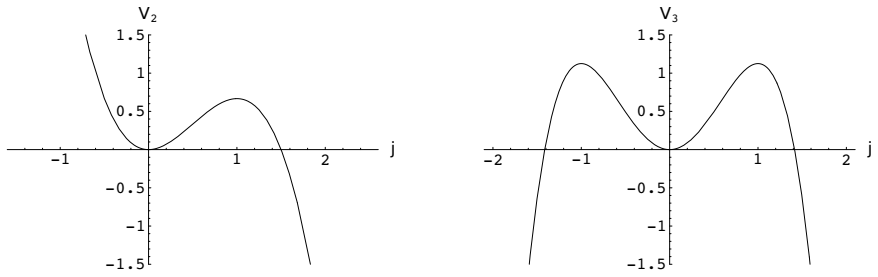

Figure 1: The 2-adic string potential $\mathcal{V}_2(\varphi)$ (on the left) and 3-adic potential $\mathcal{V}_3(\varphi)$ (on the right) of standard Lagrangian (10), where potential is presented by expression (16) with $\sigma_p = 1$.

potentials are illustrated at Figure 1. When $p \neq 2$, all potentials are an even (symmetric) function of φ.

Let us consider the above scalar field φ in a vicinity of its unstable value $\varphi = 1$, i.e., let us take $\varphi = 1 + \eta$, where $|\eta| \ll 1$. Then, EoM (11) becomes

$$p^{-\frac{1}{2m^2}\Box}(1+\eta) = (1+\eta)^p \approx (1+p\,\eta), \quad \Longrightarrow p^{-\left(\frac{M^2}{2m^2}+1\right)}\,\eta = \eta, \tag{17}$$

which gives $M^2 = -2m^2$, i.e., the scalar field η (φ) presents a tachyon.

3. Scalar p-adic matter

We are now going to slightly modify Lagrangian (10) with the intention to obtain a new Lagrangian for a similar scalar particle which is not a tachyon. Another direction of research based on Lagrangian (10) is towards zeta strings that take into account the effects of p-adic strings over all primes p; see [18] and references therein.

3.1. Non-tachyonic p-adic scalar field in Minkowski space

For a prime p, let us consider the transition $-m^2 \to m^2$ in (10); see also consideration in [1, 19, 20]. To differ from a tachyon, we denote this new scalar p-adic field by ϕ. Note that, by replacing $-m^2$ with m^2, the new related Lagrangian becomes

$$L_p(\phi) = (-1)^{\frac{D}{2}}\,\sigma_p\Big[-\frac{1}{2}\,\phi\,p^{\frac{\Box}{2m^2}}\,\phi + \frac{1}{p+1}\,\phi^{p+1}\Big], \tag{18}$$

where the change $\sigma_p \to (-1)^{\frac{D}{2}}\sigma_p$ is taken into account. Depending on space-time dimensionality D, we have

$$(-1)^{\frac{D}{2}} = \begin{cases} +1 & \text{if } D = 4k \\ -1 & \text{if } D = 4k+2 \\ +i & \text{if } D = 4k+1 \\ -i & \text{if } D = 4k+3, \end{cases} \tag{19}$$

where $k \in \mathbb{N}$. According to (19), it follows that Lagrangian (18) can be real only when space-time dimensionality $D = 2, 4, 6, ...$ Note that the kinetic term is positive when $D = 4k+2$, i.e., including $D = 10$ and 26, which are critical dimensions in string theory.

The equation of motion for the scalar field ϕ is

$$p^{\frac{\Box}{2m^2}}\,\phi = \phi^p \tag{20}$$

and it has the same trivial solutions as the previous field φ, i.e., $\phi = 0$ and $\phi = 1$ for any p and $\phi = -1$, if $p \neq 2$. There are also nontrivial solutions, such as (12)–(14), where one has to replace m^2 with $-m^2$.

When $D = 2 + 4k$, Lagrangian (18) is

$$L_p(\phi) = \sigma_p\Big[\frac{1}{2}\,\phi\, p^{\frac{\Box}{2m^2}}\,\phi - \frac{1}{p+1}\,\phi^{p+1}\Big], \tag{21}$$

and the corresponding potential becomes

$$V_p(\phi) = \sigma_p\Big[\frac{1}{p+1}\,\phi^{p+1} - \frac{1}{2}\phi^2\Big]. \tag{22}$$

Note that, now, $L_p(\phi) = -\mathcal{L}_p(\varphi)$ and $V_p(\phi) = -\mathcal{V}_p(\varphi)$.

The trivial solutions of EoM (20) have the following meaning: $\phi_p = 0$ is a local maximum and $\phi_2 = +1$ and $\phi_p = \pm 1$, with $p \neq 2$, are local minima; see also Figure 2.

Let us consider field ϕ around minima $\phi = \pm 1$. For example, let $\phi = 1 + \theta$ in the case when $D = 2 + 4k$. Then, the EoM for weak field θ, i.e., $|\theta| \ll 1$, becomes

$$p^{\frac{\Box}{2m^2}}\,(1+\theta) = (1+\theta)^p, \quad \Rightarrow \quad p^{\frac{\Box}{2m^2}}\,\theta = p\,\theta. \tag{23}$$

Let us look for a solution of EoM $p^{\frac{\Box}{2m^2}}\,\theta = p\,\theta$ in some detail. In fact, we have equation

$$e^{\frac{\ln p}{2m^2}\Box}\,\theta = \Big(1 + \frac{\ln p}{2m^2}\Box + \big(\frac{\ln p}{2m^2}\big)^2\frac{\Box^2}{2!} + ...\Big)\,\theta = p\,\theta, \tag{24}$$

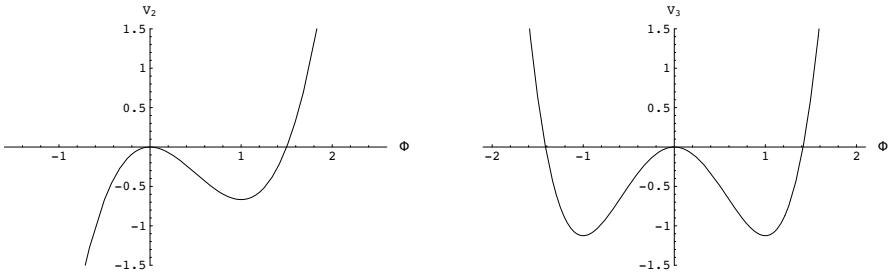

Figure 2: New potentials $V_2(\phi)$ and $V_3(\phi)$, which are defined by (22). This is the same potential as in Figure 1, but with opposite sign.

which has a solution when the following Klein-Gordon equation is satisfied:

$$(\Box - 2m^2)\ \theta = 0, \quad \text{where} \quad \Box = -\frac{\partial^2}{\partial t^2} + \sum_{i=1}^{D-1} \frac{\partial^2}{\partial {x^i}^2} \tag{25}$$

and we have that $\theta \sim e^{\pm i(-Et + \vec{k}\vec{x})}$ is a scalar field with $E^2 = 2m^2 + \vec{k}^2$.

The above consideration is related to a scalar field in the D-dimensional Minkowski space. In the next subsection, we want to study some cosmological aspects of field θ in 4-dimensional space–time.

3.2. A closed universe with p-adic matter

Let us start with a 4-dimensional gravity with a nonlocal scalar field ϕ and cosmological constant Λ, given by the Einstein-Hilbert action

$$S = \gamma \int \sqrt{-g}\ d^4x\ (R - 2\Lambda) + S_m, \tag{26}$$

where $\gamma = \frac{1}{16\pi G}$, R is the Ricci scalar and

$$S_m = \sigma \int \sqrt{-g}\ d^4x\ \big(\frac{1}{2}\phi F(\Box)\phi - U(\phi)\big), \tag{27}$$

where $F(\Box) = \sum_{n=0}^{\infty} f_n\ \Box^n$ is a nonlocal operator and $U(\phi)$ is a part of the potential. Note that, now, $\Box = \nabla_\mu \nabla^\mu = \frac{1}{\sqrt{-g}} \partial_\mu \sqrt{-g} g^{\mu\nu} \partial_\nu$.

According to the variation in action (26), with respect to $\delta g^{\mu\nu}$ and $\delta\phi$ and the principle of least action, the equations of motion for gravity field $g_{\mu\nu}$ and scalar field ϕ are as follows:

$$\gamma(G_{\mu\nu} + \Lambda g_{\mu\nu}) - \frac{\sigma}{4}\ g_{\mu\nu}\ \phi F(\Box)\phi + g_{\mu\nu}\ \frac{\sigma}{2}\ U(\phi) + \frac{\sigma}{4}\ \Omega_{\mu\nu}(\phi) = 0, \tag{28}$$

$$F(\Box)\phi - U'(\phi) = 0, \tag{29}$$

where

$$\Omega_{\mu\nu}(\phi) = \sum_{n=1}^{\infty} f_n \sum_{\ell=0}^{n-1} \Big[g_{\mu\nu} \ \big(\nabla^{\alpha} \Box^{\ell} \phi \nabla_{\alpha} \Box^{n-1-\ell} \phi + \Box^{\ell} \phi \Box^{n-\ell} \phi \big) - 2 \nabla_{\mu} \Box^{\ell} \phi \nabla_{\nu} \Box^{n-1-\ell} \phi \Big]. \tag{30}$$

For details about the derivation of equations of motion (28), one can see [21].

As a matter, I take the p-adic scalar field given by its action (21)

$$S_p = \sigma_p \int \sqrt{-g} \ d^4x \ \Big(\frac{1}{2} \phi \ p^{\frac{1}{2m^2} \Box} \ \phi - \frac{1}{p+1} \ \phi^{p+1} \Big), \tag{31}$$

where, again, $\sigma_p = \frac{m_p^D}{g_p^2} \frac{p^2}{p-1}$ and p is a prime number. Note that in (31), the space-time is 4-dimensional and the signs in the Lagrangian are those as in the case $D = 4k + 2$. The reason for this choice is to have the correct sign in front of the kinematic term.

The equation of motion for p-adic field ϕ has the same form as the previous one, (20), i.e.,

$$p^{\frac{1}{2m^2} \Box} \phi \equiv e^{\frac{\ln p}{2m^2} \Box} \phi = \phi^p, \tag{32}$$

but $\Box$ now depends on the gravity field $g_{\mu\nu}$. It has the same trivial solutions, as in the Minkowski space-time.

The potential $V_p(\phi)$ is already given by expression (22) and V_2 and V_3 are presented in Figure 2.

In the sequel, we are interested in cosmological solutions of the equations of motion (28) and (29) in the homogeneous and isotropic space given by the Friedmann-Lemaître-Robertson-Walker (FLRW) metric

$$ds^2 = -dt^2 + a(t) \Big(\frac{dr^2}{1 - kr^2} + r^2 \ d\theta^2 + r^2 \sin^2 \theta \ d\varphi^2 \Big), \tag{33}$$

where $a(t)$ is the cosmic scale factor and $k = 0, +1, -1$ for the plane, closed and open universe, respectively. Owing to the symmetries, there are only two independent equations of motion (28), which can be the trace

$$4\Lambda - R - \sigma \phi F(\Box) \phi + 2\sigma U(\phi) + \frac{\sigma}{4} \Omega = 0 \tag{34}$$

and 00-component

$$\gamma (G_{00} - \Lambda) + \frac{\sigma}{4} \ \phi F(\Box) \phi - \frac{\sigma}{2} \ U(\phi) + \frac{\sigma}{4} \ \Omega_{00}(\phi) = 0, \tag{35}$$

where $\Omega = g^{\mu\nu}\Omega_{\mu\nu}$. We will return to (34) and (35) after some elaboration of the EoM for field ϕ in (32).

Let us look for a solution of (32) in a weak field approximation around local minimum $\phi = 1$, that is, $\phi = 1 + \theta$, where $|\theta| \ll 1$. As in (23), again, we have

$$p^{\frac{\Box}{2m^2}}\,(1+\theta) = (1+\theta)^p, \quad \Rightarrow \quad p^{\frac{\Box}{2m^2}}\,\theta = p\,\theta, \tag{36}$$

where, now,

$$\Box = -\frac{\partial^2}{\partial t^2} - 3H\frac{\partial}{\partial t}, \quad H = \frac{\dot{a}}{a} \tag{37}$$

and H is the Hubble parameter.

Equation

$$p^{\frac{\Box}{2m^2}}\,\theta = p\,\theta \tag{38}$$

has solution if there is a solution of $\Box\theta = 2m^2\theta$, i.e.,

$$\frac{\partial^2\theta}{\partial t^2} + 3H\frac{\partial\theta}{\partial t} + 2m^2\theta = 0, \tag{39}$$

where the Hubble parameter $H = \dot{a}/a$ may be a function of cosmic time, which depends on the scale factor $a(t)$. The simplest case is $H = constant$ and it corresponds to the scale factor $a(t) = Ae^{Ht}$. When H is constant, equation (39) is a linear differential equation with constant coefficients and has solution in the form $\theta(t) = C\ e^{\lambda t}$, where λ must satisfy the quadratic equation

$$\lambda^2 + 3H\lambda + 2m^2 = 0. \tag{40}$$

The solution of equation (40) has the form $\lambda_{1,2} = \frac{-3H\pm\sqrt{9H^2-8m^2}}{2}$, where H and m can be connected as $H = \pm m$, which yields the simple solutions $\lambda_\pm = \pm m$. It follows that the general solution of equation (39) can be written in the form

$$\theta(t) = C_-\ e^{-mt} + C_+\ e^{+mt} = \theta_-(t) + \theta_+(t), \tag{41}$$

where C_- and C_+ are integration constants. Note that H and λ must have opposite sign. Hence, we have the following pairs:

$$\big(a_+(t), \theta_-(t)\big): \qquad a_+(t) = A_+e^{+mt}, \quad \theta_-(t) = C_-e^{-mt}, \tag{42}$$

$$\big(a_-(t), \theta_+(t)\big): \qquad a_-(t) = A_-e^{-mt}, \quad \theta_+(t) = C_+e^{+mt}, \quad . \tag{43}$$

The next step is to explore how the solution in (41) satisfies the corresponding equations of motion for a gravitational field. To this end, we

have to rewrite the Einstein–Hilbert action with weak field approximation for scalar field ϕ, i.e., we have to rewrite (26) in terms of field θ. The corresponding action is

$$S = \gamma \int d^4x \, \sqrt{-g} \, (R - 2\Lambda) + \sigma_p \int d^4x \, \sqrt{-g} \, \Big(\frac{1}{2} \, \theta p^{\frac{\Box}{2m^2}} \theta - \frac{p}{2}\theta^2 + \alpha_p \Big), \tag{44}$$

where $\alpha_p = \frac{p-1}{2(p+1)}$.

The potential $V_p(\theta) = -L_p(\Box = 0)$ is

$$V_p(\theta) = \sigma_p \big(\frac{p-1}{2}\theta^2 - \alpha_p \big) \tag{45}$$

and it has the form resembling that of the harmonic oscillator.

We can now return to the equations of motion (34) and (35). With the relevant replacements

$$\phi \to \theta, \quad \sigma \to \sigma_p, \quad U(\theta) = \frac{p}{2}\theta^2 - \alpha_p, \tag{46}$$

we have

$$\gamma(4\Lambda - R) - \sigma_p \, \theta F(\Box)\theta + 2\sigma_p \, (\frac{p}{2} \, \theta^2 - \alpha_p) + \frac{\sigma_p}{4} \, \Omega = 0, \tag{47}$$

$$\gamma(G_{00} - \Lambda) + \frac{\sigma_p}{4} \, \theta F(\Box)\theta - \frac{\sigma_p}{2} \, (\frac{p}{2}\theta^2 - \alpha_p) + \frac{\sigma_p}{4} \, \Omega_{00}(\theta) = 0, \tag{48}$$

where

$$F(\Box) = p^{\frac{\Box}{2m^2}} = \sum_{n=0}^{\infty} \Big(\frac{\ln p}{2m^2} \Big)^n \frac{1}{n!} \, \Box^n = \sum_{n=0}^{\infty} f_n \Box^n. \tag{49}$$

We have shown above that there is a field θ which satisfies the EoM $p^{\frac{\Box}{2m^2}} \theta = p \, \theta$. This simplifies the above equations and we come to

$$\gamma(4\Lambda - R) - 2\sigma_p \alpha_p + \frac{\sigma_p}{4} \, \Omega(\theta) = 0, \tag{50}$$

$$\gamma(G_{00} - \Lambda) + \frac{\sigma_p}{2} \, \alpha_p + \frac{\sigma_p}{4} \, \Omega_{00}(\theta) = 0. \tag{51}$$

Let us recall that, in the FLRW metric,

$$G_{00} = 3\Big(\frac{\dot{a}^2}{a^2} + \frac{k}{a^2} \Big), \quad R = 6\Big(\frac{\ddot{a}}{a} + \frac{\dot{a}^2}{a^2} + \frac{k}{a^2} \Big). \tag{52}$$

Computation (52) for the scale factors $a_+(t) = A_+e^{+mt}$ and $a_-(t) = A_-e^{-mt}$ gives

$$G_{00}^{(+)} = 3\Big(m^2 + \frac{k}{a_+^2}\Big) = 3\Big(m^2 + \frac{k}{A_+^2}\ e^{-2mt}\Big), \tag{53}$$

$$G_{00}^{(-)} = 3\Big(m^2 + \frac{k}{a_-^2}\Big) = 3\Big(m^2 + \frac{k}{A_-^2}\ e^{+2mt}\Big), \tag{54}$$

$$R_+ = 6\Big(2m^2 + \frac{k}{a_+^2}\Big) = 6\Big(2m^2 + \frac{k}{A_+^2}\ e^{-2mt}\Big), \tag{55}$$

$$R_- = 6\Big(2m^2 + \frac{k}{a_-^2}\Big) = 6\Big(2m^2 + \frac{k}{A_-^2}\ e^{+2mt}\Big). \tag{56}$$

Direct calculation of $\Omega(\theta) = g^{\mu\nu}\ \Omega_{\mu\nu}(\theta)$ and $\Omega_{00}(\theta)$, where (see (31))

$$\Omega_{\mu\nu}(\theta) = \sum_{n=1}^{\infty} f_n \sum_{\ell=0}^{n-1} \Big[g_{\mu\nu}\ \big(\nabla^\alpha \Box^\ell \theta \nabla_\alpha \Box^{n-1-\ell}\theta + \Box^\ell \phi \Box^{n-\ell}\theta\big) - 2\nabla_\mu \Box^\ell \theta \nabla_\nu \Box^{n-1-\ell}\theta \Big], \tag{57}$$

yields

$$\Omega_- = \Omega(\theta_-) = 3p\ln p\ \theta_-^2 = 3p\ln p\ C_-^2\ e^{-2mt}, \tag{58}$$

$$\Omega_+ = \Omega(\theta_+) = 3p\ln p\ \theta_+^2 = 3p\ln p\ C_+^2\ e^{+2mt}, \tag{59}$$

$$\Omega_{00}^{(-)} = \Omega_{00}(\theta_-) = -\frac{3}{2}p\ln p\ \theta_-^2 = -\frac{3}{2}p\ln p\ C_-^2\ e^{-2mt}, \tag{60}$$

$$\Omega_{00}^{(+)} = \Omega_{00}(\theta_+) = -\frac{3}{2}p\ln p\ \theta_+^2 = -\frac{3}{2}p\ln p\ C_+^2\ e^{+2mt}. \tag{61}$$

One can now easily verify that EoM (50) and (51) are satisfied as follows:

$$\gamma(4\Lambda - R_\pm) - 2\sigma_p\alpha_p + \frac{\sigma_p}{4}\ \Omega_\mp = 0, \tag{62}$$

$$\gamma(G_{00}^{(\pm)} - \Lambda) + \frac{\sigma_p}{2}\ \alpha_p + \frac{\sigma_p}{4}\ \Omega_{00}^{\mp} = 0, \tag{63}$$

with the conditions

$$6\gamma m^2 + \sigma_p\alpha_p - 2\gamma\Lambda = 0, \quad p\ln p\ \sigma_p\ A_\pm^2 C_\mp^2 - 8\gamma k = 0, \quad k = +1, \tag{64}$$

or, in a more explicit form,

$$\Lambda = 3m^2 + \frac{4\pi G}{g^2}\frac{p^2}{p-1}m^4, \tag{65}$$

$$\frac{1}{\big(A_\pm C_\mp\big)^2} = \frac{2\pi G}{g^2}\frac{p^3\ln p}{p-1}m^4. \tag{66}$$

Therefore, there is a solution of the corresponding equations of motion only in the pair form $\big(a_\pm(t), \theta_\mp(t)\big)$.

4. Discussion and conclusion

According to the Standard Model of Cosmology (also called ΛCDM model), at the current cosmic time the universe consists approximately of 68 % of dark energy, 27 % of dark matter and only 5 % of ordinary (visible) matter. It is worth discussing now how this p-adic scalar particle (that we would like to call *p-adic scalaron*) could be related to dark energy and dark matter.

A possible connection with dark energy. Equation (65) contains the connection between the cosmological constant Λ, mass m of p-adic scalaron and any prime number p. For a small mass m, as well as not a big value of prime number p (it makes sense to take $p = 3$) and $g^2 \geq 1$, one can neglect the second term on the RHS with respect to $3m^2$. As a result, one obtains $\Lambda \approx 3m^2$, which is written in the natural units ($\hbar = c = 1$). In the international system of units (SI), the previous relation should be rewritten as

$$m \approx \frac{\hbar}{c^2}\sqrt{\frac{\Lambda}{3}}. \tag{67}$$

From (67), we can compute the approximate value of mass m, where

$$\hbar = 1.05{\times}10^{-34}\,\mathrm{m^2kg/s},\ \ c = 3{\times}10^{8}\,\mathrm{m/s}\ \text{and}\ \Lambda = 3H^2\Omega_\Lambda = 9.8{\times}10^{-36}\,\mathrm{s^{-2}}.$$

We obtain that the mass of p-adic scalaron is

$$m \approx 2.1 \times 10^{-69}\mathrm{kg}, \tag{68}$$

which is about a 10^{-39} part of the mass of the electron ($m_e = 9.1{\times}10^{-31}\,\mathrm{kg}$).

Note that, in the above approximation (67), the mass of the p-adic scalaron does not depend on p. However, if we take into consideration the term that depends on p, and the mass of the p-adic scalaron is invariant, then Λ explicitly depends on p. At very large values of p, the dependence of Λ on p cannot be ignored. In fact, in this model, formula (65) expresses the discrete spectrum of Λ, and thus the spectrum of the vacuum energy density, as a function of the prime number p. If the Λ of our universe has this discreteness, then it makes sense to assume that the energy density of the vacuum decreased discretely during evolution from some enormous value to very small in our time.

We should not forget that a p-adic scalaron is an effective description of a scalar particle whose world line is parameterized by p-adic numbers. It should also be noted that in the spirit of adelic description of strings, there can exist a string whose world-sheet can be real and p-adic. In the context of an adelic description, the p-adic scalaron can be considered as a special state of an adelic scalar particle. See also discussion of p-adic matter in the article [20].

Based on the above, it can be assumed that the vacuum is a mixture of real and p-adic states of matter at very small distances close to the Planck

length, and that the p-adic scalaron can be an important ingredient of the cosmological constant Λ, and thus of dark energy according to the current model of the universe.

A possible connection with dark matter. Since a p-adic scalaron has an extremely small mass (68) and so the gravitational force, it is unlikely to be detected in laboratory experiments. However, since it has an attractive self-interaction, the density of p-adic scalarons could be sufficiently large at the galactic scale and could play a significant role as dark matter. In fact, p-adic scalarons have nonlinear and nonlocal self-interaction that gives a solitonic form to the effective scalar field in the 4-dimensional Minkowski space, i.e.,

$$\varphi(x) = p^{\frac{2}{(p-1)}} \exp\Big(\frac{p-1}{2\,p\ln p}\,m^2\,x^2\Big), \quad x^2 = -t^2 + \sum_{i=1}^{3}(x^i)^2. \tag{69}$$

Note that some dark matter effects at the cosmic scale can be obtained as nonlocal modification of the Einstein gravity; see [22]. A role of nonlocality in cosmic dark energy, bouncing and cosmic acceleration is also considered in the framework of string field theory; e.g., see [23, 24] and references therein.

Connection with radius of a closed universe. Equality (66) tells us that the product of $A_\pm$ of the closed universe under consideration and amplitude $C_\mp$ of the p-adic scalaron field is a constant determined by the p-adic scalaron's mass m and a prime number p. One can take so small C_+ that A_- is equal to the radius R of the corresponding closed universe. Rewriting (66) and using the SI system, we have

$$A_- = R = P_p\,\sqrt{\frac{\hbar^3}{2\pi c}}\,\frac{1}{m^2\sqrt{G}}, \qquad P_p = \frac{g}{C_+}\,\sqrt{\frac{p-1}{p^3\ln p}}. \tag{70}$$

Now, one can estimate radius the $R = A_-$ of the related closed universe (where $G = 6.67\times 10^{-11}\,\mathrm{m^3kg^{-1}s^{-2}}$) , that is,

$$R = P_p\,\sqrt{\frac{\hbar^3}{2\pi c}}\,\frac{1}{m^2\sqrt{G}} \approx P_p\ \times 10^{87}\mathrm{m}, \tag{71}$$

which is a huge number, many times larger than the radius of our observable universe.

Conclusion. The main results presented in this paper are:

- Construction of Lagrangian for p-adic matter field and investigation of its equation of motion in weak field approximation.
- It is shown that a closed universe fulfilled by p-adic matter and a cosmological constant has an exponential expansion.
- A connection between the cosmological constant, the mass of p-adic scalar particle and prime numbers is obtained.

- The mass of p-adic scalar particle is computed.
- A formula that connects the radius of the closed universe under consideration with the mass of a p-adic scalar particle is obtained and the corresponding radius is estimated.
- The corresponding notion of p-adic scalaron is proposed and its possible connection with dark energy and dark matter is conjectured.

Acknowledgments

The author thanks Ivan Dimitrijevic, Zoran Rakic and Jelena Stankovic for useful discussions.

References

[1] B. Dragovich, "A p-adic matter in a closed universe", *Symmetry* **2022**, 14, 73 (2022) 1–14.

[2] I. V. Volovich, "p-Adic string", *Class. Quant. Grav.* **4** (1987) L83–L87.

[3] P. G. O. Freund and M. Olson, "Non-archimedean strings", *Phys. Lett. B* **199** (1987) 186–190.

[4] L. Brekke and P. G. O. Freund, "p-Adic numbers in physics," *Phys. Rep.* **233** (1993) 1–66.

[5] V. S. Vladimirov, I. V. Volovich and E. I. Zelenov, *p-Adic Analysis and Mathematical Physics* (World Scientific: Singapore, 1994).

[6] B. Dragovich, A. Yu. Khrennikov, S. V. Kozyrev and I. V. Volovich, "On p-adic mathematical physics", *p-Adic Numbers Ultrametr. Anal. Appl.* **1** (2009) 1–17.

[7] B. Dragovich, A. Yu. Khrennikov, S. V. Kozyrev, I. V. Volovich and E. I. Zelenov, "p-Adic mathematical physics: The first 30 years", *p-Adic Numbers Ultrametr. Anal. Appl.* **9** (2017) 87–121.

[8] I. V. Volovich, "p-Adic space-time and string theory", *Theor. Math. Phys.* **71** (1987) 574–576.

[9] L. Brekke, P. G. O. Freund, M. Olson and E. Witten, "Nonarchimedean string dynamics", *Nucl. Phys. B* **302** (1988) 365–402.

[10] P. H. Frampton and Y. Okada, "Effective scalar field theory of p-adic string", *Phys. Rev. D* **37** (1988) 3077–3084.

[11] N. Moeller and B. Zwiebach, "Dynamics with infinitely many time derivatives and rolling tachyons", *J. High Energy Phys.* **2002** (2002) 034.

[12] V. S. Vladimirov, "On some exact solutions in p-adic open-closed string theory", *p-Adic Numbers Ultrametr. Anal. Appl.* **4** (2012) 57–63.

[13] P. G. O. Freund and E. Witten, "Adelic string amplitudes", *Phys. Lett. B* **199** (1987) 191–194.

[14] I. Ya. Aref'eva, B. G. Dragovic and I. V. Volovich, "On the adelic string amplitudes", *Phys. Lett. B* **209** (1988) 445–450.

[15] I. M. Gelf'and, M. I. Graev and I. I. Pyatetskii-Shapiro, *Representation Theory and Automorphic Functions* (Saunders, Philadelphia, PA, USA, 1969).

[16] W. Schikhof, *Ultrametric Calculus* (Cambridge University Press, Cambridge, UK, 1984).

[17] P. H. Frampton and H. Nishino, "Stability analysis of p-adic string solitons", *Phys. Lett. B* **242** (1990) 354–356.

[18] B. Dragovich, "From p-adic to zeta strings", in Proceedings of the 1st Conference on Nonlinearity (23–25 November 2019, Serbian Academy of Nonlinear Sciences, Belgrade, Serbia) (2020) 14–28, arXiv:2007.13628.

[19] B. Dragovich, "p-Adic and adelic cosmology: p-adic origin of dark energy and dark energy", in *p-Adic Mathematical Physics*, American Institute of Physics **826** (2006) 25–42.

[20] B. Dragovich, "Towards p-adic matter in the universe", Springer Proceedings in Mathematics & Statistics **36** (2013) 13–24.

[21] I. Dimitrijevic, B. Dragovich, Z. Rakic and J. Stankovic, "Variations of infinite derivative modified gravity", *Springer Proceedings in Mathematics & Statistics* **263** (2018) 91–111.

[22] I. Dimitrijevic, B. Dragovich, Z. Rakic and J. Stankovic, "Cosmological solutions of nonlocal square root gravity", *Phys. Lett. B* **797** (2019) 134848.

[23] I. Ya. Arefeva, "Nonlocal string tachyon as a model for cosmological dark energy", in *p-Adic Mathematical Physics*, American Institute of Physics **826** (2006) 301–311.

[24] I. Ya. Arefeva, L. V. Joukovskaya and S. Y. Vernov, "Bouncing and acceleration solutions in nonlocal stringy models", *J. High Energy Phys.* **2007** (2007) 087.

Talks not presented to the Proceedings

1. Irina Ya. Arefeva „Holographic Renormalization Group Flows”
2. Milivoj Belić „Weird light propagation in strange and not-so-strange systems: From accelerating Airy to fractional Schrodinger beams”
3. Goran Djordjevic „Some Notes on the Time-Dependent Harmonic Oscillator”
4. Lyudmila Efremova „About Geometrically Integrable Discrete Dynamical Systems and Their Periodic Orbits”
5. Nenad Filipović „How far we are from insilico clinical trials for cardiovascular disease?”
6. Umaaran Gogilan „Implementation of state observer-based conditioned reverse path method to the identification of a nonlinear system”
7. Katica R. (Stevanovic) Hedrih „Angular velocity and intensity change of basic vectors of tangent space of a position vector of a material system kinetic particle in two generalized functional curvilinear coordinate system”
8. Bojana (Blagojević) Ilić „Global COVID-19 growth signatures used to characterize COVID-19 non-linear infection dynamics”
9. Božidar Jovanović „Integrable canonical transformations”
10. Yuri Kivshar „Nonlinear Nanophotonics and Metasurfaces”
11. Vera Markasheva „Asymptotic behavior of entire solutions for degenerate partial differential inequalities on Carnot-Carathéodory metric spaces and Liouville type results”
12. Sofija Marković „Inferring COVID-19 severity determinants by combining epidemiological modeling and machine learning”
13. Stanko Nikolić „The nature of optical rogue waves”
14. Sergei D. Odintsov „Use Axion modified gravity cosmology”
15. Paszkal Papp „Spatial separation of precipitate in reactive media”
16. Luka Popović „Supermassive binary black holes in centers of galaxies - theory vs. observations”

17. Alexander Prokopenya „Periodic Motion of a Swinging Atwood's Machine”
18. Zvonko Rakarić „A new mathematical and mechanical oscillatory model for the detection of ultra low frequency signals”
19. Andjela Rodić „Investigating the SARS-CoV-2 virus transmission using a nonlinear compartmental epidemiological model”
20. Vsevolod Sakbaev „Dynamics of quantum states generated by the nonlinear Schrodinger equation”
21. Miguel A. F. Sanjuan „Binary Black Hole Shadows: Chaos in General Relativity”
22. Denis Shulga „Quantum relaxation effects in Microtubules”
23. Jelena Stanković „Nonlocal de Sitter Gravity and its Cosmology”
24. Marko Stojanović „Attractor behaviour of the holographic inflation model with tachyon-type potentials”
25. Bosiljka Tadić „Modeling dynamics of magnetization reversal in geometrically frustrated nanonetworks”
26. Olena Vaneeva „Symmetries and exact solutions of nonlinear models of physical and biological processes”
27. Igor V. Volovich „Integrability of quantum and classical dynamical systems”
28. James Yorke „The equations of nature and the nature of equations”
29. Ryo Yoshida „Self-oscillating polymer gels as novel biomimetic soft materials”
30. Rade Živaljević „The problem of envy-free division from the view point of algebraic topology”

List of Participants

1. Andrew Adamatzky (Bristol, UK)
2. Irina Ya. Arefeva (Moscow, Russia)
3. Ivana Atanasovska (Belgrade, Serbia)
4. Milivoj Belić (Doha, Qatar)
5. Matthew Cartmell (Glasgow, UK)
6. Željko Čupić (Belgrade, Serbia)
7. Livija Cvetićanin (Novi Sad, Serbia)
8. Ivan Dimitrijević (Belgrade, Serbia)
9. Goran Djordjević (Niš, Serbia)
10. Branko Dragovich (Belgrade, Serbia)
11. Lyudmila Efremova (Nizhny Novgorod, Russia)
12. Mirjana Filipović (Belgrade, Serbia)
13. Nenad Filipović (Kragujevac, Serbia)
14. Fotios Georgiades (Chennai, India)
15. Umaaran Gogilan (Bochum, Germany)
16. Katica R. (Stevanovic) Hedrih (Niš, Serbia)
17. Bojana (Blagojević) Ilić (Belgrade, Serbia)
18. Božidar Jovanović (Belgrade, Serbia)
19. Dušan Jovanović (Belgrade, Serbia)
20. Predrag Jovanović (Belgrade, Serbia)
21. Ljubinko Kevac (Belgrade, Serbia)
22. Yuri Kivshar (Canberra, Australia)
23. Boris Malomed (Tel Aviv, Israel)
24. Aleksandra Maluckov (Belgrade, Serbia)
25. Vera Markasheva (Dolgoprudny, Russia)
26. Sofija Marković (Belgrade, Serbia)
27. Stanko Nikolić (Doha, Quatar)
28. Aleksandar Obradović (Belgrade, Serbia)
29. Sergei D. Odintsov (Barcelona, Spain)
30. Paszkal Papp (Szeged, Hungary)
31. Stepa Paunović (Belgrade, Serbia)